Turbulent Mixing in the Indonesian Seas

Adi Purwandana

THÈSE DE DOCTORAT
DE SORBONNE UNIVERSITÉ

Spécialité : Océanographie Physique

École doctorale : 129 – Science de l'environnement

Réalisée au :

Laboratoire d'Océanographie et du Climat :

Expérimentations et Approches Numériques

Présenté par :

Adi PURWANDANA

pour obtenir le grade de :

DOCTEUR DE SORBONNE UNIVERSITÉ

Titre de la thèse :

Turbulent Mixing in the Indonesian Seas

Dirigée par :

Mme. Pascale Bouruet-Aubertot, LOCEAN, Paris (Directrice de thèse)

M. Yannis Cuypers, LOCEAN, Paris (Co-directeur de thèse)

Soutenance prévue le 23 Septembre 2019
devant le jury composé de :

M. Francis Codron	LOCEAN, Paris	Président
M. Herlé Mercier	LOPS-IFREMER, Brest	Rapporteur
M. Louis Gostiaux	MFAE/LMFA EC, Lyon	Rapporteur
M. Bruno Ferron	LOPS- IFREMER, Brest	Examinateur
M. Jérôme Vialard	LOCEAN, Paris	Examinateur
M. Agus S. Atmadipoera	IPB, Bogor	Examinateur

La turbulence dans les mers Indonésiennes

Résumé

La région des mers indonésiennes est la région la plus énergétique en termes de transfert de la marée barotrope vers la marée barocline comme démontré par des études s'appuyant sur des modèles de marée. Ces processus font des mers indonésiennes un des haut-lieux de la turbulence comme en témoigne le fort mélange des masses d'eaux originaires du Pacifique et s'écoulant à travers les détroits indonésiens vers l'océan Indien. La première partie de ce travail visait à mieux caractériser et comprendre la forte variabilité spatiale du mélange turbulent à partir de l'analyse d'un jeu de données historiques, sur une période de 26 ans, de profils de température et conductivité. La méthode classique de Thorpe, utilisée pour déduire les taux de dissipation à partir des inversions de densité, a été améliorée et validée avec des mesures microstructure de turbulence. Nous avons ainsi montré que la dissipation d'énergie cinétique turbulente est accrue dans les détroits et les passages étroits le long de la pente continentale et contrôlée majoritairement par la marée semi-diurne, M2. Nous nous sommes ensuite focalisés sur les ondes internes solitaires, un processus facilement identifié sur les images satellitaires mais rarement étudié précisément dans la région. À partir de simulations bidimensionnelles non hydrostatiques nous avons caractérisé le cycle de vie des ondes internes solitaires observées dans une zone côtière de la mer de Sulawesi. Nous avons ainsi montré que la marée interne générée dans le passage de Sibutu évolue au cours de sa propagation donnant naissance à des ondes internes solitaires qui déferlent sur la côte Nord de l'île de Sulawesi. Nous avons également estimé la part d'énergie de la marée interne transférée vers ces ondes et estimé les forts taux de dissipation associés au déferlement de ces ondes solitaires. Afin d'explorer plus en détail ces processus de haute fréquence induits par la marée, nous avons mené une campagne préliminaire dans le détroit de Lombok, un hot spot des ondes internes solitaires, en y déployant un mouillage. Nous avons ainsi montré que le maximum de dissipation se produit à une fréquence semi-diurne mettant ainsi en lumière le rôle moteur de la marée semi-diurne sur la turbulence dans cette région.

Mots-clés : turbulence, mélange, CTD, mers indonésienne, échelle de Thorpe, échelle de Ellison

---

Turbulence in the Indonesian Seas

Abstract

The Indonesian seas are the area where the largest energy transfers from barotropic to baroclinic tides occur as shown by tidal model based studies. These processes make it a hotspot for turbulence as indirectly evidenced through the strong watermass mixing of Pacific waters flowing through the Indonesian Seas toward the Indian Ocean. The first part of this work aimed at better characterizing the strong spatial variability of turbulent mixing based on the analysis of a unique 26 years historical dataset of temperature and conductivity profiles. The classical Thorpe scale method, used to infer the dissipation rates from density measurements, was improved and validated against turbulence measurements. We showed that the turbulent kinetic energy dissipation is enhanced within straits and narrowing passages, in shallowing topography and mostly driven by semidiurnal, M2 internal tides. We then focused on internal solitary waves, a process easily identified from satellite imagery but rarely studied precisely in the area. Based on two-dimensional non-hydrostatic simulations we gave evidence of the full lifetime cycle of internal solitary waves observed in a coastal area in the Sulawesi Sea. We thus showed that the internal tide generated at the Sibutu passage evolves during its propagation leading to the formation of solitary waves that extract a significant part of the internal tide energy and eventually break in the northern coast of Sulawesi Island. We investigated the mechanisms driving the enhanced dissipation rates accompanying the shoaling internal waves in this region. To further explore these high-frequency processes tidally induced, we conducted a short-time mooring experiment in the Lombok Strait, one hot spot for internal solitary waves and proved that the maximum dissipation rate occurs at semi-diurnal frequency thus giving evidence of the semi-diurnal internal tide as a main driver for turbulence there.

Keywords: turbulence, mixing, CTD measurements, Indonesian seas, Thorpe scale, Ellison scale

Acknowledgments

Alhamdulillahirrabbil 'alaamiin… This thesis is just the beginning of a huge collaborative researches between *Laboratoire d'Océanographie et de Climatologie par Experimentation et Approche Numérique* (LOCEAN) Sorbonne Université and Laboratory of Physical Oceanography-Research Center for Oceanography, Indonesian Institute of Sciences (LIPI). This research has been fully supported by Indonesian Endowment Fund for Education (LPDP) Indonesian Ministry of Finance, Campus France and Indonesian Ministry of Research and Technology.

My sincerest gratefulness goes to my advisors, firstly to my principal advisor Prof. Pascale Bouruet-Aubertot for her super patience and supportive suggestions for guiding me to find a specialty of my research interests. Secondly, thanks to Dr. Yannis Cuypers as my second advisor for his patience to guide me from nothing, for giving me an insights that every valuable thing is not always rising from a fully facilitated project. His valuable skills have inspired me very much.

My deepest appreciations to Dr. Daniel Bourgault from *Institut des Sciences de la Mer de Rimouski*, Université du Québec à Rimouski, Canada for helping me to handle the Aestus; to Prof. Darminto (Dept. of Physics, Sepuluh Nopember Institute of Technology, ITS) and Dr. Agus S. Atmadipoera (Dept. Marine Sciences, Bogor Agricultural University, IPB) for giving me a recommendations to LPDP. Also to my colleague Hendra Munandar (Head of LKBL-LIPI Research Station Lombok) and all of his staffs, for preparing us accommodations during the Lombok field research.

A special thanks to my lovely family, Titik Setyorini-Ayu Lestari, my grand son Fayzul Islam Ajda Abhar Jihadiy, my lovely daughter Fayza Tsaqifa Islamia Najda Karim, for their love, prayers and cares. You're all my inspiration.

Eventually, I dedicate this thesis to my parents, *Bu'e* Siti Suwardani, Bapak Purnomo, my little son Mochammad Ichsan Purwandana, and the next…, Khadijah Putri Purwandana/ Mochammad Achsan Purwandana, *in sya'allah*… also to my brother Toto Cahyo Purniawan.

Contents

List of Figures

List of Tables

List of Abbreviations

ITF	Indonesian Throughflow
NPSW	North Pacific Subtropical Water
SPSW	South Pacific Subtropical Water
NPIW	North Pacific Intermediate Water
SPIW	South Pacific Intermediate Water
NIIW	North Indian Intermediate Water
NISW	North Indian Subtropical Water
ISW	Internal Solitary Wave
NLIW	Non Linear Internal Wave
MODIS	Moderate Resolution Imaging Spectro-radiometer
NPS	Nusa Penida Sill
JADE	Java-Australia Dynamic Experiment
ARLINDO	Arus Lintas Indonesia Expedition
INSTANT	International Nusantara STratification ANd Transport
EWIN	Expedition of Widya Nusantara
INDOMIX	Indonesian Mixing Expedition
PE	Potential Energy
KE	Kinetic Energy
TKE	Turbulent Kinetic Energy
APE	Available Potential Energy
CTD	Conductivity, Temperature, Depth
XBT	eXpendable BathyThermograph
VMP	Vertical Microstructure Profiler
ADCP	Acoustic Doppler Current Profiler
KH	Kelvin-Helmholtz
GM	Garret and Munk model (Garrett and Munk, 1972)
DC	Diffusive Convection
SF	Salt Fingering

List of Symbols

g	gravitational acceleration	ms^{-2}
ζ	isopycnal vertical displacement	m
ζ_z	strain, vertical derivative of ζ	
N	buoyancy (Brunt-Vaisala) frequency	s^{-2}
S	vertical velocity shear	s^{-2}
f	Coriolis parameter	rad s^{-1}
ε	turbulent kinetic energy dissipation rate	m^2s^{-3}, W kg^{-1}
ν	kinematic viscosity	m^2s^{-1}
L_O	Ozmidov length scale (Ozmidov, 1965)	m
L_T	Thorpe scale (Thorpe, 1977)	m
L_E	Ellison scale (Ellison, 1957)	m
Re	Reynold number	
Re_b	turbulence intensity	
Ri	Richardson number	
Ro	Overturn ratio	
Γ	mixing efficiency (Osborn, 1980)	
K_ρ	diapycnal turbulent diffusivity	m^2s^{-1}
a	thermal expansion coefficient	$^oC^{-1}$
β	saline contraction coefficient	kg g^{-1}
R_ρ	density ratio	
Tu	Turner angle	^{o}

1 Introduction

Chapter 1
Introduction

1.1 Rationale

The milestone of physical oceanography observations in the Indonesian seas started with two Dutch Expeditions: the first one, the Siboga, took place over a year from March 1899 until February 1900 while the second one, the Snellius, took place about 30 years later, from July 1929 until November 1930. One of the remarkable discoveries by the Siboga expedition was to highlight the presence of topographic barriers separating the deep waters of the interior seas of the Indonesian archipelago from the neighboring Pacific and Indian oceans. It was argued that the presence of these topographic barriers was responsible for the almost uniform temperature, observed at depth, below 1,600 meters, a temperature of about 3°C which is warmer compared to the adjacent oceans (Anonym, 1900). A few decades later, using the Dutch ship, HNMS Willebrord Snell, the Snellius expedition was conducted, led by Dr. P.M. van Riel. The most remarkable finding was to evidence the influence of tides in the near bottom layer from current measurements at two deep anchored stations (2300 in the Makassar Strait and 1300 m depth in the western Savu Strait). **Figure 1.1** shows the stations observations of Snellius Expedition in 1929. These observations were later complemented by characterization of high frequency variations of the sea water properties that were attributed to internal tides (van Riel, 1932, 1930).

It is only decades later, after the independence of Indonesia from Dutch colonialism, that the first oceanography expeditions focusing on physical system of the Indonesian seas were conducted. The first research program was the JADE program (Java-Australia Dynamic Experiment), gathering Indonesian and French researchers. The purpose of the project that took place from 1989 until 1995 was to monitor the inflow from the Pacific Ocean and the outflow into the Indian Ocean. **Figure 1.2** shows the stations observations of the JADE Expedition in 1989. To this aim numerous moorings were deployed at the entrance passages and along the exit passages into the Indian Ocean between Bali and Australia (Fieux et al., 1994; Fieux and Molcard, 1996) as well as in various straits of the Lesser Sunda Islands (Molcard et al., 2001). The second extensive expedition is ARLINDO Project, a joint research program between Indonesia and USA that took place from 1991 until 1998, aimed to monitor the circulation and water masses in the Indonesian seas. To quantify Indonesian throughflow (hereinafter, ITF) transport precisely and simultaneously in different key locations, an

international program involving some countries: Australia, France, Indonesia, Netherlands and the United States namely INSTANT (International Nusantara Stratification and Transport) was conducted in 2003-2005. **Figure 1.3** shows the stations observations during INSTANT era. This program successfully quantified the transport from the Pacific Ocean into the Indian Ocean from numerous moorings in the inlet and outlet passages (Atmadipoera et al., 2009; Dwi Susanto et al., 2012; Gordon, 2005; Sprintall et al., 2009).

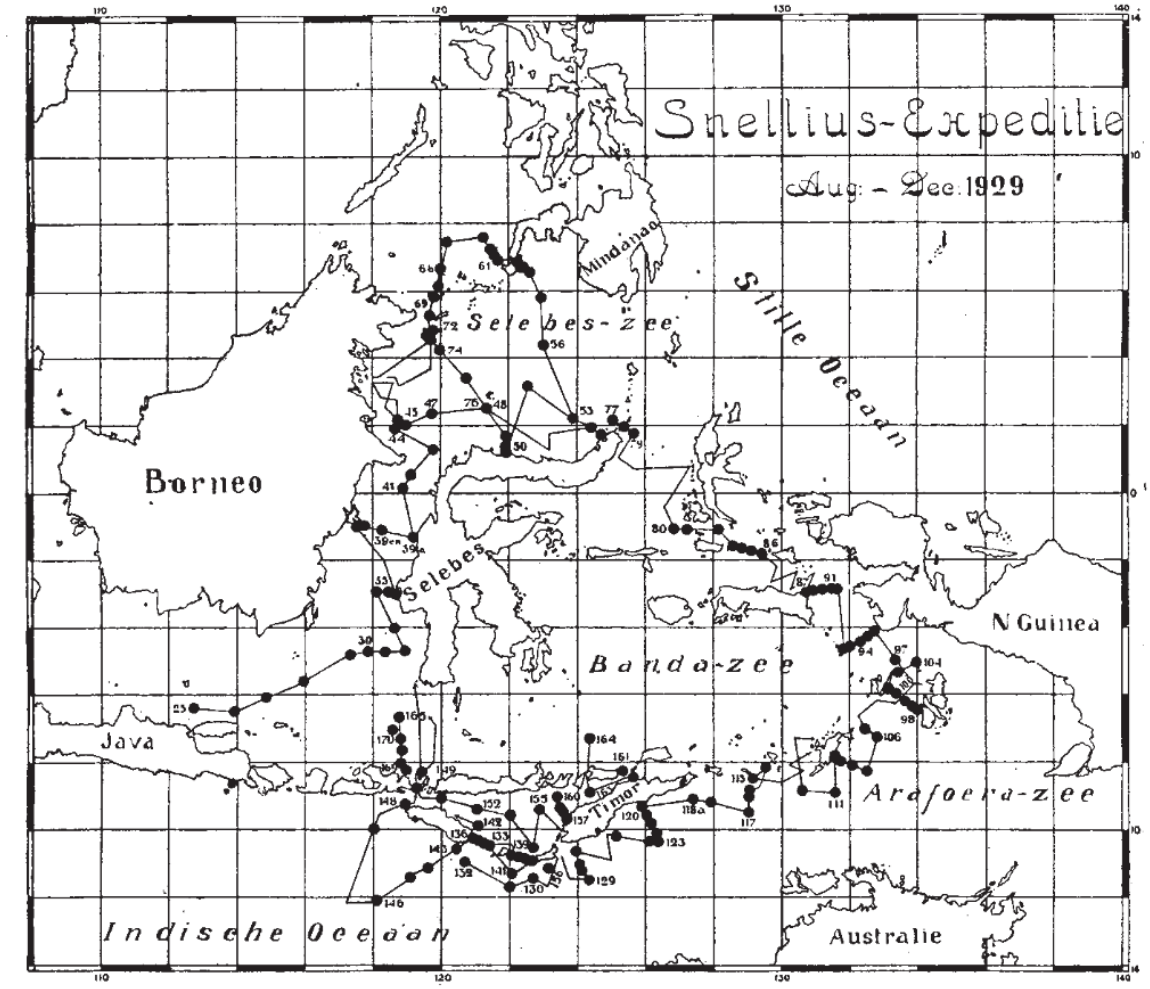

Figure 1.1 Oceanographic stations of the Snellius Expedition, August-December 1929 (from van Riel, 1930).

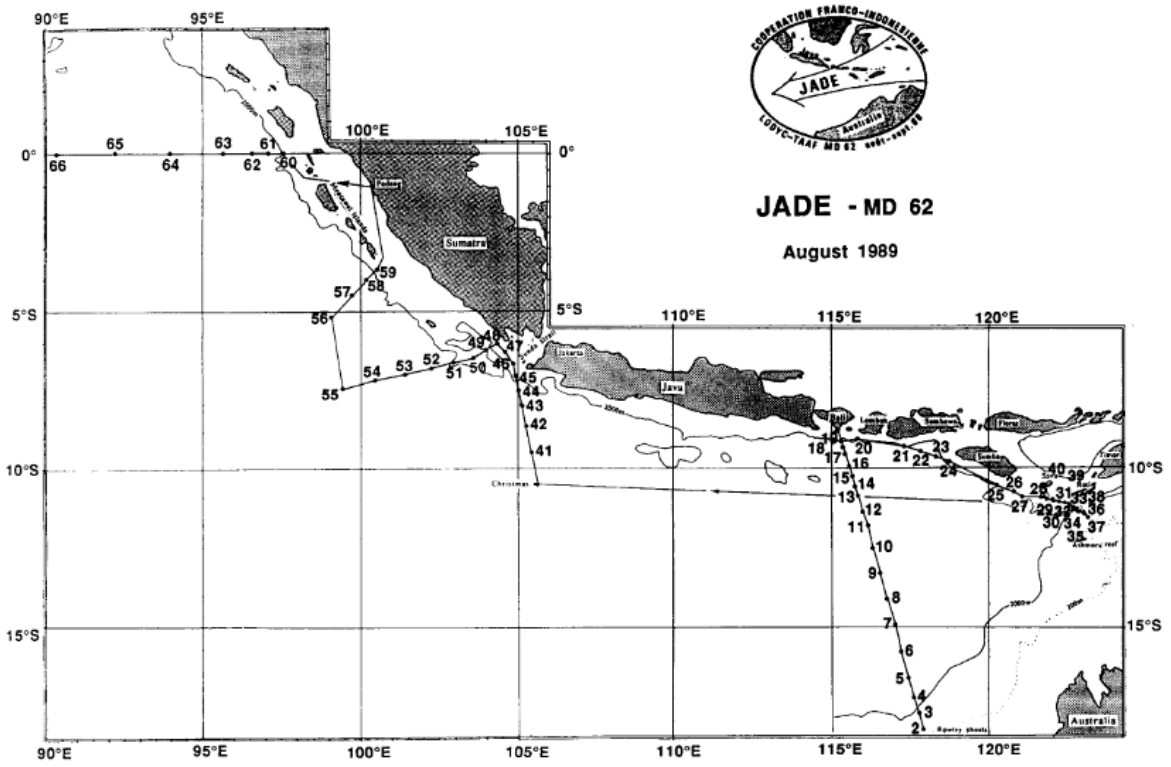

Figure 1.2 Oceanographic stations of the JADE Expedition, August 1989 (from Fieux et al., 1994).

These research programs based on observations and model studies led to a first quantification of the ITF. The 'remaining' issue, next identified, was to characterize the physical mechanisms driving the erosion of Pacific water masses along their pathways in the interior Indonesian seas and quantify mixing rates. These issues required additional observations to characterize the dynamics, especially internal tides, as well as specific measurements to measure precisely mixing rates based on microstructure measurements. This specific issue was addressed by the INDOMIX (Indonesian Mixing) program, which was conducted in 2010. This program was a joined research program between France and Indonesia, with a cruise on RV Marion Dufresne. **Figure 1.4** shows the stations observations of the INDOMIX Expedition in 2010. The most important finding from the INDOMIX program was a first quantification of dissipation rates and vertical mixing along an Eastern route of the ITF passing through the strongly turbulent Halmahera waters, the deep Banda Sea, a region with low turbulence level and a reservoir of the typical Indonesian water mass; and the outlet passages, the Ombai and Sumba Straits. The results confirmed that internal tides and induced turbulent mixing are the main drivers of the erosion of the south Pacific water masses along the eastern route of the ITF (Koch-Larrouy et al., 2015). They also

confirmed that the highest dissipation rates occurred within the straits where internal tides are generated while the weakest dissipation rates were evidenced in far field region, far away from internal tide generation sites. Enhanced dissipation rates were observed within the thermocline and consistent with the enhanced internal tidal signal (Bouruet-Aubertot et al., 2018).

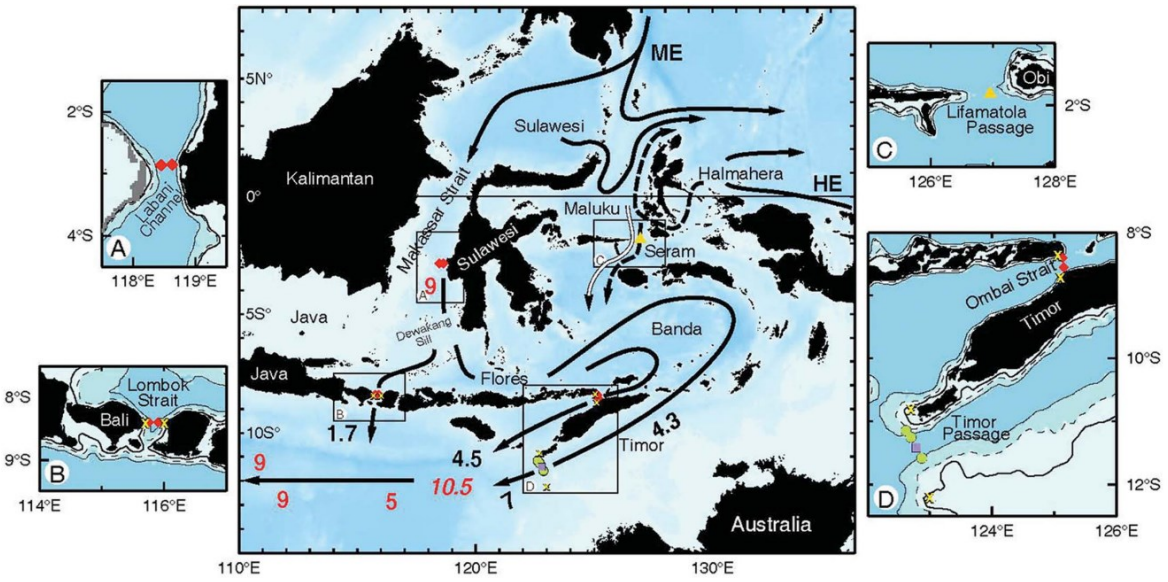

Figure 1.3 Mooring station positions of multi nationals expeditions, INSTANT. Inset A: Makassar Strait inflow moorings (USA: red diamond) in the Labani Channel. Inset C: Lifamatola Passage mooring (Netherlands: yellow triangle). Inset B and D: Lesser Sunda Island moorings in Ombai Strait and Lombok Strait (USA: red diamonds) and Timor Passage (France: purple square; Australia: green circles), and shallow coastal pressure gauge locations (USA: yellow X). The transport (in Sverdrup, 1 Sv = 10^6 m^3s^{-1}) is also indicated, with black numbers is pre-INSTANT estimates and red numbers is from INSTANT expedition (Gordon, 2001) (from J. Sprintall et al., 2004).

The microstructure turbulence measurements collected during the INDOMIX cruise provided a tool for testing indirect estimates of dissipation rates and mixing based on density overturns. The method was thus validated over most of the water column. This validation of the method based on density measurements was the first pre-requisite for a characterization of turbulent mixing on the regional scale of the Indonesian seas. In other words, the INDOMIX expedition gave us a "new energy" for further exploring the mixing rates over the entire Indonesian seas, based on the available CTD dataset from 1990 until 2016 and never been explored yet comprehensively. This is the first motivation of this thesis: provide the first comprehensive analysis of the distribution of dissipation rates and vertical eddy diffusivities in the region based on the available historical CTD datasets.

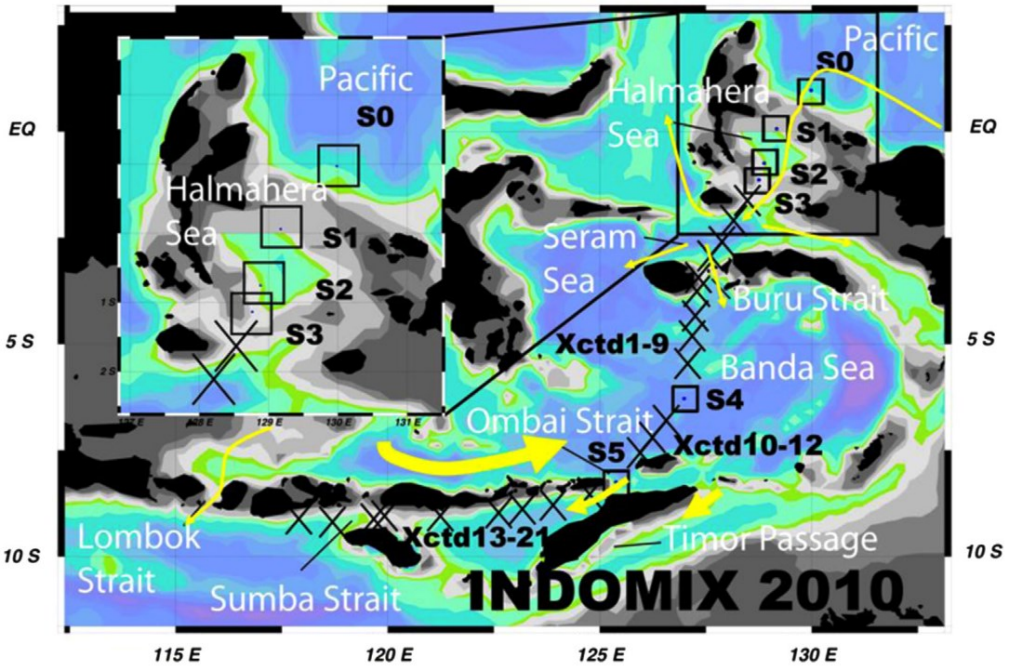

Figure 1.4 Map of the INDOMIX expeditions in 11-19 July 2010, with topography color contours. Black squares represent CTD and microstructure station casts. Black crosses represent the XCTD casts (from Koch-Larrouy et al., 2015).

Most of previous studies, either numerical or observational, focused on internal tides with the identification of generation sites and hot spots for turbulent mixing (e.g. Bouruet-Aubertot et al., 2018; Koch-Larrouy et al., 2007; Nagai et al., 2017; Nagai and Hibiya, 2015). The question of the energetics of internal tides has also been addressed with tidal models in order to get regional estimates of the energy flux from barotropic to baroclinic tides (e.g. Ray and Egbert, 2005) and regional high resolution models, aimed at providing further characterization of the energy budget and characterize the internal wave energy that is ultimately used for mixing (Hibiya et al., 1998; Nagai and Hibiya, 2015). On the other hand, observations give evidence of internal solitary waves (ISWs) that result from a nonlinear evolution of large amplitude internal tides. These ISWs are clearly seen from satellite images and may propagate over large distances until the shelf break and coastal waters (Jackson, 2007). There are also in-situ observations pointing out large amplitude ISWs of about 100 m vertical displacements (e.g. Bouruet-Aubertot et al., 2018; Susanto et al., 2005). Presumably, these ISWs may represent a significant fraction of the energy budget of internal tide but their influence is unknown. Indeed, there is no comprehensive study dealing with the fate of such ISWs from the energetics and mixing perspectives in the Indonesian seas. In this study, we analyzed a coastal dataset evidencing shoaling ISWs in Manado Bay. Based on further insights

inferred from satellite data showing the propagation of the ISWs along a pathway of internal tide, idealized two-dimensional simulations were performed to interpret the in-situ observations and provided an overall scenario of the ISWs lifetime and energy budget. The goal was to provide a comprehensive study of the internal tides generation and ISWs formation coupled with an observational dataset of the shoaling ISWs away from the generation site in a coastal area. Finally, a 3-days cruise was organized in 2017 in Lombok Strait, a hotspot for ISWs in the Indonesian Seas (Aiki et al., 2011; Astawa Karang et al., 2012; Matthews et al., 2011; Susanto et al., 2005).

1.2 Physical characteristics of the Indonesian seas

Indonesian seas have a very complex seabed topography, surrounded by several major islands (e.g. Sumatera, Borneo/Kalimantan, Java, Celebes/Sulawesi, and Papua/New Guinea) and many minor islands separated by narrow straits (Figure 1.5). The Indonesian Seas can be subdivided into two main domains: the shallow domain (<75 m) in the western region and the deep domain (>1000 m) in the eastern region consisting of deep basins connected by shallower sills. The shallow region includes the Java Sea and the Natuna Sea at the southern end of South China Sea. The basin of these shallow waters is known also as Sunda Shelf, which is part of the Asian plate, geologically. There is a narrow channel connecting Natuna Sea and Java Sea, namely Karimata Strait that separates Sumatera and Borneo Island. In the eastern Indonesian Seas, there are Makassar Strait, Sulawesi Sea, Flores Sea, Banda Sea, Seram Sea, Maluku Sea, Halmahera Sea, Savu Sea and Arafura Sea. The transition between these two regions is located along an axis connecting the western sides of Makassar and Lombok Straits. The eastern boundary of the deep-sea regions is the shallow Sahul Shelf, Arafura Sea, connecting Australia and Papua New Guinea.

1.2.1 Indonesian through flow

As the pioneer focusing on physical oceanography of the Indonesian seas, Wyrtki (1961) evidenced the spreading of Pacific waters into the Indian Ocean. Wyrtki (1961) identified the pressure gradient between the western Pacific and eastern Indian Oceans as the primary driver of the ITF, mainly caused by the monsoon (Wyrtki, 1987). More recently the modulation of the ITF by decadal phenomena such as El Niño event leading to a sea level decrease in the western Pacific hence diminishing the transport via the Lombok Strait, has been identified (Chong et al., 2000).

The predominant source of the ITF is the North Pacific water, flowing through the western branch, passing by Sulawesi Sea and Makassar Strait, and then exit through the straits of Lombok, Ombai and Timor Passage (Gordon and Fine, 1996). **Figure 1.3** also shows the general circulation patterns of the ITF with transport estimates from observations. The throughflow contains North Pacific Subtropical Water, NPSW; and North Pacific Intermediate Water, NPIW; it was estimated that around two thirds of the flow recirculates in the Sulawesi Sea and eventually flows back to Pacific while the remaining one third of the water masses enters the Makassar Strait (Masumoto and Yamagata, 1996).

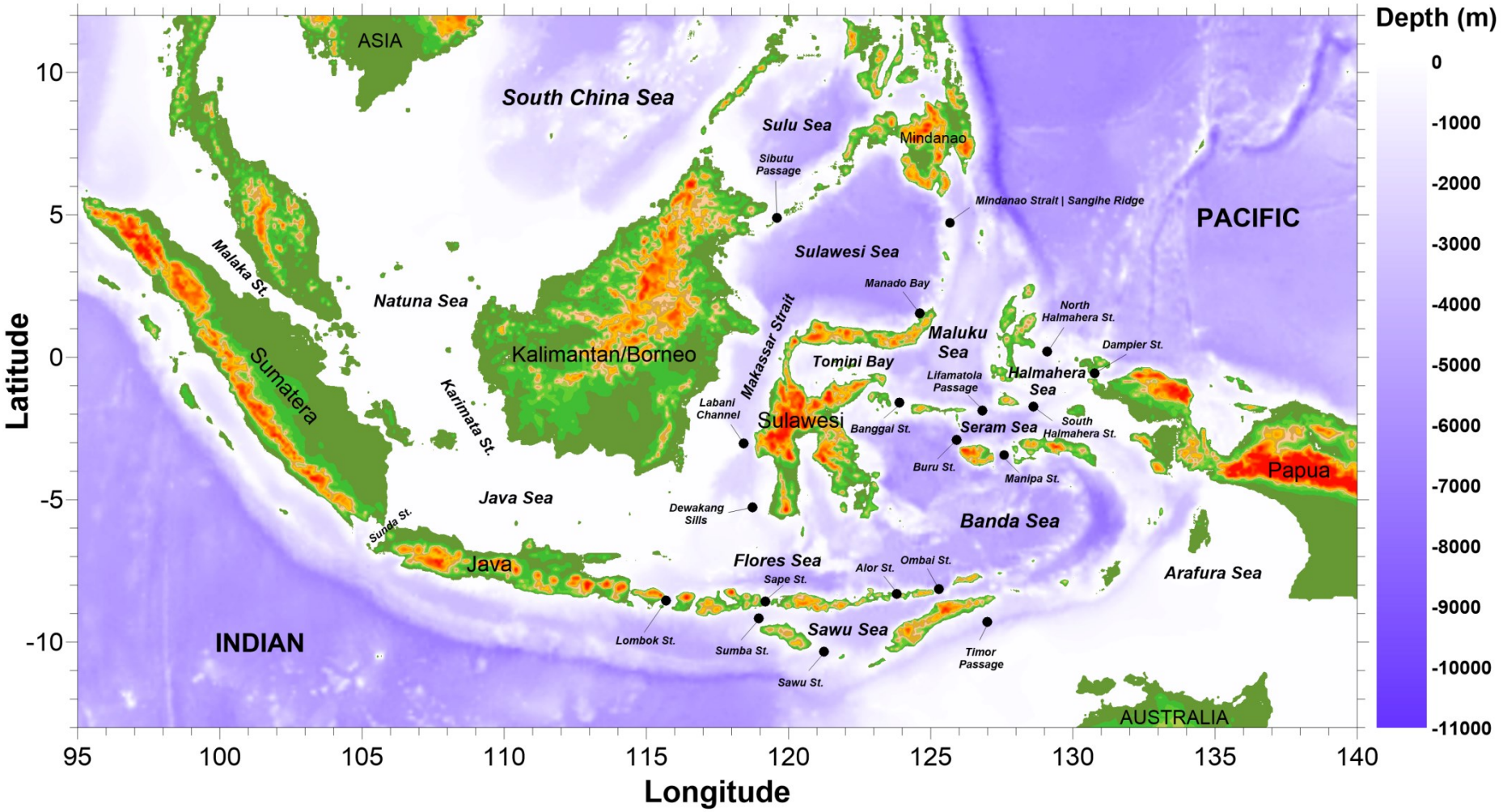

Figure 1.5 Map of Indonesian archipelago with some toponymal of the areas (waters, straits, main islands, ridge and sills) used in the dissertation.

The minor source of the ITF is South Pacific water (South Pacific Subtropical Water, SPSW; and South Pacific Intermediate Water, SPIW); passing through the eastern branch. Within this minor eastern branch, one part of this water flows through the Maluku Sea and Lifamatola Strait and the other enters the Halmahera sea via the Halmahera Strait before pursuing its way to Seram, and Banda Seas (Gordon and Fine, 1996). About 90% of thermocline water is advected by the western branch, and 10% is advected through the eastern branch (Gordon, 2005). The core layer (maximum salinity) of the NPSW and SPSW is filling the thermocline at σ_θ = 23.5 and σ_θ = 26.5 (Wyrtki, 1961); or 34.8 at 100 m for the North Pacific, and 35.4 at 150 m for the South Pacific (Ffield and Robertson, 2008). A unique water mass is present in the Banda Sea where the two branches converge. At this location, the signatures of the Pacific water masses have been erased by the mixing and the Banda Sea has its own characteristics. Several studies suggested that internal tides are responsible for the intense mixing and the resulting transformation of water masses along the ITF (Hatayama, 2004; Robertson and Ffield, 2005). Strong erosion of the Pacific water masses can be evidenced from archived data sets collected from 1929-1981 as shown in **Figure 1.6**.

Flow from Pacific Ocean experiences strong constrictions as many straits and sills inter-connect the basins in the Indonesian Seas. In the inlet passages, several straits cannot be neglected regarding their contribution to the Indonesian throughflow (ITF), i.e. Karimata, Makassar, Halmahera, and Maluku Strait with its Lifamatola Passage. The inflow from the Pacific to the Sulawesi Sea is blocked below 1400 m and to the Maluku Sea below 2340 m (Hautala et al., 1996). The outlet passages toward the Indian Ocean are located along an arc connecting Java, Timor, and Seram where the Lesser Sunda Islands are found. There are several key straits there such as the Lombok, Sumba, Sape, Sawu, Alor, Ombai and Timor passages. The principal sills permitting flow through this ridge are found at Lombok Strait (300 m), at the northeast end of Timor Strait with the depth of 1250-1400 m (van Bennekom, 1988), and southwest of Ombai Strait (1150 m). Between inlet and outlet passages, several key passages are encountered; along the western route there is a narrow passage in southern Makassar Strait along the eastern route, there is a restricting sill of 1950 m depth in the Lifamatola Strait.

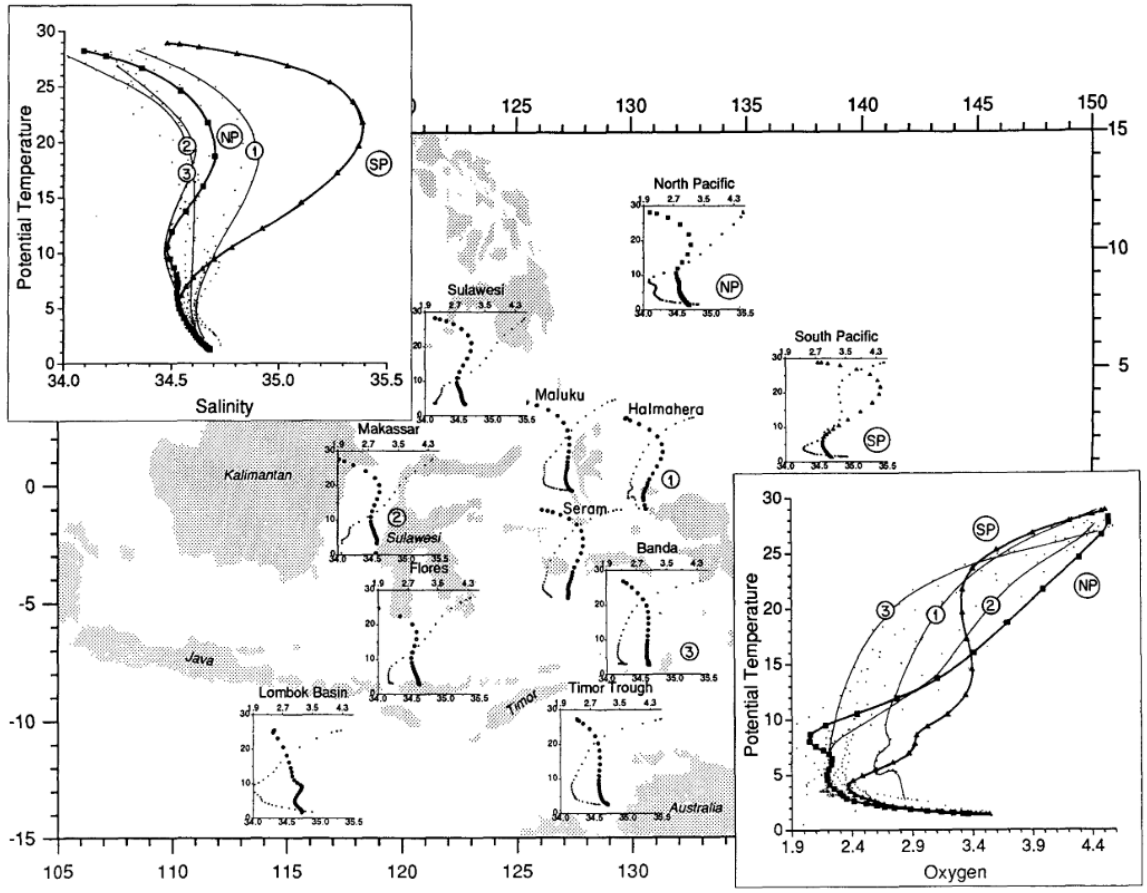

Figure 1.6 Potential temperature-salinity (*T*/*S*, thick dots plot in the main figure) and potential temperature-oxygen (*T*/DO, thin dots plot in the main figure) diagrams derived from archived data sets 1929-1981, acquired by different countries: Australia, Indonesia, United States, Netherland, Japan, USSR, Denmark, and the Philippines. Each location is labeled as follow: North Pacific (NP), South Pacific (SP), Halmahera (1), Makassar (2), Banda (3) (from Ffield and Gordon, 1992).

In the Makassar Strait, one of the main ITF passages, the volume transport measured during the 3 years long INSTANT observation program was as large as 11.6 Sv (Sverdrup, 1 Sv = $1x10^{-6}$ m^3s^{-1}) (Gordon et al., 2008). The minor throughflow via Maluku Sea (measured in the southernmost of the Maluku Sea, Lifamatola Strait) reaches around 1.1 Sv in average, and particularly a long-term mean deep transport of 2.4–2.5 Sv were reported based on mooring measurement between 2004 and 2006 (van Aken et al., 2009). A perspective study of ITF transport would be to consider the tide-induced residual currents. According to a model study by Hatayama et al. (1996) tide-induced residual currents through the Lifamatola passage, from Seram Sea to the Eastern Banda Sea, would lead to a 3.8 Sv volume transport. This tide-induced transport, which is comparable to the ITF transport, may significantly affect the water mass, heat and salt budgets there and this question should be addressed at the scale of the Indonesian Seas. A few years later, short Indonesian cruises were conducted by the Research

Center for Oceanography LIPI to determine the volume transport across smaller passages not previously sampled, namely the Alor strait and the Dampier strait. In the Alor Strait, a narrow 300 m depth channel between Alor and Pantar Islands, the southward transport into Sawu Sea was as large as 0.7 Sv flows southward into Sawu Sea (Purwandana, 2014). In the Dampier Strait, a channel between Waigeo Island and Papua Island, which connects Pacific Ocean and Halmahera Sea, was found to be as large as 0.7±0.5 Sv (Purwandana, 2008). In the other exit passages, the total mean transport were reported as large as 2.6 Sv, 4.9 Sv, and 7.5 Sv through Lombok Strait, Ombai Strait, and Timor Passage from the INSTANT program; respectively (Sprintall et al., 2009).

Recently, a throughflow from South China Sea via Karimata Strait and Java Sea has been studied. This passage is characterized by shallow waters (<70 m depth) and has been previously neglected for this reason, there the fresh water runs off from Indonesian archipelago could freshen and cool the upper layer of the ITF. The Karimata Strait is supplied by North Pacific water mass flows from South China Sea (SCS) with a stronger southward flow in boreal winter and weaker southward bottom flow in boreal summer, and northward (reversal) flow beneath the upper layer. The estimate of the averaged volume from December 2007 to March 2008 (winter) was -2.7±1.1 Sv (1 Sv = 1×10^6 m^3 s^{-1}), and from May to September 2008 (summer) is 1.2±0.6 Sv, and averges for the entire record from December 2007 to October 2008 to -0.5±1.9 Sv (Susanto et al., 2013). Negative and positive sign indicates southward and northward transport, towards SCS and Java Sea, respectively. This minor shallow ITF via Karimata Strait splits into two branches. The first branch is flowing to Indian Ocean through the Sunda Strait, and the second branch flows eastward entering the deeper region of the Indonesian Seas, freshening the major passage of ITF. Containing fresher water from SCS and Java Sea, SCS ITF plays an important role in changing the upper layer of volume and heat transport of the Makassar Strait (the western route ITF). The SCS throughflow influence is also important, in term of contribution from precipitation over the Southeast Asian continent, which then runs off into the SCS.

1.2.2 Barotropic tides in the Indonesian seas

The Indonesian Seas are well-known for being one of the most energetic region for tides. Barotropic tides are inferred from tidal models with data assimilation from the Topex/Poseidon altimeter (Ray and Egbert, 2005; Robertson and Ffield, 2005). The semidiurnal M2 constituent appears to be the largest in the internal Indonesian seas (Egbert

and Erofeeva, 2002). As shown in **Figure 1.7**.a, M2 tides are dominantly propagating from the Indian Ocean into Indonesian seas, first into Banda Sea and then into Flores and Java Sea. Its energy flux exceeds 500 kW m^{-1} while passing narrow Timor passage and Savu Strait (**Figure 1.8**).

The weaker M2 tides propagating from the Pacific Ocean enters the Indonesian Seas via Mindanao Strait, Maluku Strait and north Halmahera Strait. Its amplitude increases while entering the Sulawesi Sea and slightly decreases as it propagates through the Makassar Strait. Meanwhile, its amplitude is rapidly decreasing when entering the Maluku Sea and Halmahera Sea (**Figure 1.7**.a & **Figure 1.7**.c).

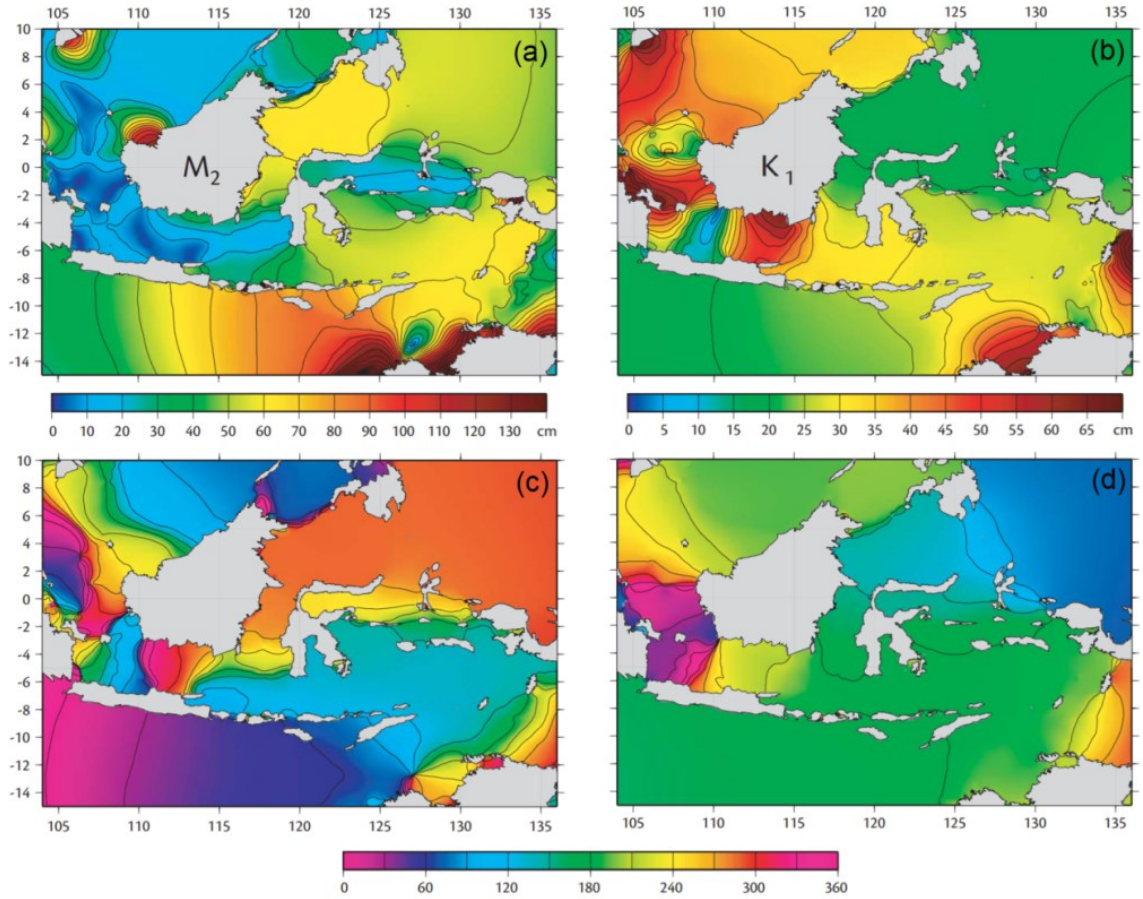

Figure 1.7 (a) Amplitude of the M2 tide based on ten years of Topex/Poseidon satellite altimetry into a nonlinear hydrodynamic model (Egbert and Erofeeva, 2002), with its corresponding phase lag presented in (c). (b) The amplitude for K1 tide, with its corresponding phase lag presented in (d) (from Ray and Egbert, 2005).

The diurnal tide, K1 shows a different spatial pattern (**Figure 1.7**.c, d). The K1 tides coming from Pacific enters the Indonesian Seas via Mindanao Strait, Maluku Strait and north Halmahera Strait. Its amplitude increases while entering the Sulawesi Sea and slightly decreases as it propagates through the Makassar Strait. In the southern Indonesian seas, the K1 tide

propagates from the Indian Ocean, through Lesser Sunda straits. In the Banda and Flores Sea, these two incoming tides meet, leading to an increase of the amplitude in the Banda and Flores Sea.

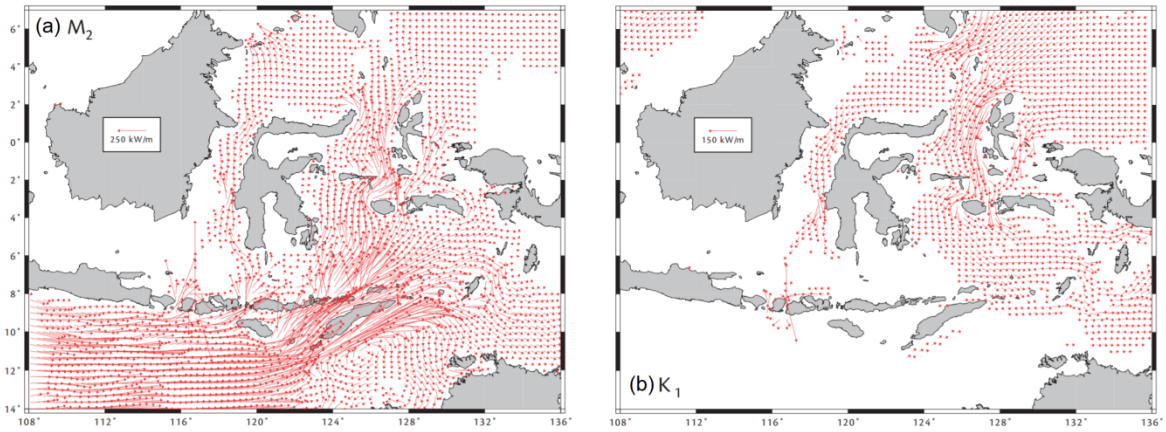

Figure 1.8 (a) Mean barotropic energy flux vectors for the M2 and (b) that for the K2. Fluxes smaller than 20 kW m^{-1} are not drawn (from Ray and Egbert, 2005).

1.2.3 Internal tides in the Indonesian seas

When the barotropic tide (horizontal velocities are uniform with depth) interacts with sloping bottom topography in a stratified fluid, internal or baroclinic tides (horizontal velocities vary with depth) are generated. This generation depends on the stratification, the steepness of the topographic slope, and the barotropic tidal strength and period (Baines, 1982; Robertson and Ffield, 2005). Once generated, internal tides undergo various evolutions during their propagation (reflexion, interactions with the mean current and internal wave field, etc.) that may lead to instabilities and internal wave breaking with ultimately energy dissipation and turbulent mixing. The impact of internal tide induced mixing on the ocean stratification is significant at a global scale and especially for the deep ocean as pointed out by numerous studies (e.g. Munk and Wunsch, 1998).

The Indonesian seas is one of the regions where the strongest internal tides are observed. This results from the specific geometry of the Indonesian Seas with numerous straits and shelf break topographies around the thousands islands of the archipelago that favour internal tide generation. Hence internal tides have been suggested the main driver for the ITF water masses transformation in the internal Indonesian seas (e.g., Hatayama, 2004; Hatayama et al., 1996; Robertson and Ffield, 2005; Schiller, 2004). Modelling studies aimed at characterizing baroclinic tides in the Indonesian Seas. The first studies based upon coarse grid

models (~0.5° or ~50 km) by Schiller (2004) and Simmons et al. (2004) demonstrated the requirement for a high spatial resolution in respect with the typical internal tidal wavelength ranging from ~20-50 km. Holloway (2001) suggested that the grid cells of 4-5 km or finer are required to resolve the internal wavelengths, especially in the shallow waters.

Using a 5 km spatial resolution model, the Regional Ocean Model System (ROMS), Robertson and Ffield (2005) tried to estimate the baroclinic tidal field, focusing on a single constituent, the M2 tide. They showed that strong baroclinic M2 tides are generated along the shelf break and within straits. These results were validated by TOPEX/Poseidon satellite crossover observation of elevation and mooring observations using INSTANT program dataset. The Indonesian Seas internal tides have a complex spatial pattern that result from the interference between internal tides propagating from different basins. The limitation of the ROMS model is its lack of representation of the mean circulation and it incapacity to simulate the nonlinear processes, such as ISWs generated by non-hydrostatic terms (Robertson and Ffield, 2005).

Higher resolution simulations of internal tides, of about 1/100 degree (~1 km grid), were performed by Nagai and Hibiya (2015) using the MITGCM. The model was forced by prescribing M2 barotropic tidal currents. This very high-resolution grid allowed to characterize internal tides generation in narrow passages, such as the Lifamatola, Manipa, Ombai, and Lombok Straits, and the Sulu and Sibutu Island chains with a wavelength of about 130 km, and propagation speeds of 3 m s^{-1}. **Figure 1.9** shows model-predicted vertical isopycnal displacement at a depth of 1000 m. Such high-resolution study indicated that there were large isopycnal displacements in some locations even though located far away from the generation sites because of interferences between internal tides generated from various sources. Such finding is in agreement with the Arlindo Mixing Project results where vigorous internal tides have been observed in the Indonesian Seas with isotherm heaving up to 90 m in the Seram Sea during 14 hour yo-yo stations (Ffield and Gordon, 1996).

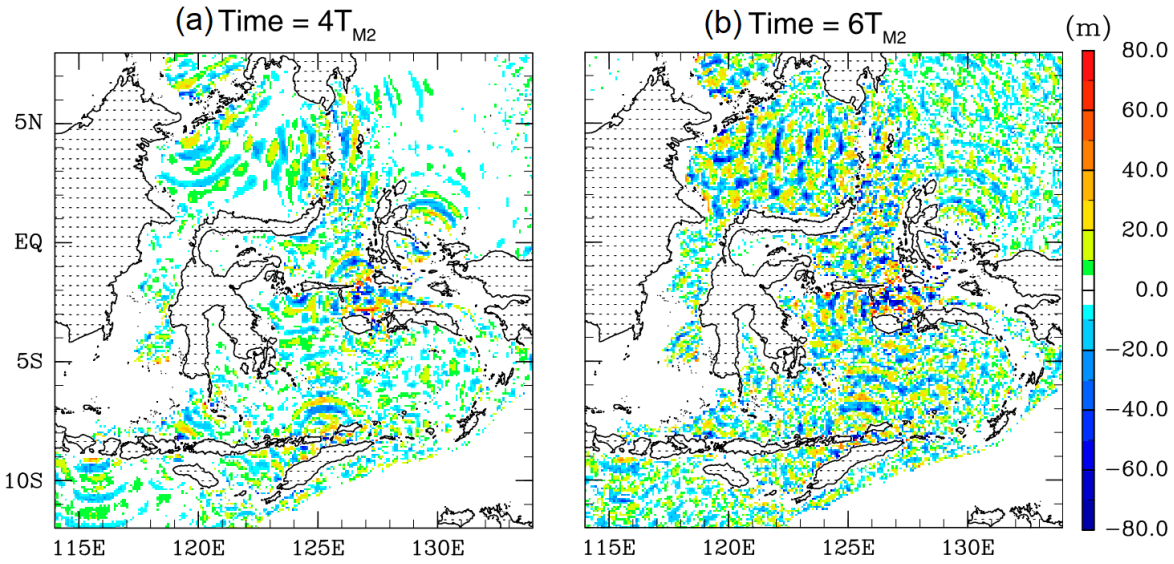

Figure 1.9 Model predicted distribution of the vertical displacement at a depth of 1000 m after (a) fourth and (b) sixth M2 tidal period (TM2) from the start of simulation (from Nagai and Hibiya, 2015).

1.2.4 Spotting internal solitary waves in the Indonesian seas

ISWs are very specific mono-crest waves, similar to solitons though they are often observed as trains of solitary waves. There are most often generated when the internal tide steepens as a result of nonlinear interactions. ISWs are associated with large vertical isopycnal displacements, are of fairly small scale and can propagate over long distances. These characteristics, not resolved by hydrostatic models, explain why their study has been neglected by previous model-based vertical mixing studies. ISWs activity is expected to contribute to the dissipated energy and mixing away from its generation sites (hereinafter termed as 'far field') in the Indonesian seas (e.g. Nagai and Hibiya, 2015). Indeed, Indonesian seas is a favorable zone for the generation of ISWs as they combine large amplitude internal tides and strong currents. The appearance of ISWs can be tracked from their sea surface signature and is well captured by Moderate Resolution Imaging Spectro-radiometer (MODIS) satellite images in the Indonesian seas where ISWs are of large amplitude (see **Figure 1.10**). Using MODIS images, Jackson (2007) performed an impressive statistical study on the ISWs appearance in this region. Here we present some locations where ISWs are frequently observed from satellite which allow localizing their source and identifying their propagation pathways.

Sulu Sea and Sulawesi

Sulu Sea and Sulawesi Sea are separated by shallow passages, namely Sibutu passages in the Sulu Islands chain. The Sulawesi Sea is connected to the Pacific Ocean by Mindanao Strait, a narrow passage, located in the northernmost of Sangihe Islands chain (see **Figure 1.10**.b). Barotropic tidal currents forcing over the passages potentially triggers the generation of internal tides that propagate in the Sulawesi Sea as frequently on the satellite images (see **Figure 1.10**.a, b).

Maluku Sea

The barotropic tidal current flowing over the sill of the Lifamatola Strait triggers the generation of internal tides that propagate in the Maluku Sea. The appearance of ISWs packet in the Maluku Sea is frequently observed on satellite images along the propagation pathway of internal between Lifamatola passage and the north tip of the Sulawesi islands (see **Figure 1.10**.c).

Banda Sea

The main source for the observed ISWs appearance in the Banda Sea is the Ombai Strait. The Ombai Strait is the largest channel in the Lesser Sunda Islands chain that directly allows the Pacific water masses flow from Makassar Strait and Flores Sea into the Banda Sea. This strait is also the deepest channel where the barotropic M2 tide incoming from the Indian Ocean passes through. This barotropic tidal current flowing over the strait is responsible for the generation of the ISWs frequently observed on satellite images (see **Figure 1.10**.d).

Western Flores Sea (Kangean waters)

One of the most striking ISW signatures is found in the Kangean waters. The ISWs appearance in the Lombok Strait is the most frequent compared to the previous three regions. These ISW are propagating from the Lombok Strait. Several studies based on satellite observations and/or numerical models have been conducted to characterize ISW generation in the Lombok strait (Aiki et al., 2011; Astawa Karang et al., 2012; Matthews et al., 2011). The Lombok Strait is a 'bypass' gate of the ITF exit passage, directly allowing the Pacific water masses flowing from the Makassar Strait towards the Indian Ocean. It is also the gate for the M2 barotropic tidal currents originating from the Indian Ocean. As shown in **Figure 1.10**.e, there is clear evidence of ISWs propagating from the Lombok Strait. The ISWs appearance in the Lombok Strait is more frequent compared to the previous three regions.

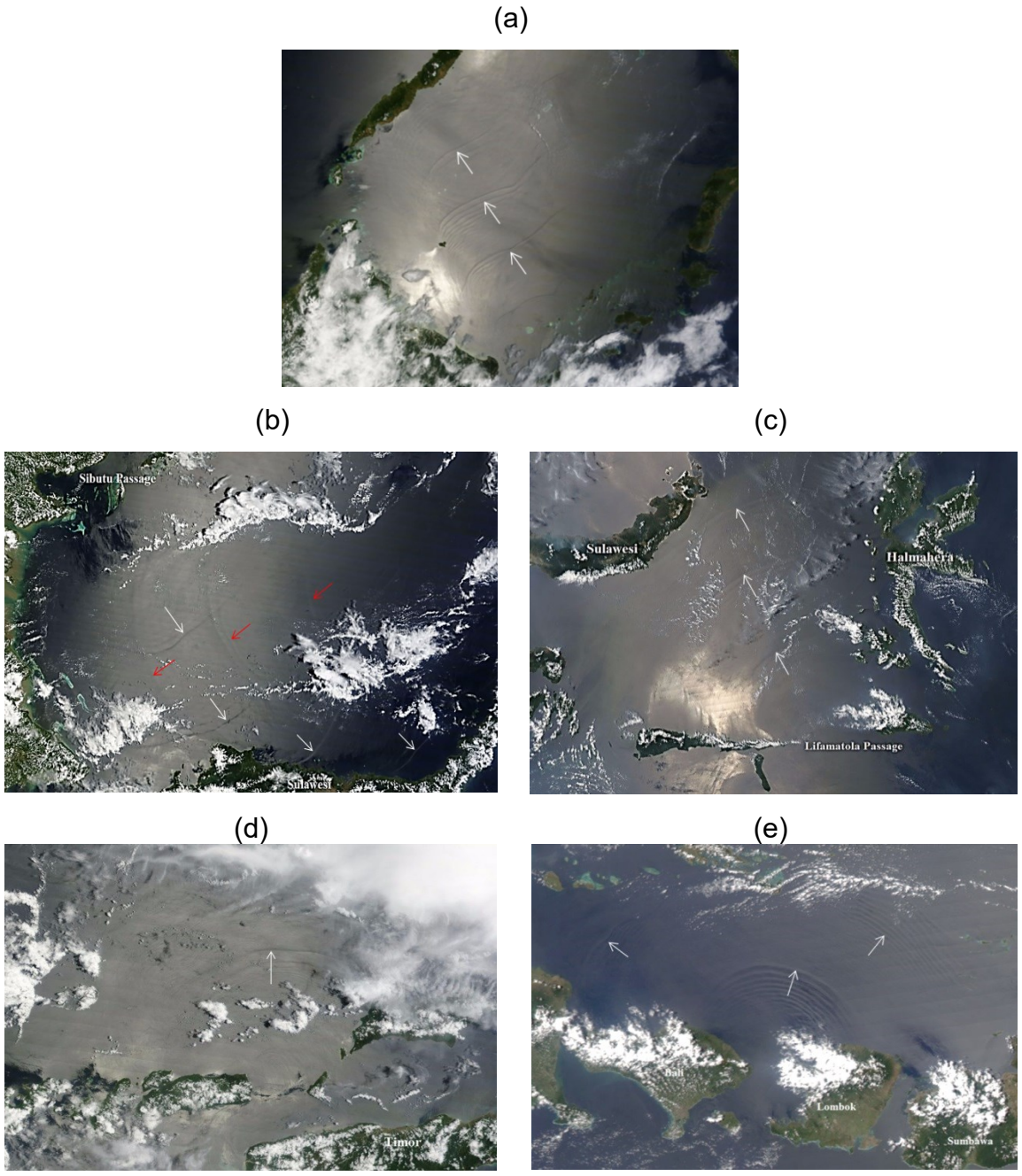

Figure 1.10 Observed ISWs packet propagating in some regions (white and red arrows): (a) in the Sulu Sea, suggesting that the generation site is in the Sibutu Passage (https://zoom.earth/#view=7.4311,119.4445,7z/date=2015-03-20,am**);** (b) in the Sulawesi Sea. The most frequently observed ISWs were propagating from the Sibutu Passage, while fewer ISWs propagating from Sangihe ridges (eastern boundary of the Sulawesi Sea), as indicated by red arrows (https://zoom.earth/#3.146001, 121.437378,8z,sat,am,2016-04-09); (c) in the Maluku Sea, suggesting that the generation site is in the Lifamatola Passage (https://zoom.earth/#0.285643,126.139526,8z,sat,pm,2015-09-27); (d) in the Ombai Strait (https://zoom.earth/#-7.544933,125.345764,9z,sat,am,2016-03-12); (e) in the Lombok Strait: captured in November 17th 2016 (https://zoom.earth/#-7.977638,115.705261,9z,sat,pm,2016-11-17).

1.2.5 Potential mixing hotspots and related water mass transformation in the Indonesian seas

Observational studies of potential mixing hotspots have been conducted based on hydrographic measurements showing the strong erosion of Pacific water masses along their pathway toward the Indian Ocean. In the absence of microstructure measurements, indirect estimates were used to characterize turbulence. Ffield and Gordon (1992) provided an overview of turbulent mixing with global estimates for each interior sea of a diffusivity coefficient inferred from a simple advection-diffusion model applied to the observed *T*/*S* profiles. Later on, Ffield and Robertson (2008) performed an analysis of a 21 years database, from 1981 to 2006, of expandable bathythermographs (XBT). They used finescale temperature variance as a proxy of vertical turbulent mixing and provided an overview of the contrasted signal along different pathways. The main, unsurprising conclusion was that mixing hotspots were preferentially along the shelf break and within straits, thus making a clear link with internal tide generation area (**Figure 1.11**). Ffield and Robertson (2008) also pointed out that mixing should be considerably reduced about 35 km away from potential mixing hotspots, which also may give insights on the spatial extension of tidally induced turbulent mixing. This suggests that internal tides rather dissipate locally, near their generation area, as a result of the direct breaking near the rough supercritical topographic features (Klymak et al., 2012). Moreover the fraction of the internal tide energy that is not dissipated near the generation site remain mostly trapped in the semi-enclosed basins, implying that a large amount of the total power transferred to internal tides is available for vertical mixing (Alford et al., 1999; Koch-Larrouy et al., 2007; Nagai et al., 2017; Nagai and Hibiya, 2015; Robertson, 2010). The part of the internal tides escaping the near field dissipation can break through various processes, such as scattering of internal wave energy from bottom topography and interaction of incident and reflected waves, as well as friction-generated boundary shear.

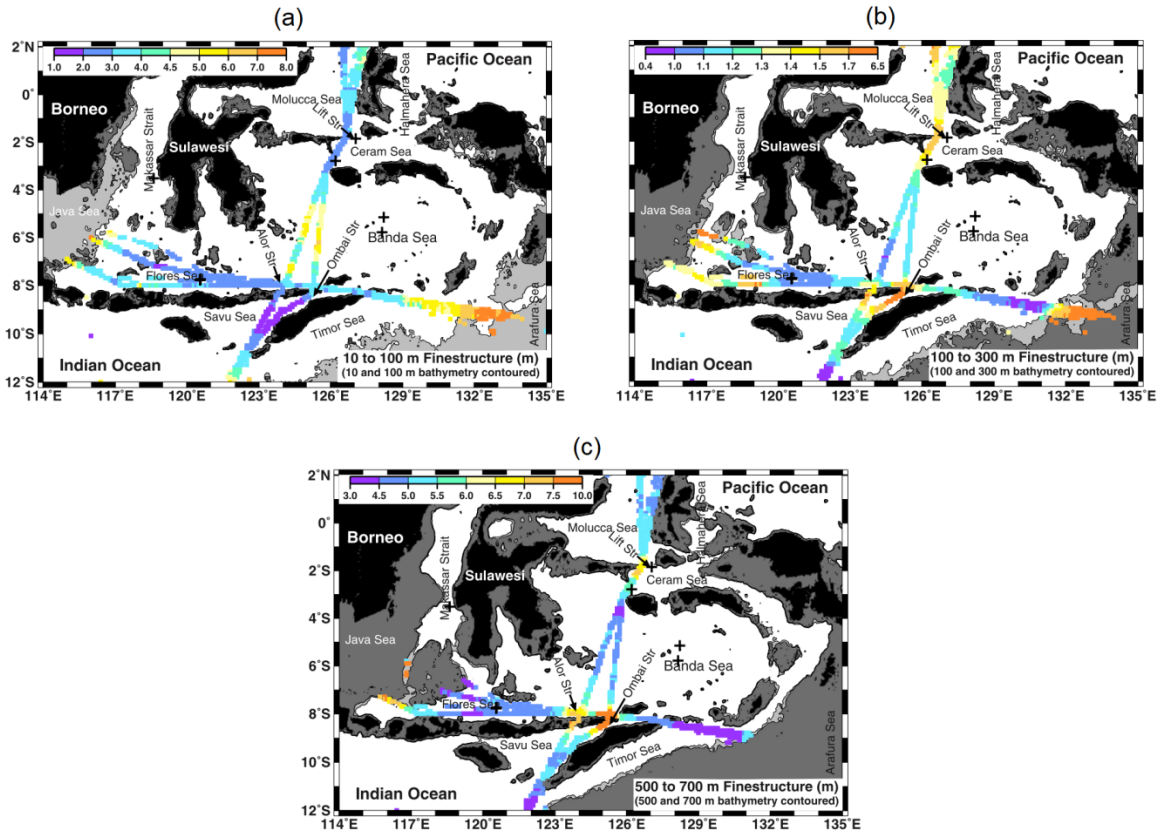

Figure 1.11 Map of 3°x3° horizontally filtered finestructure from archived XBT data sets collected from 1981 to 2006 at three depth intervals: (a) 10-100 m, (b) 100-300 m, and (c) 500-700 m (from Ffield and Robertson, 2008).

The impact of internal tides on vertical mixing was addressed in numerous modelling studies as already mentioned. The first insight was given with map of barotropic to baroclinic tides energy transfers, giving evidence of hotspots for turbulent mixing and estimates of vertical eddy diffusivity maps (Carrère and Lyard, 2003; Nagai and Hibiya, 2015). Nagai and Hibiya (2015) modelling study aimed at characterizing the generation sites for internal tides as well as the regions of dissipation: whether most of the energy dissipation occurs locally in the generation area or not. It is one key question since classical OGCM parameterization of internal tides induced mixing (no explicit representation of tides) assumes a full local dissipation of the power injected at each grid point (Koch-Larrouy et al., 2007; St. Laurent et al., 2002). **Figure 1.12** shows a map of the energy flux from barotropic to baroclinic M2 tides with numerous generation areas: in the straits of Sulu Islands, Sangihe Islands, Banggai Islands, Selayar Islands, Lesser Sunda Islands (consisted of Lombok, Sape, Alor and Ombai straits); in the narrowing passages and such as in the crossing passage separating the Seram Sea and Maluku Sea (consisted of Buru Strait, Manipa Strait, and Lifamatola passage). It was also

maximum in the shallowing region, such as in the Dewakang waters and Raja Ampat waters. The dissipation is characterized within different sub-basins and points out contrast between regions where the internal tide dissipates mostly locally, like the Halmahera sea, and regions where part of the internal tide energy dissipates away from its generation, for instance in the Ombai strait.

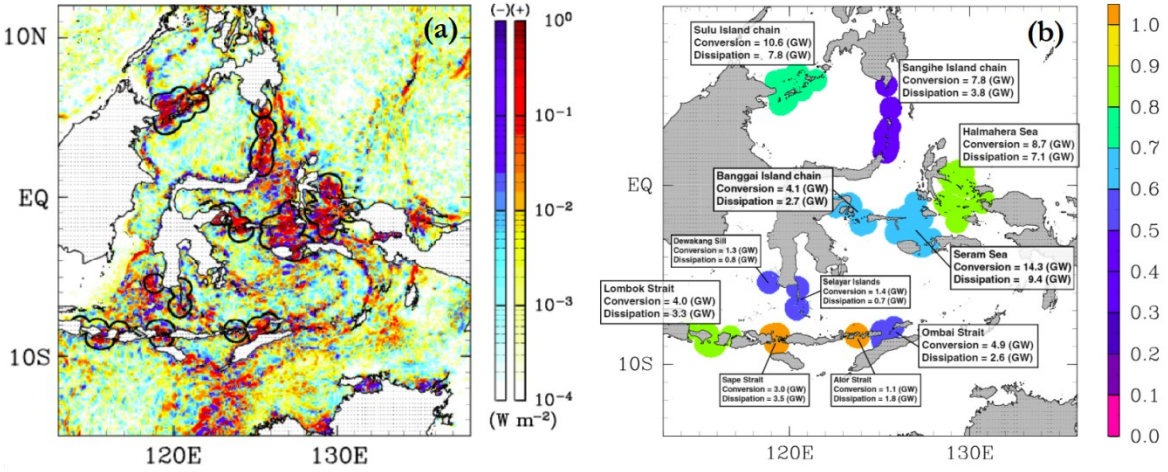

Figure 1.12 Model-predicted distributions of (a) the depth-integrated conversion rate from the M2 barotropic to baroclinic tidal energy, (b) value of local dissipation efficiency q at each near-field site (color) (from Nagai and Hibiya, 2015).

The Indonesian seas are also a region with an energetic eddy field associated with instabilities of the strong currents in the island wakes and residual circulations. A few studies only point the possible impact of eddies that may enhance the level of turbulence by focusing internal tides and contribute to lateral dispersion. The impact of this eddy field on horizontal dispersion as well as its effect on internal tide propagation has been addressed (Awaji, 1982; Hatayama et al., 1996). Recently, three-dimensional high spatial resolution (1/600°) simulations by Nagai et al. (2017) confirmed the dilution of salinity maximum of the Pacific water mass as they progress in the Halmahera Sea resulting from semidiurnal tide induced mixing but also pointed out the effect of sub mesoscales eddies generated by tidal interaction with topography on horizontal mixing (see **Figure 1.13**).

In the following, we describe the major ITF pathways (the western route via Makassar Strait and the eastern route via Halmahera Sea) and the exit passages, to identify the potential mixing sites in the Indonesian Seas where the Pacific water masses characteristics are significantly reduced.

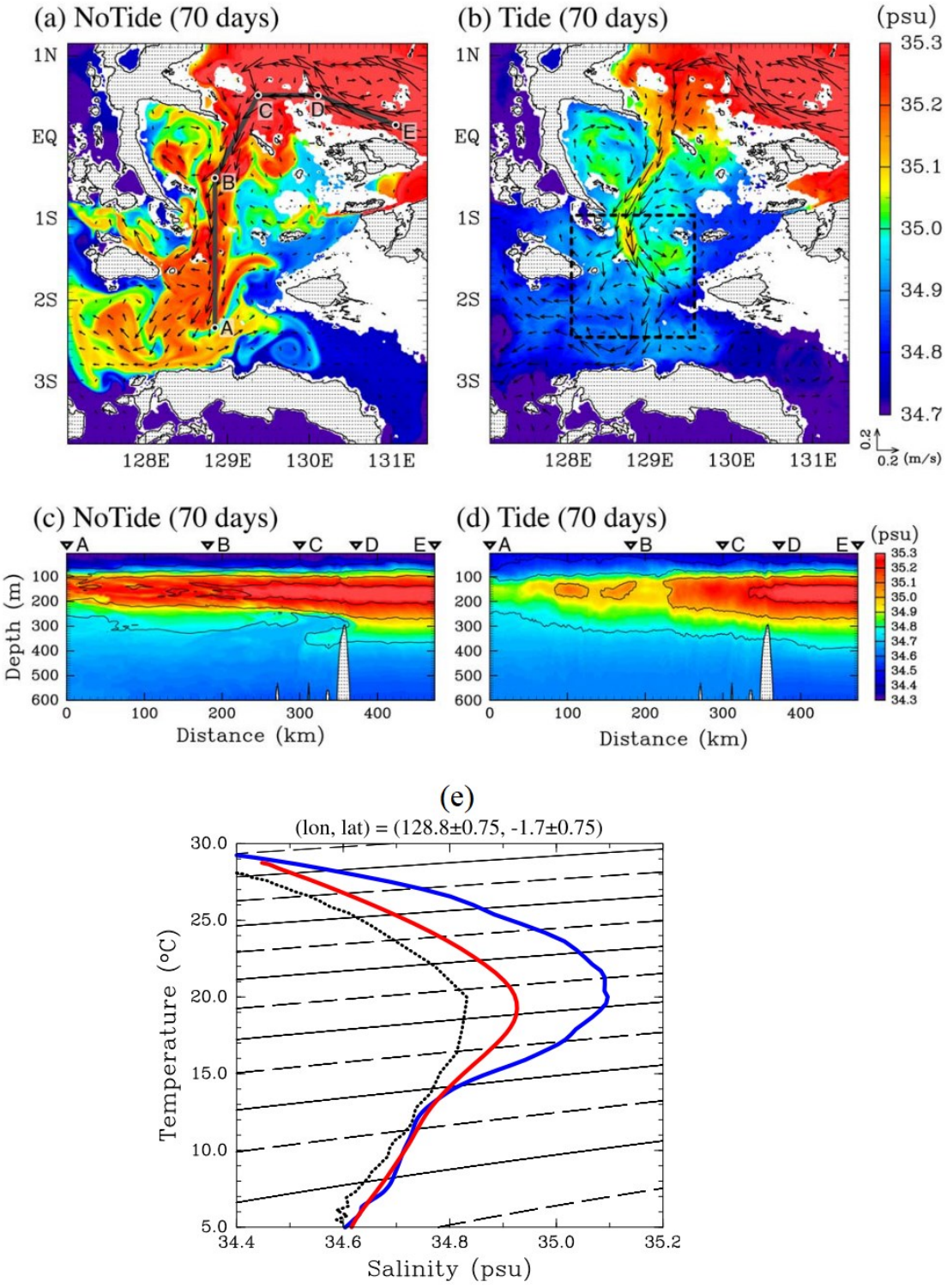

Figure 1.13 Salinity distribution in the Halmahera Sea by Nagai et al. (2017) after 70 days of simulation. (a, b) horizontal distribution at a depth of 150 m for no tide (a) and with tide (b). (c, d) vertical sections of the pathway, bold line in (a). (e) The T/S diagram in the dashed box in (b) for no tide (blue), with tide (red), and the annual mean values from World Ocean Atlas 2013 (black) for comparison (from Nagai et al., 2017).

Labani Channel and Dewakang waters

The first possible mixing hotspot along the western route in the Makassar Strait is the Labani Channel, in the southern part of Makassar Strait with its narrowing shape that favors shear instabilities. Another area of strong mixing in the southernmost of Makassar Strait is the tidal front that forms between the shallower Java Sea waters and the deeper Flores Sea waters. Small eddies form along of the front as a result of shear instabilities (e.g. Munk, 2001). Swift tidal currents in the western part of Makassar Strait, in the Java Sea, also induce important vertical mixing (Hatayama et al., 1996). Moreover, observations made during the ARLINDO Project also revealed that the impact of Dewakang sill turbulence on water-mass properties (**Figure 1.14**).

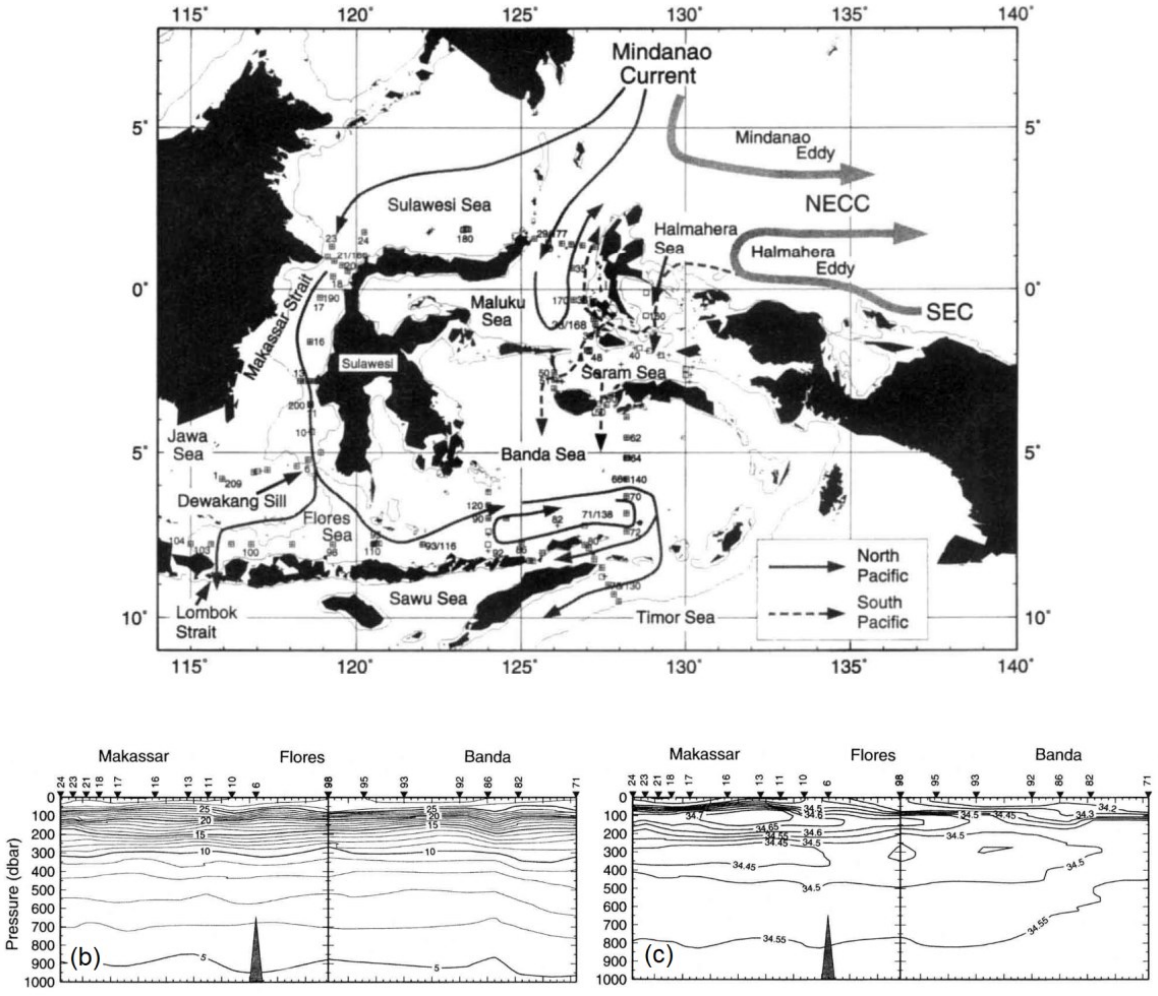

Figure 1.14 (a) General circulation of the ITF with stations of CTD casts during Arlindo Program, 1993; (b) vertical profile of potential temperature and (c) salinity of the section from the northern Makassar Strait to the Flores Sea. The black triangles on the top of (b) and (c) marked the CTD cast positions, the triangle on the bottom marked the Dewakang sill (from Gordon and Fine, 1996).

This enhanced mixing in the Dewakang waters was estimated to be as large as $6x10^{-3}$ m^2s^{-1} in the numerical study by (Hatayama et al., 1996). The turbulent kinetic energy is large especially above the sill, along sloping topography. As stated by previous study, around 20% of the tidal energy in the Indonesian archipelago is dissipated along the western route (with represents 90% of the thermocline flow of Pacific waters), and most of these water mass transformations occur in the vicinity of the Dewakang Strait (Koch-Larrouy et al., 2007).

Lifamatola Passage and Buru Strait

As pointed out by previous model-based study on internal tide generation (Nagai and Hibiya, 2015), the inter-connected channels around Lifamatola Strait, Buru Strait and Manipa Strait are one of the main internal tide generation sites in the Indonesian seas (see **Figure 1.5** to locate the area). These channels connect Maluku Sea and Seram Sea, and Seram Sea and Banda Sea, respectively. The existence of shallow sills in the Lifamatola passages triggers strong sheared flow instabilities leading to turbulence, and causing the lower thermocline water mixing with the water above, thereby setting up a baroclinic pressure gradient and ensuring the continued overflow across the sill. Such mechanism happens over the Lifamatola Sill, allowing the penetration of warmer water from Maluku Sea into the deeper Seram Sea (Hatayama et al., 1996). Such scenario is similar to the one observed in the Mindanao Strait, which makes the Sulawesi basin waters slightly warmer (Gordon et al., 2003).

Enhanced mixing due to the narrowing passage of the Buru Strait was confirmed by the turbulence measurements performed during the INDOMIX cruise. This turbulent mixing is responsible for the erosion of the signature of maximum salinity of the South Pacific Subtropical Water (SPSW), and its ultimate disappearance in the central of Banda Sea (Koch-Larrouy et al., 2015).

Halmahera Straits

The next mixing hotspot is the Halmahera Sea, with its two straits, i.e. northern and southern Halmahera Straits. The INDOMIX cruise turbulence measurements confirmed the strong kinetic energy dissipation there, with maximum values at the sills, ranging between 10^{-9} and 10^{-8} m^2s^{-3}; and vertical eddy diffusivity between $5x10^{-4}$ and $5x10^{-1}$ m^2s^{-1} (Bouruet-Aubertot et al., 2018; Koch-Larrouy et al., 2015).

Restricting passages in the Lesser Sunda Islands

We consider here the main straits of the arch of lesser Sunda Island: Sape Strait, Alor Strait, Sumba Strait, Sawu Strait, and Ombai Strait. These are regions of enhanced water mass mixing resulting from the acceleration of the current passing through narrow channels favoring shear instabilities, and very strong internal tides. Another striking feature is the appearance of internal solitary waves which are frequently observed from satellite images, mainly in the Ombai Strait (Jackson, 2007). This phenomenon was also confirmed by the INDOMIX cruise where isopycnal heaving of about 100m and enhanced kinetic energy dissipation between [10^{-7}, 10^{-5}] m^2s^{-3}, and increased eddy vertical diffusivity between [10^{-3}, 10^{-1}] m^2s^{-1} were observed (Bouruet-Aubertot et al., 2018; Koch-Larrouy et al., 2015).

In the Sumba Strait, , large dissipation values were observed of the order of 10^{-7}- 10^{-6} m^2s^{-3} using the indirect mixing estimates (Koch-Larrouy et al., 2015). In the Alor Strait, a snapshot mixing estimates revealed enhanced kinetic energy dissipation and diffusivity over the sill (Purwandana, 2014). Unfortunately, there are no mixing estimates yet in the Sawu Strait.

Lombok Strait

The Lombok Strait is one of the strongest mixing hot spot in the outflow passages,. Lombok strait is characterized by the existence of a shallow sill, the Nusa Penida Sill (NPS), with maximum depth of 350 m in the southern part of the strait (Visser, 2004). The Lombok Strait is a well-known region for large energy transfer from barotropic to baroclinic tides and potentially enhanced turbulent mixing (Carrere et al., 2012; Carrère and Lyard, 2003). Exposed to energetic tidal current coming from the Indian Ocean and strong currents, large ISWs are frequently observed in this strait from Synthetic Aperture Radar (SAR) and MODIS images. A spectacular snapshot echogram view by an echosounder EK500 of RV Baruna Jaya VIII-LIPI further characterized the appearance of high amplitude internal wave in this strait, with a speed of 1.5 m s^{-1} and wave length of 1.8 km (**Figure 1.15**). Such internal waves propagate preferentially northward from their generation site in the NPS (Susanto et al., 2005).

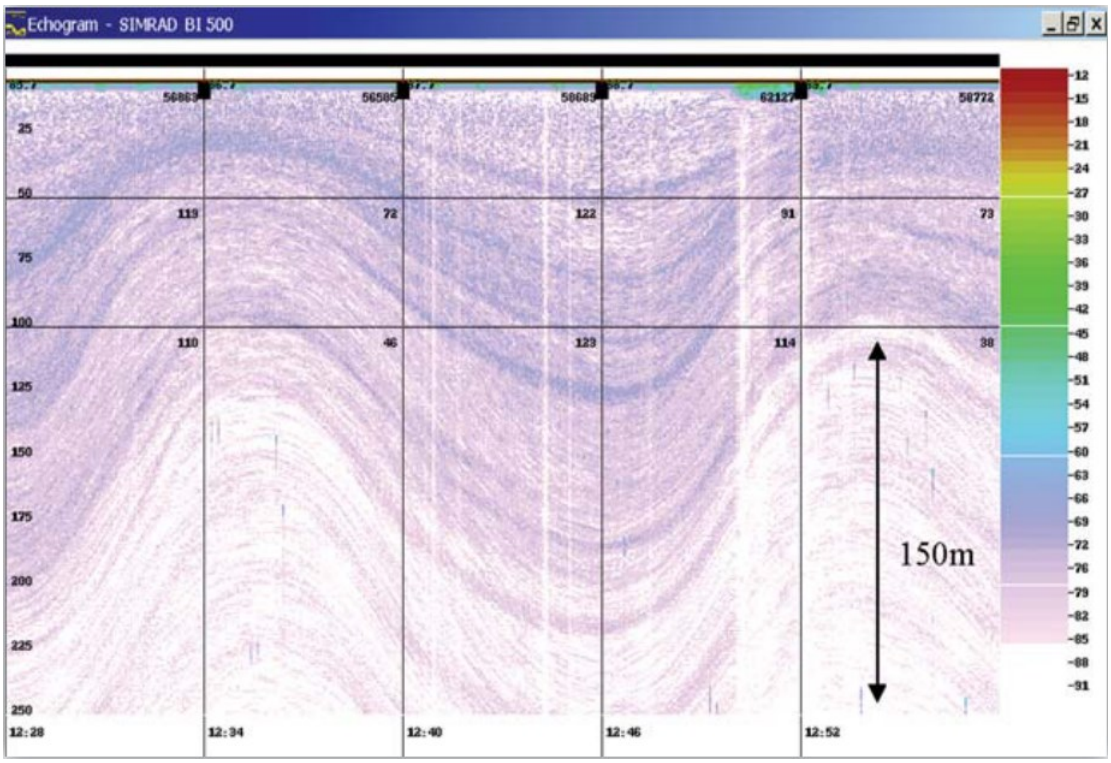

Figure 1.15 Echogram image captured by an EK500 Echosounder RV Baruna Jaya VIII, operating at frequency 38kHz during INSTANT program in 2005. The echogram shows the internal waves in the Lombok Strait. The wave amplitude (peak to trough) is nearly 150 m (from Susanto et al., 2005).

Some modelling studies show that internal waves in the Lombok Strait can propagate 100 km or more away from the strait in both directions (Aiki et al., 2011). As shown in **Figure 1.16**, the northward propagating internal wave generated at the NPS is heaving the isopycnal stronger than the one propagating southward, and the generated northward propagating ISW is pushed closer to the sill when the southward tide occurred. The ISWs more frequently appear on the northern side of the sill where the narrowing channel shape amplifies the disturbances. Besides that, the impact of the ITF leads to an amplitude increase of the ISW generated and to an ISW formation closer to the sill.

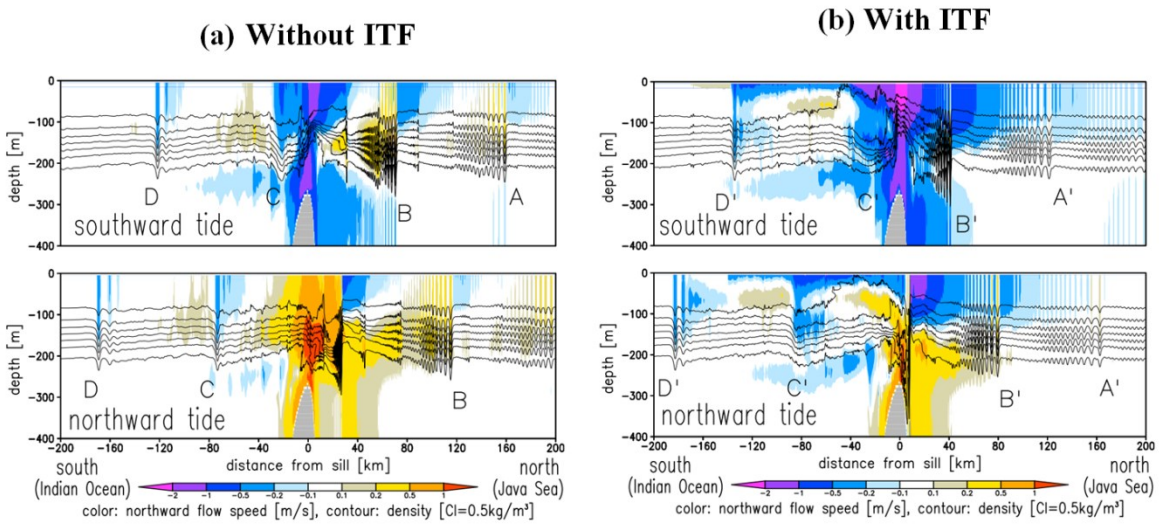

Figure 1.16 Distributions of the northward component of velocity (color) and density (contours) at the maximum (a) without ITF simulation (b) with ITF simulation. A (A')-B (B') and C (C')-D (D') is the first, the second and leading wave propagating northward and southward, respectively. Apostrophe-ed A, B, C, and D depict those leading waves for the with ITF simulation (from Aiki et al., 2011).

The direct breaking of internal tidal waves in the southern part of the Lombok Strait drives intensive vertical mixing in this area yet there has not been any observational study that characterizes its turbulence. Therefore, one of the objectives of this thesis is to conduct an experimental study focusing on internal waves and turbulence in the Lombok Strait, the last intensive mixing site for the branch of the Pacific water masses flowing directly from Makassar Strait before entering the Indian Ocean.

1.3 Aims and objectives

With complex geometrical features such as narrow passages and shallowing topography, the Indonesian seas is a region of strong turbulence. As a result, the Pacific water masses undergo drastic transformations through turbulent mixing driven mainly by internal tide activity and other higher frequency processes such as internal solitary wave shoaling in shallow areas. These processes are strongly influenced by the ITF passing above the rough and variably topography, leading to a complex interplay of shear instabilities, internal tide generation, internal wave breaking, wave-wave interaction, and bottom friction (**Figure 1.17**).

Three main questions were addressed in this PhD thesis:

1. Taking benefit of the few turbulence measurements performed in the Indonesian seas can we validate indirect mixing estimates based on hydrological measurements? If so, can we draw a relevant database for turbulence estimate based on an historical CTD dataset gathering 817 snapshot profiles over the Indonesian archipelago? How these results can be used to test the relevance of previous mixing estimates from hydrostatic models? This question is developed in Chapter 3, where a map of eddy kinetic energy dissipation rate and vertical eddy diffusivity is inferred from finestructure historical dataset. This chapter reveals and points out some mixing hot spots and these results are used to test the relevance of hydrostatic model performed by (Nagai and Hibiya, 2015).

2. Internal solitary waves are a ubiquitous feature in the Indonesian Seas that has been almost not explored. Can we provide further insights on the formation of the ISWs resulting from the steepening of the internal tide? A related issue is to draw up an energy budget for the ISWs with the fraction of internal tide energy flux ending up as ISWs, and which eventually dissipated in shallow area through breaking? To this aim we analysed a previous dataset in a coastal region, in the Manado Bay, North Sulawesi and performed 2D numerical simulations along a section starting from the internal tide generation area and ending up in the shallow region where the ISWs break.

3. How the local turbulent mixing is modulated by the periodicity of internal tide and ISW dynamics, such as in Lombok Strait? We present here a preliminary study based on the analysis of the observational dataset gained in November 2017 from the

Lombok Strait, Indonesia. A research project with extensive measurements in the area is under evaluation and scheduled in 2020.

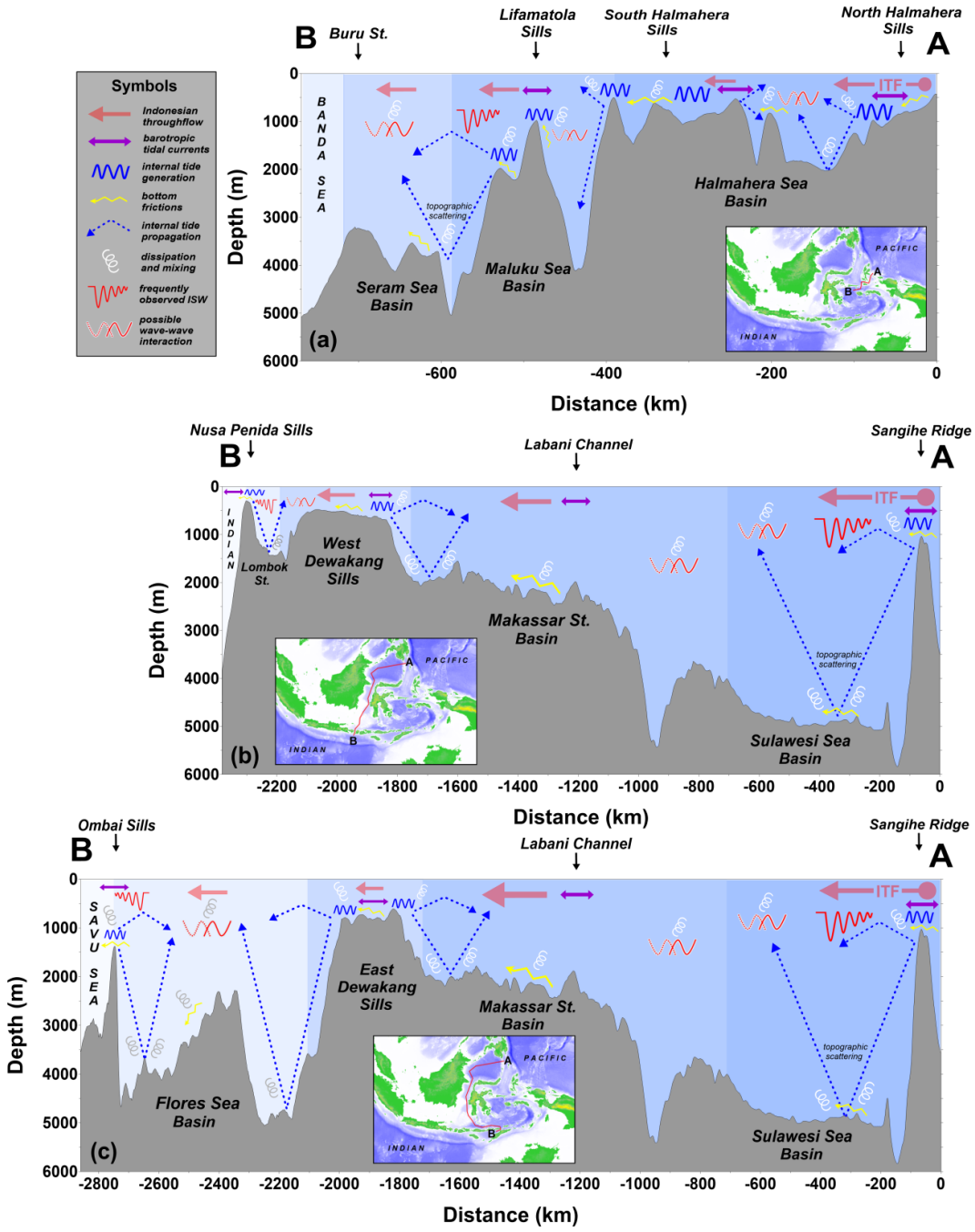

Figure 1.17 Possible representation of some dynamical processes that may happen along the Indonesian throughflow (ITF) pathways: (a) the eastern route of ITF track from northern Halmahera sills to Banda Sea via Buru Strait. The scheme featuring the ITF passages comprises of internal tide generation, its propagation and dissipation-mixing; (b) the western route of ITF track from Sangihe Ridge to Lombok Strait; (c) the western route of ITF track from Sangihe Ridge to Ombai Strait. The barotropic tidal currents oscillate horizontally over the topography lose some parts of energy due to bottom friction and/or during the internal tide generation. The dissipation and mixing possibility of the internal tides occurred during the formation and/or as they propagate away from their generation sites. The topography is inferred from ETOPO and the shaded blue colors are presented to separate the basins.

2
Turbulence and Mixing

Chapter 2
Turbulence and Mixing

2.1 The energy flux path to turbulence in the ocean

In fluid dynamics, turbulence describes a chaotic state of fluid, characterized by a wide range of temporal and spatial scales. The first mechanical description of turbulence was given by Reynolds (1883) who studied in laboratory experiments the disruption of a laminar flow as the fluid increases. Reynolds brought the idea that the state of the fluid (laminar, transitory, turbulent) was determined by the Reynolds number, a ratio between inertial and viscous forces. In the well-controlled laboratory experiment the definition of the Reynold number emerges naturally from the existence of a well-defined velocity scale U, spatial scale L and the value of the fluid kinematic viscosity ν as $Re=UL/\nu$. In 1895 Reynolds introduced the concept of a decomposition of the fluid velocity and scalar properties (density, temperature) between a mean and fluctuating (turbulent quantities) which enlightens the way small scale turbulent fluctuations could affect the mean large-scale state. .

Similarly, in the ocean, small-scale turbulence mixes the fluid properties, affecting the global ocean balance of heat salt and momentum. It is also a major driver of biogeochemical fluxes and is for instance a key process in the input of nutrient in the euphotic layer. A major issue is that it represents a sub grid scale process for state of the art ocean models which rely on a parameterization of this process, while its characterization from in-situ measurement remain challenging and sparse.

Ocean turbulence and mixing happens as a final step of the energy cascade where the energy is injected at large scale mainly by tidal flow over topography, wind, and buoyancy forcing at the sea surface. The turbulence is generally maximum at the ocean-atmosphere and ocean-bottom interface, producing thin mixed layer at these boundaries. Within the stratified ocean interior, the energy input by tides and atmosphere is transported mainly in the form of internal waves, which propagate horizontally and vertically. These waves are sustained by the presence of the buoyancy and Coriolis restoring force and by the spatial variations of the forcing. It was estimated that over at total of 2±0.6 TW are transferred to internal waves, ~1TW are generated by tides, 0.3-1 TW is generated by the atmospheric forcing and a last contribution of 0.2-0.6 TW is expected from Lee waves generation by geostrophic currents over the bottom topography (MacKinnon et al., 2017). The fraction of this energy flux

available for deep mixing and the upwelling of deep water masses sustaining the global overturning circulation remains a debated question (de Lavergne et al., 2016; MacKinnon et al., 2017; Wunsch and Ferrari, 2004). Although the energy is mainly injected into large scale internal waves (~100 km spatial scale, ~1 day time scale) a wide spectrum of internal waves build up though interaction with the mesoscale structures and wave-wave interactions. The classical picture is that within the stratified ocean interior, the energy transits from large to smalls scale waves. Wave breaking leading to turbulence eventually occur when the vertical shear associated to the small scale becomes large enough to overcome the stabilization effect of stratification. **Figure 2.1** shows a sketch of distribution of turbulent mixing processes in the ocean.

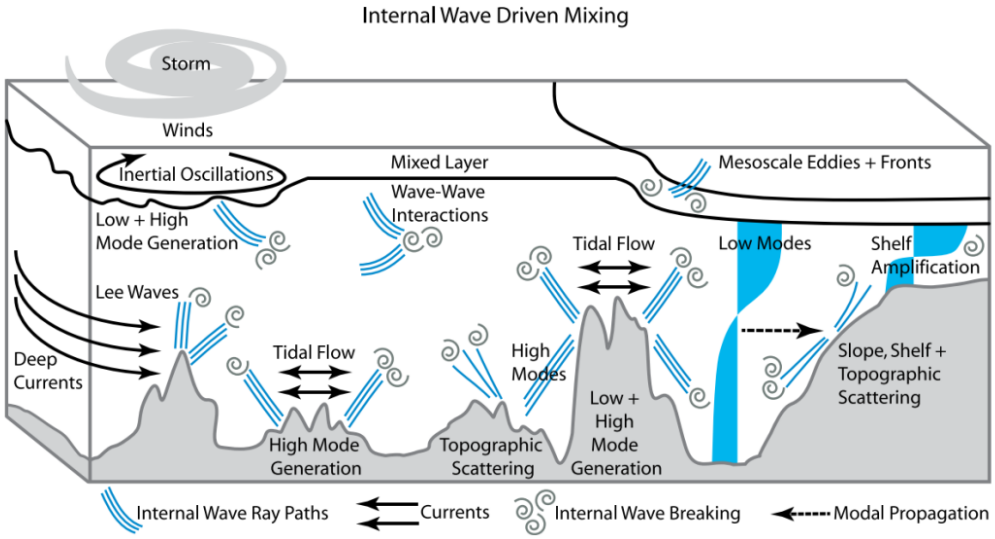

Figure 2.1 A sketch showing some of the features related to ocean turbulence. High-mode internal waves and low-mode internal waves are generated as tides interact with topography features. The lee waves are formed as the deep currents flows over topography. Atmospheric phenomena such as storms produce inertial oscillations in the mixed layer, which can also generate both low- and high-mode internal waves. Such waves can interact in the open ocean. Approaching boundary regions, internal waves can amplify or scatter and eventually break, leading to energy dissipation (from MacKinnon et al., 2017).

In the stratified ocean the concept of the *Re* number has limited application because there is generally no well-defined velocity scale and because the buoyancy force comes into play. Indeed, a competition between the stabilizing effect of density stratification and the destabilization effect of the background shear determines the onset of turbulence through the generation of a Kelvin Helmholtz instability (shear instability).The ratio of the stabilizing effect of stratification N^2 to the destabilizing effect of the squared shear is known as the Richardson number, $Ri = N^2/S^2$. The growth of a shear instability is expected when $Ri<0.25$.

Figure 2.2 shows an example of the numerical simulation of a mixing event anatomy driven by a shear instability (Smyth et al., 2001). In **Figure 2.2**.a, a pair of Kelvin-Helmholtz (KH) billow grown and start to overturn. Next in **Figure 2.2**.b, the primary billows are merging and forming a single large billow. In **Figure 2.2**.c, the transition to turbulence is fully developed, and in **Figure 2.2**.d, turbulence has decayed. In the final state the fluid is less stratified as a fraction of the kinetic energy has been transferred into potential energy increase of the system. **Figure 2.2**.c shows vertical temperature structure sampled at a fixed position and corresponding vertical displacement need to restore the gravitationally stable position (**Figure 2.2**.f).

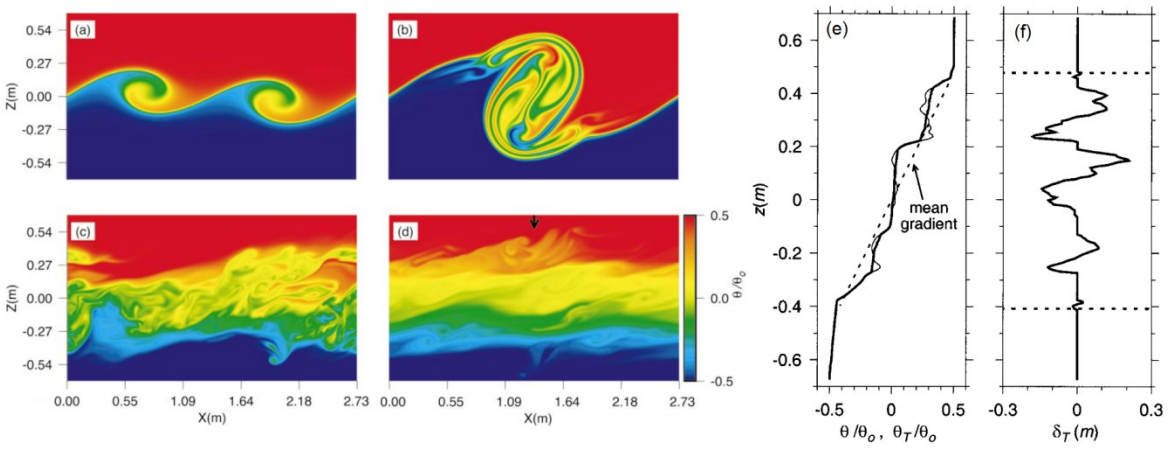

Figure 2.2 2D-simulation of non-dimensionalized temperature: (a-e) Cross sections of instantaneous flow fields simulation at: (a) t=565 s, (b) t=1414 s, (c) t=4242 s, (d) t=6222 s. The arrow in (d) corresponds to the vertical profile of (e) Temperature, with the thin (thick) solid curve represents the original (Thorpe-reordered) temperature profile. The dashed line shows the mean gradient over the overturn region (f). Horizontal dashed lines in (f) are the upper and lower patch boundaries (from Smyth et al., 2001).

2.2 Energy equation of turbulence

The flow evolution under the action of pressure, viscous, gravitational and Coriolis forces can be described by Navier-Stokes equation. For incompressible flow of velocity $u_i(x,t)$; where i denotes one of three spatial direction of displacement; x the position and t the time. The equation of motion can be written as

$$\frac{\partial u_i}{\partial t} + u_j \frac{\partial u_i}{\partial x_j} = -\frac{1}{\rho}\frac{\partial p}{\partial x_i} + \nu \frac{\partial^2 u_i}{\partial x_j^2} - \frac{g}{\rho_0}\delta_{i3} - 2\epsilon_{ijk}\omega_j u_k \tag{2.1}$$

Where p is the pressure, ρ is the density, g is the gravitational acceleration along the vertical direction i_3, ω is the rotation vector, $\boldsymbol{\epsilon}_{ijk}$ is three dimensional permutation symbol, δ is Kronecker delta, ν is the coefficient of kinematic viscosity.

Considering the Reynolds decomposition for velocity, pressure and density; the equations for the mean flow and the flow fluctuations can be written as

$$u_i = \langle u_i \rangle + u_i'$$

$$p = \langle p \rangle + p'$$

$$\rho = \langle \rho \rangle + \rho'$$

The brackets represent an ensemble mean, although in practical application it is often a time and/or spatial mean.

Consider to rewrite the viscous term of Eq. (2.1) as

$$\nu \frac{\partial^2 \langle u_i \rangle}{\partial x_j^2} = \nu \frac{\partial}{\partial x_j}\left(\frac{\partial \langle u_i \rangle}{\partial x_j}\right) = \nu \frac{\partial}{\partial x_j}\left(\frac{\partial \langle u_i \rangle}{\partial x_j} + \frac{\partial \langle u_j \rangle}{\partial x_i}\right), \frac{\partial \langle u_j \rangle}{\partial x_j} = 0 \ (continuity)$$

$$\nu \frac{\partial^2 \langle u_i \rangle}{\partial x_j^2} = 2\nu \frac{\partial}{\partial x_j} S_{ij}, S_{ij} = \frac{1}{2}\left(\frac{\partial \langle u_i \rangle}{\partial x_j} + \frac{\partial \langle u_j \rangle}{\partial x_i}\right) \tag{2.2}$$

where $2\nu \frac{\partial}{\partial x_j}$ is viscous stress tensor and $\frac{1}{2}\left(\frac{\partial \langle u_i \rangle}{\partial x_j} + \frac{\partial \langle u_j \rangle}{\partial x_i}\right)$ is the mean strain rate tensor.

The equation for the mean flow can be inferred from Eq. (2.1) and using the Reynolds decomposition,

$$\frac{\partial \langle u_i \rangle}{\partial t} + \langle u_j \rangle \frac{\partial \langle u_i \rangle}{\partial x_j} = -\frac{1}{\rho}\frac{\partial \langle p \rangle}{\partial x_i} + 2\nu \frac{\partial}{\partial x_j} S_{ij} - \frac{\partial \langle u_i' u_j' \rangle}{\partial x_j} - \frac{g}{\rho_0}\delta_{i3}\langle \rho \rangle - 2\epsilon_{ijk}\omega_j(\langle u_k \rangle + u_k') \tag{2.3}$$

where $\overline{\langle u_i' u_j' \rangle}$ is the Reynold stress tensor, which describes the turbulence effects on stresses and due to non-linear advection terms.

By multiplying Eq. (2.3) by $\langle u_i \rangle$ the first term of the left hand side becomes

$$\frac{\partial \frac{1}{2}\langle u_i\rangle\langle u_i\rangle}{\partial t} = \frac{1}{2}\left(\langle u_i\rangle\frac{\partial\langle u_i\rangle}{\partial t} + \langle u_i\rangle\frac{\partial\langle u_i\rangle}{\partial t}\right) = \langle u_i\rangle\frac{\partial\langle u_i\rangle}{\partial t} \tag{2.4}$$

And the second term of the left hand side becomes

$$\frac{\langle u_j\rangle\partial\frac{1}{2}\langle u_i\rangle\langle u_i\rangle}{\partial x_j} = \frac{1}{2}\left(\langle u_i\rangle\langle u_j\rangle\frac{\partial\langle u_i\rangle}{\partial x_j} + \langle u_i\rangle\langle u_j\rangle\frac{\partial\langle u_i\rangle}{\partial x_j}\right) = \langle u_i\rangle\langle u_j\rangle\frac{\partial\langle u_i\rangle}{\partial x_j} \tag{2.5}$$

And the third tem of the right hand side becomes

$$\frac{\partial(\langle u_i'u_j'\rangle\,\langle u_i\rangle)}{\partial x_j} = \langle u_i\rangle\frac{\partial\langle u_i'u_j'\rangle}{\partial x_j} + \langle u_i'u_j'\rangle\,\frac{\partial\langle u_i\rangle}{\partial x_j} \tag{2.6}$$

which can be written as:

$$\langle u_i\rangle\frac{\partial\,\langle u_i'u_j'\rangle}{\partial x_j} = \frac{\partial(\langle u_i'u_j'\rangle\,\langle u_i\rangle)}{\partial x_j} - \langle u_i'u_j'\rangle\,\frac{\partial\langle u_i\rangle}{\partial x_j} \tag{2.7}$$

Rewrite Eq. (2.3) with respect to Eq. (2.4), (2.5) and (2.7) to set the equation for the mean kinetic energy,

$$\begin{aligned}\frac{\partial\frac{1}{2}\langle u_i\rangle\langle u_i\rangle}{\partial t} + \langle u_j\rangle\frac{\partial\frac{1}{2}\langle u_i\rangle\langle u_i\rangle}{\partial x_j} \\ = -\frac{1}{\rho}\frac{\partial\langle p\rangle\langle u_i\rangle}{\partial x_i} + 2\nu\frac{\partial}{\partial x_j}S_{ij}\langle u_i\rangle - \frac{\partial\langle u_i'u_j'\rangle\langle u_i\rangle}{\partial x_j} + \langle u_i'u_j'\rangle\,\frac{\partial\langle u_i\rangle}{\partial x_j} - \frac{g}{\rho_0}u_3\langle\rho\rangle \\ - 2\epsilon_{ijk}\omega_j(\langle u_k\rangle + u_k'\end{aligned} \tag{2.8}$$

We can expand the viscous and advection terms to show the dissipation, shear production and transport by Reynolds stresses:

$$2\nu\frac{\partial}{\partial x_j}S_{ij}\langle u_i\rangle = 2\nu\frac{\partial}{\partial x_j}\left[\frac{1}{2}\left(\frac{\partial\langle u_i\rangle}{\partial x_j} + \frac{\partial\langle u_j\rangle}{\partial x_i}\right)\right]\langle u_i\rangle = \nu\left(\frac{\partial\langle u_i\rangle}{\partial x_j}\right)^2 + \nu\left(\frac{\partial\langle u_i\rangle}{\partial x_j} + \frac{\partial\langle u_j\rangle}{\partial x_i}\right)\frac{\partial\langle u_i\rangle}{\partial x_j} \tag{2.9}$$

Eventually we get,

$$\left(\frac{\partial}{\partial t} + \langle u_j\rangle\frac{\partial}{\partial x_j}\right)\frac{\langle u_i\rangle^2}{2} = -\frac{1}{\rho}\frac{\partial\langle p\rangle\langle u_i\rangle}{\partial x_i} + \nu\left(\frac{\partial\langle u_i\rangle}{\partial x_j} + \frac{\partial\langle u_j\rangle}{\partial x_i}\right)\frac{\partial\langle u_i\rangle}{\partial x_j} - \nu\left(\frac{\partial\langle u_i\rangle}{\partial x_j}\right)^2 - \langle u_i'u_j'\rangle\frac{\partial\langle u_i\rangle}{\partial x_j} + \frac{\partial\langle u_i\rangle\langle u_i'u_j'\rangle}{\partial x_j} - \frac{g}{\rho_0}u_3\langle\rho\rangle \tag{2.10}$$

Total kinetic energy | Pressure work | Transport by viscous stresses | dissipation | shear production | Reynold advection flux divergence | Buoyancy production

The 'direct' dissipation term of the mean energy $\nu\left(\frac{\partial\langle u_i\rangle}{\partial x_j}\right)^2$ is expected to be small and most of the dissipation will occur at the smaller turbulent scales. The transfer of energy from the mean flow to the turbulent kinetic energy (TKE) is ensured by the production

With the same procedure, the equation describing turbulent kinetic energy is obtained by multiplying Eq. (2.3) by u_i' and averaging

$$\left(\frac{\partial}{\partial t}+\langle u_j\rangle\frac{\partial}{\partial x_j}\right)\frac{\langle u_i'\rangle^2}{2}=-\frac{1}{\rho}\frac{\partial\langle p'u_i'\rangle}{\partial x_i}+\nu\left(\frac{\partial u_i'}{\partial x_j}+\frac{\partial u_j'}{\partial x_i}\right)\frac{\partial\langle u_i'\rangle}{\partial x_j}-\nu\left(\frac{\partial\langle u_i'\rangle}{\partial x_j}\right)^2-\langle u_i'u_j'\rangle\frac{\partial u_i'}{\partial x_j}+\frac{\partial\langle u_i'\rangle\langle u_i'u_j'\rangle}{\partial x_j}-\frac{g}{\rho_0}\langle u_3'\rho'\rangle \tag{2.11}$$

Considering stationary condition, and neglecting the advection, this last equation is simplified to get the balance between the production and the dissipation of turbulent kinetic energy:

$$P=\varepsilon-B \tag{2.12}$$

where P, ε and B are shear production, TKE dissipation rate and buoyancy, respectively; defined as

$$P=\langle u_i'u_j'\rangle\frac{\partial\langle u_i\rangle}{\partial x_j} \tag{2.13}$$

$$\varepsilon=\nu\left(\frac{\partial\langle u_i'\rangle}{\partial x_j}\right)^2 \tag{2.14}$$

$$B=-\frac{g}{\rho_0}\langle u_3'\rho'\rangle \tag{2.15}$$

2.3 Internal waves

The ocean is a stratified medium, it is generally characterized by a thin mixed layer followed by a region of strong variation of the density, the pycnocline extending over a few tens of meters, and finally a weakly stratified ocean down to the bottom. Under the action of an oscillating external force, such as tides or converging/diverging inertial currents, the density surface or isopycnal layer in the ocean interior will oscillate. In particular, a stratified water column will be displaced by barotropic tidal flow. When this tidal flow encounters a topographic feature, a vertical motion is induced and the oscillating water mass will be subjected to the buoyancy restoring force, and internal waves at the tidal frequency, namely internal tides are generated. Internal tides and internal waves in general generate oscillation of density and currents that are often well described by linear harmonic motion in the form $exp(i(k.x+l.y+m.z-\omega t))$, radiating phase and energy in three dimensions (St. Laurent et al., 2012). The dispersion relationship for this harmonic motion can be obtained by linearizing the momentum and continuity equations and reads

$$\omega^2 = (f^2\,\mathrm{m}^2 + N^2(k^2 + l^2))/(k^2 + l^2 + m^2) \tag{2.16}$$

which can also be written

$$\omega^2 = f^2\sin^2(\varphi) + N^2\cos^2(\varphi) \tag{2.17}$$

where (k, l, m) are wave numbers, ω is the wave pulsation, φ is the angle made between the wavenumber vector and the horizontal, f the Coriolis parameter and N the buoyancy frequency.

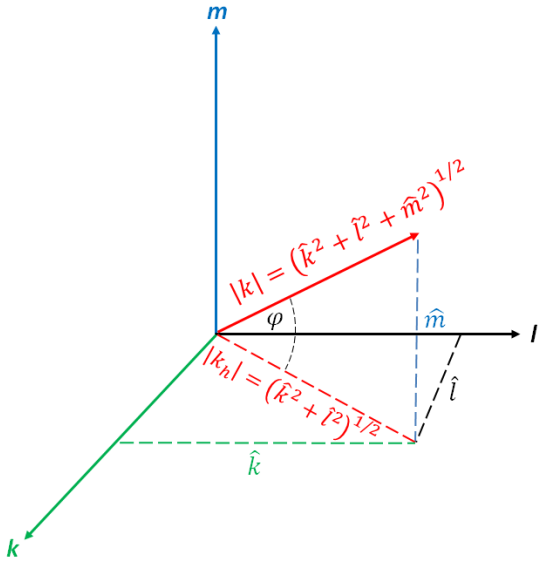

Figure 2.3 Schematic of an internal wave. The red arrow represents the wavenumber direction, which is also the direction of phase propagation making an angle φ with the horizontal plane.

Several important consequences of the dispersion relationship are that:

- The frequency of internal waves is in the range $f < \omega < N$
- The frequency of internal waves is fixed by their propagation direction φ and vice versa but do not depend on the wavenumber.
- The group velocity $Cg = (\partial\omega/\partial k, \partial\omega/\partial l, \partial\omega/\partial m) = \nabla_K \omega$ which represents the propagation speed of energy, propagates at right angle with the phase, that is with an opposed direction on the vertical but the same direction in the horizontal.

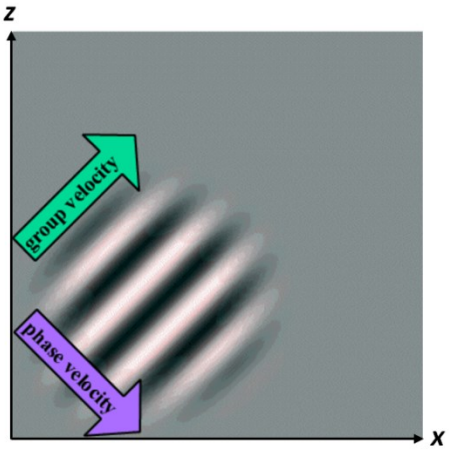

Figure 2.4 Schematic of a wave group, the white and black shades schematize the phase of the wave group; green and blue arrows indicate group and phase velocities, respectively.

As previously stated, the most energetic source of internal waves is the tides. The conversion rate of barotropic energy to baroclinic energy ($\rho' gW$) results from forced vertical oscillations of stratified layers near topography by the barotropic vertical velocity, it can be seen as a source term in the linear internal waves energy equation:

$$\partial_t E + \nabla.(p'\mathbf{u}') = \rho' gW \tag{2.18}$$

where E is the internal waves energy W the barotropic vertical velocity and $\mathbf{u}', p'$, ρ' the baroclinic velocity, pressure and density, respectively ; $p'\mathbf{u}'$ represents the linear internal waves energy flux. In numerical simulations, the internal tides can be represented from fully non-linear numerical models including explicit tides, but this require very high resolution of the bathymetry and it is extremely time consuming. Alternatively, some conversion maps can be made from semi analytical linear models and used as an input power map for GCM. However, the solution is then only strictly valid for linear tides and topographic variations small compared to the total depth. This kind of model can therefore cannot be used for the continental slope, or regions of very rough topography such as the Indonesian seas. An example of the conversion map to internal tides is shown in **Figure 2.5** (Nycander, 2005). It can be seen that internal tides generation is strongly inhomogeneous and is concentrated along topographic features, in particular oceanic ridges.

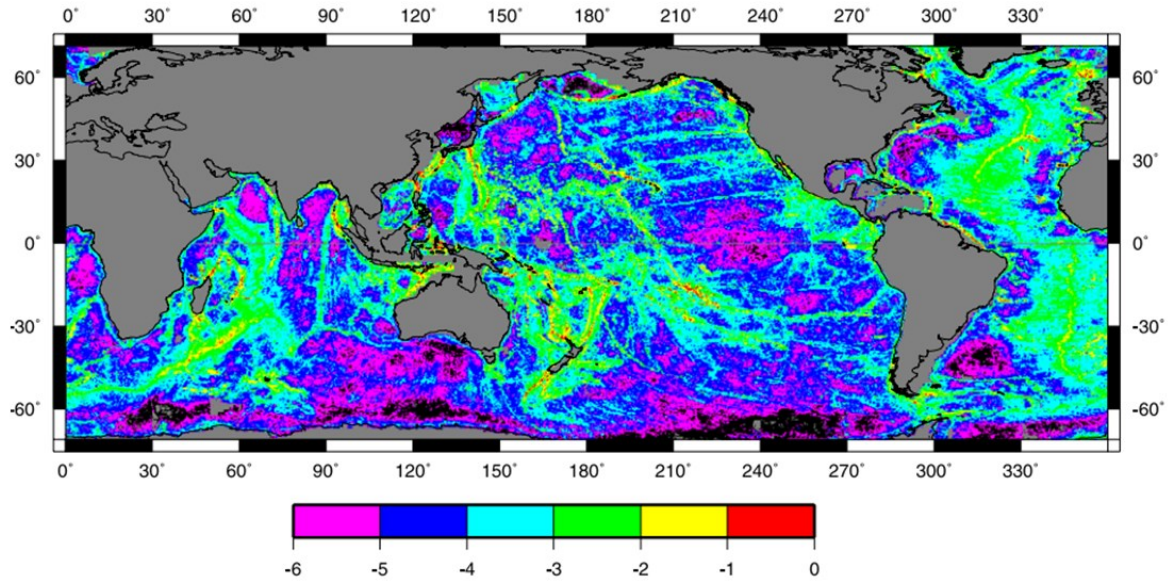

Figure 2.5 Global distribution of the energy flux in $\log_{10}$ scale (W m^{-2}) from the diurnal M2 tidal component to internal waves. The black color means less than 10^{-6} W m^{-2} (from Nycander, 2005).

2.3.1 Spectrum

In the ocean, a wide spectrum of internal waves builds up though interactions with the mesoscale structures and wave-wave interactions Garrett and Munk (1975) suggested that far from boundaries the frequency and wavenumber spectra of internal waves should reach an equilibrium that could be described by a universal shape (**Figure 2.6**). The model is based on mooring and towed instruments observations and assumes that wavenumbers and frequencies are related by the dispersion relationship (Eq. 2.16) while the spectrum is isotropic on the horizontal direction.

Figure 2.6 also shows the combined vertical wavenumber frequency velocity spectrum $\hat{E}_{m,\omega}(m,\omega)$, when this one is integrated over the wavenumber m one gets the frequency spectrum, which is a red spectrum with a global ω^{-2} decrease and an energy divergence around f mimicking the inertial peak. When integrated over the frequency, the wavenumber spectrum is obtained, with again a global k^{-2} decrease of energy. Most of the energy is contained in the low wavenumber and low frequency, yet most of the dissipation is expected at the small wavenumber. Therefore, most of the energy is expected to be transferred through wave-wave interaction from large to a small critical scale ${m_c}^{-1}$ where they dissipate through shear instability. This spectrum has been of fundamental importance because it allowed to build the most relevant wave-wave parameterization of turbulence to date by Henyey et al. (1986). The parameterization by Henyey et al. (1986) computes that rate of transfer of energy toward small scale of small-scale "test" waves being refracted by the background GM field shear.

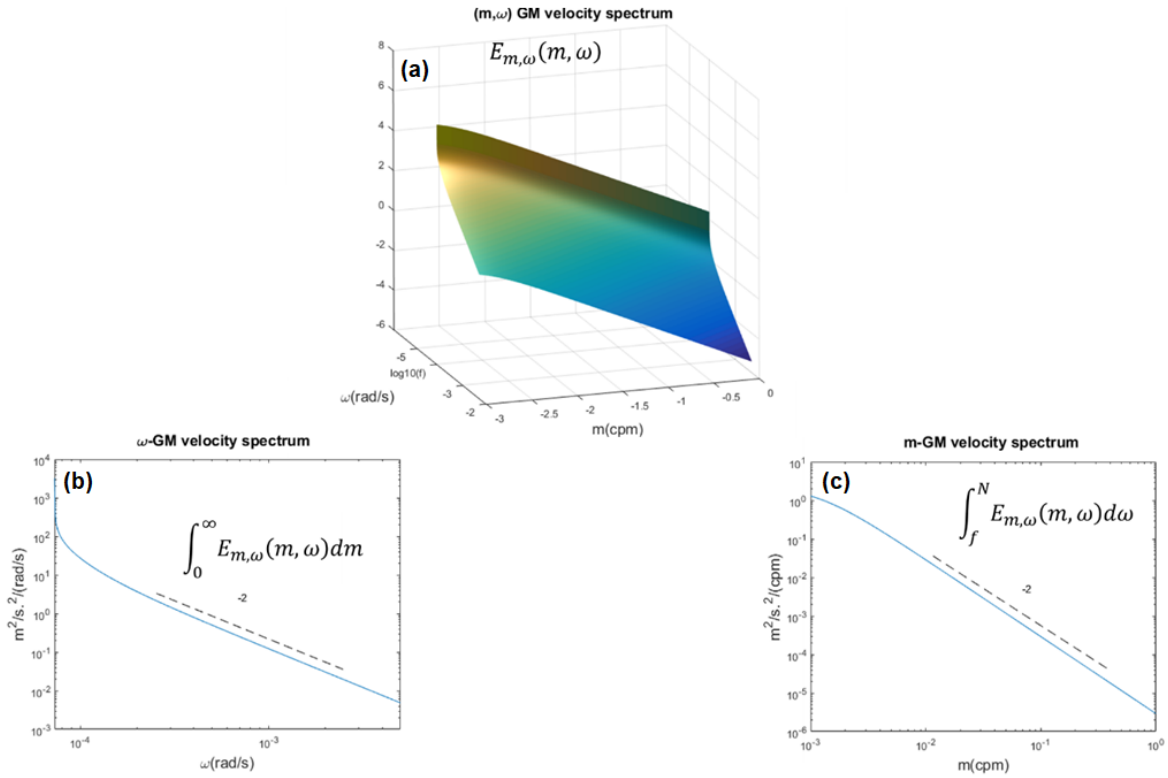

Figure 2.6 The plots of Garrett-Munk (1975) spectrum of internal waves in the ocean: (a) The joint wavenumber frequency spectrum $\hat{E}_{m,\omega}$, the spectral energy is plotted vertically in logarithmic coordinates as a function of frequency and wavenumber; (b) $\hat{E}_m$ the wavenumber spectrum (c) $\hat{E}_\omega$ the frequency spectrum.

The basic formulation

$$\varepsilon = \langle \frac{dE}{dt} \rangle = \langle \hat{E}(m_c) \frac{dm}{dt} \rangle \tag{2.19}$$

where $\langle \hat{E}(m_c) \rangle$ represents the wave number energy spectrum at the critical wavenumber m_c energy of test waves. The evolution of the wavenumber along internal wave energy ray path is derived by the Eikonal equation:

$$\frac{dm}{dt} = -k.\nabla U \tag{2.20}$$

where k is the horizontal wavenumber of the test wave and U the background (GM) velocity. The following approximation is then made:

$$\varepsilon \cong \langle \hat{E}(m_c) \rangle \langle -k.\frac{\partial U}{\partial z} \rangle \cong \langle \hat{E}(m_c) \rangle \langle |k| \rangle \langle | \frac{\partial U}{\partial z} | \rangle \tag{2.21}$$

Plugging the GM formulation in the last equation,

$$E_{GM} \in \omega^{-2} \tag{2.22}$$

Henyey et al. (1986) get

$$\varepsilon \in f N^2 \cos^{-1}(N/f) \tag{2.23}$$

The previous formulation has been modified during the following years to take into account deviation of energy level and frequency content from the GM spectrum and to incorporate practical oceanic measurements and their resolution limitations (Gregg, 1989; Polzin et al., 1995). This concept of the wave route to turbulence and associated parameterization has been fundamental in the past year which helped us to build turbulence map at the global scale (Kunze et al., 2006; Whalen et al., 2012) when direct estimates from microstructure were lacking. Yet this wave-wave interaction failed to reproduce turbulence observed in highly energetic region such as the Indonesian seas (Bouruet-Aubertot et al., 2018) or specific nonlinear processes such as the fission of large internal tides into train of internal solitary waves

2.3.2 Generation mechanism of internal solitary waves

Internal solitary waves (ISW) are short horizontal scale (~km) high frequency (~minute^{-1}) large amplitude (pycnocline deviation reaching tens of meters) waves that can propagate over several hundreds of kms. In the ocean, they are mostly generated from a large amplitude internal wave, which is most of the time generated by tides. The region of convergence and divergence generated by the surface horizontal currents associated with these waves modify the sea surface roughness, these changes can be detected from space in by satellite imagery (SAR, MODIS). **Figure 2.7**.a shows geographical distribution of observed nonlinear internal waves by MODIS satellite from August 2002 to May 2004, with a mechanisms the way satellite imagery detects the appearance of the ISW is shown in **Figure 2.8**.

The most impressive observations of oceanic ISW were reported close to sill affected by strong tidal forcing such as the Camarinal sill in the strait of Gibraltar (Alonso et al., 2002), the Knight Inlet sill in British Columbia (Farmer and Smith, 1980), the Sibutu passage in the Sulu sea (Apel et al., 1985) and Stellwagen bank in Massachusetts Bay (Halpern, 1971). Maxworthy (1979) was the first to provide dynamical explanations to the formation of large ISW train near sills using hydraulic model experiments. The basic process can be explained by

the fact that a tidal flow over a sill can get periodically supercritical, that is the ratio of the barotropic tidal flow velocity to the internal wave phase speed (the Froude number, *Fr*) overcomes the value of 1. Let's consider the increasing and decreasing phase of the ebb tide (**Figure 2.7**). When the tidal flow increases, the critical value of the *Fr* is reached, a stationary depression then grows on the downstream side of the sill (**Figure 2.7**.b(i)). When the tidal flow decreases, the *Fr* drops below one and the large depression formed can then propagates upstream (**Figure 2.7**.b(ii)), and eventually evolves into a solitary wave packet (**Figure 2.7**.b(iii)) following the KdV mechanism described by Eq.(2.24).

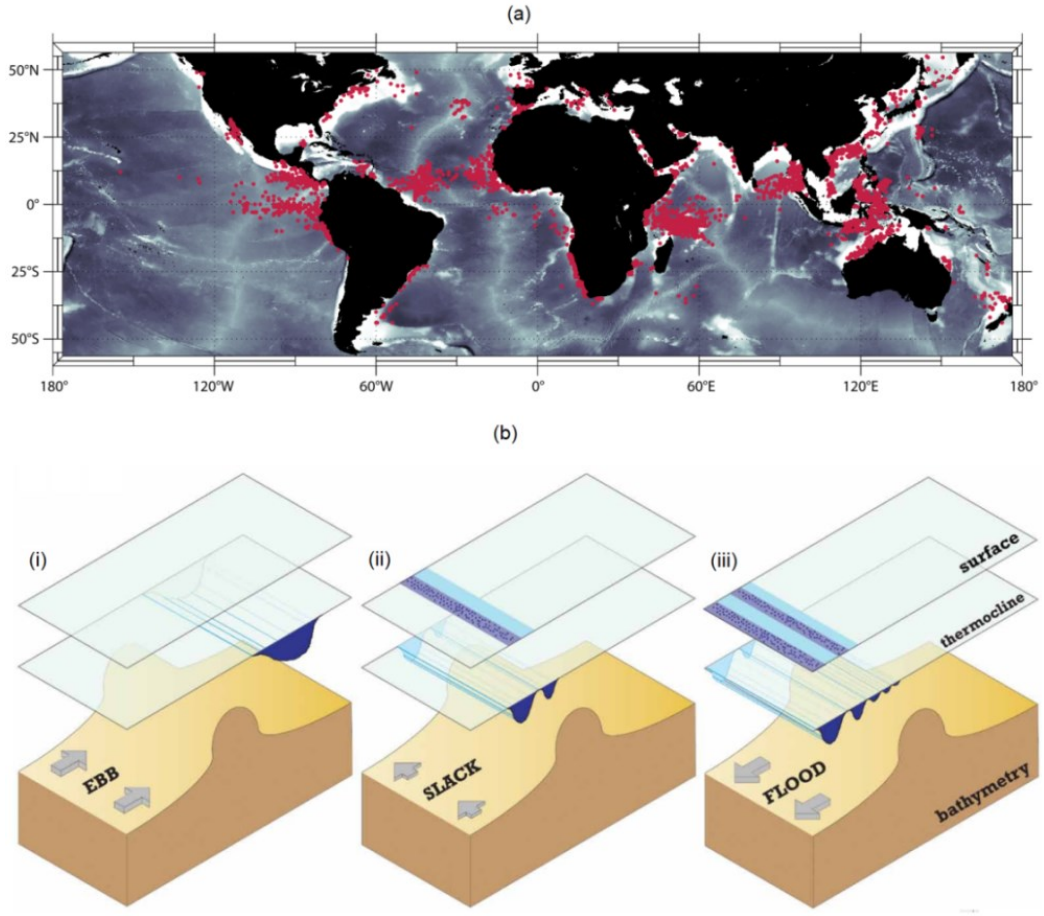

Figure 2.7 (a) Geographical distribution of observed nonlinear internal waves observed in 250 m resolution MODIS satellite from August 2002 to May 2004. (b) the scheme of internal wave generation (i) the stratified flow moves toward the sill and as it slackens, the lee wave propagates upstream over the sill (ii) and eventually evolves as internal wave packet as the flow get stronger (iii) (from Jackson et al., 2012).

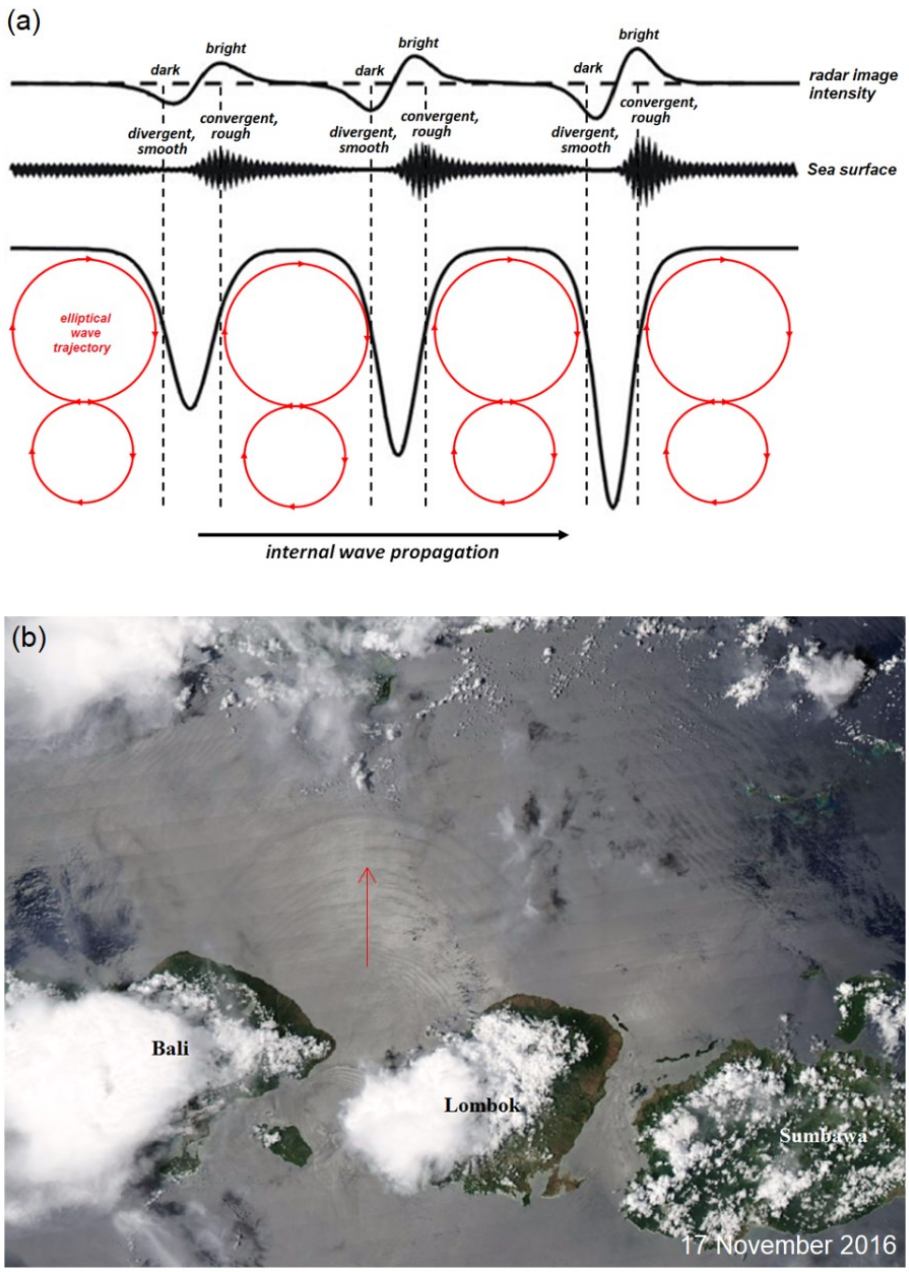

Figure 2.8 (a) Scheme of detectable internal solitary waves activity signature by satellite images (modified from https://earth.esa.int), (b) the observed internal wave by MODIS satellite in the Lombok Strait, Indonesia from on November 17th 2016 (https://zoom.earth).

Later it was shown that ISW could appear even for sub-critical internal tides (Gerkema, 1996). In this case, although the internal tide may have initially a more sinusoidal wave pattern, if the amplitude of the internal tide is large enough to include phase speed variation between trough and crests, it will evolves progressively in a frontal structure (nonlinear steepening) and breaks into an ISW train under non hydrostatic dispersive effects. This process was well modeled by Gerkema (1996) using a tidally forced Korteweg de Vries

equation (KdV) equation. It is believed that this process is for instance the main mechanism for ISW observed in the South China Sea (Zhao et al., 2004).

The process of the fission of a large wave into a sequence of ISW is well modeled by the KdV:

$$\frac{\partial \eta}{\partial t} + c\frac{\partial \eta}{\partial x} + \alpha\eta\frac{\partial \eta}{\partial x} + \beta\frac{\partial^3 \eta}{\partial^3 x} = 0 \tag{2.24}$$

where η (t, z) is the vertical displacement of the pycnocline, t is the horizontal coordinate, and z is depth. Indeed ISW are often formed when a forced internal wave steepens under the action of the nonlinear term $\alpha\eta\frac{\partial \eta}{\partial x}$ and develops a nonlinear leading edge, this steepening is finally balanced by the tendency of the different harmonics composing the nonlinear wave to disperse under the action of the dispersive term $\beta\frac{\partial^3 \eta}{\partial^3 x}$. A solution representing this equilibrium is given by the classical solitary wave profile,

$$\eta(t,z) = \eta_0 sech^2\left[\frac{\left(c_1 + \frac{\alpha\eta_0}{3}\right)(t_0 - t)}{\Delta}\right] \tag{2.25}$$

Parameter a, β, and c_1 are coefficients of nonlinearity, dispersion, and phase speed of long internal waves, respectively; η_0 is the wave amplitude and (c_1+$a\eta_0$/3) is the term of phase speed of the solitary wave. The width of the wave is given by $\Delta^2 = 12\beta/(a\eta_0)$. Coefficient α, β are determined by background density and horizontal density profiles as:

$$\alpha = \left(\frac{3}{2}\right)\frac{\int_{-H}^{0}(c-U)^2(d\Phi/dz)^3 dz}{\int_{-H}^{0}(c-u)(d\Phi/dz)^2 dz}dz \tag{2.26}$$

$$\beta = \left(\frac{1}{2}\right)\frac{\int_{-H}^{0}(c-U)^2\Phi^2 dz}{\int_{-H}^{0}(c-u)(d\Phi/dz)^2 dz}dz \tag{2.27}$$

2.4 Turbulence measurements

One classical way to estimate turbulence is to apply a parameterization in the framework of (Henyey et al., 1986) described previously to classical hydrological and/or currents measurements. Yet this method relies on the assumption of the specific wave-wave interaction mechanism and may not be relevant if this mechanisms not the main driver of turbulence. The turbulent diffusion can sometimes be estimated experimentally by measuring directly the dispersion of tracer such as the (CF3SF5) as conducted by Ledwell et al. (2011). Yet, the most usual way to characterize turbulence in observations is to determine the rate of turbulent kinetic energy dissipation per unit mass, denoted by ε. Its unit are m^2s^{-3} or equivalently Wkg^{-1}. It has typical values range from 10^{-10} m^2s^{-3} in the deep ocean to 10^{-3} m^2s^{-3} in the most energetic regions, such as in the rapid tidal currents, surf zone and straits (Thorpe, 2004).

The most direct and accurate way to measure ε is to use a microstructure sensor which can be mounted on a profiler (Gregg, 1987) or a glider, this on measures one component of the shear at the cm scale and thus provide a direct estimate using the approximation of isotropic turbulence which allows to write,

$$\varepsilon = \nu \left\langle \left(\frac{\partial u_i'}{\partial x_j} \frac{\partial u_i'}{\partial x_j} \right) \right\rangle = \frac{15}{2} \upsilon \left\langle \frac{\partial u'}{\partial z} \right\rangle^2 \tag{2.27}$$

When microstructure measurements of turbulence are lacking the observational estimates rely on typical turbulent scaling of the dissipation rate with more accessible length scales.

2.4.1 Turbulent length scales

Ozmidov length scale (L_O)

Ozmidov scale represents the scale at which buoyancy forces equal inertial forces. It is usually considered as the upper bound of the turbulence convective inertial range, that is the range between the largest overturns and the dissipation scale. Indeed above this scale overtuns are inhibited by the stabilizing effect of stratification (Moum, 1996a). This scale is expressed as (Gargett, 1988),

$$L_O \equiv (\varepsilon/N^3)^{1/2} \tag{2.28}$$

with ε and N is dissipation rate and buoyancy frequency, respectively. Interestingly, if one can derive a typical scale representative of the largest overturns from measurements then this scale can be compared to L_O and the relationship Eq. (2.28) inverted to get an estimation of ε. This is the goal of two length scales that can be computed from observations: the Thorpe scale and the Ellison scale.

Thorpe scale (L_T)

It was introduced in 1977 by Stephen A. Thorpe in 1977 to estimate the dissipation from the vertical scale of turbulence induced density overturns. Thorpe scale is defined as the root mean square of the vertical displacement (d) that would be applied to water parcels within a turbulent patch to gain a gravitationally stable position from a gravitationally unstable position. **Figure 2.9** shows the sketch of density reordering process from which d and L_T are derived . The Thorpe displacement is expressed as,

$$L_T = \sqrt{\langle d^2 \rangle} \tag{2.29}$$

The angle brackets denote an averaging process in the vertical.

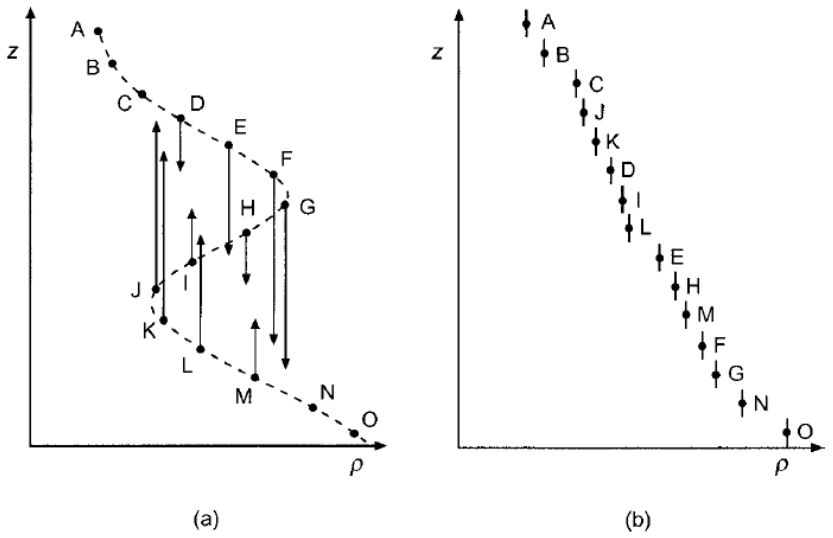

Figure 2.9 The sketches showing the vertical displacement, *d* to gain a stable positions: (a) observed density profile contains a 'shaking' pattern with higher density lying above the lower density, and (b) a stable profile of density after (a) is reordered. The vertical arrows show the vertical displacement needed to get statically stable positions (from Thorpe, 2005).

Since most of the significant displacement results from the largest overturns, L_T is proportional to the L_O by with a proportionality constant a defined from direct microstructure shear observations (Dillon, 1982; Ferron et al., 1998; Stansfield et al., 2001):

$$L_O = a\, L_T \tag{2.30}$$

The value of a can vary between studies, ranging from 0.65 to 0.98 (Finnigan et al., 2002), with the most common used value as 0.8 as firstly parametrized by Dillon (1982).. Considering the proportionality between the two scales, the dissipation rate ε then can be estimated as

$$\varepsilon = a^2\, {L_T}^2 \langle N \rangle^3 \tag{2.31}$$

The angle brackets of N denote an average of the buoyancy frequency inside the overturning region.

Ellison length scale (L_E)

An alternative to the Ozmidov is the Ellison scale which defines a typical overturn scale from turbulent fluctuations and the mean gradient.. This scale is firstly introduced by Ellison (1957), and is expressed as

$$L_e = \left[\overline{c'^2}\right]^{1/2} / \bar{c}_z \tag{2.32}$$

where c' can be density or temperature turbulent fluctuations from the mean density or temperature and $\bar{c}_z$ is the vertical gradient of the mean density or temperature.

2.4.2 Determination of vertical diffusivity, K_ρ

Once the dissipation rate is estimated, the vertical diffusivity driving the mixing then can be estimated via a relation,

$$K_\rho = \Gamma \varepsilon \langle N^{-2} \rangle \tag{2.33}$$

Where Γ is the mixing efficiency, can be as constant, 0.2 (Thorpe, 2005); or varying depends on the energetics of the regimes classification, considering the strength of the dissipation rate to counter the stratification (termed as turbulence intensity parameter/Reynolds buoyancy, Re_b, will be described further technically in Chapter 3). Since some microstructure observations verified that the using of constant mixing efficiency overestimate in the low and high energetic regimes, some parameterizations have been made (Bouffard and Boegman, 2013; Shih et al., 2005) to avoid that issue.

2.4.3 Mixing efficiency

The ratio of the buoyancy flux to the production of TKE is known as the rate is the flux Richardson number, *Rf*, which using Eq. (2.12) reads

$$R_f = \frac{P}{\varepsilon} = \frac{B + \varepsilon}{\varepsilon} \tag{2.34}$$

The mixing efficiency in the stratified flows can be expressed as a function of flux Richardson number,

$$\Gamma = \frac{R_f}{(1 - R_f)} = \frac{B}{\varepsilon} \tag{2.35}$$

Osborn (1980) suggested that $\Gamma \leq 0.2$ and following this study, the maximum value Γ = 0.2 has become the canonical value used in mixing studies (Oakey, 1982; Peters et al., 1988) even though higher value up to 0.4 (Moum, 1990) and lower values have also been suggested (Arneborg, 2002; Moum, 1996b). There is actually no physical reasons for Γ = 0.2, and dimensional analysis suggested that it should depend on several non-dimensional numbers. Numerous studies have investigated is dependence on gradient of Richardson number, *Ri* and buoyancy Reynold number, which is also known as turbulent intensity parameter, Re_b

$$Re_b = \frac{\varepsilon}{\nu N^2} \tag{2.36}$$

with ν = 1.2 x 10^{-6} m^2s^{-1} is seawater viscosity. For instance, the mixing efficiency was characterized as the quadratic growing function of Ri and the decreasing function of Re_b (Lozovatsky et al., 2006; Lozovatsky and Fernando, 2013) as $\Gamma \sim Re_b^{-1/2}$ within a range of $3\times10^4<Re_b<3\times10^7$ (Lozovatsky and Fernando, 2013) or $10^2<Re_b<10^3$ (Shih et al., 2005). **Figure 2.10** shows the dependence of the mixing efficiency to Ri and Re_b inferred from observations.

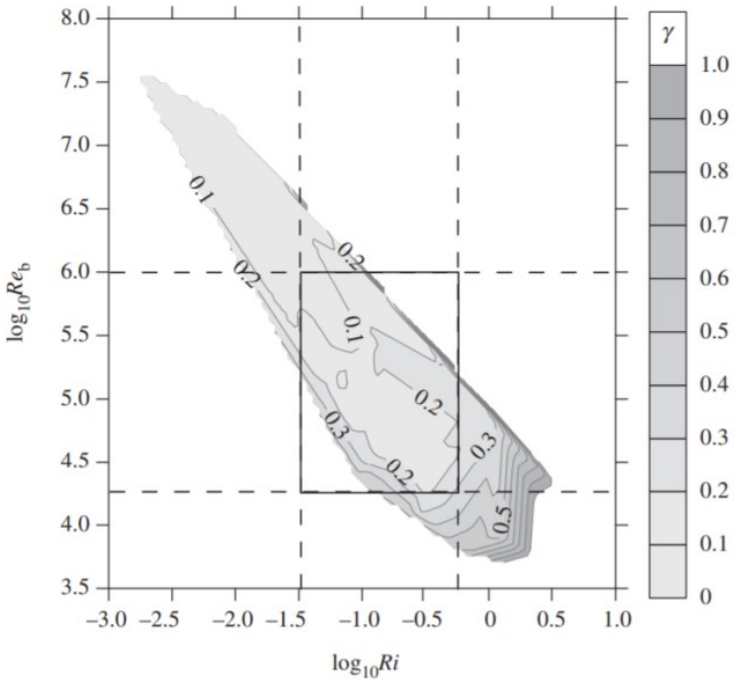

Figure 2.10 The mixing efficiency Γ contour plot as a function of Ri and Re_b from Lozovatsky and Fernando (2013). The rectangle confines the range of $0.03 < Ri < 0.4$ where a relatively constant mixing efficiency was approximated (Lozovatsky and Fernando, 2013).

Furthermore, some studies indicated that assuming a mixing efficiency constant of Γ = 0.2 as defined by Osborn (1980) tends to overestimate the diffusivity, K_ρ (Bouffard and Boegman, 2013; Ivey et al., 2008; Shih et al., 2005). Latest study by Bouffard and Boegman (2013) suggested that Γ is a function of turbulence regime. The turbulent regimes can be determined from the turbulence intensity parameter Re_b, which is the ratio between the destabilizing effect of turbulence to the stabilizing effect of stratification and viscosity (Ivey et al., 2008). The energetics regime of the turbulence is reflected from Re_b values. An intermediate Re_b reflects the transitional regime, when the stratification affects the isotropy. A molecular regime takes place when the turbulent diapycnal flux becomes zero so that heat or salt molecular diffusivity drives the turbulence. Note that despite these advances, there is still

no consensus on the way we should parameterize the mixing efficiency, for instance several studies have evidences that a constant mixing efficiency near the Osborn values could often persist in the turbulent regime of Bouffard and Boegman (Monismith et al., 2018; Vladoiu et al., 2019). In fact, recent papers have rather advocated for the use of the constant mixing efficiency of Osborn until we get a consensus on the parameterization (Gregg et al., 2018; Monismith et al., 2018).

Table 2.1 Mixing efficiency, developed based on turbulent intensity parameter (Bouffard and Boegman, 2013).

Regimes	Re_b	Γ_{BB}
Molecular regime	$Re_b<1.7$	$10^{-7}\ N^2/\varepsilon$
Buoyancy controlled regime	$1.7<Re_b<8.5$	$0.1\ \varepsilon^{1/2}/(Pr^{1/4}\nu^{1/2}N)$, $Pr=7$
Transition regime	$8.5<Re_b<400$	0.2
Energetic regime	$Re_b\geq400$	$4\nu^{1/2}\ N/\varepsilon^{1/2}$

2.4.4 Double diffusion influence on mixing

A step like structures in a density profile is often an evidence of the profile instability that can result from turbulence and/or double diffusion. The double diffusion results from an opposite trend of temperature and salinity in regarding the water column stability in conjunction with the two order of magnitude ratio between the molecular diffusivity of heat and salt (Stern, 1960). Two situations can be found, termed as diffusive convection and salt fingering. .

Diffusive convection (DC) occurs if both temperature and salinity increase with depth. In this case, the potential energy to maintain the instability comes from the destabilizing temperature component of density. Vertically, the DC is characterized by a series of homogenous layer of temperature and salinity separated by their sharp gradient. Salt fingering (SF) occurs when salinity and temperature both decrease with depth. In this case, the salinity component is destabilizing. In either case, this instability results from a release of potential energy stored in the water column. The stationary TKE balance for double diffusive instability is therefore simply:

$$\varepsilon = -B$$

As opposed to more classical shear driven turbulence, there if no TKE production term by the shear and the buoyancy flux acts as a source of TKE that is balanced by the dissipation rate.

Figure 2.11 shows the possibility of the occurrence of DC and SF in the Pacific water masses, where the decrease of salinity maximum in the lower thermocline is accompanied by the decrease of temperature, hence DC is common in this region. In the deeper layer, the increase salinity minimum with of Pacific intermediate water with depth is often accompanied by the increase of temperature adiabatically with depth.

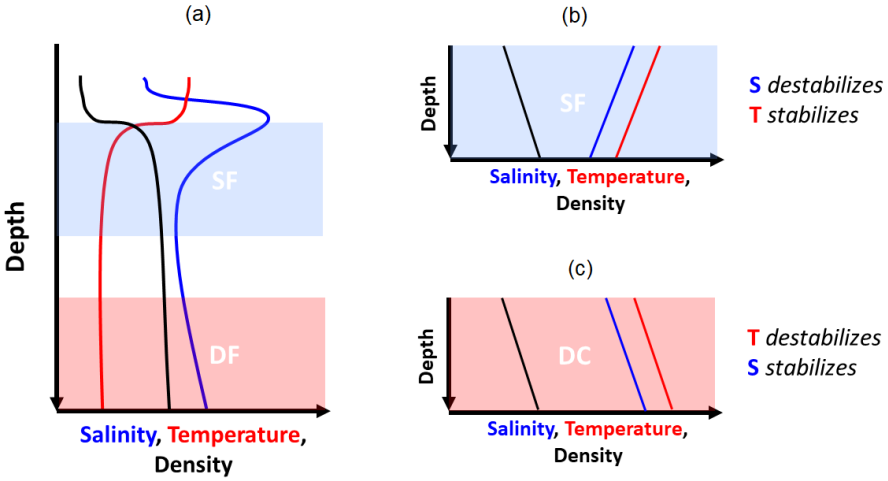

Figure 2.11 The sketch shows a wide band of double diffusion possibility in the Pacific water masses (a). The salt fingering (SF) occurred when both temperature and salinity decrease with depth (b), and diffusive convection (DC) occurred when both salinity and temperature increase with depth (c).

Double diffusion can be quantified using Turner angle (*Tu*), which is defined as (Ruddick, 1983),

$$Tu = tan^{-1}\left(\frac{1+R_\rho}{1-R_\rho}\right) \tag{2.37}$$

where R_ρ is the vertical density ratio, $R_\rho = \beta Sz/\alpha Tz$ with Sz and Tz are vertical gradients salinity and potential temperature, respectively; $\alpha = -(1/\rho_0)(\partial\rho/\partial T)_{S,p}$ is thermal expansion coefficient, $\beta = (1/\rho_0)(\partial\rho/\partial S)_{T,p}$ is the saline contraction coefficient, and ρ_0 is a reference density. The DC instability is characterized by strong regime [-90° < *Tu* <-51°] and weak regime [-51° < *Tu* <-45°] and the SF instability is characterized by strong regime [72° < *Tu* <90°] and weak regime [45° < *Tu* <72°]. The stable region is characterized by [-45° < *Tu* <45°]. In this thesis, we did not attempt to characterize double diffusion processes but found that regime favourable to double diffusion were often characterized by noisy density profiles and numerous false overturns (Chapter 3); a problem likely resulting from the fine structure generated on density profile by double diffusion instability.

3

Spatial Structure of Turbulent Mixing in the Indonesian Seas

Chapter 3
Spatial Structure of Turbulent Mixing in the Indonesian Seas (Submitted Paper to *Progress in Oceanography*)

3.1 Introduction

The Indonesian seas are the only low latitude passage connecting the Pacific and Indian Oceans. The flow, from the Pacific to the Indian Ocean, is known as the Indonesian throughflow (ITF) (Sprintall et al., 2004) and drives the transport of Pacific water masses of the thermocline layer (i.e. North Pacific Subtropical Water, NPSW; and South Pacific Subtropical Water, SPSW) and intermediate layer of the Pacific water masses (i.e. North Pacific Intermediate Water, NPIW; and South Pacific Intermediate Water, SPIW) into the Indian Ocean (Bingham and Lukas, 1994; Fine et al., 1994; Tsuchiya et al., 1989; Wyrtki, 1961). The general current system in the Indonesian seas with its main branches is shown in **Figure 3.1**. There are two main ITF routes connecting the two oceans, i.e. the western route and the eastern route. The western route of ITF is the main pathway of the north Pacific water masses, it comprises the Sulawesi Sea, Makassar Strait, and the Flores Sea; while the eastern route is known as the main pathway of the South Pacific water masses and comprises the Halmahera Sea, Maluku Sea, Banda Sea; and semi-enclosed sea, Seram Sea. Along the western route, the North Pacific water masses flow through the Mindanao Strait enters the Sulawesi Sea and Makassar Strait, and then bifurcates in the Dewakang waters, one-portion exits through the Lombok Strait and the other is deflected eastward and enters the Flores and the Banda Sea. Through the eastern route, the South Pacific water masses flow through the north Halmahera Strait, enters the Halmahera Sea and bifurcates in the southern Halmahera Strait, then a portion enters the Maluku Sea and the remaining enters the Seram and Banda Sea.

The core layer of the Pacific thermocline (NPSW/SPSW) and intermediate (NPIW/SPIW) layers are centered in the isopycnal 24-24.5 σ_θ and 25-26.5 σ_θ, respectively (Atmadipoera et al., 2009; Kashino et al., 1996). The NPSW and SPSW are characterized by salinity maxima, S_{max} [34.5-35] psu while the NPIW and SPIW are characterized by salinity minima S_{min} [34.2-34.5] psu. The North Pacific water masses are advected by the Mindanao Current (MC) from the subtropical Pacific and enter the western route via the Mindanao Strait leading to the Sulawesi Sea; while the South Pacific water masses are advected by the New Guinea Coastal Under Current, NGCUC, and enters the eastern route via the Halmahera Sea

(Wattimena et al., 2018). Further details on the characteristics of the western Pacific water masses and the circulation driving the throughflow can be found in some previous studies (Bingham and Lukas, 1994; Fine et al., 1994; Kashino et al., 1996; Kashino et al., 1999; Kashino et al., 2005; Ffield and Robertson, 2008).

Several studies show that the ITF has a significant impact on the large scale thermohaline circulation through the input of a low salinity anomaly that eventually exits poleward within the Agulhas current system (Gordon, 2005; Gordon and Fine, 1996). Turbulent mixing induces a cooling anomaly of sea surface temperature, which could impact the on deep atmospheric convection and the rainfall spatial structure. The wind convergence in this region is also weakened as a result of the weakening the equatorial Pacific trade winds and the strengthening of the along-shore South Java wind (Koch-Larrouy et al., 2010).

The vertical mixing in the ITF passages and the resulting freshening and cooling of the Indonesian seas upper water were attributed primarily to the intense tidal activity (Gordon, 2005; van Aken et al., 1988). This hypothesis was recently confirmed by Ray and Susanto (2016) who showed a clear spring-neap cycle of SST in near major straits using higher spatial and temporal resolution satellite SST.

The driving mechanisms of water mass transformation were also investigated using regional circulation models with explicit or parameterized tidal mixing (Hatayama, 2004; Koch-Larrouy et al., 2015, 2010, 2007; Nagai and Hibiya, 2015; Sprintall et al., 2003). In 2004, a study was performed by Hatayama (2004) to clarify the mechanism by which tidally induced vertical mixing transforms the ITF water properties in the Indonesian seas using 3D non-hydrostatic numerical simulations of tidally generated internal tides in the Dewakang sills. Hatayama (2004) found that the internal waves induce vigorous vertical mixing in the sill region, where the salinity maximum and the minimum core layers of the ITF thermocline water are considerably attenuated. The vertical eddy diffusivity attains a maximum value of 6×10^{-3} m^2s^{-1}. Koch-Larrouy et al. (2007) studied water mass transformation for the whole Indonesian region using a ¼° regional model with parameterized internal tides mixing. The internal tide-induced mixing parameterization was built based on the St. Laurent et al. (2002) scheme, using horizontal maps of energy transfer from barotropic tides to baroclinic tides but with a different assumption on the vertical profile of the internal tide energy. The model results showed a maximum of energy dissipation within the thermocline, with an average of 1.5×10^{-4} m^2s^{-3}. They also showed that tidal energy is the major source of mechanical mixing responsible for the strong transformation of Pacific water masses in the Indonesian seas. The parameterization was based on two strong assumptions: firstly, they consider that most of the

internal tide energy cannot escape the complex semi-enclosed seas topography so that the local dissipation efficiency, i.e. the fraction of internal tide energy that dissipates near the wave generation regions was set to unity. Secondly, the vertical structure of the energy dissipated was chosen based on the stratification profile, which focused almost all the energy dissipation in the pycnocline. The limitation of these two assumptions was discussed by Y. Cuypers et al. (2017) for the Timor basin. Nagai and Hibiya (2015) used a high-resolution simulation (1/100°) of the Indonesian seas, with explicit M2 tides but no background circulation, using the MITGCM, which is well suited to complex topography representation. They found that the generated internal tides dissipate 50–100% of their energy close to their generation sites (termed as 'near-field' areas), that is typically within a half wavelength of the gravest internal tide mode (~65 km) while the remaining baroclinic energy propagates away and dissipated far from the generation sites (termed as 'far-field' areas). The depth and area-averaged vertical diffusivity within the eastern Indonesian seas is estimated to be 2.2×10^{-4} $m^2 s^{-1}$ which also agrees well with the previous estimates (Ffield and Gordon, 1992; Koch-Larrouy et al., 2007, hereinafter KL07). Yet they also reported local discrepancies with KL07 parameterization, with significantly overestimated (or underestimated) vertical eddy diffusivity in the near field (or the far field). Later in 2017, using a high resolution 3D hydrostatic model taking into account four major diurnal and semidiurnal tidal constituents and the atmospheric forcing (Nugroho et al., 2017) found elevated depth-integrated dissipation rates in straits and narrowing passages in agreement with previous studies.

Some dissipative regions were identified in the ITF pathways based on numerical models and observations. In the eastern route, the dissipative regions are localized in the Halmahera Straits, Manipa Strait, Lifamatola Strait, Buru Strait, Ombai Strait, Alor Strait, Sumba Strait, and Sawu Strait (Adhyatma et al., 2019; Koch-Larrouy et al., 2015; Nagai et al., 2017; Nagai and Hibiya, 2015; Purwandana et al., 2014; Suteja et al., 2015). In the western route, the most dissipative regions are located in the entrance gate of the ITF, Mindanao Strait; Labani Channel, Dewakang waters, and Lombok Strait (Koch-Larrouy et al., 2010; Nagai and Hibiya, 2015). Direct estimates of vertical mixing using microstructure measurements in the Indonesian seas are still limited. The first direct estimates were performed in 1998 during the ARLINDO Microstructure experiment in the Banda Sea. As reported by Alford et al. (1999), vertical mixing in the central Banda Sea is weak, except for a few spots of intense mixing induced within 100-300 m by a wind-induced baroclinic near-inertial wave (Alford and Gregg, 2001). The mean vertical diffusivity of $(9.2 \pm 0.55) \times 10^{-6}$ $m^2 s^{-1}$

is much smaller than the estimated values of $1x10^{-4}$ m^2s^{-1}, obtained by Ffield and Gordon (1992) and Hautala et al. (1996) through indirect methods. This low average value is not surprising as it was observed in the deep region, where there is weak barotropic to baroclinic energy conversion. In the end, they suggested further observations at different times, since the ITF transport varies seasonally, and at different locations along the ITF paths.

The INDOMIX cruise was performed along the eastern route of the ITF (Koch-Larrouy et al., 2015, Bouruet Aubertot et al 2018) to fill the lack of direct mixing estimates in the Indonesian Seas. The analysis of the microstructure profiles and the Thorpe Scale method applied over the CTD and XCTD profiles confirmed very strong energy dissipation within straits, ranging between [10^{-7}, 10^{-4}] m^2s^{-3}, and the lower values at stations further away from the straits. Significant decrease away from the generation sites was observed with [10^{-9}, 10^{-8}] m^2s^{-3} dissipation rates at the center of the Halmahera Sea and the lowest values at the Banda station, [10^{-11}, 10^{-10}] m^2s^{-3}, further away from the generation sites. The vertical eddy diffusivity values were large, between $5x10^{-4}$ and $5x10^{-1}$ m^2s^{-1}, except in the Banda Sea, where values are similar to the ones found in the open ocean, 10^{-6} m^2s^{-1}. In general, they found that enhanced mixing occurs preferentially above rough topography, such as in the Ombai Strait, the northern straits of the Halmahera Sea's, the Buru Strait and Sumba Strait. The relevance of fine-scale parameterization of the dissipation rate was addressed Bouruet-Aubertot et al. (2018) based on this dataset. Such parameterizations provide estimates of the dissipation rate from standard hydrographic and/or currents measurements. Bouruet-Aubertot et al. (2018) found that the most classical form of this parametrization, which assumes a close to Garret-Munk (hereinafter GM) field (Gregg, 1989; Henyey et al., 1986; Polzin et al., 1995) was only available in the far field, in the central Banda sea. In the intermediate field (central Halmahera sea) the Mackinnon-Gregg parameterization was in good agreement with the observations, yet this last parameterization requires to fix an average dissipation rate for the region as a free parameter which is not universal (Xie et al., 2013). In the near field area, none of these parameterizations gave reliable estimates.

A large number of CTD profiles covering most of the Indonesian seas and sampled since 1990 are available to build an observational based regional map of dissipation rates. Therefore, we propose to quantify the mixing properties from all CTD profiles collected from various research cruises and various seasons using the Thorpe scale method. This method has been shown to be generally in good agreement with microstructure measurements estimates provided that the statistics are sufficient (Dillon, 1982; Ferron et al., 1998; Frants et al., 2013; Klymak et al., 2008) and as opposed to fine-scale wave-wave parameterization does not rely

on a specific mechanism driving turbulence. However, it shows several caveats as recently discussed by Mater et al. (2015) and interpreted by Scotti (2015). Hence, Thorpe scale estimates were first tested against the microstructure estimates available in the Indonesian Seas. Based on this comparison, Thorpe scale estimates were validated and used for a regional study over the Indonesian Seas thus providing a footprint of mixing hotspots. Thorpe scale estimates were also used as a reference to test the relevance of numerical outputs (Klymak and Legg, 2010) and the key driving mechanisms for turbulence were identified from this comparison.

The paper is organized as follows. Section 3.2 describes the dataset and the methods used to estimate kinetic energy dissipation rate and vertical eddy diffusivity from observations and presents briefly the numerical simulations. Results are presented in section 3.3: the hydrography with a focus on the erosion of the Pacific water masses salinity along their various pathways is described in section 3.3.1, the improved Thorpe scale method for dissipation rate is tested against microstructure measurements in section 3.3.2 as well as outputs from numerical simulations, section 3.3.3 focuses on the characterization of dissipation and mixing within the thermocline waters, originating from the Pacific and provides evidence of the major role of internal tides. The comparison with numerical models and analysis of their caveats are conducted in section 3.3.4. Conclusions are eventually drawn in section 3.4.

3.2 Methodology

3.2.1 Dataset

CTD dataset stored in the Research Center for Oceanography-Indonesian Institute of Sciences (LIPI) and Indonesian Ministry of Marine Affairs is analyzed to infer the dissipation rates and vertical diffusivity. A total of 817 geographically distributed single cast CTD profiles, sampled using Sea-Bird Electronics (SBE) by Indonesian research vessels, Baruna Jaya I, Baruna Jaya VII and Baruna Jaya VIII from 1990 until 2016, were used. The profiles were acquired from various international expeditions, i.e. 185 stations of ARLINDO Project (sampled in 1993, 1994, 1996); 71 stations of INSTANT (International Nusantara Stratification and Transport) Program sampled between 2003-2006; 507 stations from annual monitoring project of the Research center for Oceanography Indonesian Institute of Sciences (LIPI) in the frame of *Expedition of Widya Nusantara* (EWIN); and 61 stations from Stock Assessment Project of the Indonesian Ministry of marine Affairs, sampled between 2015-2016. Hourly CTD cast in some regions of the internal Indonesian seas was also analyzed. This data set was completed outside Indonesian waters by the available CTD profiles (of 1405 casts) sampled with the same instruments, mostly from World Ocean Database (WOD) (https://www.nodc.noaa.gov/OC5/WOD/pr_wod.html) in order to map the general water masses properties in the Pacific and Indian Oceans at the entrance and exit of the Indonesian seas. To get a qualified dataset, we only take into account the casts with vertical resolution ≥1 m. Only regions deeper than 100 m depth were considered. The detail and geographical positions of the dataset are shown in **Figure 3.1** and **Table 3.1**.

As stated by SBE, CTD probes sample at a maximum rate of 24 Hz. Typically, the accuracy of the sensors is ±0.0003 S m^{-1} for the conductivity and 0.001°C for the temperature. All profiles are processed using a standard pre-processing of the raw data according to the modules given by SBE Data Processing to get regularly 1 m bin-averaged value. Part of this dataset had been published in previous studies (Ffield and Gordon, 1996; Gordon, 2005; Gordon and Fine, 1996; Gordon and McClean, 1999; Ilahude and Gordon, 1996). Only downcast data are used in this study to avoid contamination by the CTD/rosette frame. Since near-surface layer profiles are often contaminated by some turbulence due to the vessel's motion, we discarded the first 5 meters layer from the profiles.

In order to check the relevance of our improved Thorpe scale method (see section 3.2), we use vertical microstructure profiler (VMP) and CTD data sets sampled during INDOMIX 2010 expeditions in: northern Halmahera Strait (S_A, 129.1742° E; 0.0605° N);

central Halmahera Sea (S_B, 128.8830° E; 0.7520° S); southern Halmahera Strait (S_C, 128.7630° E; 1.357° S); central Banda Sea (S_D, 126.9980° E; 6.2855° S); Ombai Strait (S_E, 125.2440° E; 8.2838° S); and also the VMP from TOMTOM 2015 expeditions in: northern Timor Passage (S_F, 127.2105° E; 9.0228° S); central Timor Passage (S_G, 127.3098° E; 9.2673° S); southern Timor Passage (S_H, 127.483° E; 9.6199° S). The station positions are shown in Figure 3.1.

Table 3.1 Historical CTD datasets processed to infer the dissipation rate and vertical diffusivity in this study. Repeated CTD measurements in the Indonesian seas analyzed in this study. The sub-regions map and CTD geographically distributed stations are shown Figure 3.2 in and the repeated CTD casts are shown in Figure 3.1.

Sub-region	Repeated Cast				Number of Single Casts
	Month year)	Number of casts	Station/Position/Topography depth (m)	Location	
Sulawesi Sea (SLA)	Feb 1994)	5	S_1/123.2313 E, 1.8658 N/3686 m	Central Sulawesi Sea	70
	Aug 1993)	3	S_2/122.2931 E, 1.8811/4972 m	Central Sulawesi Sea	
Makassar Strait (MAK)	Feb 1994)	6	S_7/118.5997 E, 3.5192 S/1998 m	Labani Channel	118
	Jun 2013)	12	S_6/118.5043 E, 3.0299 S/2226 m	Labani Channel	
	Sep 2002)	9	S_3/118.1475 E, 0.0668 N/2010 m	Deep western Makassar St.	
		9	S_4/118.2076 E, 0.13556 N/2180 m	Deep western Makassar St.	
		9	S_5/118.3270 E, 0.0442 N/2374 m	Deep western Makassar St.	
Flores Sea (FLO)	Jan 1994)	6	S_9/120.5122 E, 7.8002 S/4972 m	Central Flores Sea	44
	Sep 1993)	4	S_8/120.4977 E, 7.7977 S/4972 m	Central Flores Sea	
Banda Sea (BAN)	Des 1996)	7	S_{12}/131.4972 E, 5.0189 S/4625 m	Eastern Banda Sea	110
	Feb 1994)	6	S_{11}/128.1995 E, 5.1581 S/3686 m	Central Banda Sea	
	Aug 1993)	5	S_{10}/128.1992 E, 5.7897 S/4940 m	Central Banda Sea	
Maluku Sea (MAL)	Feb 1994)	5	S_{14}/126.9930 E, 1.8462 S/2038 m	Lifamatola Passage	139
	Aug 1993)	8	S_{13}/126.0030 E, 2.5297 S/3500 m	Buru St.	
Halmahera Sea (HAL)	-	-	-	-	53
Lesser Sunda seas (LES)	Feb 1994)	4	S_{16}/125.6397 E, 8.0505 S/1734 m	Ombai St.	283
	Aug 1993)	4	S_{15}/125.6397 E, 8.0505 S/2216 m	Ombai St.	

As stated by SBE, CTD probe samples at a maximum rate of 24 Hz. Typically, the accuracy of the sensors is ±0.0003 S m^{-1} for the conductivity and 0.001°C for the temperature.

All profiles have been processed using a standard pre-processing of the raw data according to the modules given by SBE Data Processing to get regularly bin-averaged value, 1 m; and some of the dataset had been published in other studies (e.g. Ffield and Gordon, 1996). Only downcasts data are used in this study to avoid contamination of the CTD/rosette frame. A standard procedure contained in the SBE data processing module consists of some steps to minimize the effects of instrument noise and measurements errors. Since near-surface layer profiles are often contaminated by some turbulence due to vessel's motion, we discarded the first 5 meters layer from the profiles. Note that dealing with largely contaminated by double diffusive events outside Indonesian seas region (i.e. in the Pacific and Indian Oceans) which potentially complicating the real vertical turbulent patches, only CTD stations located in the interior Indonesian seas are involved in the turbulent mixing analysis.

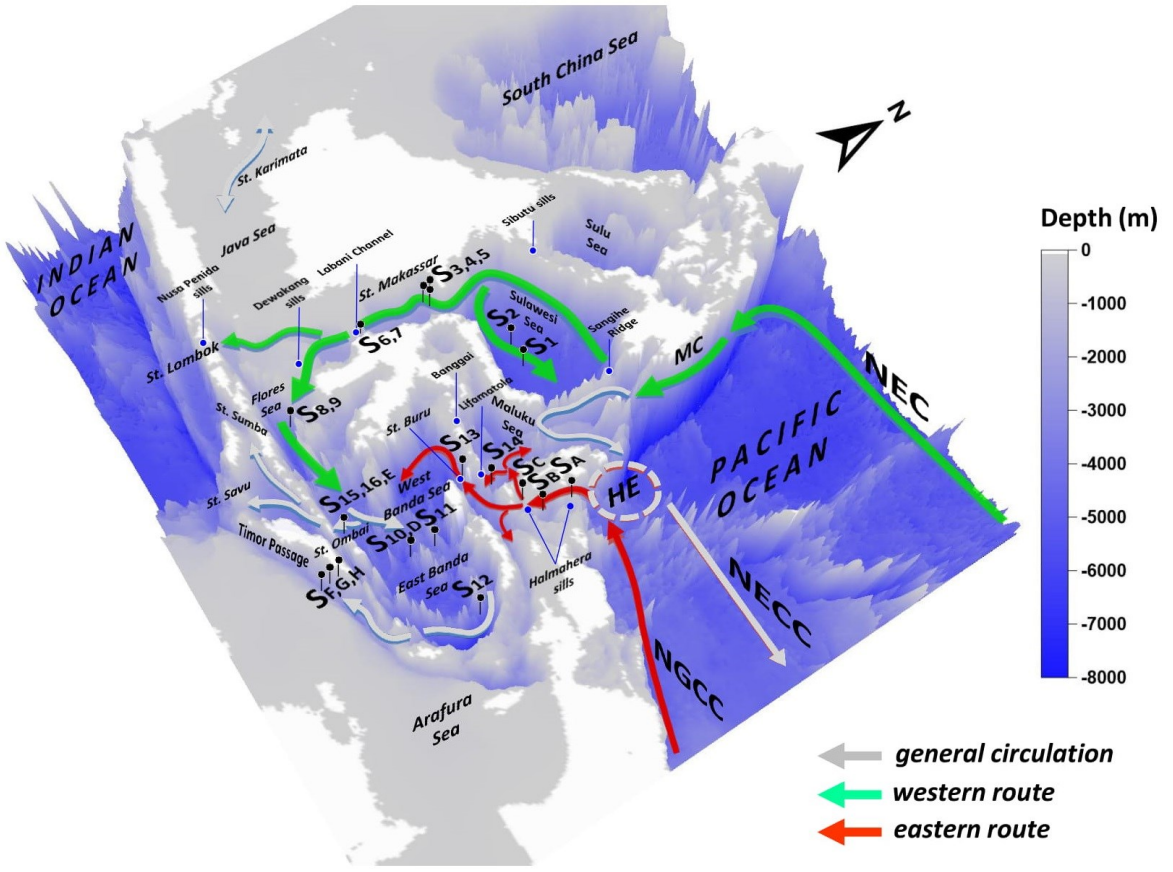

Figure 3.1 Schematic of the general circulation in the Indonesian seas and its surrounding waters with basins and some restricted features (straits, channel, and sills) toponymal on the topography provided by ETOPO; the locations of repeated profiling CTD casts (black pins, S_1-S_{16}) and VMP stations (black pins, S_A-S_H). The North Pacific water masses flow in the Indonesian seas through the western route of ITF (green arrows), which is forced by the north equatorial current (NEC) that bifurcates southward as Mindanao Current (MC). The South Pacific water masses flow in the Indonesian seas through the eastern route (red arrows), which is forced by New Guinea coastal current (NGCC) originating at the bifurcated current of the Halmahera eddy (HE) and the north equatorial counter current (NECC).

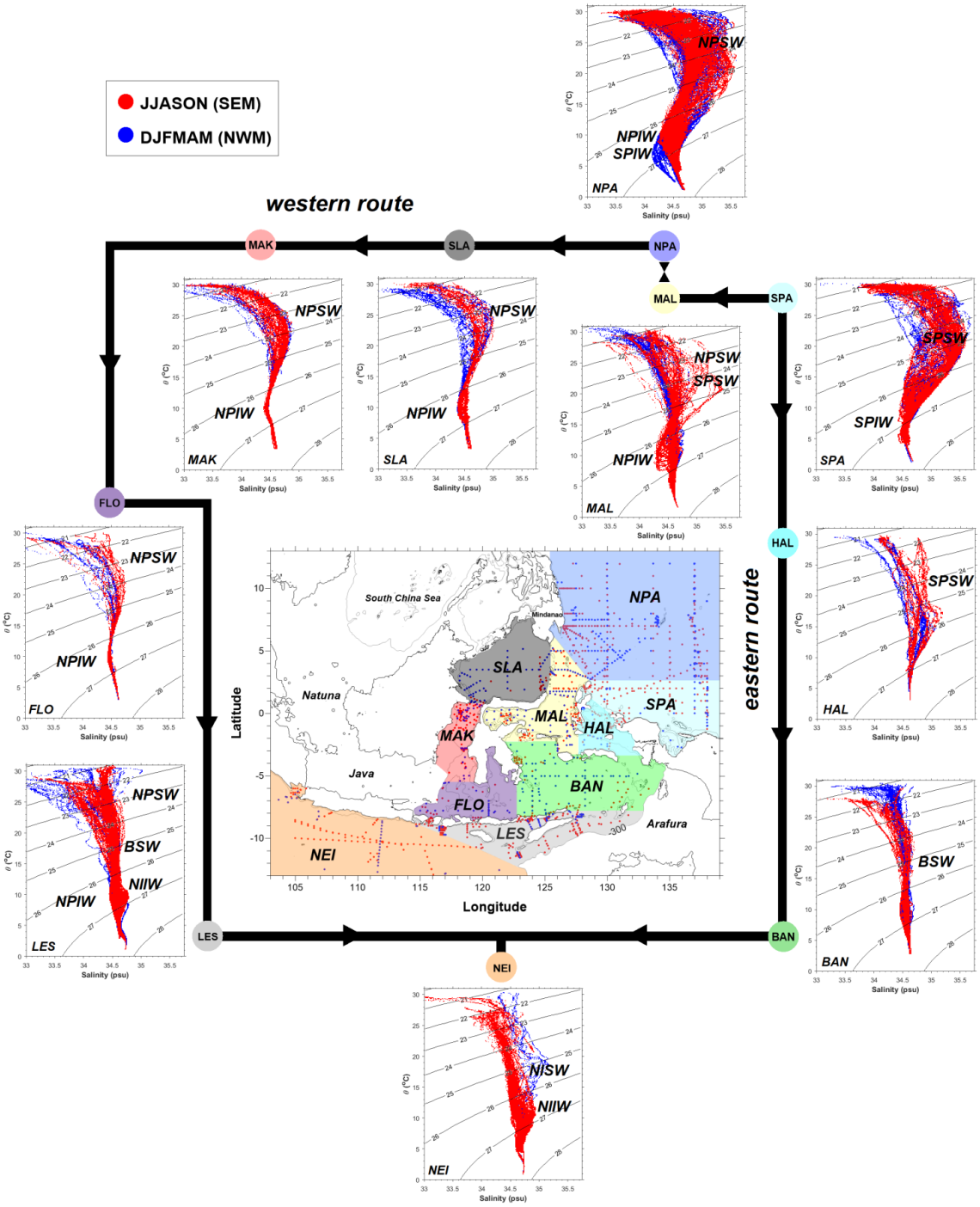

Figure 3.2 *T/S* relationship constructed from all archived datasets, classified seasonally (red plots are southeast monsoon stations, blue plots are northwest monsoon stations), and divided into sub-regions following the basin toponymal: NPA (North Pacific), SPA (South Pacific), HAL (Halmahera Sea), SUL (Sulawesi Sea), MAK (Makassar Strait), FLO (Flores Sea), BAN (Banda Sea), MAL (Maluku Sea), LES (Lesser Sunda seas) and NEI (Northeastern Indian). The core layer of the water masses are also indicated: North Pacific Subtropical Water (NPSW), North Pacific Intermediate Water (NPIW), South Pacific Subtropical Water (SPSW), South Pacific Intermediate Water (SPIW), Banda Sea Water (BSW), and North Indian Intermediate Water (NIIW).

3.2.2 *Mixing estimates*

Observations of temperature and salinity profiles can be used to quantify the diapycnal mixing properties (Ferron et al., 1998; Kunze et al., 2006; Park et al., 2014; Yang et al., 2014). Mixing estimates are based on density overturns following the method initially proposed by Thorpe (1977) and extended by Dillon (1982). The first stage of the method consists in computing the typical vertical extension of density overturns, referred to as Thorpe length scale, L_T, following Thorpe (1977).

Turbulent overturns generates density inversions. Thorpe method is performed by reordering the density profile into a stable density profile (Dillon, 1982). The positive (negative) value of Thorpe displacement in the turbulent region or patch indicates that the water mass parcel will move up (down) to search their static stability. Thorpe scale (L_T) value is defined as an rms value for each turbulent patch,

$$L_T = \left(\frac{1}{n}\sum_{i=1}^{n} d_i^2\right)^{1/2} \tag{3.1}$$

where n represents the number of samples within a turbulent patch. It has been shown that L_T is having a linear relationship with the Ozmidov scale L_O, with a proportionality coefficient of order unity. The Ozmidov scale represents the "largest' turbulent scale in a stratified environment for a given stratification N and dissipation rate ε, it scales as $L_O = (\varepsilon/N^3)^{1/2}$. As in several previous studies (Dillon, 1982; Ferron et al., 1998; Moum, 1996a), we use the value $L_O/L_T = 0.8$ to infer the dissipation rate. Then, the rate of turbulent kinetic energy dissipation per unit mass at each overturn region can be expressed as

$$\varepsilon_{Thorpe} = 0.64 {L_T}^2 N^3 \tag{3.2}$$

In order to omit any spurious overturns in the profile we need to carefully define the noise level on the density estimates. The density resolutions can be estimated by the standard deviation of de-trended potential density over 10 m segments in nearly homogenous density profiles (Frants et al., 2013). Note that since the density profile is never perfectly mixed, this noise estimate may be biased high by taking into account in the RMS value physical density overturns contributions. To limit this bias we selected 'calm' deep layers far away from rough topography, in the central Banda Sea (125° - 130° E, 5° - 7° S) and central Sulawesi Sea (120° - 124° E, 2° - 4° N). We estimate the density noise level from the nearly homogenous deeper layers (>1500 m depth). All measurements were performed using the same instruments, i.e.

SBE 911 and we found a mean value of the noise level of $\delta\rho$ = 2.09x 10^{-4} kg m^{-3}, which is a bit higher than other studies, 1x10^{-4} kg m^{-3} (Gargett and Garner, 2008), 1.75x10^{-4} kg m^{-3} (Park et al., 2014). We considered a safety multiplication factor of two for the noise level for further processing, yielding a value of 4.18x10^{-4} kg m^{-3}.

We use some overturn selection criteria to reject any false overturns resulting from a mismatch between temperature and salinity data is present in the overturn regions (patch). The first criterion is the water mass test to inspect any spike in the temperature and salinity profile due to a mismatch between conductivity and temperature sensor (Galbraith and Kelley, 1996; henceforth GK96). Real density overturns will preserve a tight relationship between density, temperature, and salinity. Either mixed or unmixed water masses should be laid on the local *T-S* relationship. GK96 characterize the tightness of this relationship is with the parameter $\xi = \max(\xi_T, \xi_S)$; where ξ_T and ξ_S is the linear correlation of density-temperature and density-salinity, respectively. The value near zero indicates a tight *T–S* relationship and large values signify a loose relationship, and it was suggested an upper bound of 0.5 for valid overturns. This threshold is quite sensitive, and may potentially discard many detected overturns (Stansfield et al., 2001) hence subject to adaptation. Following Stansfield et al. (2001), we choose a slightly higher threshold of 0.66.

A method proposed by Gargett and Garner (2008) is also applied to reject a suspected false overturn, they define the overturn ratio, $Ro=\min(L^+/L, L^-/L)$; where L^+ and L^- are, respectively the vertical distances occupied by positive and negative Thorpe displacement within an overturn of vertical extent *L*. A single perfect overturn should contain equal lengths of positive and negative displacements, hence Ro= 0.5 and imperfect overturn would have Ro less than 0.5. We use a threshold of $Ro\geq0.2$, as suggested by (Gargett and Garner, 2008).

The Thorpe method provides estimates of ε only for the most energetic overturns which are both larger than the typical 1 m resolution of measurements and that generate density inversions larger than the noise level. As a result, the statistics of ε based on detected overturns only are largely biased toward high values. It is, therefore, necessary to provide a background dissipation rate where no overturns are detected. We introduce a setting for the background dissipation rate as $\varepsilon_{background} = \max(1x10^{-10}, \varepsilon_{GM\text{-}background})$ where 10^{-10} is the lowest dissipation rate threshold, defined based on the typical minimum dissipation rate observed by microstructure measurements in a quite region, the Banda Sea (Alford et al., 1999; Bouruet-Aubertot et al., 2018; Koch-Larrouy et al., 2015). We assume that it is the smallest resolved

dissipation rates may be representative of the weak background dissipation rate. This value has also been used generally by previous authors (Alberty et al., 2017; Cuypers et al., 2017b; Frants et al., 2013; Koch-Larrouy et al., 2015). The $\varepsilon_{GM\text{-}background}$ is the Garrett and Munk dissipation rate. Yet this value may underestimate the background dissipation rate in region of higher stratification, indeed higher dissipation rate is generally observed in the pycnocline even far from direct source of internal waves (Gregg 1989). For the $\varepsilon_{GM\text{-}background}$, we assume that this background value follows the typical dissipation rate associated with Garret and Munk (hereinafter, GM) wave field (Garrett and Munk, 1975). This choice was guided by the fact that the INDOMIX campaign revealed that in the Banda sea, far from direct energy sources, the low dissipation rate was consistent with wave-wave parameterization assuming a GM internal wave field (Bouruet-Aubertot et al., 2018). The $\varepsilon_{GM-background}$ is given by the fine-scale parameterization for internal waves (Gregg, 1989):

$$\varepsilon_{GM-background} = \varepsilon_0 \left(\frac{N^2}{{N_0}^2}\right)\left(\frac{S_{10}^4}{S_{GM}^4}\right) \tag{3.3}$$

where ε_0 = 7x10^{-10} m^{3}s^{-3} and N_0 = 3 cph is the canonical Garret and Munk (hereinafter GM) dissipation rate and respected buoyancy frequency reference, respectively. We assume that the local shear variance S_{10}^4 is equal to the canonical shear variance, S_{GM}^4, so that $\varepsilon_{GM-background}$ is a simple function of stratification and verifies:

$$\varepsilon_{GM-background} = \varepsilon_0 \left(\frac{N^2}{{N_0}^2}\right) \tag{3.4}$$

which is considered as a lower bound for the dissipation rate in the absence of detectable density overturns. This improved dissipation rate estimate that takes into account the background dissipation rate, termed as $\varepsilon_{Th\text{-}GM}$, thus provides continuous profiles of ε as opposed to the standard Thorpe method, ε_{Th}. Bin-averaged profiles of the former method may lead to significantly lower ε values than the classical method where the bins overlap different vertical segments with overturn and without overturn. We inspect this issue for the 100 m bin averaged profiles from the repeated CTD data sets and found an increasing value by a factor of up to 10^2 if we do not consider the background dissipation rates. From the dissipation rate, the turbulent diffusivity K_ρ can be determined as:

$$K_\rho = \Gamma \frac{\varepsilon}{N^2} \tag{3.5}$$

where Γ, the mixing efficiency, represents the ratio of the buoyancy flux to the viscous dissipation rate ε. Over the past years Γ has generally been chosen as constant, Γ=0.2 which is

the upper bound proposed by Osborn (1980). Several studies have suggested that the value of the mixing efficiency could vary by two orders of magnitude as a function of turbulent intensity (Bouffard and Boegman, 2013), yet there is no consensus on the parameterization of Γ (e.g. Vladoiu et al., 2019). In the meantime, a recent compilation of Γ estimates by Monismith et al. (2018) suggested that in most part of the ocean, the mixing efficiency was indeed close to Γ=0.2. Owing to these uncertainties, we computed the Γ inferred from turbulent intensity (Bouffard and Boegman, 2013): an average value close to the 0.2 Osborn value was obtained within each vertical layer: 0.193±0.007; 0.191±0.013; 0.192±0.010; and 0.182±0.021 for 50-300 m, 300-500 m, 500-800 m and 800-2000 m layers, respectively. Hence, Γ was taken equal to 0.2.

Finally, in order to inspect the spatial variability of the dissipation rates and vertical diffusivity, we built maps of hydrological and turbulent properties by gridding horizontally the data over 0.5° and by vertical averaging over several depth intervals of 50-300 m, 300-500 m, 500-800 m, 800-2000 m as well as density classes layer to focus on the Pacific water masses. Note that the horizontal scale of 0.5° is also close to the half wavelength of the internal tide gravest mode which was suggested by Nagai and Hibiya (2015) as the typical radius of the near field around a mixing hot spot.

3.2.3 Numerical model outputs

The Thorpe based estimates of ε were used to test the relevance of dissipation rates inferred from three recent numerical models. The first model is the 3D hydrostatic MITGCM model with $1/100^{o}$ horizontal resolution and 100 vertical levels with a spacing ranging from 5 m at the ocean surface to 1200 m at the maximum depth of 10,028 m by (Nagai and Hibiya, 2015), hereinafter NAG15. This high-resolution model covers the full Indonesian seas region but is forced by the dominant barotropic M2 tides only and considers no initial horizontal gradient and velocity. The dissipation rate in this model is averaged over one tidal period once a quasi-steady state is achieved, that is after around 20 M2 tidal periods. We used this model to provide both a global comparison and local comparison at INDOMIX and TOMTOM stations with our Thorpe estimates.

The second model is the 3D non-hydrostatic MITGC model with $1/600^{o}$ horizontal resolution by (Nagai et al., 2017), hereinafter NAG17. The model is forced by M2, S2, N2, K2 and ITF, this model is limited to the Halmahera Sea.

The third model is the 3D hydrostatic model NEMO 2.3 for the Indonesian seas region (INDESO Project) with 1/12° horizontal resolution by (Nugroho et al., 2017; personal communication), hereinafter NUG17, which included atmospheric and geopotential tidal forcing M2, S2, N2, K2, K1, O1, P1 and Q1. NUG17 simulations was performed in limited period, started January 3rd 2007 until December 31st 2011. NAG17 and NUG17 were only used for local comparison at the INDOMIX stations, which match the spatial coverage of NAG17 and the temporal coverage of NUG17.

3.3 Results and discussion

3.3.1 Hydrography

The large dataset ensemble we consider allows to track the water mass transformation along the ITF with unprecedented spatial coverage. **Figure 3.2** shows *T*/*S* diagrams in each basin from the archived data sets used in this study while Figure 3.3 provides a horizontal map of the salinity for given density ranges. Both figures illustrate the transformation of North and South Pacific waters along the eastern (Sulawesi Sea/SLA-Makassar Strait/MAK-Flores Sea/FLO-Lesser Sunda Seas/LES) and western routes (Halmahera Sea/HAL-Maluku Sea/MAL-Banda Sea/BAN-Lesser Sunda Seas/LES).

The descriptive analysis below refers to the vertical characteristics of the water masses as shown in **Figure 3.2**. The north Pacific sub-region (NPA) and South Pacific sub-region (SPA) are regions characterized by the presence of NPSW and SPSW in the thermocline layer, and SPIW and NPIW in the intermediate layer. In the NPA and SPA (σ_θ 22-26; S_{max}>35 psu), core layers of NPSW/ SPSW in the thermocline layer and NPIW/SPIW (σ_θ 26-27; S_{min} 34.1-34.5 psu), in the intermediate layer are clearly identified.

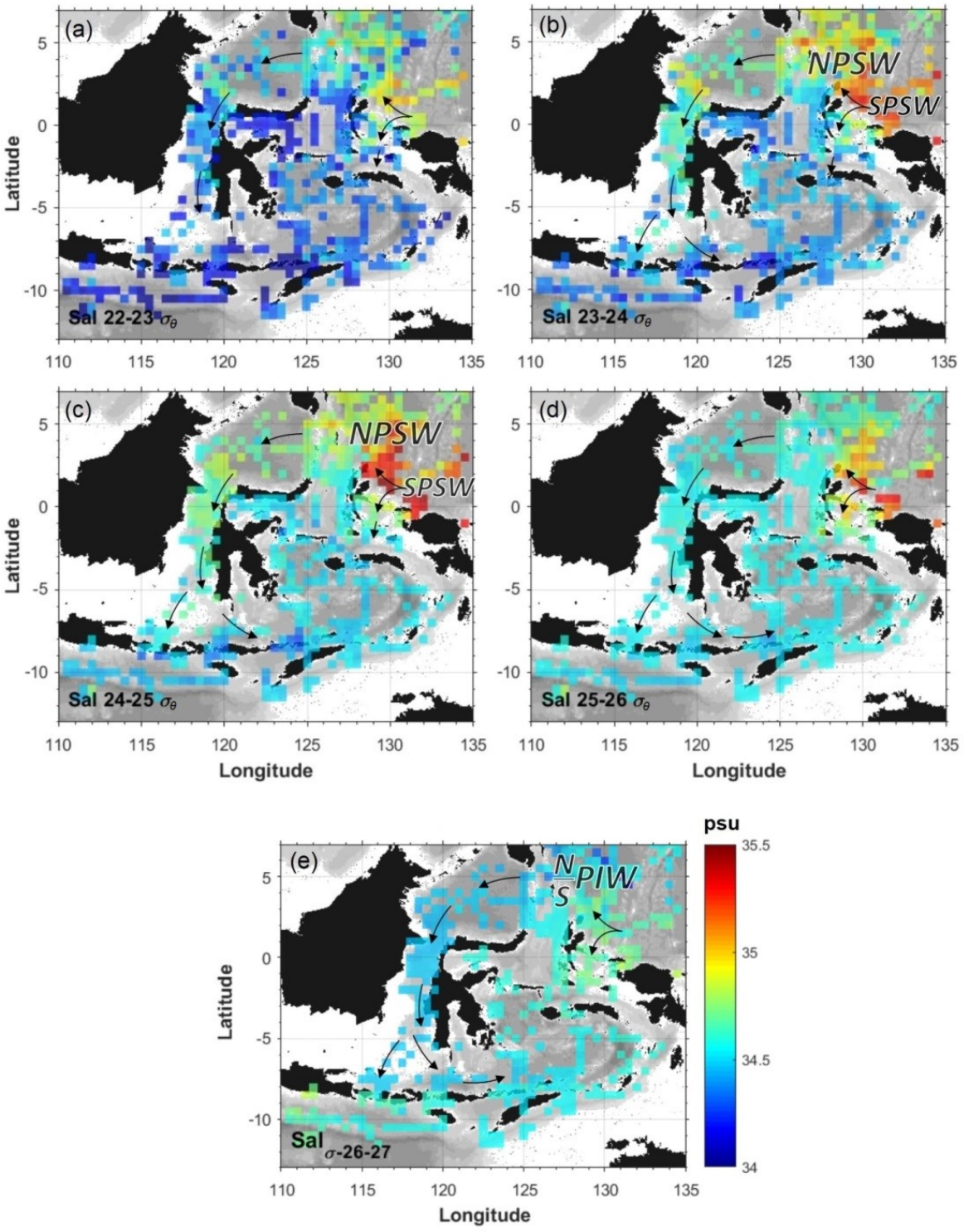

Figure 3.3 Horizontal distribution of mean salinity (in psu) for four selected isopycnal ranges: (a) $\sigma_{\theta\,22\text{-}23,}$ (b) $\sigma_{\theta\,23\text{-}24}$, the upper thermocline which corresponds to the upper layer of the NPIW and SPIW; (c) $\sigma_{\theta\,24\text{-}25}$, the lower thermocline which corresponds to the lower layer of the NPIW and SPIW; (d) $\sigma_{\theta\ 25\text{-}26}$ and (e) $\sigma_{\theta\ 26\text{-}27}$, which corresponds to the Pacific intermediate layer (NPIW, SPIW).

Western route (SLA, MAK, FLO) hydrography

The North Pacific water masses enter the Sulawesi Sea via Sangihe passages, known also as a passage for the reversing throughflow from the Sulawesi Sea towards the Pacific Ocean. Note that only one-third of the ITF forcing by Mindanao Current enters the Makassar Strait, the rest two-thirds bifurcates back entering the Pacific Ocean via Sangihe inter-islands passages (Kashino et al., 2001). The NPSW and NPIW show weak erosion in the SLA and MAK basins suggesting a relatively weak mixing in the northern Makassar Channel. Part of the water masses originating from Makassar Strait directly exit through the Lombok Strait while a major part is deflected eastward in the Flores Sea before entering the BAN sub-region. The FLO basin is separated from MAK by shallow restricting sills (Dewakang waters), and the FLO water masses exhibit eroded but still present NPSW and NPIW, with cooler NPSW. In the BAN sub-region, there are almost no more signatures of Pacific waters in the thermocline with water masses showing almost linear *T*/*S* profiles (homohaline).

Eastern route (HAL, MAL, BAN) hydrography

In contrast to the western route, water masses experience a rapid transformation along the eastern route, SPSW is already largely eroded in the HAL within isopycnals 23-25 σ_θ. This drastic erosion of the S_{max} along the shorter eastern route compared to that along the longer western route evidences a higher vertical mixing level along this route. In the MAL region, most of the profiles shows a nearly homohaline pattern very similar to the HAL water characteristics which suggest that MAL is mostly fed by the HAL and Seram Sea via the Lifamatola passage, as mentioned as well by van Aken et al. (2009). A few casts sampled during the southeast monsoon months (June-November) show S_{max} and S_{min} characteristic of the thermocline and intermediate Pacific water masses, respectively, indicating a small influence from North Pacific water masses. This seasonal signature of North Pacific waters is consistent with Yuan et al., (2018). They have shown that the MAL is fed partially by north Pacific water masses, with a maximum input during southeast monsoon months (June-November) as the MC penetrates further southward into the northern part of the MAL before being retroflected eastward as the North Equatorial Counter Current, NECC (see **Figure 3.1**). A few profiles also show some characteristics of the North Pacific waters which is consistent with Gordon and Fine (1996a) and Kashino et al. (1999) who showed that the MAL is also fed by south Pacific water masses via the strait between Talaud and Morotai Islands (Gordon and Fine, 1996; Kashino et al., 1999).

Exit passages (LES) hydrography

The LES region, which refers to the seas surrounding the islands between Java Island in the westernmost part and Wetar Island in the easternmost part (114°-128° E, 7.5°-12° S) is the exit passages for both the eastern and western route. It is constituted by a series of straits with the most important ones (>300 m depth) being Lombok, Sape, Alor, Ombai, Sumba and Savu straits, Timor Passage and the Savu Sea. The water masses there show strongly mixed profiles with almost no more signature of NPSW and NPIW, but some intrusion of S_{max} NIIW (26-27 σ_θ) are observed. These signatures of the Indian water masses (North Indian Subtropical Water/NISW and North Indian Intermediate Water/NIIW) observed in the T/S profiles (**Figure 3.2**) result from the intrusion of Indian water masses via Sumba Strait and Timor passage as evidenced by previous studies (Cuypers et al., 2017b; Purwandana, 2014). In the northeastern Indian (NEI), only a few stations contain remaining NPSW signature in the upper thermocline (**Figure 3.2**: NEI, 22-24 σ_θ), which presumably results from the input of water masses flowing directly from the Makassar Strait via the Lombok Strait as already described as well by previous study (Atmadipoera et al., 2009).

Our 0.5° grid averaging maps of the salinity as shown in **Figure 3.3** also illustrates the penetration of the S_{max} of NPSW and S_{min} SPSW via the western and eastern route at 23-25 σ_θ and 26-27 σ_θ, respectively. It also shows a detailed view of the fast erosion of the SPSW along the eastern route against the smoother water mass transformation of the NPSW along the western route. Locally, some fresher layers are observed in some straits in the LES sub-region, those are in the Lombok Strait (115°-117° E; 8°-9° S), the Sape Strait (119°-120° E; 8°-9° S), and the straits of Alor islands (123°-126° E; 8°-9° S) at 22-25 σ_θ (**Figure 3.3** a, b, c), illustrating the incorporation of fresher surface water in the thermocline by the strong mixing in these spots. Conversely, there was increasing salinity at 26-27 σ_θ or the intermediate layer (**Figure 3.3** e).

3.3.2 Relevance of the turbulence estimates: comparison with microstructure measurements

We test the relevance of our improved Thorpe scale dissipation rate estimates at several locations from INDOMIX 2010 cruise ($S_{A,B,C,D,E}$ in **Figure 3.1**), where both classical CTD and microstructure VMP measurements were performed (Bouruet-Aubertot et al., 2018; Koch-Larrouy et al., 2015). Similar comparisons were conducted at several TOMTOM 2015 stations ($S_{F,G,H}$ in **Figure 3.1**), but with temperature and salinity measurements from the SBE sensor of the VMP microstructure profiler. The comparison between our Thorpe scale

method with direct observations and existing 3D models is shown in **Figure 3.4**. The $S_{A,C,}$ hereinafter referred to as near-field stations, were located close to the straits and strong internal tides generation spots. The $S_{B,F,G,H}$ were located at an intermediate distance of ~40 km from the internal tide generation area in the narrow passages, and are referred as intermediate-field stations, following Bouruet-Aubertot et al. (2018); eventually S_D is located in the deep region of the Banda Sea far away from the internal tide generation regions (far-field station). The dissipation rates are smoothed with a 10-50 m moving average. Our improved Thorpe scale algorithm ($\varepsilon_{Th\text{-}GM}$), shows a relatively good agreement with microstructure dissipation rates while the mean dissipation rate computed from the detected overturns only (ε_{Th}) is biased toward high values for all stations (**Figure 3.4**). Some discrepancy between the ε_{VMP} and $\varepsilon_{Th\text{-}GM}$ can be observed in the Ombai Strait, with a very strong ε_{VMP} dissipation rate around 700 m which is not reproduced by the Thorpe estimate (**Figure 3.4.**e). This peak in the dissipation rate may result from a solitary wave passage that was identified from a propagating band with small-scale sea surface roughness during the microstructure measurements (Bouruet-Aubertot et al., 2018). This solitary wave, characterized by large amplitude, short duration, thermocline depressions and strongly sheared current surges (Jeans and Sherwin, 2001), may not have been sampled by the CTD thus explaining the dissipation rate discrepancy. This hypothesis is confirmed by the good agreement between ε_{VMP} and $\varepsilon_{Th\text{-}GM}$ obtained when omitting the last two VMP casts (black curve in **Figure 3.4.**e).

At the INDOMIX stations, the models NAG17 and NUG17 compared relatively well with the VMP data (**Figure 3.4.**a-e), reproducing the global dissipation rate contrast between stations as already noticed by Nagai et al. (2017) and Nugroho et al. (2017). However, the vertical structure differs significantly with a systematic discrepancy observed below 300 m for weakly energetic regions at stations S_B and S_D where regional models overestimate the dissipation rate by up to two orders of magnitude (**Figure 3.4.**b and **3.4**.d). It can also be noticed that NUG17 underestimates the dissipation rate below 500 m in the North and South Halmahera strait (S_A and S_C) compared to both observations and higher resolution models NAG15 and NUG17. This may result from the limited resolution of 1/12° of this model which does not allow to reproduce completely the rough and small-scale bathymetry of the region and the resulting dissipation rate associated with high vertical modes above the bottom. The models provide a satisfactory representation of the contrasted dissipation rate between stations, especially in the upper 500 m depth, as they performed a closer estimate to the VMP profiles (**Figure 3.4.**b-d). Below 500 m depth, the models seem to overestimate. The NAG15 underestimates the dissipation rate at S_A quite likely because of the model missing mesoscale

processes (**Figure 3.4.**a). The mesoscale circulation is indeed energetic with intra-seasonal Rossby wave dynamics induced by the atmospheric forcing in the central equatorial Pacific (Wattimena et al., 2014). At the weakly energetic stations S_B and S_D (**Figure 3.4.**b and **3.4**.d), NAG15 overestimates the dissipation rate but is closer to the observations than NAG17 and NUG17, yet this improvement likely occurred for the wrong reasons, e.g. the overestimation of the background dissipation rate being partly compensated by the missing dissipation rate from the mesoscale circulation.

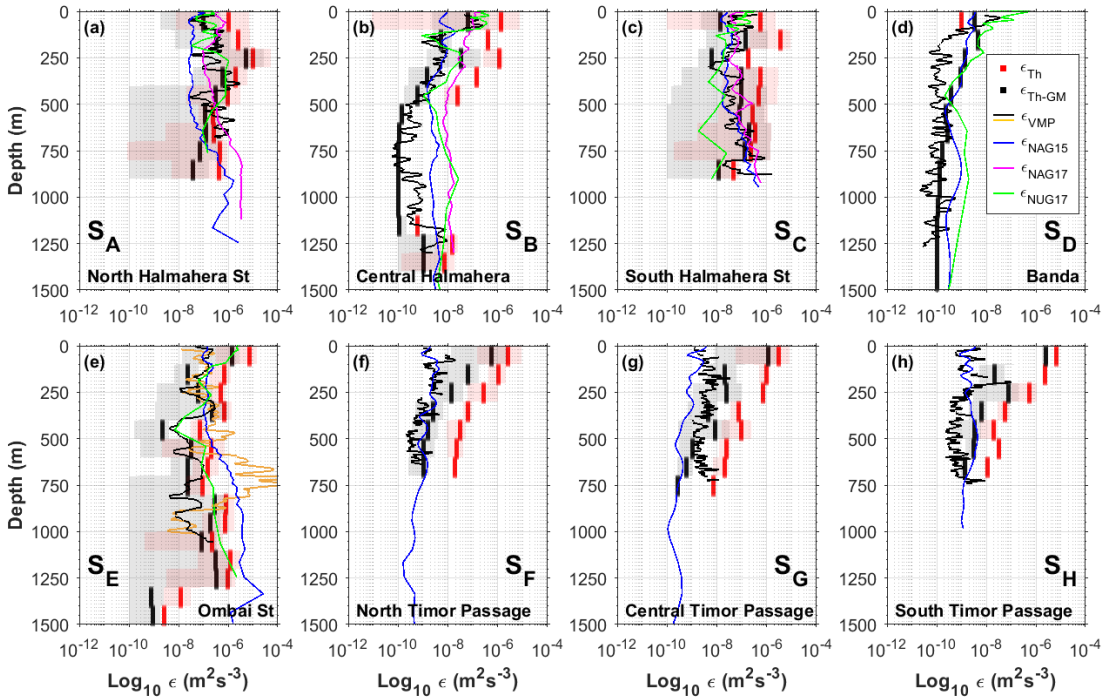

Figure 3.4 Comparison mean plots between microstructure measurements (continuous black line plots), existing 3D models (NAG15, NAG17, NUG17) and our Thorpe scale dissipation rates estimate, 100 m binned vertically (black plots). The minima-maxima values for the Thorpe based estimates (shaded colors) calculated with Garrett-Munk (GM) background dissipation rate (shaded grey), considering only the overturns (shaded red) are also shown. The three model-based estimates at respected locations: NAG15 (Nagai and Hibiya, 2015) plotted in blue, NAG17 (Nagai et al., 2017) plotted in magenta, NUG17 (Nugroho et al., 2017) plotted in green. The profiles are averaged values of several repeated down casts at relatively fixed stations in the: (a) north Halmahera Strait (S_A, 129.1742 E; 0.0605 N), (b) central Halmahera Sea (S_B, 128.8830 E; 0.7520 S), (c) south Halmahera Strait (S_C, 128.7630 E; 1.357 S), (d) central Banda Sea (S_D, 126.9980 E; 6.2855 S), (e) Ombai Strait (S_E, 125.2440 E; 8.2838 E), (f) northern Timor Passage (S_F, 127.2105 E; 9.0228 S). The orange plot in (e) is the mean plot involving all 6 VMP casts while the black plot omits the last two VMP casts since they were ~9 hours separated time. (g) Central Timor Passage (S_G, 127.3098 E; 9.2673 S); and (h) southern Timor Passage (S_H, 127.4830 E; 9.6199 S). The dissipation estimates are calculated using density base, except for the Timor Passage, the estimate used the temperature profile since the salinity profile is not proper. Note that the NAG17 covered and inspected only the Halmahera waters ($S_{A,B,C}$) and the NUG17 inspected vertically only the INDOMIX 2010 VMP stations ($S_{A,B,C,D,E}$).

Discrepancy from TOMTOM

We found a significant discrepancy between Thorpe base dissipation rates with TOMTOM microstructure measurements in the upper 50 m. This issue may arise from the use of potential temperature profile instead of density, which is more sensitive to the inversion in the upper layer (thermocline layer), as shown in **Figure 3.4**.f, g, h. We further compare NAG15 at the TOMTOM VMP stations in the Timor passage (**Figure 3.4** f, g, h), where the order of magnitude of the dissipation rate is correctly reproduced by NAG15, with yet some underestimation in the central Timor passage, possibly due to the missing ITF in the model.

A correlation analysis between our improved Thorpe estimates and microstructure measurements (binned over 100 m intervals) displayed in **Figure 3.5**.a indicates a fairly good correlation: the linear regression is characterized by a slope close to one, where around 89% of the dispersion of the values are within a factor of 10. The observed dispersion seems consistent owing to the turbulence intermittency for CTD and microstructure measurements that are not exactly concomitant and the uncertainty associated with the Thorpe estimates. The model estimates also yield clear linear correlation with the VMP but with a slope significantly milder than one (**Figure 3.5**.b, c, d). The bias is most of the time toward an over-estimate of dissipation for the lowest values and an under-estimate of dissipation for the highest values. The same trend can be observed when $\varepsilon_{Tb\text{-}GM}$ is regressed against the model's dissipation rate. These comparisons suggest that our improved method, $\varepsilon_{Tb\text{-}GM}$, agrees relatively well with the direct estimates and reproduce the huge variations of the dissipation rate in the Indonesian seas, thus providing a footprint to test model estimates over an extended sampled area.

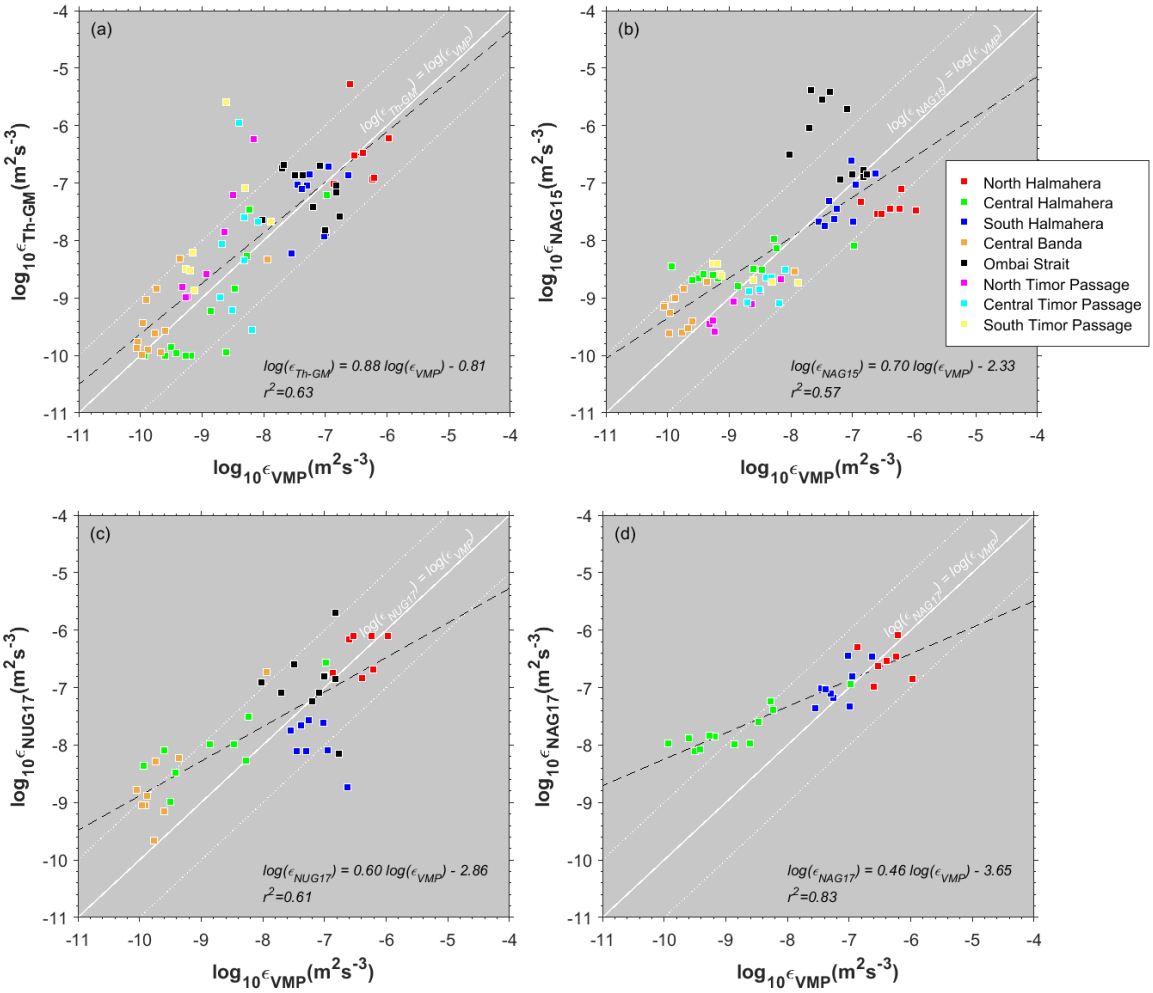

Figure 3.5 Comparison between two estimates of the 100 m bin averaged dissipation rate of the microstructure measurements (ε_{VMP}) and: (a) Thorpe based estimates ($\varepsilon_{Th\text{-}GM}$), (b) NAG15 ($\varepsilon_{NAG15}$), (c) NUG15 ($\varepsilon_{NUG17}$), (d) NAG17 ($\varepsilon_{NAG17}$). Dotted white lines are the slope of $\log_{10}(\varepsilon_{Th\text{-}GM,\ NAG15,\ NUG17,\ NAG17})/\ \log_{10}(\varepsilon_{VMP})$ = 0.1 and 10; while the solid white line is that of 1; and dashed black line is the linear correlation between the indirect estimates (Thorpe and models) with the direct estimates (VMP).

3.3.3 Turbulence and mixing of the Pacific water masses layer

We now focus on the characterization of mixing for specific density ranges matching the Pacific water masses in each sub-region. **Figure 3.6** shows the dissipation rate and vertical diffusivity in two layers, representing the thermocline/pycnocline layer (22-26 σ_θ) and intermediate and deeper layers (>26 σ_θ). This figure highlights the enhanced dissipation rate in the narrow passages and enhanced vertical diffusivity in most of deeper layer and narrow passages. Vertical diffusivity values are essentially mimicking the dissipation rate pattern horizontally with an increasing trend at depth as a result of the decreasing stratification. Considering a range of 22-26 σ_θ representing the core layer of NPSW/SPSW (**Figure 3.6**.a)

and >26 σ_θ for the NPIW/SPIW (**Figure 3.6**.b), we found that the NPSW/SPSW layer is exposed to higher dissipation rate 1-2 order of magnitude larger than that in the lower and intermediate layer (NPIW/SPIW). **Table 3.2** resumes the mean and standard deviation of dissipation rate and vertical diffusivity for a specified range of density anomaly.

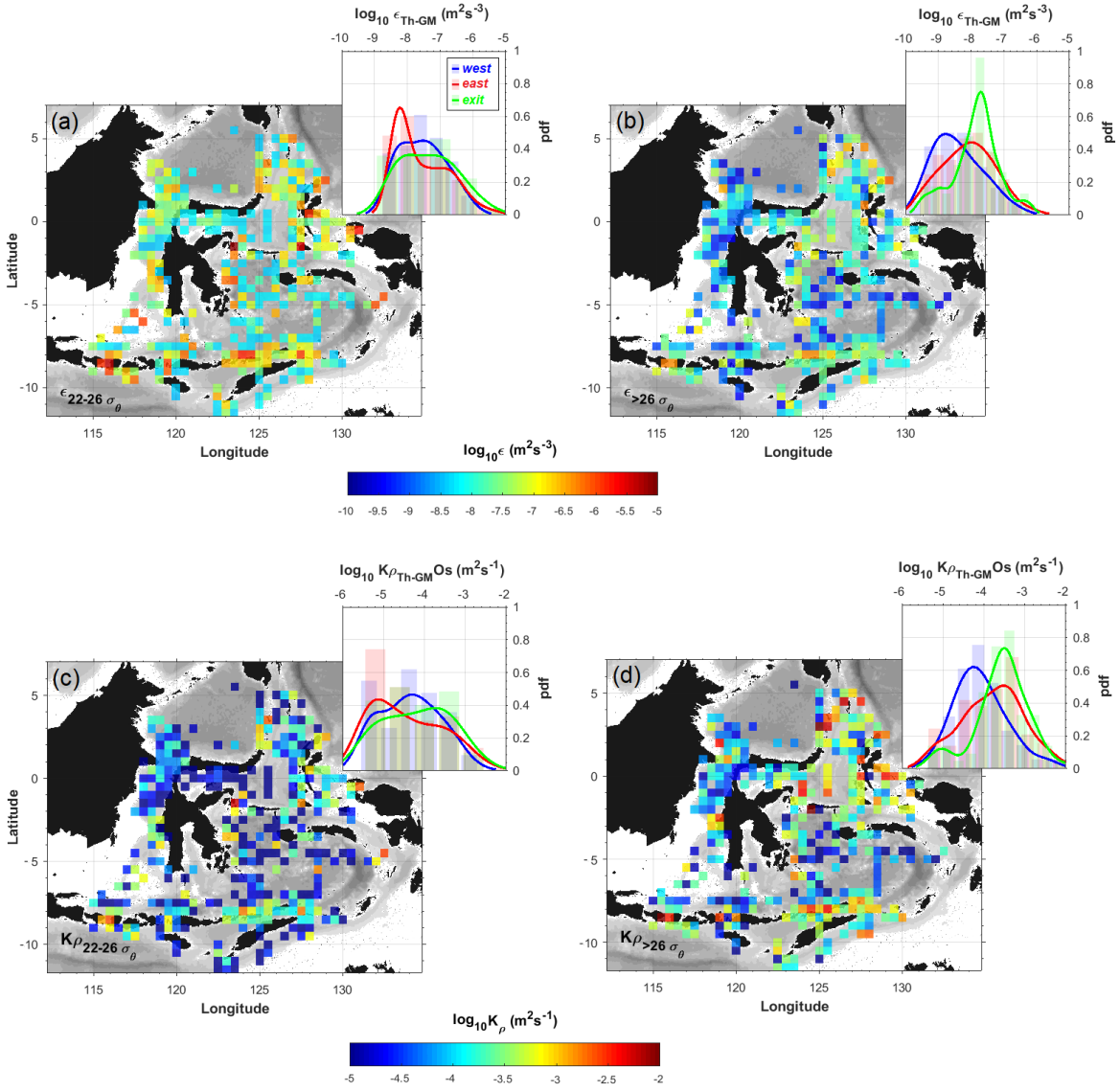

Figure 3.6 A half degree grid mean of density anomaly-based dissipation rate (a, b) and vertical diffusivity (c, d) inferred from geographically distributed historical data sets at 22-26 σ_θ and >26 σ_θ. The insert in each panel is the pdf histogram of the respected parameter, classified by route-based region (the western route: SLA, MAK, FLO; the eastern route: MAL, HAL, BAN; exit passages: LES) inferred from the spatially gridded cells of the historical data sets for four depths range, plotted with the number of bins is based on the Freedman-Diaconis rule. Continuous line plots represent kernel distribution estimates.

Table 3.2 Mean and its standard deviation of the dissipation rate (ε, m^2s^{-3}) and vertical eddy diffusivity (K_ρ, m^2s^{-1}) for specified density anomaly range (σ_θ, kg m^{-3}) inferred from spatially distributed historical data sets.

σ_θ	$\varepsilon_{Th\text{-}GM}$ (m^2s^{-3})													
	Sulawesi Sea (SLA)		**Makassar Strait (MAK)**		**Flores Sea (FLO)**		**Banda Sea (BAN)**		**Maluku Sea (MAL)**		**Halmahera Sea (HAL)**		**Lesser Sunda Seas (LES)**	
	mean	**stdev**	**mean**	**stdev**	**mean**	**stdev**	**mean**	**stdev**	**mean**	**stdev**	**mean**	**stdev**	**mean**	**stdev**
21-22	$1.1\cdot10^{-7}$	$10.3\cdot10^{-7}$	$6.6\cdot10^{-8}$	$97.8\cdot10^{-8}$	$3.9\cdot10^{-9}$	$39.3\cdot10^{-9}$	$9.7\cdot10^{-9}$	$168.4\cdot10^{-9}$	$9.7\cdot10^{-9}$	$168.4\cdot10^{-9}$	$2.1\cdot10^{-8}$	$30.9\cdot10^{-8}$	$2.8\cdot10^{-8}$	$29.1\cdot10^{-8}$
22-23	$6.8\cdot10^{-8}$	$71.0\cdot10^{-8}$	$5.7\cdot10^{-8}$	$87.5\cdot10^{-8}$	$1.4\cdot10^{-8}$	$18.1\cdot10^{-8}$	$1.5\cdot10^{-7}$	$14.3\cdot10^{-7}$	$1.5\cdot10^{-7}$	$14.3\cdot10^{-7}$	$2.6\cdot10^{-7}$	$27.0\cdot10^{-7}$	$9.7\cdot10^{-8}$	$10.8\cdot10^{-8}$
23-24	$1.1\cdot10^{-7}$	$9.70\cdot10^{-7}$	$3.6\cdot10^{-8}$	$43.3\cdot10^{-8}$	$1.4\cdot10^{-7}$	$15.5\cdot10^{-7}$	$1.5\cdot10^{-7}$	$16.4\cdot10^{-7}$	$1.5\cdot10^{-7}$	$16.4\cdot10^{-7}$	$2.1\cdot10^{-7}$	$16.8\cdot10^{-7}$	$3.9\cdot10^{-7}$	$47.7\cdot10^{-7}$
24-25	$9.9\cdot10^{-8}$	$87.9\cdot10^{-8}$	$1.1\cdot10^{-7}$	$13.0\cdot10^{-7}$	$3.1\cdot10^{-7}$	$25.2\cdot10^{-7}$	$1.7\cdot10^{-7}$	$1.7\cdot10^{-7}$	$1.7\cdot10^{-7}$	$16.5\cdot10^{-7}$	$8.8\cdot10^{-8}$	$76.0\cdot10^{-8}$	$2.9\cdot10^{-7}$	$36.5\cdot10^{-7}$
25-26	$1.7\cdot10^{-7}$	$16.5\cdot10^{-7}$	$1.1\cdot10^{-7}$	$12.9\cdot10^{-7}$	$1.1\cdot10^{-7}$	$10.0\cdot10^{-7}$	$2.0\cdot10^{-7}$	$26.2\cdot10^{-7}$	$2.0\cdot10^{-7}$	$26.2\cdot10^{-7}$	$2.9\cdot10^{-7}$	$23.3\cdot10^{-7}$	$4.4\cdot10^{-7}$	$87.1\cdot10^{-7}$
26-27	$7.6\cdot10^{-8}$	$62.9\cdot10^{-8}$	$3.5\cdot10^{-8}$	$53.8\cdot10^{-8}$	$3.0\cdot10^{-8}$	$26.3\cdot10^{-8}$	$4.6\cdot10^{-8}$	$99.3\cdot10^{-8}$	$4.6\cdot10^{-8}$	$99.3\cdot10^{-8}$	$3.5\cdot10^{-8}$	$29.4\cdot10^{-8}$	$6.7\cdot10^{-8}$	$70.1\cdot10^{-8}$
>27	$2.4\cdot10^{-9}$	$47.5\cdot10^{-9}$	$1.2\cdot10^{-9}$	$19.9\cdot10^{-9}$	$2.1\cdot10^{-9}$	$37.0\cdot10^{-9}$	$3.8\cdot10^{-9}$	$55.8\cdot10^{-9}$	$3.8\cdot10^{-9}$	$55.8\cdot10^{-9}$	$6.6\cdot10^{-9}$	$42.8\cdot10^{-9}$	$1.6\cdot10^{-8}$	$26.2\cdot10^{-8}$
	K_ρ (m^2s^{-1})													
21-22	$2.1\cdot10^{-4}$	$13.6\cdot10^{-4}$	$1.6\cdot10^{-4}$	$16.8\cdot10^{-4}$	$8.1\cdot10^{-5}$	$48.3\cdot10^{-5}$	$1.3\cdot10^{-4}$	$6.3\cdot10^{-4}$	$1.3\cdot10^{-4}$	$6.3\cdot10^{-4}$	$3.2\cdot10^{-4}$	$13.0\cdot10^{-4}$	$3.8\cdot10^{-4}$	$37.3\cdot10^{-4}$
22-23	$6.7\cdot10^{-5}$	$74.8\cdot10^{-5}$	$2.2\cdot10^{-4}$	$21.1\cdot10^{-4}$	$1.1\cdot10^{-4}$	$9.0\cdot10^{-4}$	$3.7\cdot10^{-4}$	$23.1\cdot10^{-4}$	$3.7\cdot10^{-4}$	$23.1\cdot10^{-4}$	$4.0\cdot10^{-4}$	$27.0\cdot10^{-4}$	$2.7\cdot10^{-4}$	$26.2\cdot10^{-4}$
23-24	$1.0\cdot10^{-4}$	$7.8\cdot10^{-4}$	$3.5\cdot10^{-5}$	$33.7\cdot10^{-5}$	$7.0\cdot10^{-5}$	$53.9\cdot10^{-5}$	$1.8\cdot10^{-4}$	$18.4\cdot10^{-4}$	$1.8\cdot10^{-4}$	$18.4\cdot10^{-4}$	$1.9\cdot10^{-4}$	$16.2\cdot10^{-4}$	$4.9\cdot10^{-4}$	$68.4\cdot10^{-4}$
24-25	$1.2\cdot10^{-4}$	$10.0\cdot10^{-4}$	$2.1\cdot10^{-4}$	$23.2\cdot10^{-4}$	$1.7\cdot10^{-4}$	$13.3\cdot10^{-4}$	$1.6\cdot10^{-4}$	$14.2\cdot10^{-4}$	$1.6\cdot10^{-4}$	$14.2\cdot10^{-4}$	$9.1\cdot10^{-5}$	$59.7\cdot10^{-5}$	$2.9\cdot10^{-4}$	$28.0\cdot10^{-4}$
25-26	$6.4\cdot10^{-4}$	$50.4\cdot10^{-4}$	$2.8\cdot10^{-4}$	$27.4\cdot10^{-4}$	$1.7\cdot10^{-4}$	$15.5\cdot10^{-4}$	$3.3\cdot10^{-4}$	$40.2\cdot10^{-4}$	$3.3\cdot10^{-4}$	$40.2\cdot10^{-4}$	$3.8\cdot10^{-4}$	$24.6\cdot10^{-4}$	$4.5\cdot10^{-4}$	$49.6\cdot10^{-4}$
26-27	$9.8\cdot10^{-4}$	$92.3\cdot10^{-4}$	$2.4\cdot10^{-4}$	$28.9\cdot10^{-4}$	$2.3\cdot10^{-4}$	$21.1\cdot10^{-4}$	$2.7\cdot10^{-4}$	$32.2\cdot10^{-4}$	$2.7\cdot10^{-4}$	$32.2\cdot10^{-4}$	$8.0\cdot10^{-4}$	$42.8\cdot10^{-4}$	$7.6\cdot10^{-4}$	$77.7\cdot10^{-4}$
>27	$4.1\cdot10^{-4}$	$65.5\cdot10^{-4}$	$55.3\cdot10^{-4}$	$55.3\cdot10^{-4}$	$7.0\cdot10^{-5}$	$89.4\cdot10^{-5}$	$2.1\cdot10^{-4}$	$30.3\cdot10^{-4}$	$2.1\cdot10^{-4}$	$30.3\cdot10^{-4}$	$1.6\cdot10^{-3}$	$5.7\cdot10^{-3}$	$9.1\cdot10^{-4}$	$117.0\cdot10^{-4}$

In the NPSW/SPSW layer (laid on the density layer 22-26 σ_θ in **Table 2**), some distinctive high dissipation rate and vertical diffusivity [ε>10^{-7} m^2s^{-3}; K_ρ>10^{-4} m^2s^{-1}] are observed in each sub-region which is consistent with the presence of mixing hot spots, either a rough topography and/or narrow passages (**Figure 3.6**.a and **3.6**.c). The NPSW/SPSW is subjected to higher dissipation rate and vertical diffusivity than that of NPIW/SPIW (laid on the density layer >26 σ_θ in **Table 3.2**); this explains the strong erosion of the salinity maxima of the NPSW/SPSW. The dissipation rate and vertical diffusivity in the intermediate layer are small, yielding to a lower erosion of the NPIW (**Figure 3.6**.b and **3.6**.d). In general, the maxima of the dissipation rates are higher along the eastern route than the western route with notably very strong dissipation rates in the Halmahera Sea contributing to the abrupt salinity erosion of the SPSW there. It can be noted that the tail of the histogram for the 22-26 σ_θ layer extends to higher values up to 10^{-5} m^2s^{-3} along the eastern route, yet the eastern route histogram also shows a strong peak at low values of 10^{-8} m^2s^{-3}. This low values peak results from the low dissipation rate and vertical diffusivity in the semi-enclosed waters of the Tomini Bay and central Maluku Sea (120.5°-126° E; 1° S-1° N). It should be noted though that this region contributes weakly to the ITF transport and is rather a calm recirculation area. Yet, the mean dissipation rate in both layers still shows the highest mean in the exit passages (2.4x10^{-7} m^2s^{-3} for layer 22-26 σ_θ; 4.6x10^{-8} m^2s^{-3} for layer >26 σ_θ), followed by the eastern route (1.9x10^{-7} m^2s^{-3} for layer 22-26 σ_θ; 4.1x10^{-8} m^2s^{-3} for layer >26 σ_θ), and by the western route (9.6x10^{-8} m^2s^{-3} for layer 22-26 σ_θ; 1.9x10^{-8} m^2s^{-3} for layer >26 σ_θ). These findings are consistent with salinity mean maps (**Figure 3.3**), showing that the signature of S_{max} of the SPSW is abruptly eroded in the Maluku and Halmahera basins, while the S_{max} of the NPSW and the S_{min} of the NPIW are more progressive and less eroded along the western route thus penetrating farther in the internal Indonesian seas.

Western route (SLA, MAK, FLO)

Along the western route, the thermocline layer (22-26 σ_θ) is characterized by a dissipation rate and vertical diffusivity of ~ [10^{-9}-10^{-6}] m^2s^{-3} and ~ [10^{-5}-10^{-4}] m^2s^{-1}, respectively (**Figure 3.6**.a). Elevated dissipation rates of >10^{-8} m^2s^{-3} were observed in the entrance of ITF, Sangihe ridge (124°-126° E; 1°-5° N), western Sulawesi Sea, and Dewakang waters (117°-119° E; 3°-7° S). Elevated diffusivity of >10^{-4} $m^{-2}s^{-1}$ was also observed in the Sangihe ridge and Dewakang waters. The low to moderate pycnocline dissipation rates ~ [10^{-9}-10^{-8}] m^2s^{-3} and weak diffusivity of ~ 10^{-5} m^2s^{-1} are found in the central Sulawesi sea, Flores sea and central Makassar strait.

The deeper layer (>26 σ_θ) is characterized by sub-region averaged dissipation rate <10^{-7} m^2s^{-3} and a diffusivity >10^{-4} m^2s^{-1} with a local hot spot in the Sangihe ridge where the dissipation rate reaches ~10^{-6} m^2s^{-3} (**Figure 3.6**.b), and the vertical diffusivity exceeds 10^{-4} $m^{-2}s^{-1}$. Low dissipation rate <10^{-9} m^2s^{-3} and diffusivity <10^{-4} $m^{-2}s^{-1}$ are observed in the central Sulawesi Sea, central Makassar Strait, and the central Flores Sea.

Eastern route (HAL, MAL, BAN)

In the eastern route, the thermocline layer (22-26 σ_θ) is characterized by strong dissipation rate and vertical diffusivity of ~ [10^{-8}-10^{-6}] m^2s^{-3} and ~10^{-4} m^2s^{-1}, respectively; while the intermediate and deeper layer (>26 σ_θ) is characterized by moderate to high dissipation rate and vertical diffusivity of ~ [10^{-8}-10^{-7}] m^2s^{-3} and [10^{-4}-10^{-3} m^2s^{-1}], respectively. The highest dissipation rate are found in the Halmahera Sea, Banggai islands waters (123°-125° E; 1°-2.5° S), and Lifamatola passage. The lowest dissipation rate ~10^{-8} m^2s^{-3} and vertical diffusivity <10^{-4} m^2s^{-1} are observed in the western Maluku Sea (the Tomini Bay waters) and the central Banda Sea.

The deeper layer (>26 σ_θ) is characterized by sub-region averaged dissipation rate <10^{-8} m^2s^{-3} and a diffusivity of >10^{-4} m^2s^{-1}. In average, the Banda Sea and has lower dissipation rate and diffusivity compared to that in the Halmahera Sea and Maluku Sea.

Exit passages (LES)

The LES sub-region is characterized by a strong dissipation rate with mean values in the range [10^{-8}-10^{-7}] m^2s^{-3} in both the thermocline layer (22-26 σ_θ) and the deeper layer (>26 σ_θ). Locally, very strong dissipation rate >10^{-7} m^2s^{-1} is observed in the Lombok Strait, the Sape Strait (north of Sumba Strait), Ombai Strait, and Timor passage. The mean vertical diffusivity reaches of 10^{-4} m^2s^{-1} in the thermocline while the intermediate and deeper layers are characterized by ~ [10^{-4}-10^{-3}] m^2s^{-1}.

The distribution of the ε and K_ρ for the thermocline and intermediate and deep density ranges along the western route (SLA, MAK, FLO), the eastern route (MAL, HAL, BAN) and the exit passages (LES), are shown as inserts in **Figure 3.6**. In the thermocline layer ~ [22-26] σ_θ, the median of ε is widely distributed from strong to moderate values ~ [10^{-8}-10^{-6} m^2s^{-3}] while K_ρ evolves from weak to high values ~ [10^{-5}-10^{-3} m^2s^{-1}] with yet significantly lower mean values in the western route compared to the eastern route and exit passages. Below, in the intermediate and deeper layer >26 σ_θ, the distribution of K_ρ and ε is shifted toward lower

values, [$<10^{-8}$ m^2s^{-3}; $<10^{-4}$ m^2s^{-1}] in the western and eastern route regions, while in the exit passages K_ϱ and ε are shown moderate to high values of ~ [10^{-8}-10^{-7} m^2s^{-3}; 10^{-4}-10^{-3} m^2s^{-1}].

Temporal variations

Time-averaged dissipation rates inferred from CTD yoyo stations are displayed in **Figure 3.7** for stations lasting at least one semi-diurnal period. For comparison, we also show the epsilon estimated without background dissipation rate (ε_{Th}), which shows 1-2 order of magnitude higher than those involving the background dissipation rate ($\varepsilon_{Th\text{-}GM}$). As consequence, we found that the K_ρ estimated using ε_{Th} is ~1-2 order of magnitude higher than those estimated using $\varepsilon_{Th\text{-}GM}$ (**Figure 3.8**) and found the increasing values with depth due to the less stratified water column.

The minimum and maximum values are shown when overturns are resolved by the CTD, else the background ε value that depends on the background buoyancy is displayed. Elevated dissipation rate >10^{-7} m^2s^{-3} is observed in the near field stations, Ombai Strait (LES: S_{15}, S_{16}), Buru Strait (MAL-S_{13}), Lifamatola passage (MAL-S_{14}) and Labani Channel (MAK: S_6, S_7) (**Figure 3.7**). In the MAK sub-region, the turbulence is enhanced by 1-2 orders of magnitude in the Labani Channel (S_6, S_7) stations compared to that of in the deep sea of Makassar Strait basin (S_3, S_4, S_5). In the far field stations of SLA, FLO, and BAN, as expected, low dissipation rates are observed ($<10^{-9}$ $m^{-2}s^{-3}$) with weak variations. A noticeable exception is in the BAN-S_{11} which is located close to the central Banda ridge. Local generation of internal tide may enhance the dissipation rate in this site. Large vertical diffusivities, K_ϱ>10^{-3} m^2s^{-1} are observed in MAK (S_7, S_6; the Labani Channel), MAL (S_{13}, S_{14}; the Buru Strait and Lifamatola passage, respectively), LES (S_{15}, S_{16}; the Ombai Strait).

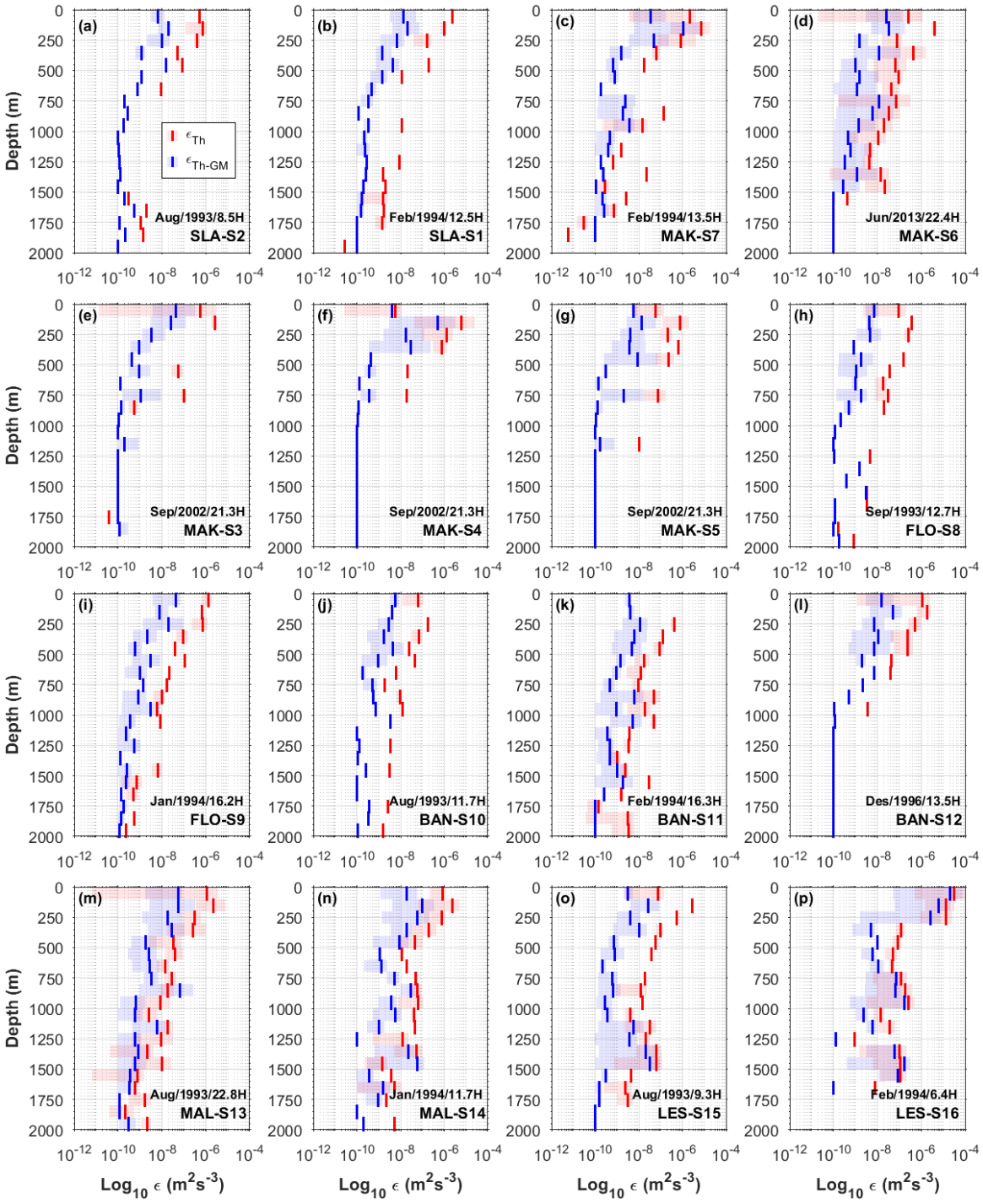

Figure 3.7 The 100 m bin averaged dissipation rate, ε ($\log_{10}$, m^2s^{-3}) for all repeated CTD cast (S_1-S_{16}), estimated by involving the background dissipation rate (blue) and that of considering only the overturns (red). The minima and maxima are presented in shaded plots. Month/year/duration (hours) of sampling are also indicated.

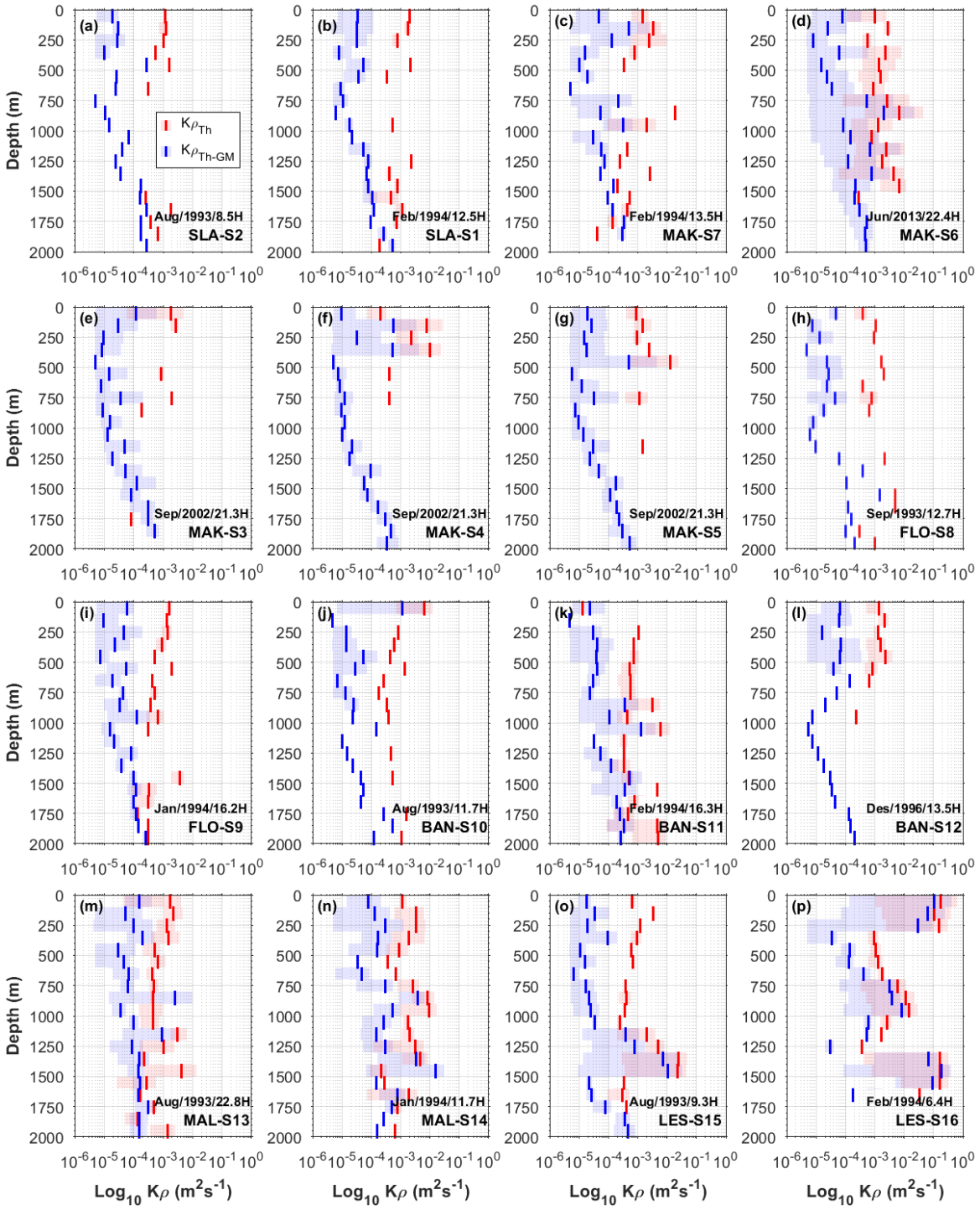

Figure 3.8 The 100 m bin averaged vertical diffusivity, K_ρ ($\log_{10}$, m^2s^{-1}) for all repeated CTD casts (S1-S16), the diffusivity estimated by ε_{Th} is displayed in red while that estimated by $\varepsilon_{Th\text{-}GM}$ is displayed in blue. The minima and maxima are presented in shaded plots. Month/year/duration (hours) of sampling are also indicated.

A remarkable internal tidal heaving was observed mainly in straits narrowing passage, as shown by the isopycnal displacement in **Figure 3.9**. The dissipation rate integrated over the density range of the pycnocline layer (22-26 σ_θ) shows a semi-diurnal pattern with temporal variations reaching up to one order of magnitude, in the range ~ [10^{-7}-10^{-6}] m^2s^{-3} with the

strongest variation observed in the Ombai Strait (**Figure 3.9**.h). The semi-diurnal pattern is not clear in the deeper layer (>26 σ_θ) which shows a very wide range of dissipation rates within ~ [10^{-9}-10^{-4}] m^2s^{-3}. In this deeper layer, the strongest variations are observed in the near field stations of Ombai Strait and South and North Halmahera.

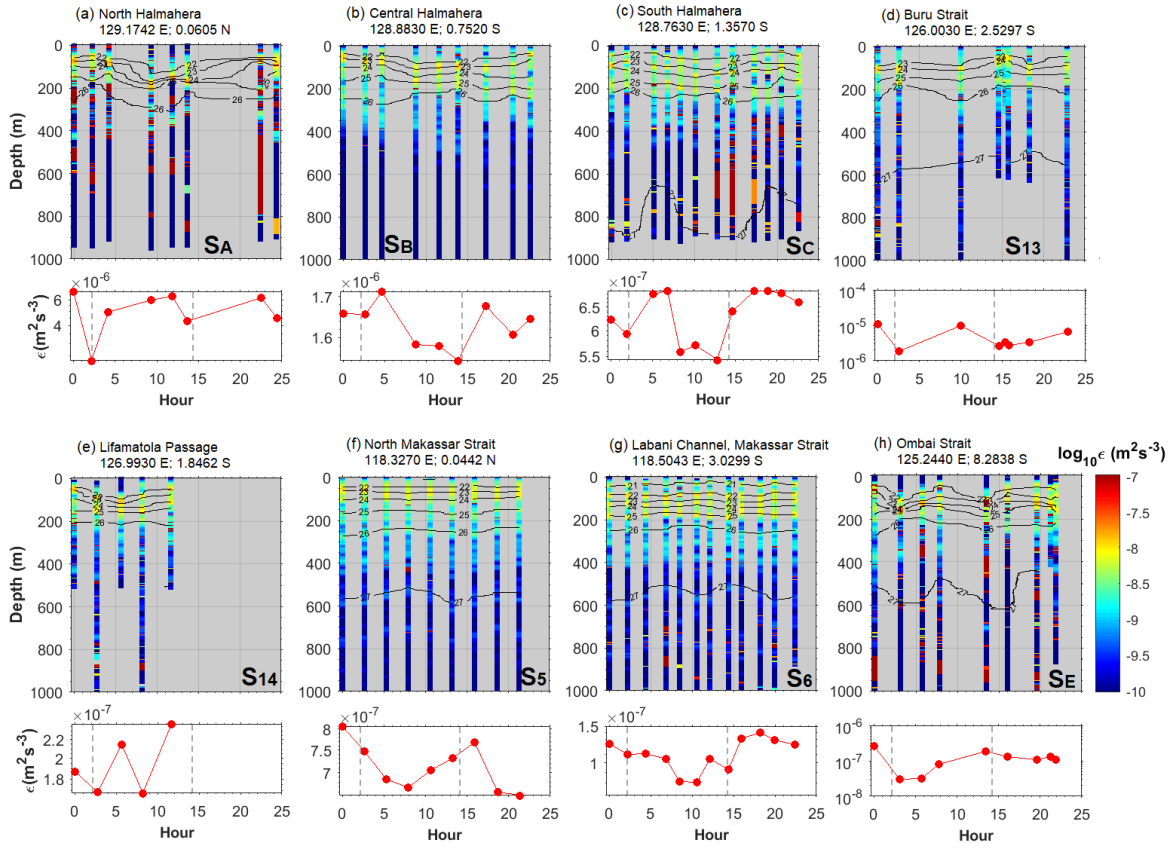

Figure 3.9 Temporal evolution of the Thorpe based dissipation rate estimates (colored bar) and isopycnal (black contours) in some mixing hot spots stations. Dotted red line plots below each time-space profile are the depth integration of the dissipation rate of layer 22-26 σ_θ or pycnocline layer, intended to show its temporal variation due to the internal tide; with dashed vertical grey lines indicate 12 hours period.

3.3.4 Model comparisons: spatial variations of turbulence and insights on mechanisms

We eventually compare our Thorpe based dissipation rate estimates map with the Nagai and Hibiya (2015) model, NAG15. The maps from the observations and the model were obtained by gridding the dissipation rates over a horizontal grid of 0.5° resolution and by vertical averaging over several depth intervals of 50-300 m, 300-500 m, 500-800 m, and 800-2000 m. Note that we choose to compare depth ranges since the NAG15 has a uniform stratification and density layers may not intersect the same bathymetric features in the model and in the observations. As previously noted by Nagai and Hibiya (2015), the spatial

distribution of the model dissipation rate shows enhanced values in the near field areas that is within a few tens of km (~a half wavelength of the gravest internal tide mode) from the expected internal tide generation sites (see for instance in Nagai and Hibiya (2015) Figure 9 for M2 internal tide conversion rate). These hot spots are located in the straits of Lesser Sunda seas, the entrance of Makassar Strait, Dewakang waters, Lifamatola passage, and Sangihe ridge. As shown in **Figure 3.10** (b, d, f, h) the location of these hot spots is consistent with the observations (**Figure 3.10** (a, c, e, d)).

Very contrasted dissipation rates, in the range of ~ $[10^{-10}–10^{-6}]$ m^2s^{-3}, are observed for both Thorpe based and model in the Indonesian seas. The hot spots are observed in the near-field area, such as in the straits of Lesser Sunda seas, the entrance of Makassar Strait, Dewakang waters, Lifamatola passage, and Sangihe ridge. The dissipation rate is generally the highest in the thermocline layer (50-300 m) and has a global decreasing trend deeper. The highest dissipation rate in the thermocline layer is consistent with the refraction effect of stratification which tends to focus internal tide energy (Cuypers et al., 2017a) as well as with the maximum of the ITF transport in this depth range. Low dissipation rates $<10^{-8}$ m^2s^{-3} are observed in the deep basin of Makassar Strait, Flores Sea, Sulawesi Sea, Banda Sea, central Halmahera Sea, and Maluku Sea, for almost all depth ranges. The deepest layer (800-2000 m) is most of the time characterized by low dissipation rates except in several mixing hot spots such as the Ombai Strait, the Lifamatola passage, southern Halmahera Strait and in the entrance of Maluku Sea.

The distributions of the observed and modeled dissipation rates for four depth ranges are displayed in **Figure 3.11**. In both model and observations, the same trends are observed, the higher dissipation rates are found in the exit passages followed by the eastern route and the western route. For all regions, the distribution shifts toward lower values with increasing depth. In the observations, the dissipation rate evolves from the highest values in the exit passage upper layer [50-300] m with a mean and a median of $2.0x10^{-7}$ m^2s^{-3} and $3.3x10^{-8}$ m^2s^{-3}, respectively to the weakest values in the western route deep layer [800-2000] m with a mean and a median of $1.2x10^{-9}$ m^2s^{-3} and $1.7x10^{-10}$ m^2s^{-3}, respectively.

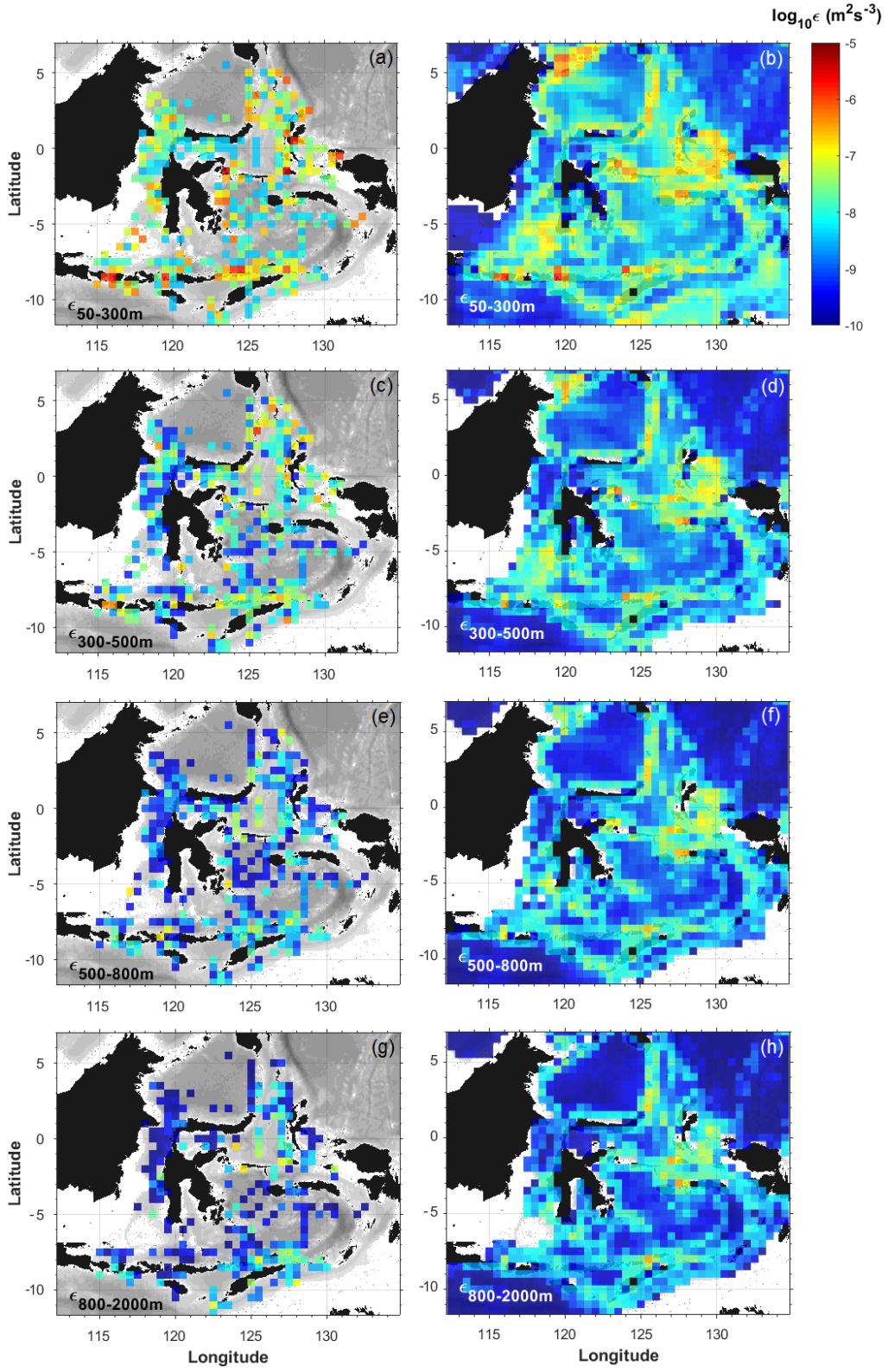

Figure 3.10 A half degree grid mean horizontal distribution for four layer depths of the dissipation rate (in $\log_{10}$ scale, m^2s^{-3}) from historical data sets (first column, $\varepsilon_{Th\text{-}GM}$) and from the 2D hydrostatic model, ε_{NAG15} (Nagai and Hibiya, 2015; personal communication) for selected layers: (a, b) 50-300 m, (d, e) 300-500 m, (g, h) 500-800 m, (j, k) 800-2000 m.

The NAG15 model shows a global weaker range of variation from $1.0x10^{-7}$ m^2s^{-3} and $1.6x10^{-8}$ m^2s^{-3} for the mean and the median, respectively in the exit region upper layer to $1.4x10^{-8}$ m^2s^{-3} and $4.3x10^{-9}$ m^2s^{-3} in the western route deeper layer. Yet, the ratio between the observed dissipation rates and the model-based estimates remains below an order of ten for all layers and routes (**Figure 3.11**.i, j, k, l). The most noticeable differences are found at depth [800-2000] m for weak dissipation rate where the model seems to overestimate the dissipation rate as shown by the distribution of the ratio between the model and observations, which shows a mean value ratio of ~5 (scaled in log in **Figure 3.11**.l) in the western and eastern route. This is consistent with the direct microstructure comparison made in Section 3.3.2, which shows a global overestimation of the weak dissipation rate at depth by a similar order of magnitude. The overestimation of the dissipation rate in deep and relatively low energetic regions seems to be a common bias in models. It is likely due to the lack of specific set up to dissipate the internal tides once generated (Nugroho et al., 2017), seemingly related to the limited capability of the numerical model in preserving dissipation rates smaller than the background values (Nagai et al., 2017).

Another noticeable discrepancy arises in the thermocline layer [50-300] m where the observed dissipation rate is higher than the model ones; this is more pronounced in the western route where the distribution of the ratio of the model to the observed log of the dissipation rate shows a mean of ~0.4 (scaled in log in **Figure 3.11**.i). As previously stated this is likely resulting from the lack of ITF and mesoscale circulation in the NAG15 model. The discrepancy is particularly marked in the Makassar Strait the major branch of the ITF where the underestimation in the model reaches up to two orders of magnitude. This large discrepancy may originate from the strong stratification induced by the freshwater input from the mainland and background current characterized by a relatively strong shear resulting from a persistent southward Indonesian throughflow below 50 m depth (the core of the ITF is at about 100 m depth) and a northward flow in the deeper layer (Mayer and Damm, 2012).

The observed distributions of vertical diffusivity for four depth ranges are displayed in **Figure 3.12**. As observed for the dissipation rate, the strongest diffusivities are observed in the exit passages followed by the eastern and the western route for upper and intermediate layers, [50-800] m and comparable distribution patterns in the deeper layer [800-2000] m. For all layers and regions the mean value are above typical open ocean value of $1x10^{-5}$ m^2s^{-1}. For all regions, the median of the distribution shifts toward higher values with increasing depth as a result of the decreasing stratification. Below 300 m depth, the vertical diffusivity evolves from the highest values in the exit passage deeper layer [800-2000] m with a mean and a median of

$1.6x10^{-3}$ m^2s^{-1} m^2s^{-3} and $2.7x10^{-4}$ m^2s^{-1}, respectively to the weakest values in the western route intermediate layer [300-500] m, with a mean and a median of $4.8x10^{-4}$ m^2s^{-1} and $2.6x10^{-5}$ m^2s^{-1}, respectively.

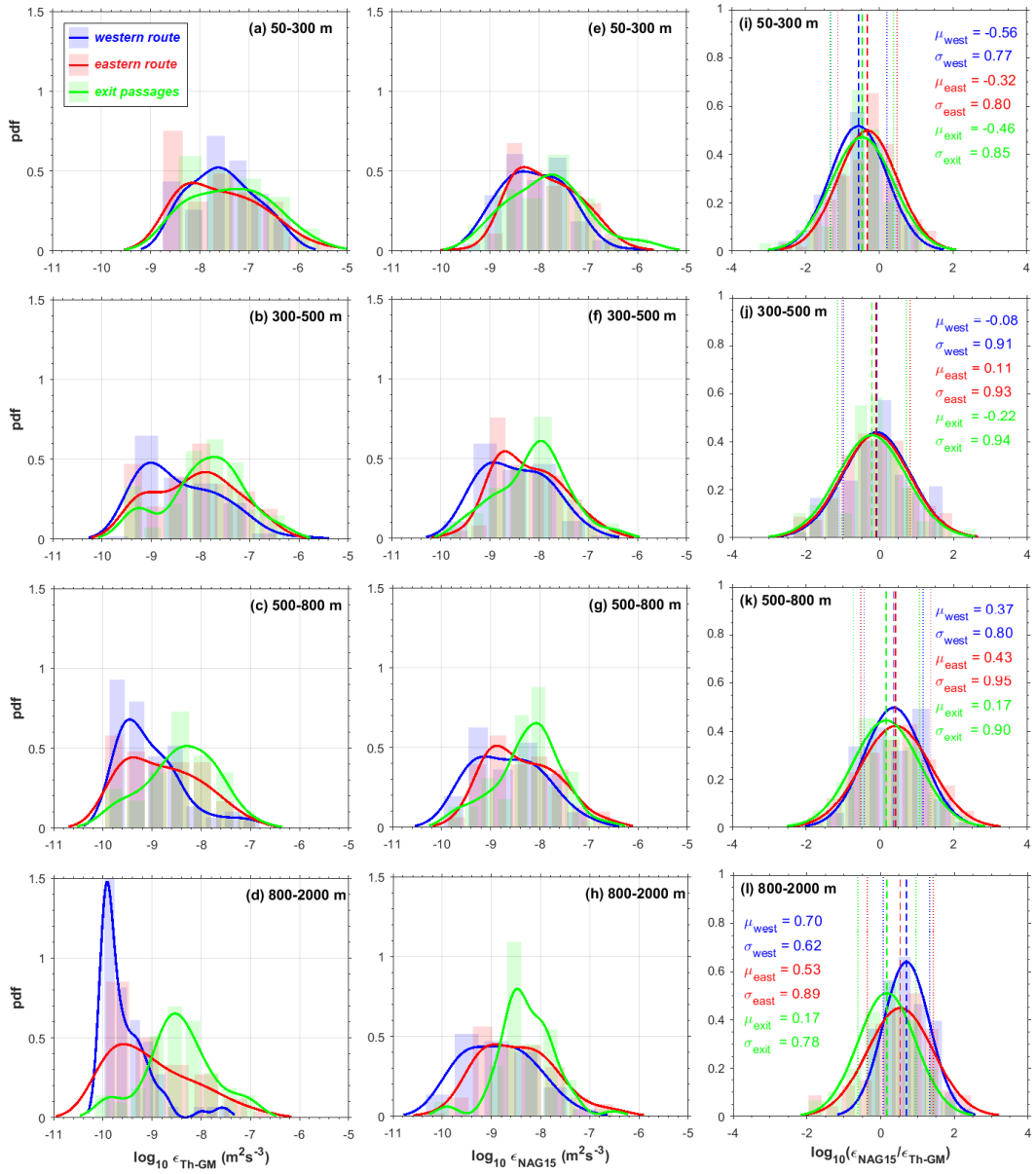

Figure 3.11 PDF histogram of the dissipation rate from historical data set, $\varepsilon_{Th\text{-}GM}$ (a, b, c, d) and those from NAG15 model, ε_{NAG15} (e, f, g, h), inferred from the spatially gridded cells of the historical data sets for four depth ranges, plotted with the number of bin based on the Freedman-Diaconis rule, with respected kernel distribution estimates. The western route (SLA, MAK, FLO), eastern route (MAL, HAL, BAN) and exit passages (LES) regions are presented in blue, red and green colors, respectively. The PDF histogram ratio of the model to the observed dissipation rate, $\varepsilon_{Th\text{-}GM}$ with respected normal distribution fits is displayed in (i, j, k, l). The mean and standard deviation are also indicated with dashed and dotted lines, respectively. Note that, only the dissipations of the model at the grid cells where the observation grid cells exist are taken into account.

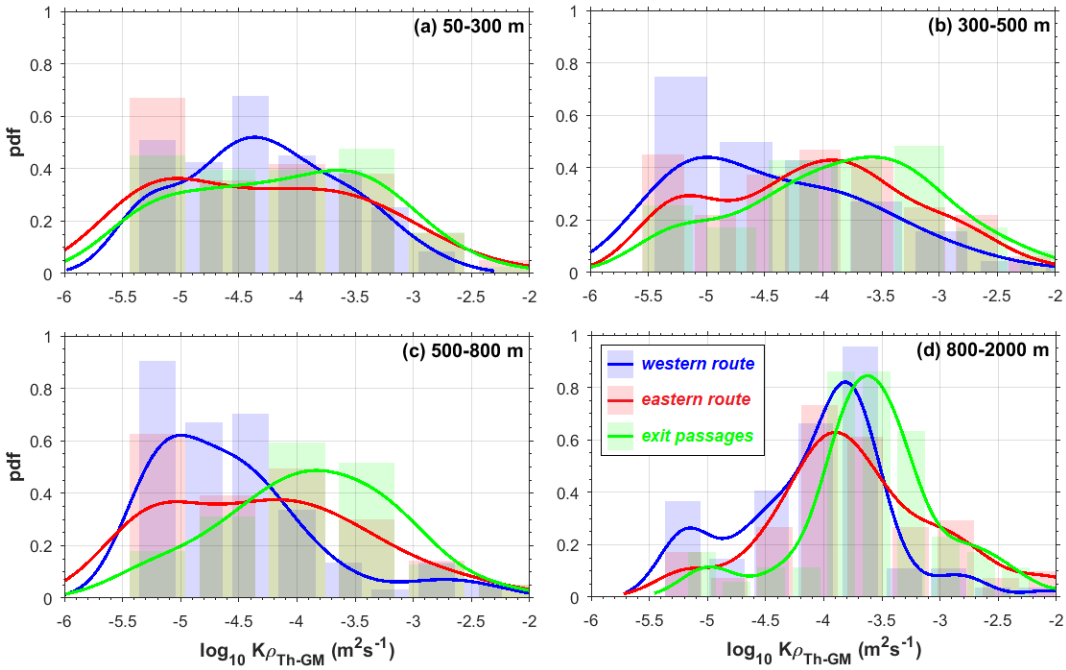

Figure 3.12 PDF histogram of the vertical diffusivity, K_ρ inferred from the spatially gridded cells of the historical data sets for four depths range, plotted with the number of bin based on the Freedman-Diaconis rule, with respected kernel distribution estimates. The western route (SLA, MAK, FLO), eastern route (MAL, HAL, BAN) and exit passages (LES) regions are presented in blue, red and green colors, respectively.

3.4 Concluding remarks

Direct turbulence measurements are extremely sparse in the Indonesian seas, which led us to apply the indirect Thorpe scale method to infer dissipation rates and diapycnal diffusivities using an unprecedented data set of 756 profiles including 507 profiles from annual RCO-LIPI cruises. The Thorpe method we used includes carefully spurious overturns detection based on previous works (Galbraith and Kelley, 1996; Gargett and Garner, 2008), and also pay attention to the definition of the background dissipation rate (i.e. when no overturns are detected). It is estimated by combining a minimum dissipation rate based on both Thorpe and microstructure, and a definition based on stratification from a simplified version of the Gregg (1989) parameterization. The robustness of our improved Thorpe scale method with background dissipation rates was tested against the microstructure measurements from INDOMIX 2010 and TOMTOM 2015 data sets. We show an unbiased relationship with the direct estimates over a large dynamical range.

Our dissipation rate and vertical diffusivity maps are consistent with previous observations based on limited direct microstructure samples (Alford et al., 1999; Bouruet-Aubertot et al., 2018; Koch-Larrouy et al., 2015); from the isotherm displacements based on historical XBT profiles, a preliminary precursor to identify the turbulence active spots in the Indonesian seas (Ffield and Robertson, 2008); but they allow a much more improved spatial sampling of the ITF routes, notably by providing mixing estimates along the western route, which was not investigated by these previous studies. We found a clear contrast of the dissipation rate along the ITF routes and exit passages from the historical data set, which previously has been indicated in models (Koch-Larrouy et al., 2007; Nagai and Hibiya, 2015; Nugroho et al., 2017).

The relevance of different numerical models to reproduce the spatial dissipation pattern was addressed. This allowed us to evidence the main mechanisms responsible for the observed turbulence. The dissipation rate inferred from high-resolution 3D MITGCM forced by M2 tides is consistent with the observational estimates in the hot spots of strong turbulence, suggesting that the baroclinic tidal energy dissipation is likely the main driving mechanism. Our results yet also show a negative bias of the model in the thermocline layer where the ITF is intense, notably in the Makassar Strait and in the north of Maluku Island, which suggest that the ITF and mesoscale circulation significantly enhance the dissipation through direct shear generation and/or interaction with internal tides with the tide. We also

found a general positive bias of the NAG15 dissipation rate in low dissipation range of the far-field which suggest that the background dissipation rate in this model is too high. Two models, NUG17 and NAG17, including the ITF were also compared with the VMP measurements at the INDOMIX 2010 stations, they showed better agreement than NAG15 in the upper layer of energetic stations but still have an overestimation of the background dissipation rate. The map of the dissipation rate built here provides a useful footprint for testing mixing representation in state of the art and future regional models of the Indonesian seas. It is also worth noting that a side product of this study is an improved map of salinity for Pacific waters, which seems in better agreement with recent modeling (NUG17) than the conventional WOA13 map.

3.5 Acknowledgments

Indonesian Endowment Fund Scholarship Program (LPDP) - Indonesian Ministry of Finance also sponsors this study. We are grateful to Research Center for Oceanography LIPI for the data sets of the RV Baruna Jaya I and VIII, Balai Riset Perikanan Laut (BRPL) - Indonesian Ministry of Marine Affairs (KKP) for the STOKAS 2015-2016 data sets; and to the crew of RV Baruna Jaya I, VII and VIII for helping the data acquisition. We thank B. Sloyan and RV Solander crew for helping us to conduct the VMP measurements in the Timor passage as part of the IMOS Long-term monitoring of the Indonesian Throughflow and TOMTOM project.

3.6 Appendix

3.6.1 Snapshot CTD stations by year

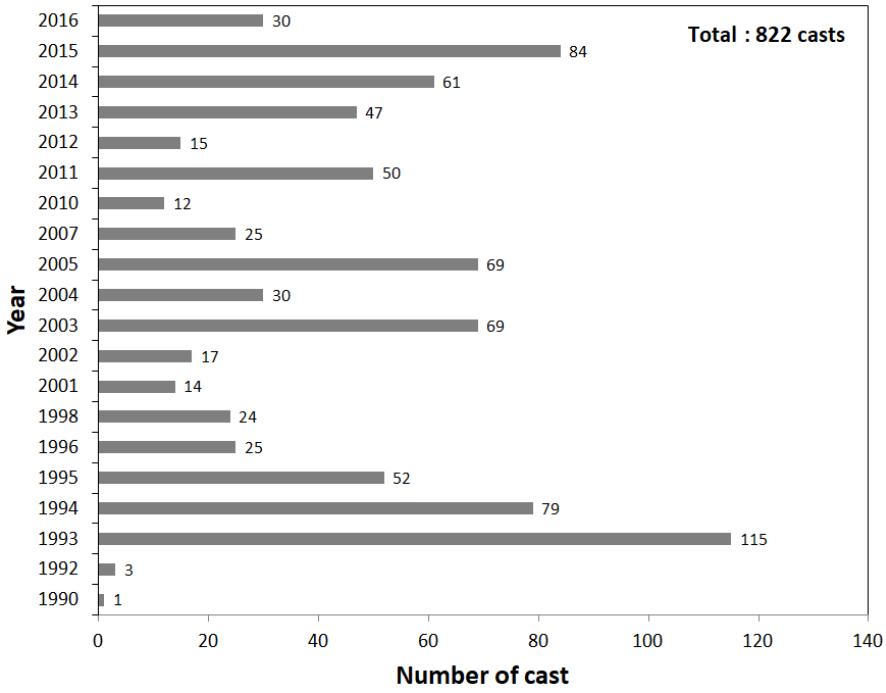

Figure 3.13 The number of CTD profiles in each year analyzed in this study, involving only the casts observed in the Indonesian seas region.

3.6.2 Spatial grid averaging for the sparsely distributed CTD casts

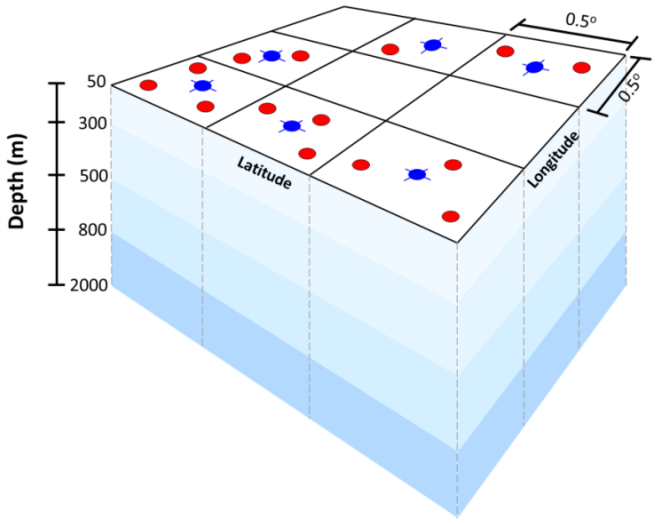

Figure 3.14 Spatial horizontal grid averaging method with 0.5° degree longitude and latitude; and vertical layer averaging for several layer depths: 50-300 m, 300-500 m, 500-800 m, 800-2000 m. Red and blue dots represent vertical profile of CTD stations available in each grid and their mean profiles, respectively.

3.6.3 Overturn selection criterion

Double diffusion impact

We inspect the potential for the DC and SF events form our CTD data set. The Pacific salinity intrusion, which is observed in large part of the Indonesian seas naturally, induces a potential for salt fingering in the region of decreasing salinity with depth. The In the upper layer, (50-300 m), high percentages (~60-70%) of the water column are observed to be in the SF favourable regime along the western route of ITF: north of Maluku Sea, Sulawesi Sea, Makassar Strait and Dewakang waters, and Flores Sea (**Figure 3.15**) . In the intermediate layer (300-800 m), the percentage can reach up to nearly 100% locally in the eastern route of ITF such as in the Halmahera Sea and surrounding waters, Maluku Sea, north of Banda Sea. High percentage >60% are also observed in the lower intermediate layer (500-800 m), such as in the south of Lombok Strait and Sumba Strait. As shown in **Figure 3.15**, the potential for DC event is less frequent than for SF in the Indonesian seas; with less than 10 % DC dominated in average over the entire the region. More than 15% DC potential are observed in the lower layer (>500 m) of the eastern passages of ITF such as in the Halmahera Sea, Seram Sea and in the exit passages of the ITF, such as in the Ombai Strait and eastern Flores Sea (north of Ombai Strait).

The distribution patterns of DC and SF found in this study reveals that the double diffusive events are frequently observed in the region where two different water types interact with each other. The SF favourable regimes are found in the upper and lower thermocline where the NPSW and SPSW layers exist and interact with the internal Indonesian seas; also, an interaction exists between NIIW with the ITF in the lower intermediate layer. In a few instances, the DC favourable regimes are found in the deeper layer, in the region where the ITF in the Flores Sea contacts with the Banda Sea and in the Halmahera Sea where the SPSW contacts with the Halmahera waters.

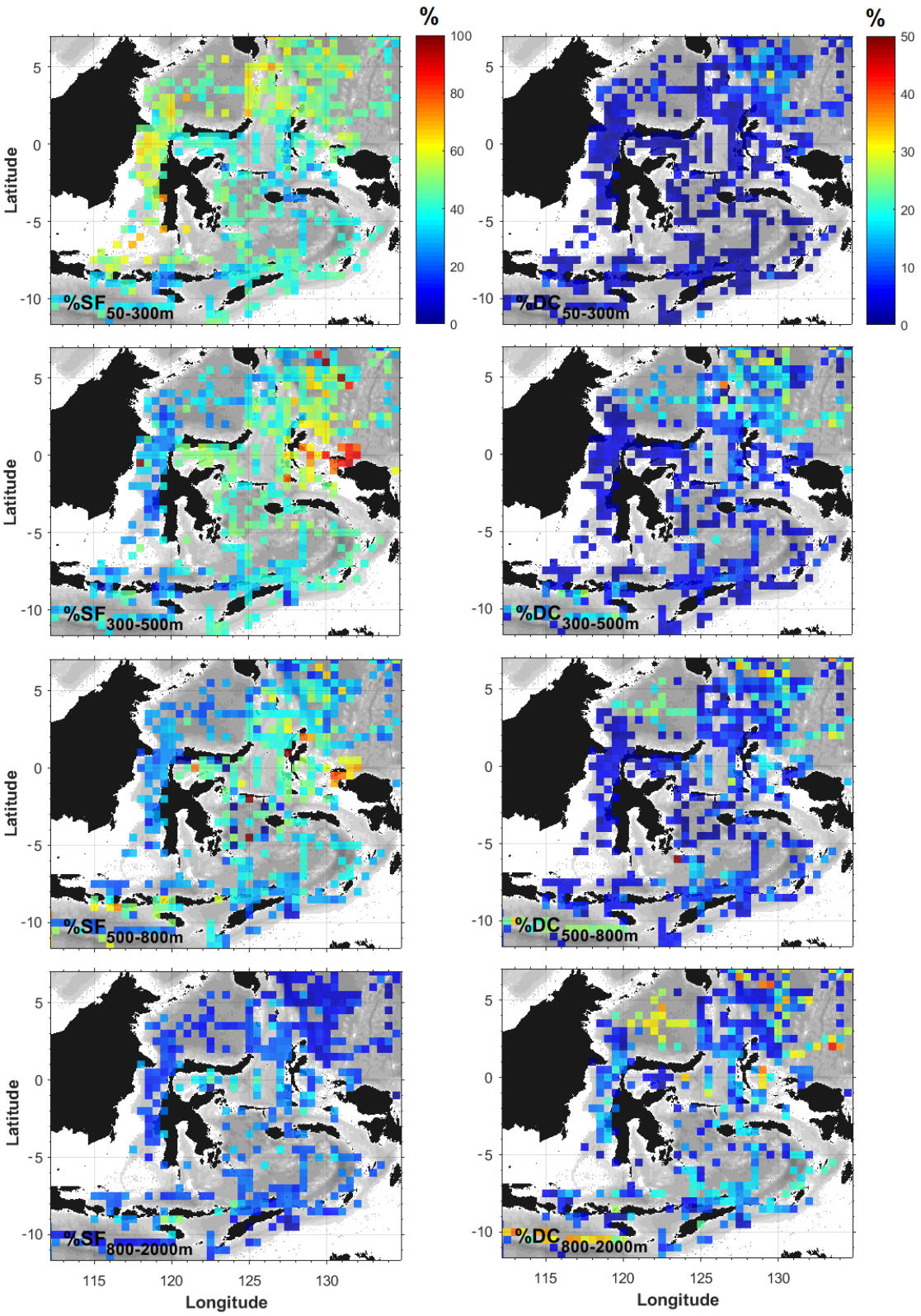

Figure 3.15 A half-degree gridded mean spatial distribution of percentage of the parcels exposed to potential salt fingering with criterion [45° < *Tu* <90°] for selected layers: (a) 50-300 m, (b) 300-500 m, (c) 500-800 m, (d) 800-200 m; and that of exposed to the diffusive convection (DC) potency with criterion [-90° < *Tu* <-45°] for selected layers: (e) 50-300 m, (f) 300-500 m, (g) 500-800 m, (h) 800-200 m.

The double diffusion events may contribute significantly to heat and/or salinity fluxes only in cases where turbulence is sufficiently weak to allow slow double diffusion instabilities to grow. A threshold value of the Re_b>25 was proposed in different studies (Gregg, 1988; Inoue et al., 2007; Padman and Dillon, 1987; Yamazaki, 1990). In the large majority of our observations, we found that the Re_b was above this threshold, so that double diffusion may be neglected. Interestingly, the poor value of the overturn ratio and/or water mass test seem to be correlated with DC or SF, which suggests the possible contamination by false overturns when double diffusion is acting (**Figure 3.16**, **Figure 3.17**). This is particularly the case in the Pacific, just outside the Indonesian sea. On the opposite, it also suggests that our overturn ratio threshold ($Ro \geq 0.2$) and water mass test threshold ($\xi \leq 0.66$) are quite good to eliminate spurious overturns favored by double diffusive favourable conditions. The physical reason why double diffusion favourable regime seems to increase false overturn detection is not clear, (theoretically double diffusion should not generate any density overturns) but we can suspect that small scale structure induced for instance by salt fingering may be badly resolved by the salinity sensor and increase noise level in the measurements. A summary of overturn selection criterion applied in this study is shown in **Figure 3.18** together with the double diffusion favourable conditions.

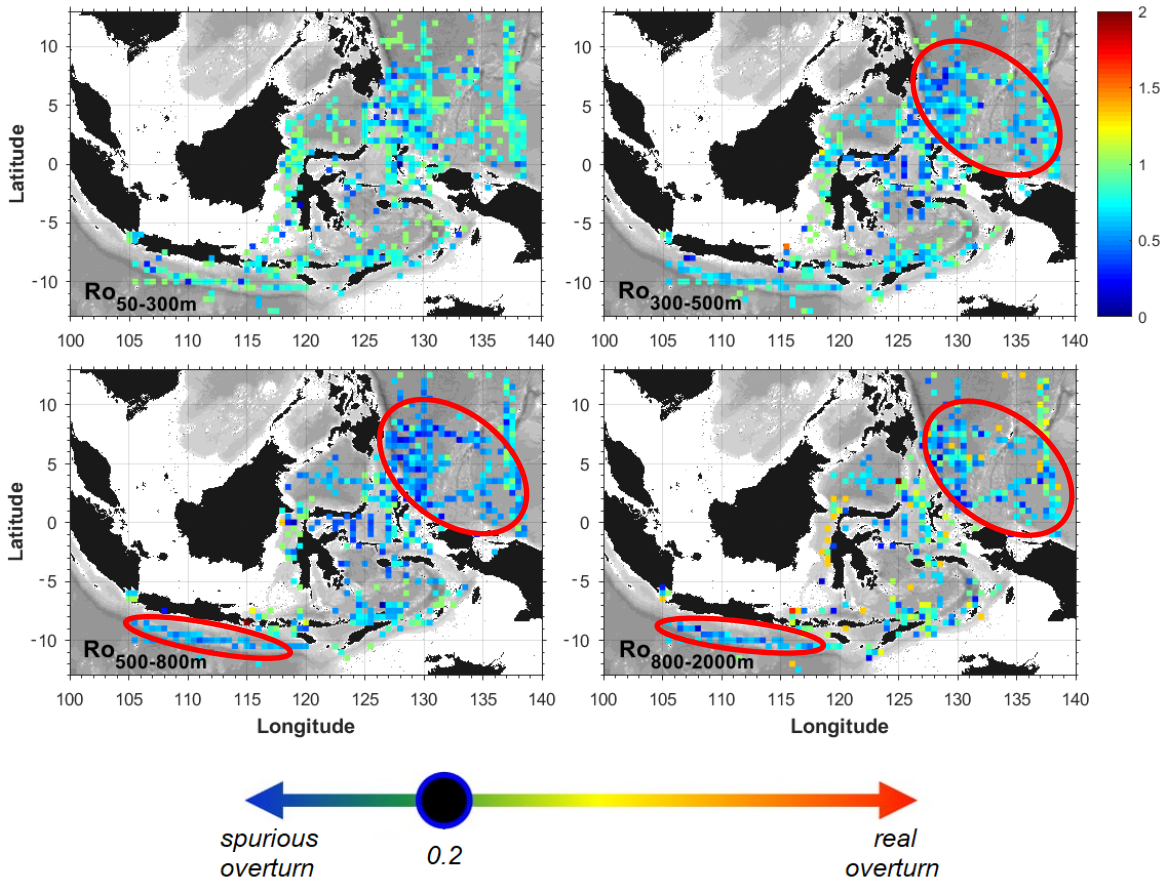

Figure 3.16 Inspection of spurious overturn based on the overturn ratio values, *Ro*. *Ro* = 0.2 is the threshold used in this study, suggesting numerous CTD stations in some regions in some regions contain spurious overturns (*Ro* < 0.2) related to noise within their profiles (red circles).

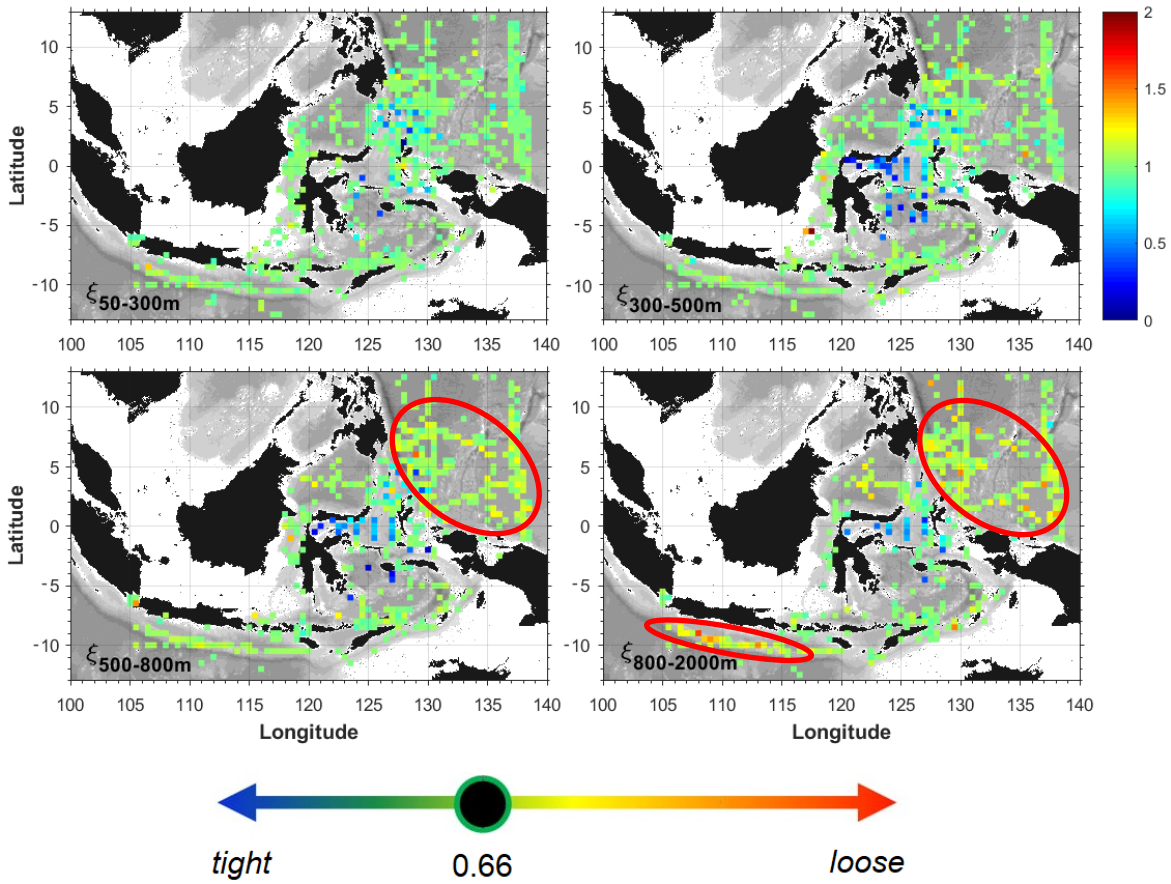

Figure 3.17 Inspection of spurious overturn based on the *T/S* tightness relationship values, ξ. ξ = 0.66 is the threshold used in this study, suggesting numerous CTD stations in some regions with very loose *T/S* relationship (ξ>0.66, red circles).

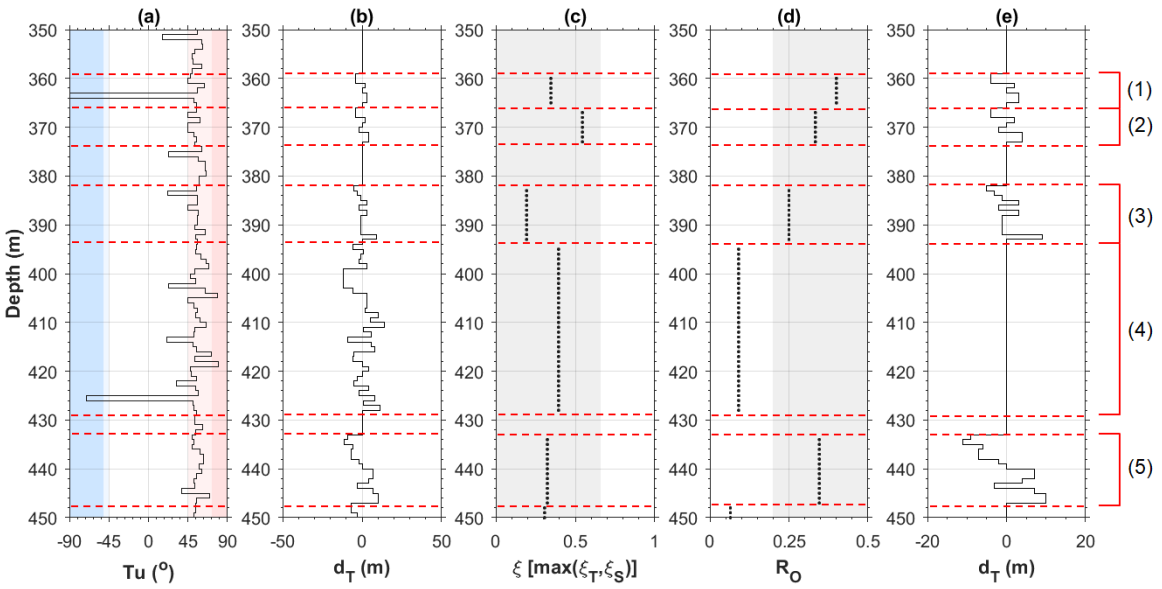

Figure 3.18 An example of overturn selection criterion applied in this study: (a) vertical profile of Turner angle with shaded regions of strong ($-90^{o} \leq Tu \leq -51^{o}$) and weak diffusive convection ($-51^{o} \leq Tu \leq -45^{o}$) potential (dark and light blue, respectively); strong ($72^{o} \leq Tu \leq 90^{o}$) and light salt fingering ($45^{o} \leq Tu \leq 72^{o}$) potential (dark and light red, respectively). (b) Observed vertical displacements, (c) T/S tightness test with $\xi < 0.66$ threshold (gray shaded region), (d) overturn ratio criteria with $R_o > 0.2$ thresholds (gray shaded region. (e) Remaining overturn considered as turbulent event. The types of turbulent according to Tu criterion give: (1) turbulence occurrence in double diffusive favorable conditions, (2, 3, 5) turbulent within salt fingering favorable condition and (4) spurious turbulent.

3.6.4 Analysis of step structures in the repeated stations

Local destruction of stratification by strong mixing events can result in step like structures in the density profiles, identification of such steps can therefore also be a proxy for the identification region of strong water mass mixing. (Koch-Larrouy et al., 2015; Middleton and Foster, 1980; Park et al., 1994). Note that these features are clearly identified from 16 repeated stations (**Figure 3.19**). Most of the time the region of strong step like structures are indeed correlated with density inversion (**Figure 3.20**).

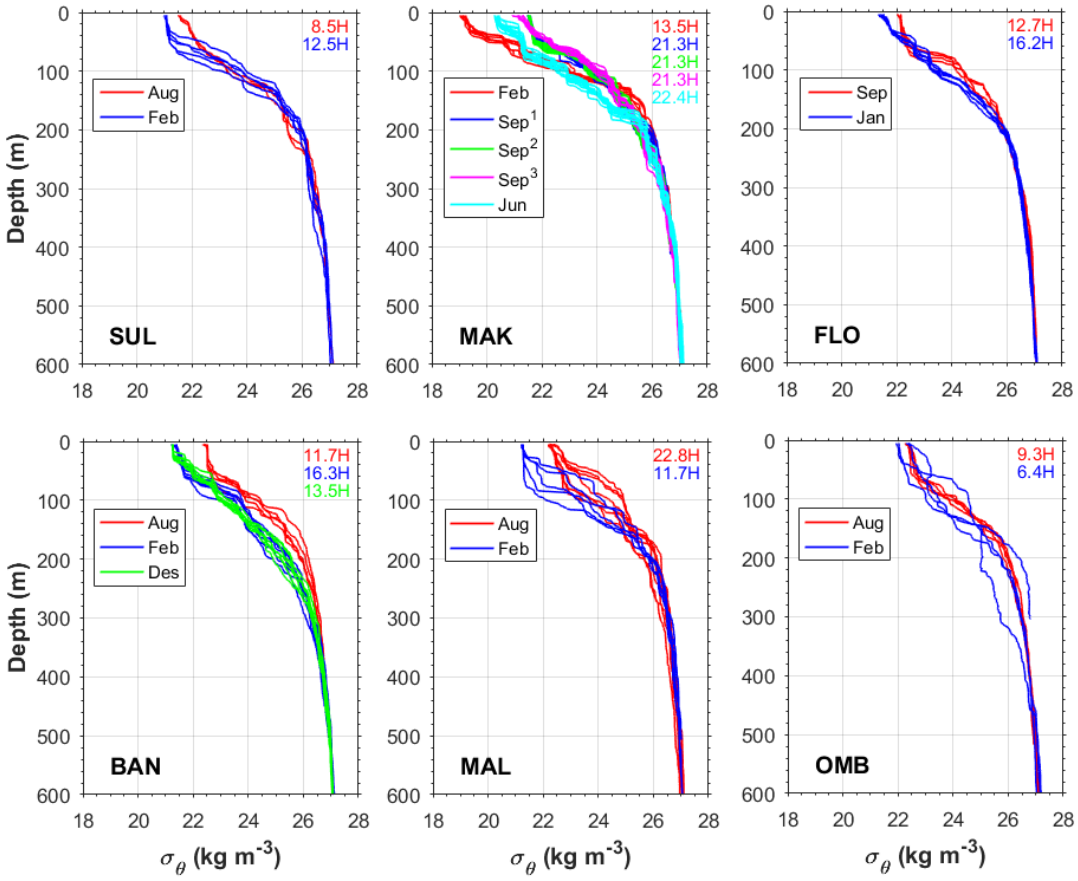

Figure 3.19 Short temporal variability of the density profiles (kg m^{-3}) in some regions: Sulawesi Sea (SUL), Makassar Strait (MAK), Flores Sea (FLO), Banda Sea (BAN), Maluku Sea (MAL), including the Buru and Lifamatola straits, and Lesser Sunda seas (LES), which is represented by the Ombai Strait here. Duration of the each tow-yo measurements is indicated (in hours) on each plot. The profiles are shown only for the 600 m depth to show clearly the temporal variation.

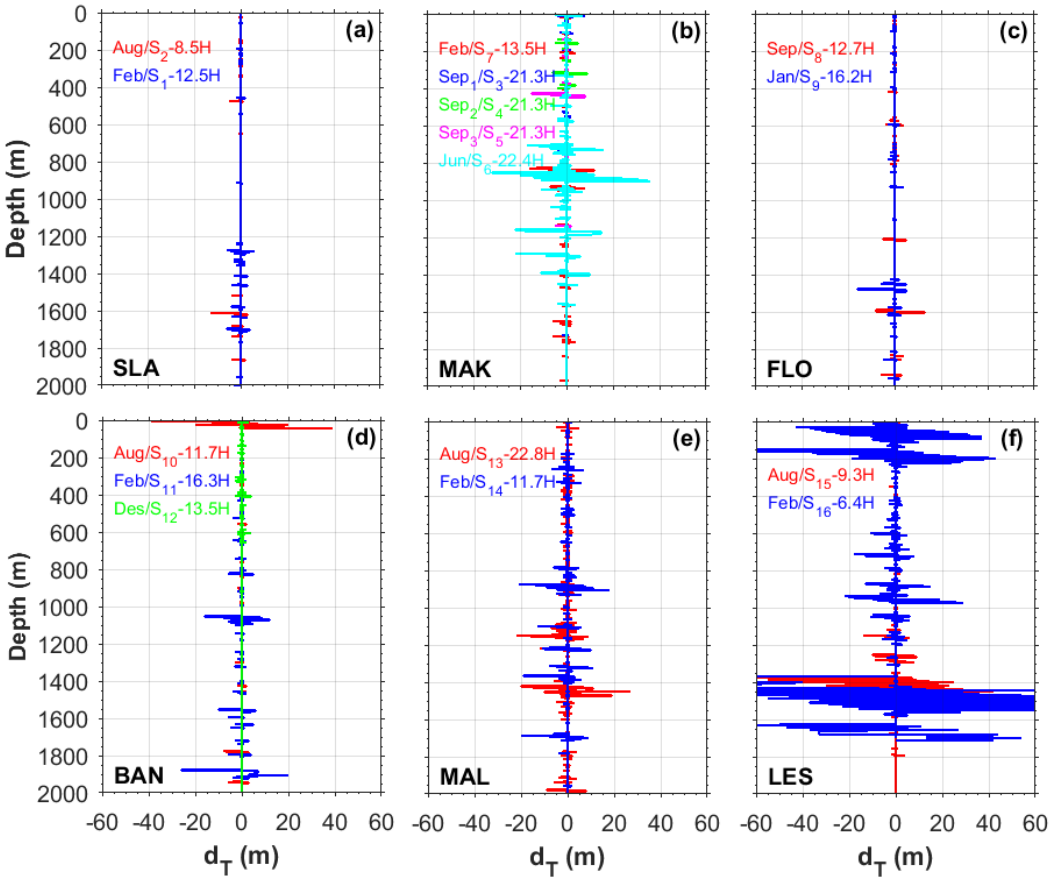

Figure 3.20 Short temporal variability of the Thorpe vertical displacements (m) in some regions: Sulawesi Sea (SUL), Makassar Strait (MAK), Flores Sea (FLO), Banda Sea (BAN), Maluku Sea (MAL), including the Buru and Lifamatola straits, and Lesser Sunda seas (LES), which is represented by the Ombai Strait here. Time length of each cast is indicated in hours in each plot.

3.6.5 Frequency of density inversions

The portion of density inversions observed in the repeated stations also indicates a higher percentage of the overturned parcels in the near field region in narrowing passages and straits (shaded rows) and very few in far field (open seas) region (**Table 3.3**). The higher percentage is found in the Ombai Strait S16, those are 21.91% and 30.39% of the profile within the depth range of 50-300 m and 800-2000 m, respectively.

The same trends are also evident from the horizontal distribution plot as shown in **Figure 3.21**. Higher percentages of >10% are observed in the lower layer (300-2000 m) in the energetic area, Lesser Sunda seas (in the straits of Lombok, Ombai); in the straits of Buru, Manipa, Halmahera, Banggai and Lifamatola). In the upper 300 m, no clear trend is observed. The lower overturn percentage is found in offshore locations more distant from islands, such as in the central Makassar Strait, Flores Sea, Banda Sea, and central Timor passage. As a summary, the overall portion of overturning events is much larger in shallow straits and

narrow passages such as the near field sub-regions, MAL, HAL and LES where this fraction reaches 6.0%, 5.8% and 5.7% respectively. It is much weaker for the far field sub-regions, SUL, MAK, FLO and BAN, where it reaches 2.7%, 2.0%, 2.2% and 3.2%.

Table 3.3 The percentage of overturned portion inside a certain layers at repeated stations: SLA (Sulawesi Sea), MAK (Makassar Strait), FLO (Flores Sea), BAN (Banda Sea), MAL (Maluku Sea), LES (Lesser Sunda seas). Horizontal shaded rows represent nearfield stations (Labani Channel and the straits of Buru, Lifamatola and Ombai). The shaded table cell represents nearfield area.

Site	Year	Location	% of overturned portion			
			50-300 m	300-500 m	500-800 m	800-2000 m
SLA	1993	Central (S2)	1.86	3.34	0.67	3.08
	1994	Central (S1)	1.83	0.40	0.33	4.13
	1994	Labani Channel (S7)	2.13	1.33	0.11	5.19
MAK	2002	Western (S3)	0.49	0.00	0.59	0.09
	2002	Western (S4)	1.74	1.75	1.17	0.00
	2002	Western (S5)	1.00	1.56	0.42	0.07
	2013	Labani Channel (S6)	0.93	1.54	3.39	2.15
FLO	1993	East (S8)	0.60	0.50	2.58	2.95
	1994	East (S9)	1.59	0.83	2.76	3.68
BAN	1993	Central (S10)	0.20	1.14	1.14	3.28
	1994	Central (S11)	0.40	1.33	4.50	6.03
	1996	East (S12)	1.38	3.00	3.41	0.17
MAL	1993	Buru Strait (S13)	2.89	5.85	3.96	9.90
	1994	Lifamatola (S14)	3.59	7.30	8.32	11.33
LES	1993	Ombai Strait (S15)	0.50	1.00	0.98	7.11
	1994	Ombai Strait (S16)	21.91	5.13	18.10	30.39

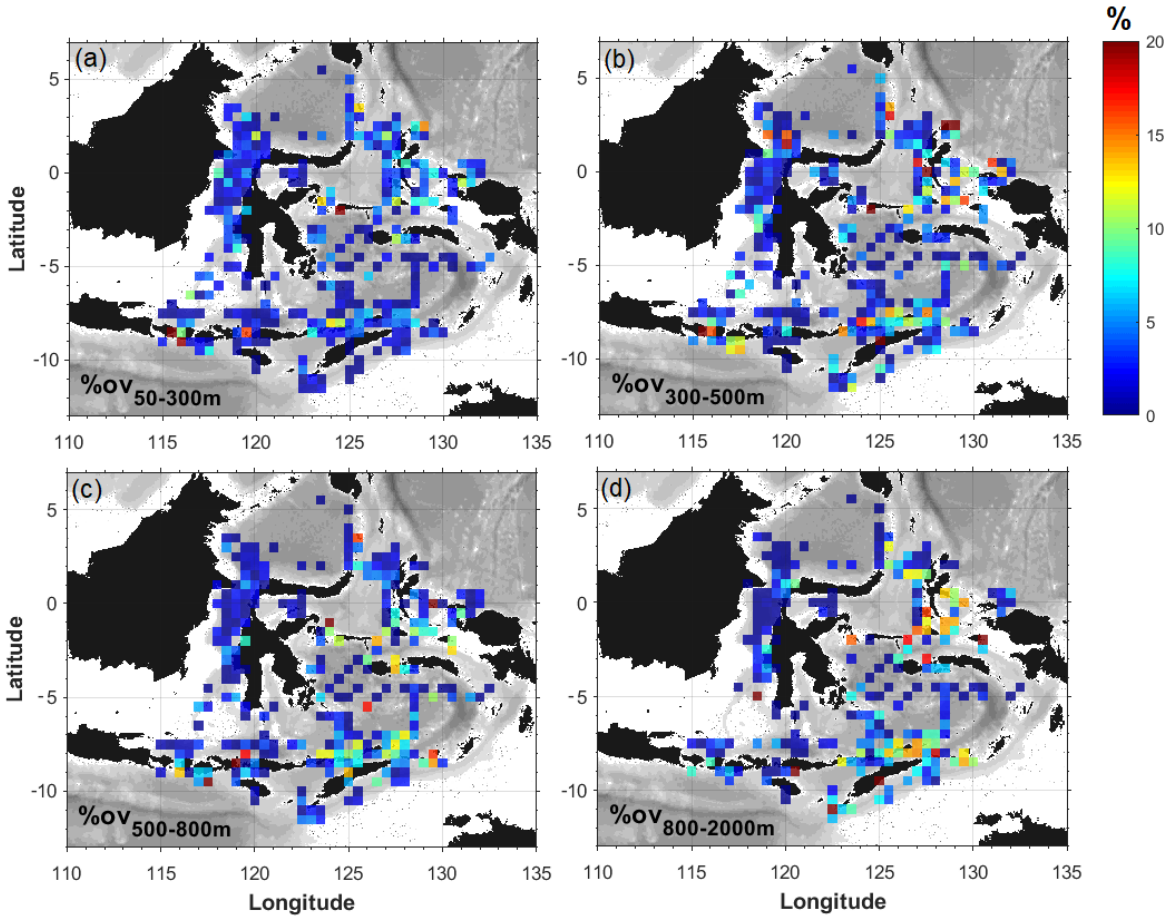

Figure 3.21 A half-degree gridded mean spatial distribution of percentage of the overturned parcels for selected layers: (a) 50-300 m, (b) 300-500 m, (c) 500-800 m, (d) 800-200 m.

3.6.6 Repeated CTD cast sampling times

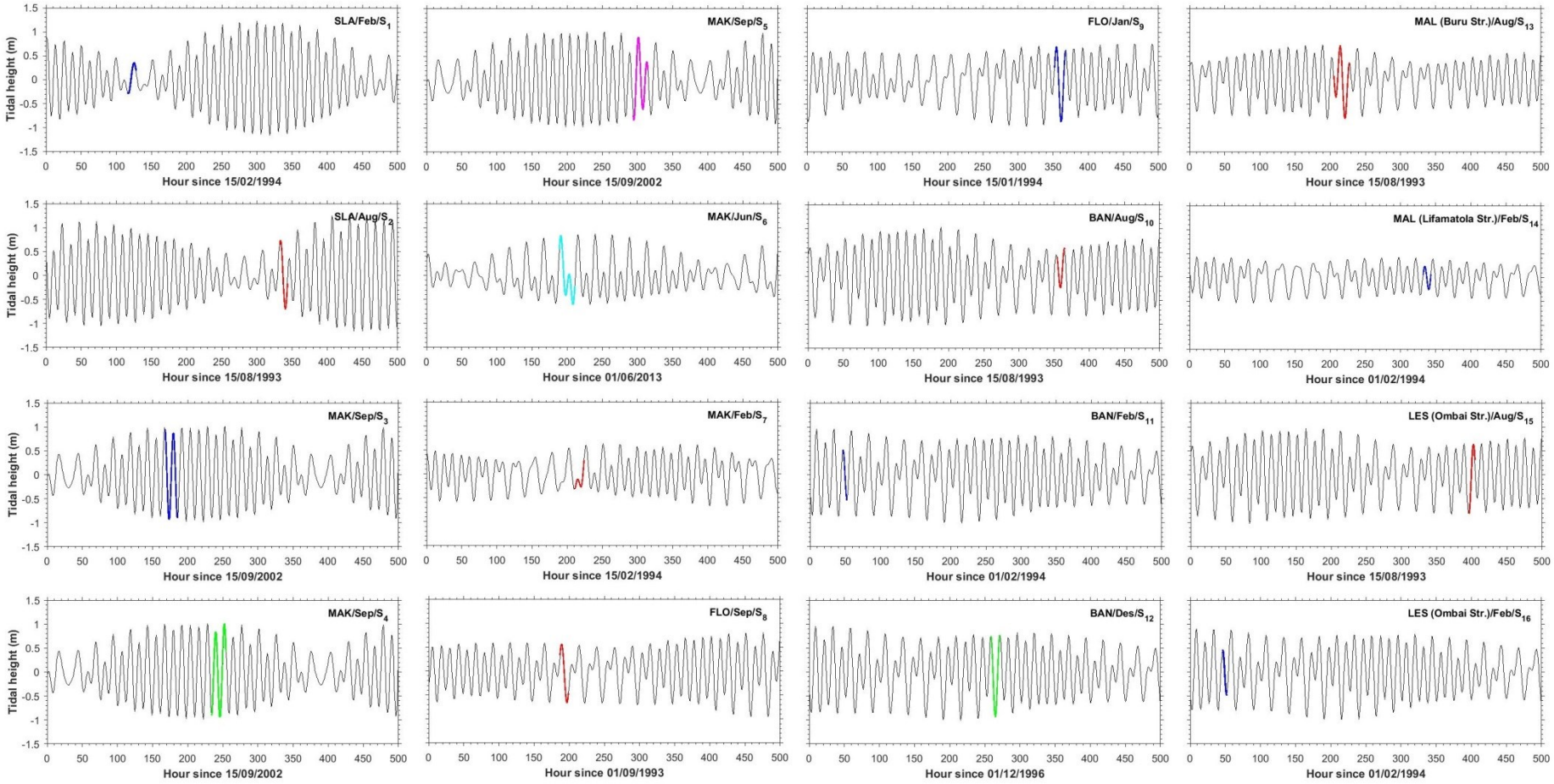

Figure 3.22 Repeated CTD cast sampling times for the data sets in Chapter 2, overlaid on the tidal height chart of the Oregon State University tidal inversion software, OTIS (Egbert and Erofeeva, 2002).

4

Mixing Estimates Enhanced by Shoaling Internal Solitary Wave in the Manado Bay, Sulawesi, Indonesia

Chapter 4
Mixing Estimates Enhanced by Shoaling Internal Solitary Wave in the Manado Bay, Sulawesi, Indonesia (Paper to be submitted)

4.1 Introduction

Internal solitary waves (ISWs), that induce large vertical isopycnal displacements, can be remotely detected as sea-surface alternating bands of slicks and rough patches (Moum et al., 2003). In most cases the formation of theses waves results from the nonlinear steepening of internal tides and/or from the relaxation of Lee waves under supercritical conditions (Alford et al., 2015).

Once generated ISWs can propagate over several hundreds of km before encountering the shelf slope where they can break, reflect, and sometimes inverse their polarity resulting in a wave of elevation due to changing in the thickness of the upper and lower layer (Li et al., 2015). A number of studies have confirmed that shoaling and breaking of ISW can induce turbulence and mixing (Bourgault et al., 2008, 2007; Klymak and Moum, 2003). During the breaking process, short energetic waves of elevation propagating upslope, also referred to as boluses, can also be formed and contribute to the upslope transport of properties (Helfrich,1992; Venayagamoorthy and Fringer 2006, 2007; Bourgault et al., 2007). This process contributes significantly to the vertical fluxes of nutrients and input into the euphotic layer (Moum et al., 2003; Walter, 2014). Shoaling ISWs may also have considerable implications for the cross-shelf transport of nutrients, sediments, contaminants (Bourgault et al., 2014; Hosegood and Van Haren, 2004) and larval transport (Pineda and López, 2002). Therefore, ISWs in the coastal ocean are a significant dynamical process from a fundamental and practical point of view with strong implications for many physical and biological processes.

Indonesian seas, as a region of strong internal tides favorable to the generation of ISWs (Nagai and Hibiya, 2015), have been identified as a hotspot for ISW generation based on MODIS satellite images (Jackson, 2007). The profusion of ISWs in this region is presumably due to the large number of shallow inter-island sills that separate deeper basins where strong internal tides are generated. A typical hotspot for internal tide generation is the Sibutu sills, a shallow passage separating the Sulu sea and the Sulawesi Sea (Apel et al., 1985; Kartadikaria et al., 2011). The ISWs, evidenced from satellite images, that originate from the Sibutu passage

and propagate in the Sulawesi Sea, support this idea (**Figure 4.1**.d, e). The purpose of this paper is to provide further insights on this process with idealized numerical simulations of the ISWs lifetime as well as focus on their fate when approaching the coastal area with the first in-situ characterization of ISW in the shallow waters of Manado Bay.

Some previous studies showed that Sibutu sills, the shallow passage separating the Sulu sea and the Sulawesi sea, is a hot spot for internal tide generation in both Sulu and Sulawesi Seas (Apel et al., 1985; Kartadikaria et al., 2011). ISW breaking represents a significant source of energy dissipation for internal tides that impact coastal dynamics (Venayagamoorthy and Fringer, 2007). Since the discovery of new living fossil fish species, Coelacanth (*Latimeria menadoensis*) in the deep cave of Manado Bay in 1998, the Indonesian government has given intensive attention to this area as a national coral reef conservation zones within the world coral-triangle zone. In this context the intense diapycnal mixing and cross-shelf transport induced by the shoaling of high-frequency ISWs (e.g. Koseff et al., 1993) may strongly impact the biological system. Trapped core, nonlinear and non-hydrostatic boluses accompanying the shoaling processes near the bottom can transport density, nutrients, larvae, or sewage onshore (Nam and Send, 2011; Venayagamoorthy and Fringer, 2007). This paper aims to characterize ISWs in the Sulawesi Sea, starting from their generation site near the Sibutu sills until their shoaling in the Manado Bay. The analysis is based on idealized 2D numerical simulations and is complemented by in-situ observations of shoaling ISWs in the Manado Bay. This analysis constitutes a preliminary step towards estimating the biological response toward sediment resuspension induced by ISW breaking and nutrient-enrichment of the pelagic layer.

The paper is organized as follows. Section 4.2 describes the methodology, highlighting available dataset from the observations and the numerical model setting. Methods used to estimate kinetic energy dissipation rate and vertical eddy diffusivity estimates from both observations and numerical simulations, are also detailed. Section 4.3 focuses on the internal tide generation and its nonlinear evolution while section 4.4 is dedicated to the shoaling process. Results are eventually summarized and discussed in section 4.5.

4.2 Methodology

4.2.1 In situ observations

The data were collected from 10 to 14 May 2009 in the Manado Bay waters. The RV Baruna Jaya VIII from Research Centre for Oceanography, Indonesian Institute of Sciences (LIPI) was anchored on the shelf-break, approximatively 0.3 km from the Manado Bay coast. A shipboard 75 kHz *RD Instrument* acoustic Doppler current profiler (ADCP) and a 120 kHz single beam *Simrad* EK500 echosounder were operated during the experiment to measure the current profiles and biological scattering layer intensity (echogram), respectively. Processed current measurements have a 1-minute temporal resolution and a 5-meters vertical bin. High-resolution bathymetric measurements were also provided by the EM1002 *Multibeam* echosounder. Once a presumed ISW signal was observed by the echosounder, a sequence of CTD profiles was performed using *Seacat profiler Seabird Electronics* (SBE) *CTD* probes with sampling rate 4 Hz. The profiles were collected with repeated profiling as the internal waves appeared in the echosounder, with sampling interval around 5 to 8 minutes in order to characterize the high-frequency variability of temperature and salinity. The standard SBE processing module was applied. The data were bin-averaged over 0.5 m. Since most measurements in the near-surface layer were contaminated by the vessel's heaving, measurements within the first 5 meters were discarded. The detail of the operated measurements is shown in **Table 4.1**.

Table 4.1 In situ measurements in the Manado Bay from 10 to 14 May 2009.

Date	Hour of the cast (GMT+7)	Note
12 May 2009	07.33; 08.59; 10.00; 10.08; 10.15; 11.25; 11.31; 11.36; 11.41; 12.50; 12.55; 12.59; 13.05; 13.10; 14.03; 14.10; 14.16;14.23; 14.29; 14.35; 14.40; 14.48	*with SADCP measurement, no echosounder measurement*
	17.36; 17.45; 17.54; 17.58; 18.05; 18.10; 18.16; 18.22; 18.28; 18.33	*with SADCP measurement and echosounder measurement*
13 May 2009	05.07; 05.15; 05.21; 05.27; 05.33; 05.40; 05.45; 05.51; 05.57; 06.03; 06.08; 06.14; 06.20	*with echosounder measurement*
14 May 2009	*no CTD cast*	*no SADCP measurement, with echosounder measurement*

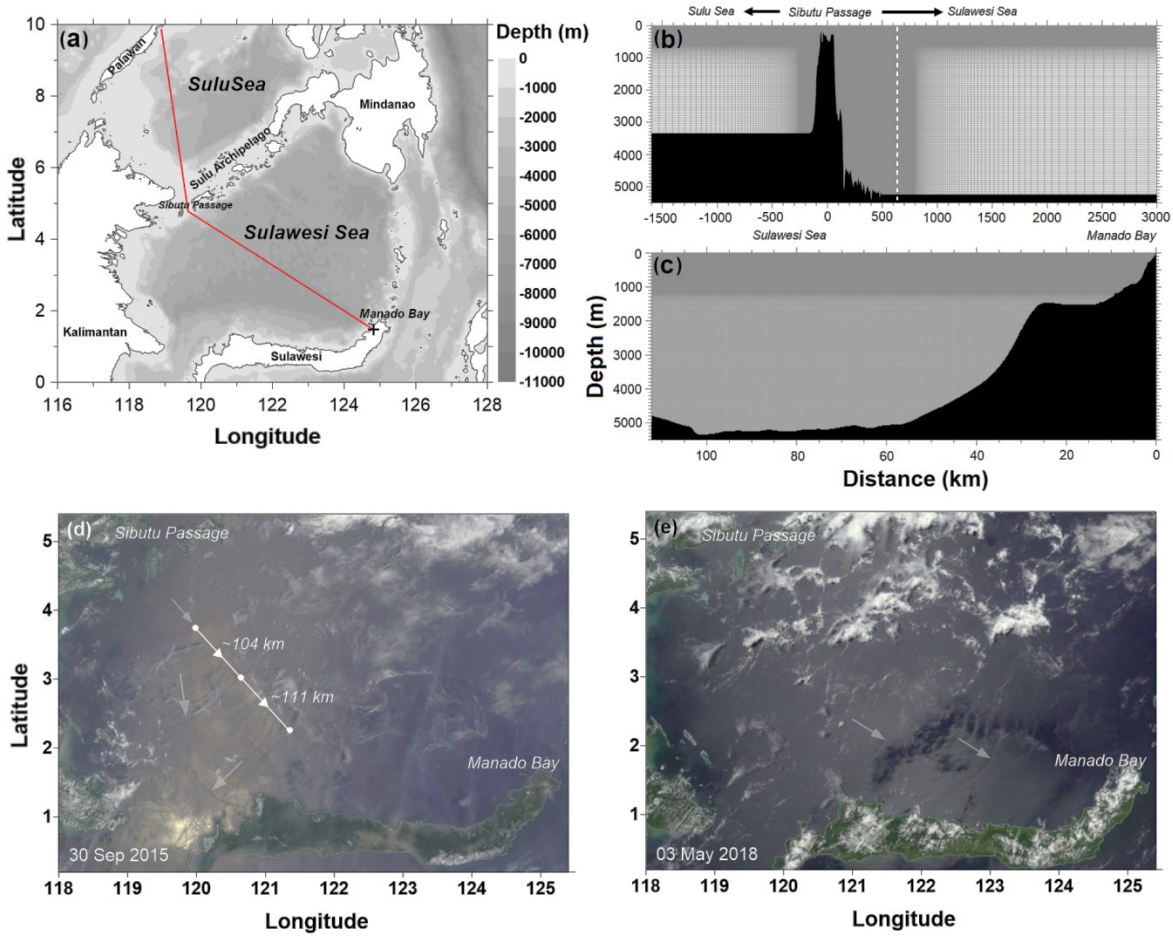

Figure 4.1 Model domain used in this study: (a) Map of simulation domain with transect (red line) from the Sulu Sea to Sulawesi Sea, crossing the Sibutu Passage. Note that such transect is used to retrieve the topography for the 2D model and does not intend to represent the direction of ISW propagation specifically. (b) The vertical grid for the ISW generation simulation which is artificially extended with low horizontal resolution on the left and the right ends in order to damp the waves and avoid reflection in the domain. The expected Manado Bay position is marked with a white vertical dashed line. This transect corresponds with the red line in (a). (c) The ISW shoaling simulation grid setting. The density of the gray lines in (b) and (c) depicts the spatial grid resolutions. (d, e) Satellite images, taken on September 30th, 2015 (https://zoom.earth/) and May 3rd, 2018 (https://worldview.earthdata.nasa.gov), respectively, are used here to estimate the distance between the trains of ISW (indicated by grey arrows), the white dots in (d) mark the leading ISWs.

4.2.2 Numerical modeling

Aestus

Idealized two-dimensional numerical simulations were performed for further insights on the in-situ measurements and for qualitative insights of the internal tide and ISW spatial structures. The two-dimensional non-hydrostatic model of Bourgault and Kelley (2004), *Aestus,* was chosen.

Two sets of simulations were performed. Firstly, we simulated the generation of internal tides by the barotropic tidal flow over the Sibutu Sill and their subsequent degeneration into trains of ISW as they propagate away from their generation site. This simulation had sufficient resolution to resolve internal tides and ISW over the entire domain length but was too coarse to resolve ISW breaking. The most likely ISWs generation site being over Sibutu Passage (see **Figure 4.1**.d, e) the bottom topography of this passage was chosen for the generation simulation. A second higher resolution simulation was performed in order to simulate the deformation and breaking of a train of ISW propagating over the Manado Bay shelf. The output of the first simulation was used as an initial condition for the second high-resolution simulation. Briefly, the model solves the laterally averaged momentum equations:

$$\frac{\partial u}{\partial t} + u\frac{\partial (\mathrm{u})}{\partial x} + w\frac{\partial (u)}{\partial z} = -\frac{1}{\rho_0}\frac{\partial p}{\partial x} + \frac{1}{B}\left[\frac{\partial}{\partial x}\left(B\nu_h \frac{\partial u}{\partial x}\right) + \frac{\partial}{\partial z}\left(B_\nu \frac{\partial u}{\partial z}\right) - C_D u|u|\right] \tag{4.1}$$

$$\delta\left[\frac{\partial w}{\partial t} + u\frac{\partial (w)}{\partial x} + w\frac{\partial (w)}{\partial z}\right] = -\frac{1}{\rho_0}\frac{\partial p}{\partial z} + \frac{\rho}{\rho_0}g + \frac{\delta}{B}\left[\frac{\partial}{\partial x}\left(B\nu_h \frac{\partial w}{\partial x}\right) + \frac{\partial}{\partial z}\left(B\nu_v \frac{\partial w}{\partial z}\right)\right] \tag{4.2}$$

along with the continuity equation

$$\frac{\partial Bu}{\partial x} + \frac{\partial Bw}{\partial z} = 0 \tag{4.3}$$

the depth-integrated continuity equation

$$\frac{\partial \eta}{\partial t} = -\frac{1}{B|_{z=0}}\frac{\partial}{\partial x}\int_{-\eta}^{H} Bu\, dz \tag{4.4}$$

and for the tracer (we use density as the tracer) equation

$$\frac{\partial \rho}{\partial t} + \frac{\partial (u\rho)}{\partial x} + \frac{\partial (w\rho)}{\partial z} = \frac{1}{B}\left[\frac{\partial}{\partial x}\left(BK_h \frac{\partial \rho}{\partial x}\right) + \frac{\partial}{\partial z}\left(BK_v \frac{\partial \rho}{\partial z}\right)\right] \tag{4.5}$$

The notations are the followings: t is time; x and z are the horizontal and vertical coordinates, respectively, with its origin at the undisturbed sea surface and positive downward; $u(x, z, t)$ is the horizontal velocity component; $w(x, z, t)$ is the vertical velocity (positive upward); $p(x, z, t)$ is the pressure; ϱ_0 is a constant reference density; $\varrho(x, z, t)$ is the seawater density; $B(x, z)$ is the width of the model domain; g is gravity; $\nu_h(x, z, t)$, $\nu_v(x, z, t)$, $K_h(x, z, t)$ and $K_v(x, z, t)$ are coefficients of eddy viscosity and diffusivity, respectively; and $C_D(x, z)$ is a drag coefficient for quadratic bottom friction along the cross-section. The simulation is forced by prescribing the tidal surface elevation upstream of the Sibutu Passage:

$$\eta = \eta_t \sin(\omega t + \theta) \tag{4.6}$$

where ω is the tidal frequency; θ is the initial phase; η_t is the tidal elevation amplitude.

Model Configuration

Sea surface elevation in the Sulu Sea is provided by TPXO8-atlas with $1/30^o$ resolution, generated by Oregon State University tidal inversion software (OTIS). OTIS solves the astronomical tide equations and assimilates observations from tide gauge and TOPEX/Poseidon altimetry using a global inverse model (Egbert and Erofeeva, 2002). The barotropic tides in the southeastern part of the Sulu Sea at 119.5 E, 6.5 N; 3362 m depth are predicted using eight principal tidal constituents.

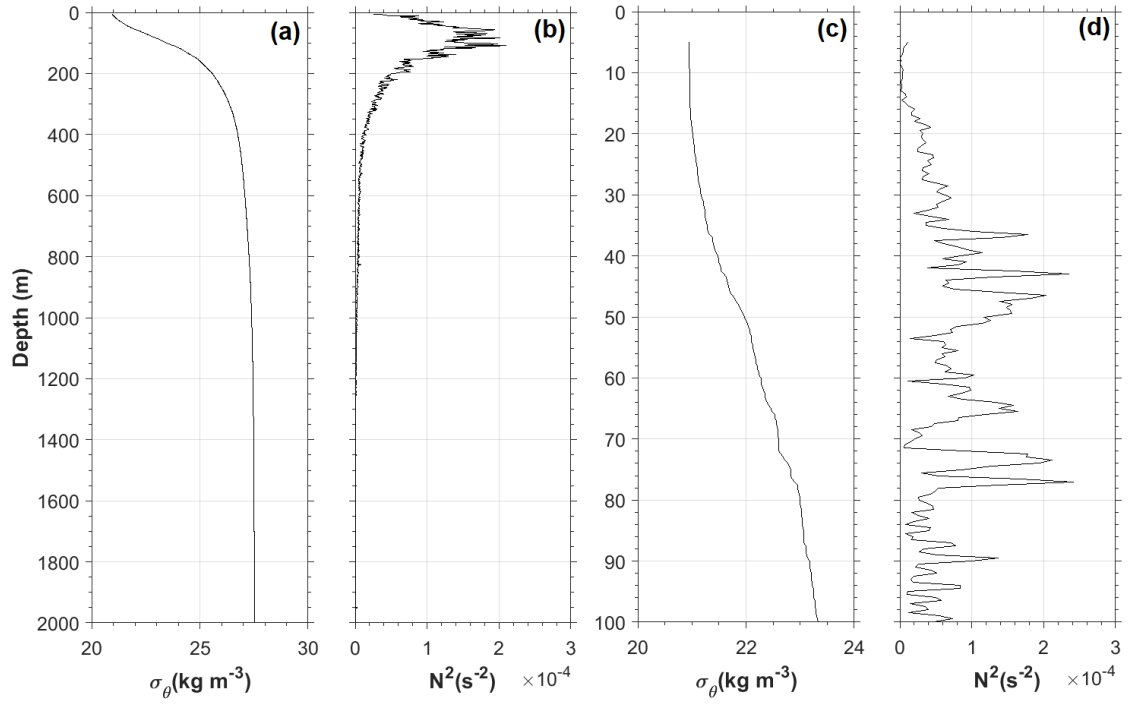

Figure 4.2 (a) Mean density and (b) mean squared-buoyancy, derived from 70 CTD casts observed in various cruises in the Sulawesi Sea region from various season used in the simulation. (c) Average density and (d) squared-buoyancy profiles measured on 12-13 May 2009 in Manado Bay.

The initial density field used in the simulations is uniform on the horizontal and is built from an average profile of 70 CTD profiles sampled in the Sulawesi Sea. The dataset is provided by the historical dataset of the Research Center for Oceanography (RCO) LIPI. The density field and squared buoyancy frequency profile used in this simulation, as well as the observed density and buoyancy profiles in the Manado Bay, are shown in **Figure 4.2**.

For the generation simulation, horizontal turbulent diffusion is parameterized using the Smagorinsky scheme (Smagorinsky, 1963) as:

$$v_h = \begin{cases} (C_s \Delta x)^2 \sqrt{2S^2 - N^2}, & \text{if } 2S^2 \geq N^2 \\ 10^{-6}\ m^2 s^{-1}, & \text{otherwise} \end{cases} \quad (4.7)$$

where Δx is the horizontal grid size, S^2 is the square of the strain rate tensor (see appendix in Bourgault and Kelley (2004) for details), $N^2=(g/\rho_0)\partial\rho/\partial z$ is the buoyancy frequency and C_s = 0.1 is the Smagorinsky coefficient. The vertical eddy viscosity v_v is parameterized in the same way except that the vertical grid size Δz is used as the relevant length scale. Similar expressions are used for the eddy diffusivities K_h and K_v except that the minimum values are set to 10^{-7} m^2s^{-1} if $2S^2 \leq N^2$. For the high-resolution simulation, there was no parameterization but rather an implicit numerical diffusion resulting from truncation errors. No-flux boundary conditions are applied perpendicular to solid boundaries and to the sea surface. The bottom stress is discretized in a way such that it converges towards the no-slip condition for $\Delta z \rightarrow 0$, using the quadratic stress formulation from the law of the wall, i.e.

$$\tau_c/\rho_0 = \nu_v \left.\frac{\partial u}{\partial z}\right|_{z=H} = -C_D |u_b| u_b \quad (4.8)$$

where τ_c= 0.1 Pa is the critical shear stress and

$$C_D = \left(\frac{\kappa}{\ln[(\Delta z/2)/z_0]}\right)^2 \quad (4.9)$$

is the drag coefficient, u_b is the horizontal velocity in the bottom cell, z_0= 1 x 10^{-3} m is bottom roughness length and κ = 0.41 is the Von Kármán constant.

We set the grid resolution as fine as possible in the limit of reasonable computation time. The domain size of the generation experiment is Lx x Lz = 247303 km x 5240 m, with resolution nx x nz = 2993 x 235 (see **Figure 4.1**.b) and open boundary conditions. Note that the valid domain considered in the generation experiment is between -200 km, in the Sulu Sea part, to +737 km in the Sulawesi Sea part. In the rest of the domain, the horizontal resolution rapidly decreases which dampens the waves and act as sponge layers. In the valid domain [-200≤x≤737] km, the resolution is uniform in the x-direction, where Δx = 350 m; and decreases asymptotically to Δx = 67 km at x=-1566 km and to Δx = 10000 km at x=245737 km. The vertical grid size is fixed and set to Δz = 5 m at [2.5≤z≤502] m for the whole domain and decrease gradually to Δz = 50 m at [502<z≤1415] m, and a constant Δz = 50 m below. The domain size of the shoaling experiment is Lx x Lz = 120 km x 5831 m, with resolution

nx x nz = 3151 x 715 (see **Figure 4.1**.c) and open boundary conditions. The resolution is non-uniform in the x-direction where Δx = 2 m at [0≤x≤5] km, decrease asymptotically its resolution, Δx = 2-200 m at [5<x≤9] km, and a constant Δx = 200 km at x>9 km. The vertical grid size is fixed for the whole domain, with increasing asymptotically Δz = 5 to 2 m at [2.5≤z≤60] m, a constant of Δz = 2m at [60<z≤1000] m, decreasing asymptotically Δz = 2 to 25 m at [1000<z≤1457] m, a constant Δz = 25 m below.

We ensured that the physical dispersion is well reproduced by the model. The horizontal grid spacing required for a proper resolution of non-hydrostatic effects is such that $\Delta x<h_1$ where h_1 is the depth of the internal interface, defined as the depth of the velocity node for the first vertical mode (see https://woodshole.er.usgs.gov/operations/sea-mat/klinck-html/dynmodes.html). When this condition is not satisfied, numerical dispersion overwhelms physical dispersion (Vitousek and Fringer, 2011). Using the mean buoyancy profile as shown in **Figure 4.2**.c, d; with h_1= 667 m and 50 m for generation and deformation simulation, respectively. The grid *leptic* ratio, $\lambda=\Delta x/h_1$, was within [0.008-0.08] and of [0.04-0.5] for the generation and deformation simulations, respectively; ensuring negligible numerical dispersion, $\lambda<O(1)$, and relevant non-hydrostatics effects.

The periodic appearance of the ISWs formed over the Sibutu Passage suggests a generation mechanism driven by the tidal current of the semi-diurnal period in the Sulu Archipelago (Apel et al., 1985) and over the Sibutu Passage (Kartadikaria et al., 2011). The comparison between the simulated barotropic currents and the OTIS currents over the sill is shown in **Figure 4.3**. u component of the current in the model corresponds to the current along the major tidal axis and is much larger than the v component along the minor tidal axis. We display in **Figure 4.3** $U_{sim}=u_{sim}$ neglecting the minor v component. For further analysis, we will only use U_{sim} for both the generation and shoaling simulations. In order to test the relevance of the modeled current, U_{sim} is compared with the OTIS velocity U_{OTIS} component projected along the major axis.

As shown in **Figure 4.3**, U_{sim} fits well with U_{OTIS} reproducing notably the diurnal inequality resulting from the superposition of a dominant semi-diurnal and a sub-dominant diurnal forcing with a ratio of current amplitude, $(U_{M2}/U_{K1})_{OTIS}$ ~ 2.5. The RMS difference calculated over 24 and 48 hours simulations yield 0.065 and 0.067 m s^{-1}, respectively; and the relative error calculated as a ratio between RMS difference to signal $\sqrt{U^2_{OTIS}/2}$, where U_{OTIS}= 0.35 m s^{-1}, yields 26-27%; indicating that our simulation setting is satisfactorily reproducing the barotropic velocity over the sill.. The background mean current of the Sibutu

throughflow was not taken into account in this study. Note that the passage is an important passage regarding the Indonesian throughflow (ITF) transport (Gordon et al., 2012; Qu and Song, 2009) and the background currents may affect the internal tide generation and propagation characteristics (see the study by Aiki et al., 2011; Matthews et al., 2011 in Lombok Strait).

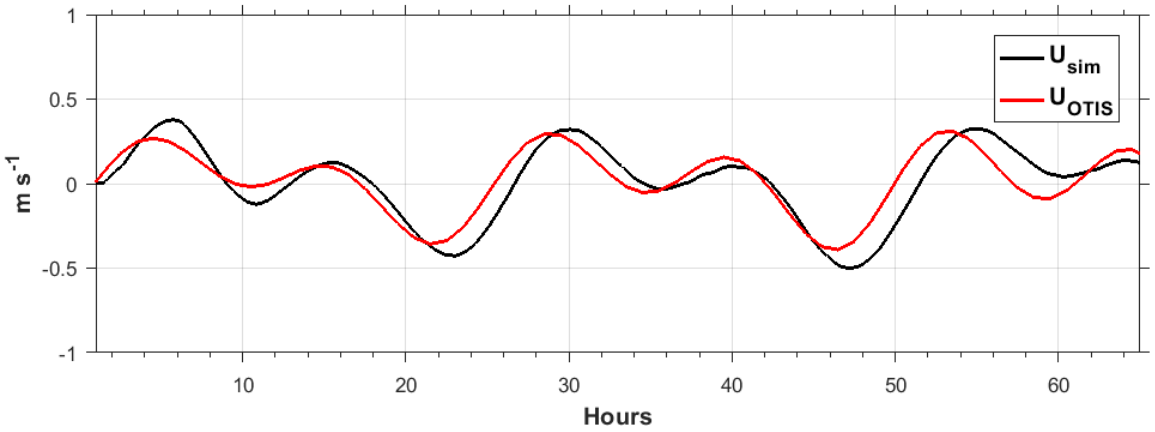

Figure 4.3 Comparison between zonal and meridional model-perspective barotropic currents (depth averaged current, black plots) over the Sibutu Passage from Gen simulation with zonal and meridional current component predicted by OTIS (red plots) at 119.8420 E, 5.4125 N. Note that, the term of zonal and meridional currents in the model is different to the three dimensional perspective, as described in the text.

Several ISWs were generated in the generation simulation. The second ISW packet parameters (velocities, amplitude, width, phase speed) was taken as the initial condition for the ISW of the shoaling simulation. The density and velocities corresponding to this ISW train were re-interpolated on the finer grid of the shoaling simulations.

4.2.3 Mixing estimates

Mixing estimates are based on density overturns following the method initially proposed by Thorpe (1977) and extended by Dillon (1982). The first stage of the method consists in computing the typical vertical extension of density overturns, referred to as Thorpe length scale, L_T, following Thorpe (1977). Thorpe displacements are first computed by reordering the density profile into a stable density profile the Thorpe scale is defined as the standard deviation of Thorpe displacement within the overturn:

$$L_T = \left(\frac{1}{n} \sum_{i=1}^{n} d_i^2 \right)^{1/2} \tag{4.10}$$

where n refers to the number of fluid parcels within the overturn and d_i to the Thorpe displacement of fluid parcel i. Dissipation rate ε is next inferred by assuming that the available potential energy associated with density overturns, $1/2\ L_T^2 N_{sorted}^2$, provides an upper bound for turbulent kinetic energy, ε/N, with $1/N$ as typical time scale; $N^2=g(d\varrho/\mathrm{d}z)/\varrho_0$ is the squared buoyancy frequency. This is equivalent to assume that Thorpe scale, L_T, and Ozmidov scale, L_o are proportional, with $L_o=\varepsilon^{1/2}N^{-3/2}$ (Ozmidov, 1965). L_O/L_T was fixed to the mean value, 0.8; obtained by Dillon (1982), leading to the following expression for ε :

$$\varepsilon_{Thorpe} = 0.64 L_T^2 N^3 \tag{4.11}$$

The computation of Thorpe scale is sensitive to the noise level threshold and this issue is addressed in an appendix with details on the different criteria applied to eliminate spurious overturns.

The Thorpe scale method provides ε estimates where density overturns are detected. As a result, the statistics of ε is biased toward high values when no assumption is made for the main part of the water column where no density overturns are detected. It is necessary to provide a background dissipation rate where no overturns are detected. We introduce a setting for the background dissipation rate as $\varepsilon_{background} = \max(\varepsilon_{Overturn\text{-}background}, \varepsilon_{GM\text{-}background})$ where $\varepsilon_{Overturn\text{-}background}$ is the minimum resolvable dissipation rate by the CTD sensors, and $\varepsilon_{GM\text{-}background}$ is the Garrett and Munk dissipation rate. We set $\varepsilon_{Overturn\text{-}background}$ of 1 x 10^{-10} m^2s^{-3} as it has been used generally by previous authors (Alberty et al., 2017; Cuypers et al., 2017b; Frants et al., 2013; Koch-Larrouy et al., 2015). For the $\varepsilon_{GM\text{-}background}$ we assume that this background value follows the typical dissipation rate associated with Garret and Munk (hereinafter, GM) wave field (Garrett and Munk, 1975), given by the fine-scale parameterization for internal waves:

$$\varepsilon_{GM-background} = \varepsilon_0 \left(\frac{N^2}{N_0^2}\right)\left(\frac{S_{10}^2}{S_{GM}^2}\right) j(f/N) \tag{4.12}$$

where ε_0 = 6.7x10^{-10} m^3s^{-3} is the canonical Garret and Munk (hereinafter GM) dissipation rate at latitude 30°, N_0 = 2πx3 rad s^{-1} is the canonical GM buoyancy frequency and $j(f/N)$=f acosh$(N/f)/f_{30}$ acosh(N_0/f_{30}) is the latitudinal dependence, where f_{30} is the Coriolis parameter at 30°. We assume that the local shear variance S_{10}^2 is equal to the canonical shear variance S_{GM}^2. Working in the near equatorial zone, we found the term $j(f/N)$ results in unrealistically dissipation rate in the -1°<latitude <1° band. This discrepancy is likely due to the fact that the GM field assumes a wave field at equilibrium feed at low frequency by inertial waves while the main source of low frequency energy is the internal tides in the Indonesian seas. Hence, we set

this term to be unity to avoid large discrepancy in the near equator stations. The background ε thus verifies:

$$\varepsilon_{GM-background} = \varepsilon_0 \left(\frac{N^2}{{N_0}^2}\right) j(f/N) \tag{4.13}$$

Mixing properties were also characterized by the turbulent diffusion, which is usually expressed as a function of the turbulent buoyancy flux, B: $B = K_\rho N^2$. This turbulent buoyancy flux is related to the dissipation rate through the mixing efficiency Γ, i.e. $B = \Gamma\varepsilon$; so that the turbulent diffusion coefficient is expressed as $K_\rho = \Gamma\varepsilon N^{-2}$.

One issue recently addressed is whether mixing efficiency could be assumed constant, equal to 0.2, following Osborn (1980). Recent studies (e.g. Bouffard and Boegman, 2013; Ivey et al., 2008) rather suggested that Γ decreases for strongly turbulent regimes and that the Osborn value overestimates turbulent diffusion in this case. The turbulent regimes can be determined from the turbulence intensity parameter Re_b, which is the ratio between the destabilizing effect of turbulence to the stabilizing effect of stratification and viscosity (Ivey et al., 2008) as:

$$Re_b = \frac{\varepsilon}{\nu N^2} \tag{4.14}$$

with ν = 1.2 x 10^{-6} $m^2s^{-1}$the seawater viscosity.

Bouffard and Boegman (2013) proposed a formulation of K_ρ for four different regimes defined as a function of Re_b: *an isotropic energetic* regime for Re_b >400, a *transitional* regime, where the stratification starts to affect the isotropy, for 8.5 < Re_b < 400 and a buoyancy controlled regime for which the amount of reversible buoyancy flux is a function of *Pr*, for 1.7 < Re_b < 8.5 and a *molecular* regime when the turbulent diapycnal flux tends to zero, for Re_b <1.7; giving K_ρ dependence as

$$K_\rho = 4\nu {Re_b}^{1/2} \tag{4.15}$$

In the transitional regime, i.e. 8.5 < Re_b < 400; K_ρ is valid as Osborn (1980) model:

$$K_\rho = 0.2\nu Re_b \tag{4.16}$$

In the buoyancy control regime, i.e. $1.7 < Re_b < 8.5$; the amount of reversible buoyancy flux is a function of *Pr*. With $Pr = 7$, then K_ρ is following the model:

$$K_\rho = \frac{0.1}{7^{1/4}} \nu Re_b{}^{1/2} \tag{4.17}$$

We also estimate K_ρ using the Bouffard and Boegman (2013) formula to be compared with the Osborn (1980) formula.

The Thorpe method was also applied to the numerical simulations for which the large turbulent overturns are well resolved and not smoothed out by high numerical diffusion following (Klymak and Legg, 2010). These criteria are met for our shoaling simulations where the ~2 m grid resolution in both vertical and horizontal is much smaller than the typical large overturns of ~10 m scale and where the numerical dispersion is very low as indicated by low *leptic* ratio.

4.3 Internal Tides Generation

4.3.1 Generation processes

The barotropic tidal current over the shallow topography of the Sulu Archpelago triggers propagating internal tides in the Sulu and Sulawesi Seas. Both northwestward and southeastward propagating waves, respectively, emanated from the Sulu Archipelago are frequently visible by satellite images. In the Sulu Sea, as those long waves propagate, a steepening pattern due to nonlinearity effects is frequently observed (Apel et al., 1985; Liu et al., 1985). Far away from its generation site, in the southeastern most of the Sulawesi Sea, some MODIS images (see **Figure 4.1**.d, e) also confirmed the appearance of the ISW directing toward the northern coast of Sulawesi Island and ended up in the Manado Bay, pointing out that such features frequently happen in Manado Bay. Actually, the satellite images can either show ISW pointing to the northwestern, north central or northeastern (Manado sector). This variability is likely resulting from the refraction of the ISW by strong currents in the Sulawesi Sea, a feature that would disserve more investigation in the future. Here we have simply assumed in our model a direct propagation from the generation site toward the Manado Bay.

As shown in **Figure 4.4**, a semidiurnal pattern is clearly observed over the Sibutu Passage. The oscillating barotropic tidal current generates alternatively waves of depression toward the Sulu Sea and the Sulawesi Sea. After a few tidal period, waves beams build up suggesting that the wave generation fall in the classical internal tide regime (St. Laurent and Garrett, 2002) and that the subsequent fission of this internal tides generates the observed ISWs, as is investigated in the following.

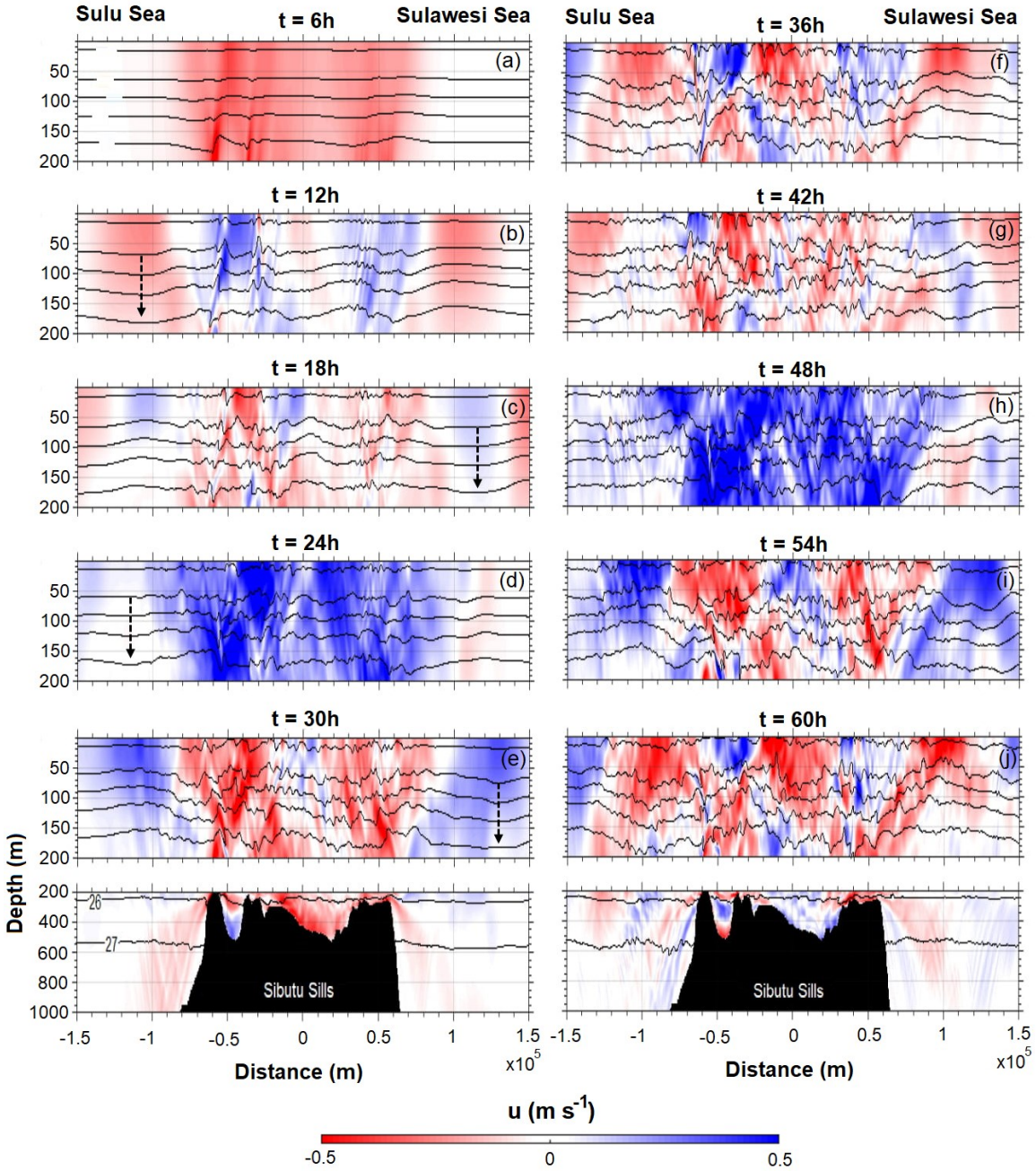

Figure 4.4 Isopycnal contours overlaid upon zonal current (see the colorbar for the magnitude and direction), started since six hours of the simulation over the Sibutu Sills. Zero distance is centered at Sibutu Passage sill; the seas of Sulu and Sulawesi are on the left and the right sides of the sill, respectively. Dashed arrows indicate the appearance of wave of depressions.

The mechanism of ISWs formation, whether through a lee wave mechanism or through nonlinear evolution of the internal tide, is next examined. Possible lee wave mechanism was first addressed by computing the Froude number, *Fr,* over the sills. *Fr* was estimated using the mean amplitude of the barotropic current and the mean stratification inferred from the Sulu Sea database (https://www.nodc.noaa.gov/OC5/WOD/pr_wod.html). With a mean barotropic current

amplitude of ~0.38 m s^{-1} and a mode-1 phase speed of 0.96 m s^{-1} the flow was found to be subcritical with Fr = 0.39 (<1) hence excluding possible quasi-steady lee wave mechanism for ISWs generation (Maxworthy, 1979). In the meantime, the excursion parameter kU_0/ω, which represents the excursion of a fluid particle relative to the horizontal scale of the bathymetry ($2\pi/k$) is typically of order 0.2, considering a sill width of ~100 km, which also excludes upstream propagating lee wave generation. The occurrence of ISWs is most often related to the internal tide phase, supports the hypothesis of generation through nonlinear effects leading to waves of depression in the pycnocline. The temporal-spatial plots of the density, zonal and vertical currents as shown in **Figure 4.5** indicates the growing of nonlinearity accompanying the propagation of the internal tides away from the Sibutu Passage. First, it can be noticed that the signal separates between a lower mode-1 propagating faster and higher modes with slower propagation (**Figure 4.5**.c). Then, starting from ~300 km the lower mode splits into a sequence of ISW.

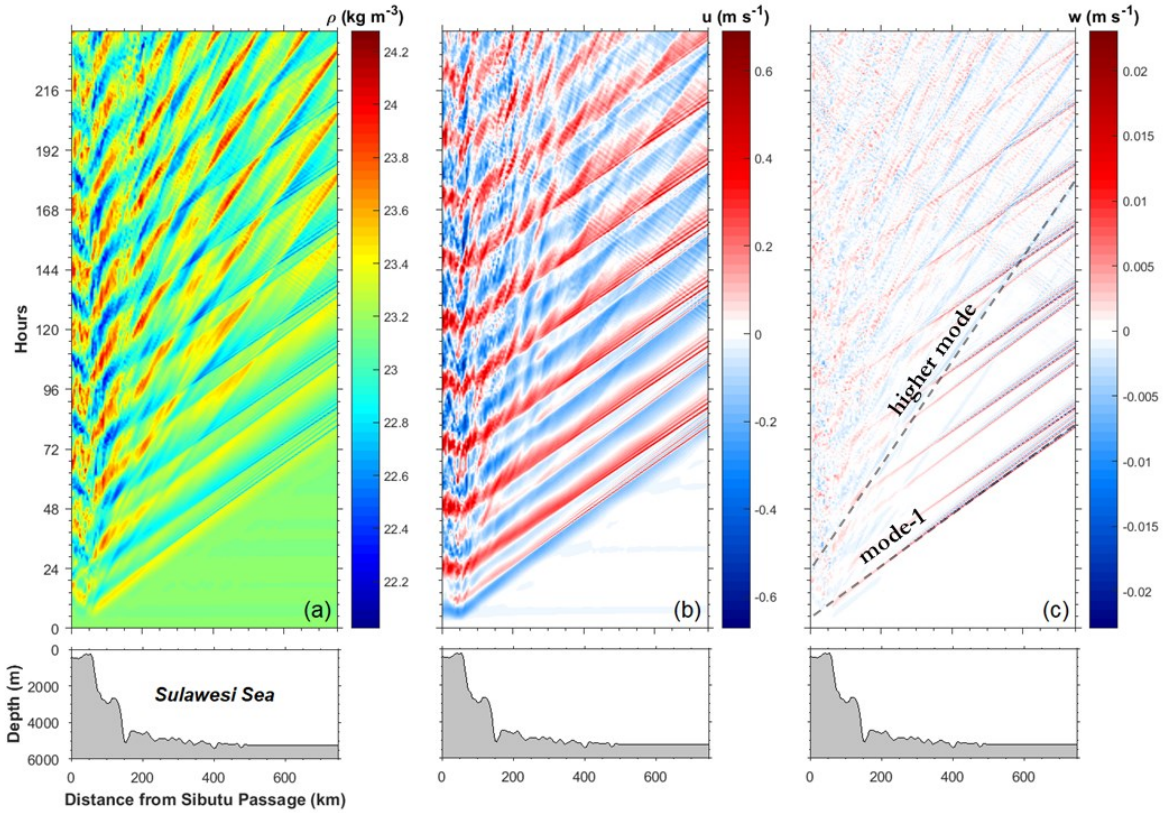

Figure 4.5 The temporal-spatial plots at 100 m depth (~the core of pycnocline layer) of the: (a) isopycnal displacements, (b) zonal currents and (c) vertical currents. The corresponding bottom topography is shown in the lowest panel with zero distance is located at the center of Sibutu Passage.

ISW packets are generated with a semi-diurnal period occurrence in the simulations. The formation and propagation of the first ISW packet in the Sulawesi Sea is evidenced in **Figure 4.6** with the time-space evolution of the 22.5 isopycnal in the pycnocline. The propagation speed, inferred from the travel time of the first leading wave is around ~2.7 m s^{-1}, which compares well with the estimated value by Jackson (2007) via satellite image, 3.0 m s^{-1}. The distance between two leading ISW packets is around 86 km, which is also close to the estimated distance as shown in **Figure 4.1**.d, e. The typical horizontal scale of each ISW is of about 10 km (**Figure 4.6**, at t = 84 h). One can notice the modulation of the ISW train wave packet with the diurnal period: one ISW wave packet of maximum amplitude is observed every diurnal period, which is consistent with the modulation of the M2 internal tide by the K1 diurnal tide. This typical ISW is about the same as the one observed in the South China Sea (Ramp et al., 2004).

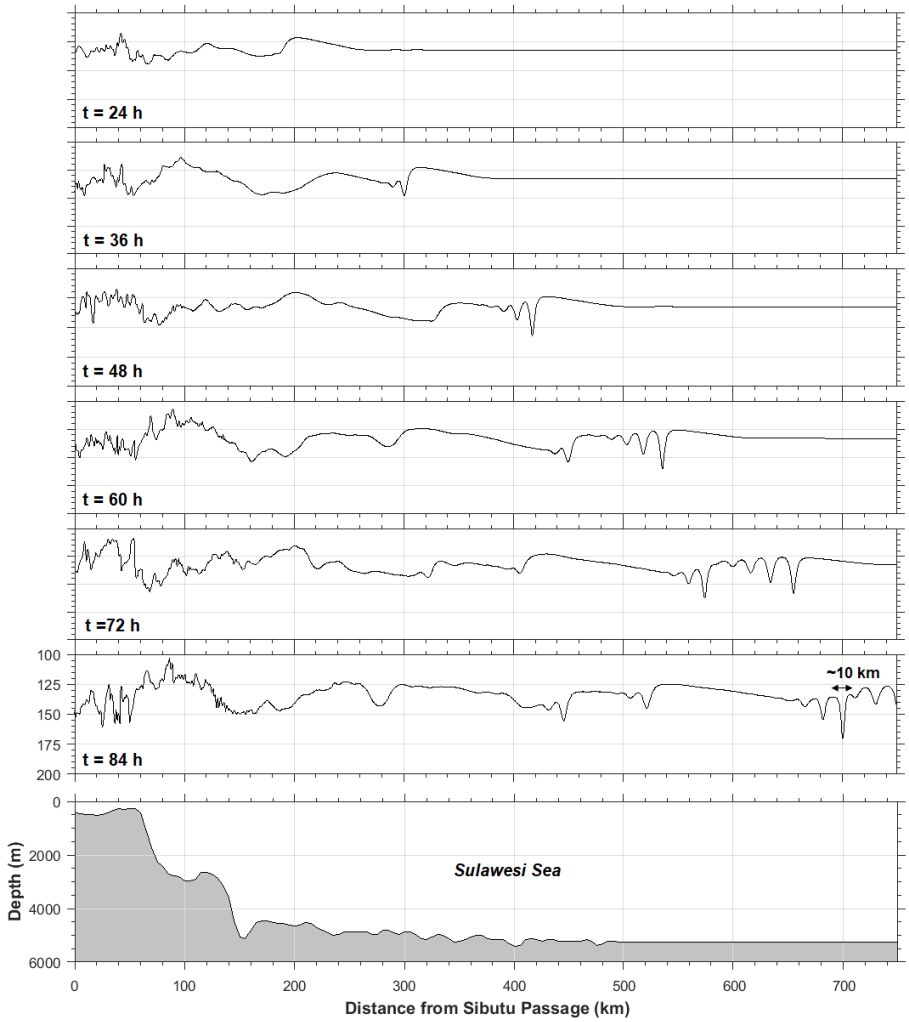

Figure 4.6 The six hours temporal spacing evolution, started from t=24 h (first panel) to t=84 h (lowest panel) of the σ_θ = 22.5 isopycnal displacement from the generation simulation (central Sibutu Passage, left side 0 km), crossing the Sulawesi Sea towards Manado Bay located in the right side. Double heads arrow at t = 84 h indicates the wavelength of the leading ISW.

4.3.2 *Energetic aspects*

The depth integrated energy flux was computed along the section (Alford and Zhao, 2007; Garcia Lafuente et al., 1999; Lamb and Nguyen, 2009; Nash et al., 2005) based upon the general formulation:

$$\overline{F_E}(x) = \frac{1}{\tau}\int_0^{\tau}\int_{-H}^{0}(u'p' + u'Ek + u'Ea)\,dz\,dt \tag{4.18}$$

where τ is an integer number of tidal periods. The term $u'p'$ is pseudo energy flux due to pressure perturbance, a contribution of internal tide (baroclinic) to total pressure field; $u'Ek$ and $u'Ea$ is the kinetic energy flux and potential energy flux, respectively. Practically, we apply Eq. (4.18) for three wave fields, i.e. the total, low frequency/tidal and high frequency/ISW. The ISW energy flux is estimated with the wave propagation speed of 2.7 m s^{-1} and a high pass filter period of <4 hours for the density and currents fields; the M2 energy flux is estimated with a low pass filter period of >6 hours; while the total energy flux is estimated directly without any filter applied.

The perturbation velocity u', is defined as

$$u'(z,t) = u(z,t) - u'(z) - u_o'(t) \tag{4.19}$$

$u(z,t)$ is the modeled velocity, $u'(z)$ is the time mean of velocity, and $u_o'(t)$ is determined by considering baroclinity

$$\frac{1}{H}\int_{-H}^{0} u'(z,t)dz = 0 \tag{4.20}$$

The pressure anomaly $p'(x, z, t)$ is calculated from the density anomaly using the hydrostatic equation

$$p'(x,z,t) = p_{surf}(x,t) + g\int_z^0 \rho'(x,z',t)\,dz' \tag{4.21}$$

The constant of integration in Eq. (4.21), namely the pressure perturbation at the surface pressure $p_{surf}(t)$, cannot be inferred from the baroclinity condition, prescribing that the depth-averaged pressure perturbation must vanish (Gerkema and Van Haren, 2007) which is only strictly valid for a flat bottom. However, this constant of integration is not required here since we are interested in the depth integrated energy flux, which does not depend on this constant.

$$p_{surf}(t) = \frac{1}{H}\int_{-H}^{0} p'(z,t)dz = 0 \tag{4.22}$$

The density anomaly is estimated as

$$\rho'(z,t) = \rho(z,t) - \rho'(z) \tag{4.23}$$

$\rho'(z)$ is the time averaged density profile.

The kinetic energy is calculated by:

$$Ek = \frac{1}{2}\rho_0(u^2 + w^2) \tag{4.24}$$

The potential energy density per unit length is calculated by:

$$Ea = \frac{1}{2}\rho_0 N^2 \zeta^2 \tag{4.25}$$

where ζ is the isopycnal vertical displacement, defined as $(\bar{\rho} - \rho)/\, d\rho/dz$, with $\bar{\rho}$ is the mean density profile that corresponds to the state of minimum potential energy and ρ is the density profile.

The different terms of the energy flux are referred to as F_p; F_{Ek} and F_{Ea} for the pressure, kinetic and available potential energy fluxes, respectively. Time filtering was also applied to infer the baroclinic tidal flux as well as the high frequency contribution of ISWs. A low-pass filtering with a 1/6 h frequency cut-off was applied to the velocity, density and pressure perturbations to compute the baroclinic tidal energy flux while a high-pass filtering with a 1/4 h cut-off frequency was applied to compute the ISWs energy flux. The time-space evolution of pressure, kinetic and available potential energies fluxes and its depth integrated over 5TM2-15TM2 period is displayed in **Figure 4.7** and **Figure 4.8**, respectively. Pressure fluxes are by far the largest, with instantaneous values reaching a few tenths kW m^{-1}, compared to E_k and E_a fluxes. The ISW energy fluxes become significant at about 300 km away from the generation site and around 12 hours after the internal tide generation at the center of the Sibutu Passage (see also **Figure 4.6**). This supports our previous suggestion that the ISWs formation are formed due to non-linear effects, as shown in **Figure 4.8** (third panel).

In order to quantify precisely the energy fluxes evolution as the internal tide propagates away from its generation site, we inspect the time-averaged energy fluxes over 10 semi-diurnal tidal periods, within [5:15] TM2, at several locations (see **Table 4.2**). The time-averaged total energy flux is of about 15 kW m^{-1} in the generation area. Consistently, the energy flux of the tidal component is close to the total energy flux in this area. As the internal tide propagates away, we observe a continuous decrease of the energy flux leading to a 50%

decrease at 700 km away from the Sibutu Passage. This decrease is correlated with the increase of the ISW depth-integrated energy flux at 700 km away from the Sibutu Passage, reaching a value of 3.54 kW m^{-1}, about half the tidal energy flux value. The maximum ISW energy flux is also given for comparison to provide insights on the local impact of ISW dissipation: values up to 185 kW m^{-1} are obtained, more than one order of magnitude than the time-averaged value.

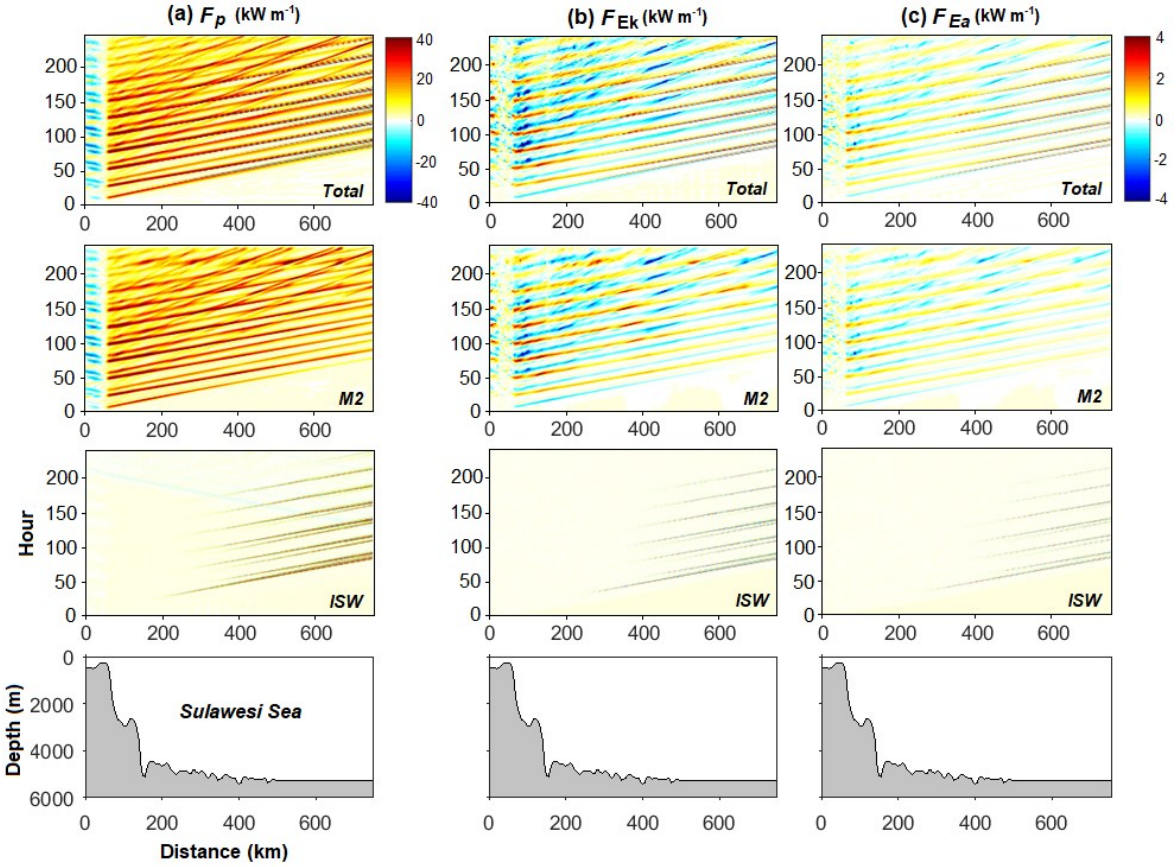

Figure 4.7 The time-space plots of depth integrated energy flux from the contribution of: (a) pressure perturbation flux, F_p=*u*'*p*'; (b) kinetic energy flux, F_{Ek}=*u*'*Ek* and (c) potential energy flux, F_{Ea}=*u*'*Ea*. The first (upper), second and third panel is the total, low frequency/tidal and high frequency/ISW components, respectively.

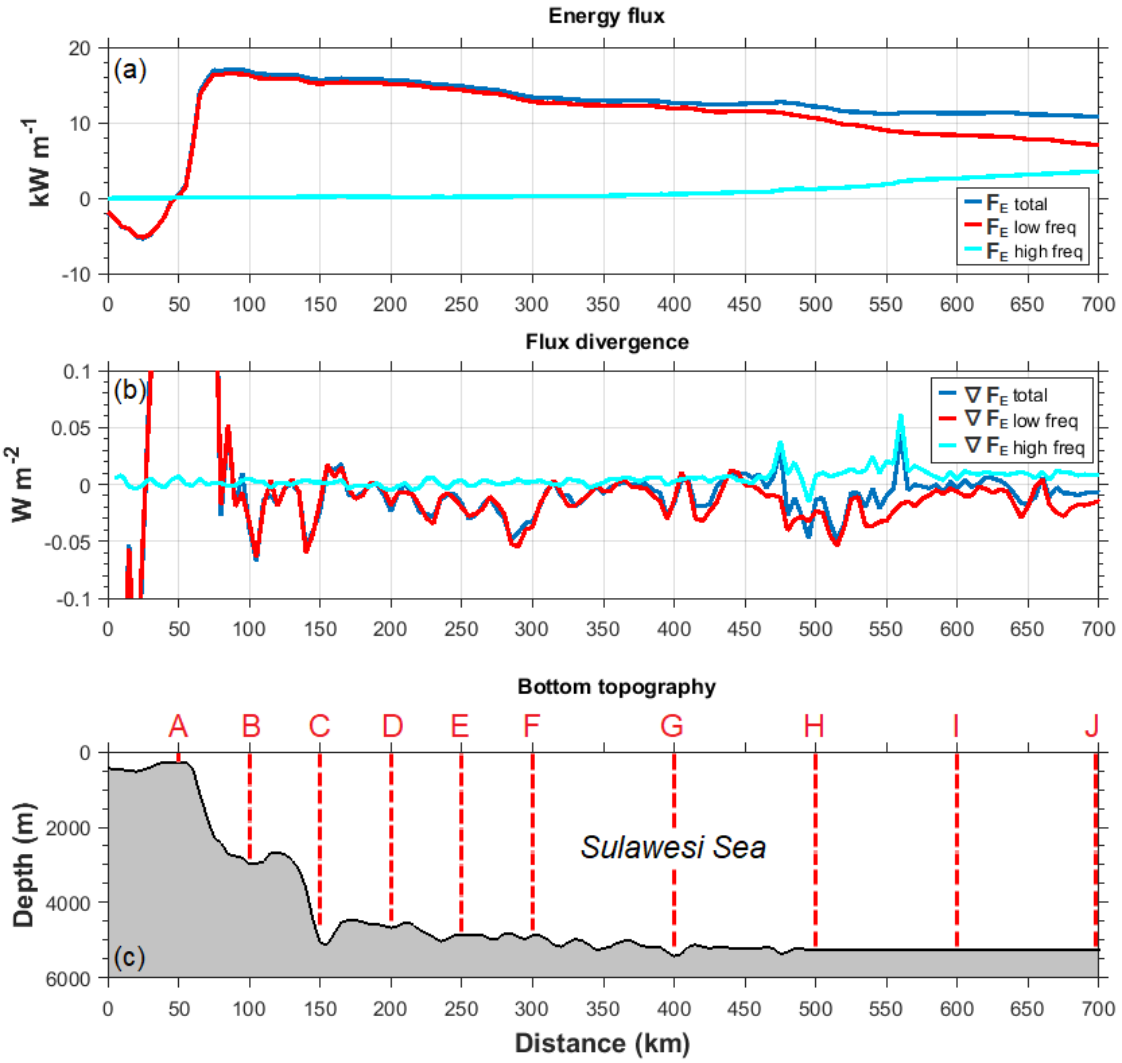

Figure 4.8 The time average (5TM2-15TM2) of (a) the depth integrated energy flux (F_E), quantified at all frequency wave field (total), low frequency (tidal) and high frequency (ISWs); (b) same as (a) but for the divergence of the fluxes, and (c) bottom topography with positions A-J denote the locations at which the average energy flux is quantified in Table 4.2.

Table 4.2 Time-averaged over [5:15] TM2 of the depth integrated total energy flux, F_E; the "low-frequency" M2 component (period larger than 6 h); and the high frequency component "ISW" (period smaller than 4h) at some locations in the Sulawesi Sea. The maximum value of the ISW energy flux is given in the last column. The reader may refer to Figure 4.8 for the locations (the lowest-left panel).

Location	Distance from the center of Sibutu Passage (km)	Depth (m)	Flux components (kW m^{-1})			
			Total	Tidal/low frequency	ISW/high frequency	
					Mean	Max
A	50	282.5	0.46	0.28	0.06	4.2
B	100	2965	16.82	16.27	0.12	4.3
C	150	5065	15.64	15.15	0.19	3.6
D	200	4665	15.57	15.11	0.15	6.3
E	250	4865	14.85	14.32	0.17	16
F	300	4865	13.36	12.75	0.24	40
G	400	5415	12.61	11.89	0.52	95
H	500	5265	12.12	10.58	1.21	119
I	600	5265	11.24	8.36	2.62	138
J	700	5265	10.78	7.02	3.54	185

Figure 4.8.a underlines the progressive growth of the ISWs energy flux at the expense of the tidal energy flux from 300 km and beyond: the ISW energy flux reaches 32% of the total energy flux while the tidal component has decreased to a value of 64% of the total energy flux. The divergence of the energy fluxes displayed in **Figure 4.8**.b provides insights on energy transfers and an upper bound for energy dissipation. As expected, the maximum energy flux divergence is observed in the Sibutu Passage (not shown) with a 1.5 W m^{-2} flux divergence, which corresponds to an average dissipation rate of $7.5\text{x}10^{-6}$ W kg^{-1} over the 200 m depth water column. In the far-field area, the flux divergence is by far smaller of maximum absolute value of the order of $5\text{x}10^{-2}$ W m^{-2}. In this area, this flux divergence mostly feeds the ISWs growth but would correspond to a significant dissipation of $1\text{x}10^{-8}$ W kg^{-1} over the 5000 m depth. Eventually, based on the maximum ISWs energy flux at 700 km one can infer an upper bound for local dissipation induced by ISW breaking: taking 10 km as the typical scale and a 200 m depth interval over which breaking occurs and typical order of density 10^{-3} kg m^{-3} one finds a dissipation of the order of $1.85\text{x}10^{5}/(200\text{x}10^{3})$ W m^{-3} ~ $9.2\text{x}10^{-5}$ W kg^{-1}. This value is of the same order of magnitude as that measured during INDOMIX cruise at Station 5 where an ISW was observed (Bouruet-Aubertot et al., 2018).

4.4 Shoaling Internal Solitary Waves

4.4.1 High frequency and small-scale patterns over the Manado shelf break and slope in the Shoaling simulation

The time evolution of vertical sections of the cross-slope current and isopycnal inferred from the shoaling simulation provides an overview of the small-scale and high frequency processes developing over the shelf break and slope (**Figure 4.9**). A 35 minutes time evolution has been chosen in order to focus on the breaking of the ISWs train and its further evolution towards the coast. The vertical structure of the cross-shore current is close to that of the first baroclinic mode, which is consistent with the ISWs generation mechanism from the fission of the first and most energetic tidal mode (**Figure 4.9**.a and b).

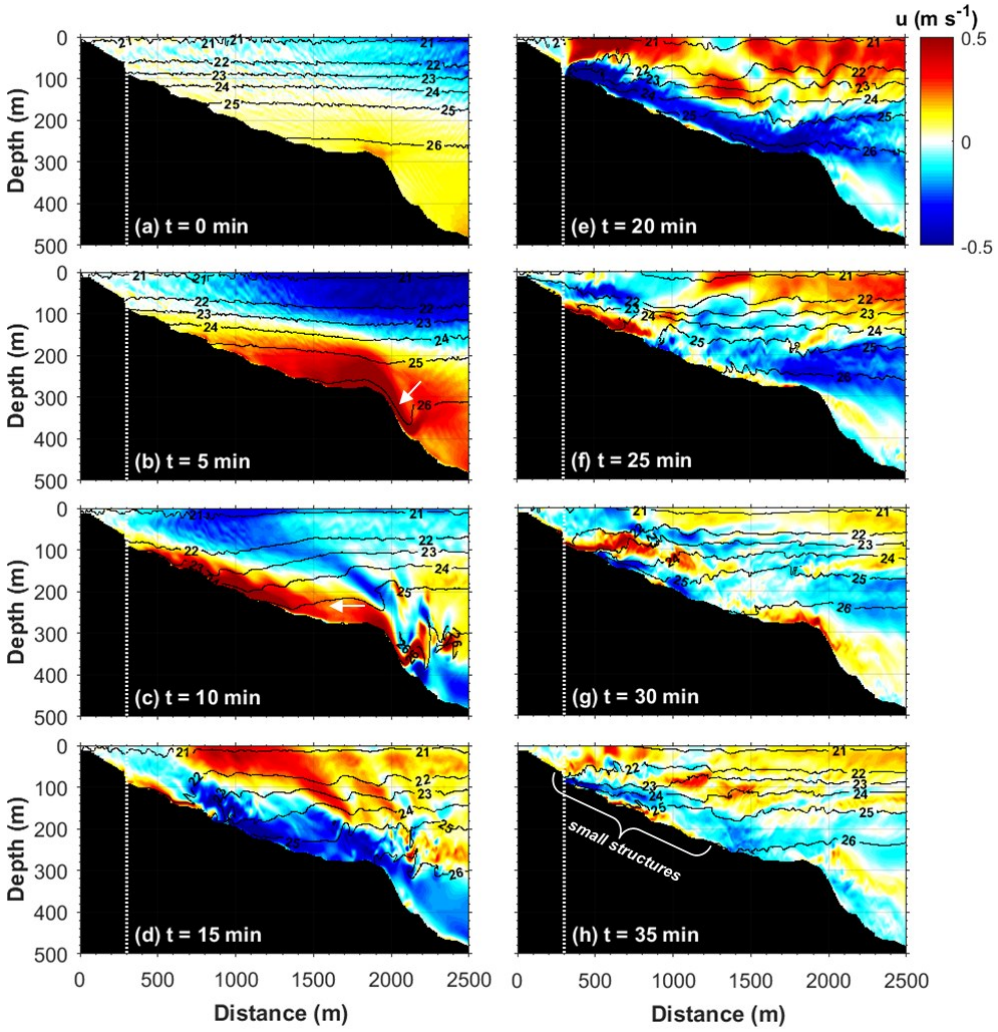

Figure 4.9 Spatio-temporal evolution of 2D non-hydrostatic modeled density field (line contours) overlaid on the cross-shore current (colored contours) in Manado Bay. The vertical dashed white line is the location of observations. Offshore and onshore velocity is represented by red (positive) and blue (negative) values, respectively.

A steepening of the isopycnal at the shelf-break is observed at depth as a result of the increasing upslope cross-shore current (**Figure 4.9**.b). This steepening of the isopycnal then leads to the generation of small-scale patterns that break locally while some wave structures are propagating upslope at depth (**Figure 4.9**.b, c; white arrows). Wave patterns are also observed in the upper layer. The growth of small-vertical scales is fast, leading to a layering of the flow with a few 10s m characteristic vertical scale (**Figure 4.9**.d-f). Small-scale structures are eventually observed over the full section especially in the bottom layer (**Figure 4.9**.h). The modeled density and cross-shore current at the observations location is compared with the observations in the next subsection.

Depth averaged power spectra of the zonal and meridional measured current components in the Manado Bay show dominant diurnal and semi-diurnal tidal constituents (**Figure 4.10**). These two tidal constituents also dominate the baroclinic cross-shore current as evidenced by a time-depth section of the low-pass filtered currents in the Manado Bay (**Figure 4.11**.a).

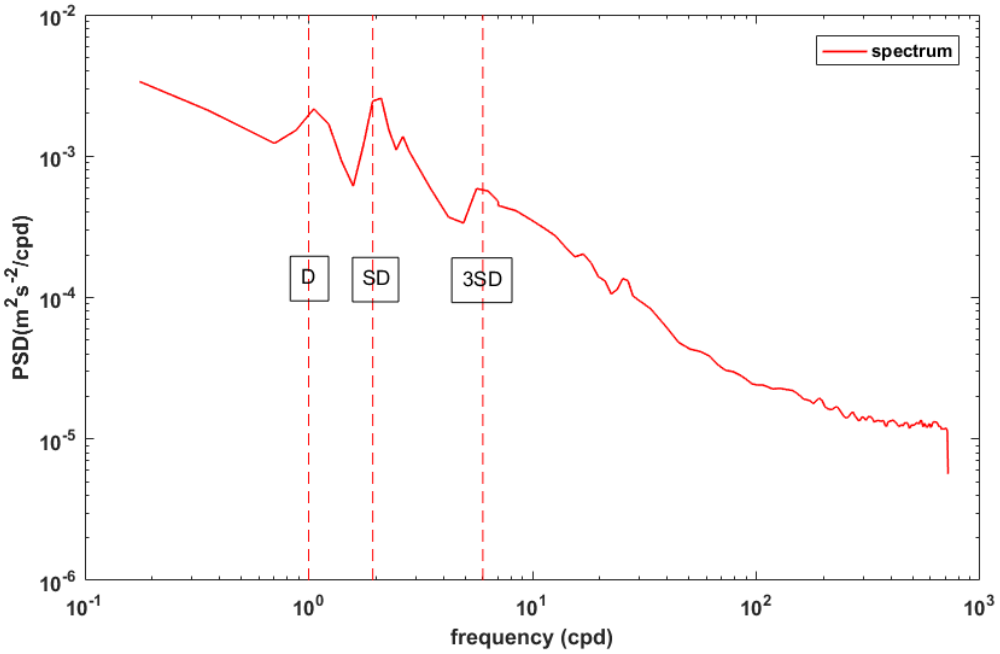

Figure 4.10 Power spectra of measured velocities, in the Manado Bay. The dashed red lines depict three tidal frequencies, the diurnal, D, the semi-diurnal, SD, and the third diurnal, 3SD .

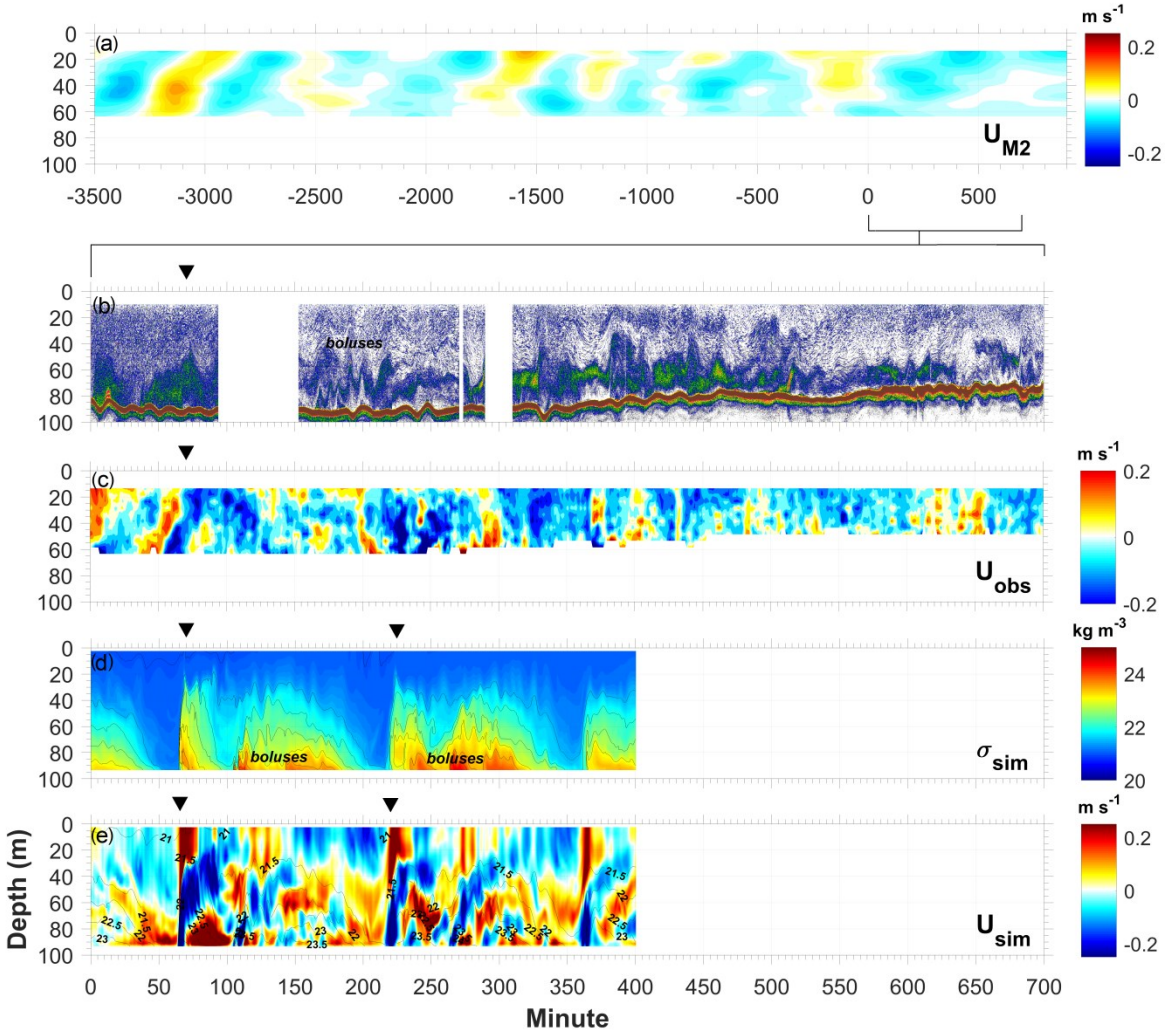

Figure 4.11 (a) Low pass filtered in-situ cross-shore current (6 hours cut off); (b) echogram image on May 13th 2009; (c) in-situ cross-shore current; (d-e) Density contours and density contour lines overlaid on cross-shore current (U_{sim}), respectively from the shoaling experiment. Note that U_{obs} is the cross-shore component inferred from the in-situ zonal and meridional currents. Negative (blue) and positive (red) current contours represent offshore and onshore directions, respectively. Reversed black triangles represent the current fronts that appear in the model and in the observations. Zero minute is minute since May 13th 2009 at 02.41 GMT+7.

Small-scale features are nicely evidenced on the echogram image, which covers a low tide to high tide period on May 13th (**Figure 4.11**.b). Large sharp wave of elevations are observed (**Figure 4.11**.b, d) at the early stage of the observation and simulation. A close inspection at **Figure 4.11**.b also reveals boluses that are small-scale wave of elevations propagating near the bottom, which are irregularly spaced. In the shoaling simulation, the first solitary wave of depression starts to break over the Manado shelf edge, approximately 2 km from the coast, (see **Figure 4.9**). Since our observations were located further upslope at depth of 70-100 m, the evolution of the density and cross-shore current of the shoaling simulation

are examined at this location (~95 m depth, white dashed line on **Figure 4.9**), and are compared with the features observed in the echogram image.

Our shoaling simulation shows similar patterns to those observed in the echogram image on May 13th, with the generation of a front of elevation associated with sharp variation in the current structure and the subsequent appearance of boluses inducing short duration oscillations of density and currents (see **Figure 4.11**.d) inducing short duration oscillations of density and currents. These boluses result from the interaction between the intruding density current generated by the breaking ISW and the sloping topography (as can be seen in **Figure 4.9**.e and **Figure 4.11**.e at ~70 minutes) generated by the breaking ISW and the sloping topography. This process is about the same as the one described by Bourgault and Kelley (2007) during the shoaling of an ISW of depression, staggered boluses and seem to be a robust feature associated with ISW shoaling.

By comparing the current structures from the observations and the simulation, we also found that the magnitude of the simulated current is stronger compared to the observed current (**Figure 4.11**.c, e). However, this two-dimensional simulation may differ from that in three dimensional or real conditions. Any deflection of the cross-shore current thus becoming along-shore may reduce the amplifying processes of the current magnitude induced by the reflection by the sloping topography. Moreover, the generation of internal waves by the interaction of baroclinic tides as well as their propagation is a 3-D process that is not reproduced by our 2D model, therefore a significant part of the ISW energy reaching Manado bay may be lost by refraction and radial spreading.

4.4.2 Energetics of the shoaling ISW trains

A first insight on the energetics of the breaking ISWs is inferred from the shoaling simulation. The energy of the incoming internal tide is also computed for comparison. We focused on the first ISW train in order to focus on the effect of the incoming wave on the unperturbed condition of the Manado Bay waters (**Figure 4.12**.a). The total energy contained in the first ISW packet is inferred over the length of that packet which corresponds to the domain [$-L_2$; L_2], while that of the first ISW train is estimated over the length of the first ISW in the packet that is [$-L_1$; L_1]. Here we set L_1 [35:65] km, and L_2 [35:106] km (**Figure 4.12**.a). The available potential energy, *APE* per unit length is given by:

$$APE = \frac{1}{2}\int_{H}^{z=0}\int_{-L}^{L}\rho_0 N^2\zeta^2 dxdz \tag{4.26}$$

Our estimate yields an *APE* of 72.7 MJ m^{-1} for the first leading wave and an *APE* of 152.9 MJ m^{-1} for the ISW train. The kinetic energy, *KE* per unit length is given by:

$$KE = \frac{1}{2}\int_{H}^{z=0}\int_{-L}^{L}\rho(u(x,z)^2 + w(x,z)^2)dxdz \tag{4.27}$$

Our estimate yields a *KE* of 83.2 MJ m^{-1} for the first leading wave and 171.5 MJ m^{-1} for the ISW train. Hence, we obtain a total energy of 155.9 MJm^{-1} for the first leading wave and 324.4 MJ m^{-1} for the ISW train. We found *KE*/*APE* of 1.14 and 1.12 for the first leading wave and the train, respectively. These values are slightly smaller compared to the order of ratio calculated for waves of elevation in the Oregon continental shelf (1.9) (Klymak and Moum, 2003), and for deep sea solitons observed in the South China Sea (1.4) (Klymak et al., 2006).

The energy loss resulted from the shoaling and breaking processes over the cross-shelf region, E_{diss} was inferred from the time integration of the dissipation rate of the area that has been estimated using density inversion of the Thorpe method over the cross-shelf region:

$$E_{diss} = \frac{1}{2}\int_{H}^{z=0}\int_{x=0}^{3}\int_{t=0}^{tx}\rho\varepsilon\, dz\, dx\, dt \tag{4.28}$$

The estimates were made over a 3 km length cross section of the Manado Bay shelf and over 125 minutes (**Figure 4.12**.b). Around 11.04 MJ m^{-1} was dissipated through turbulence as it shoals over the shelf which corresponds to about 3.5% of the ISW train energy.

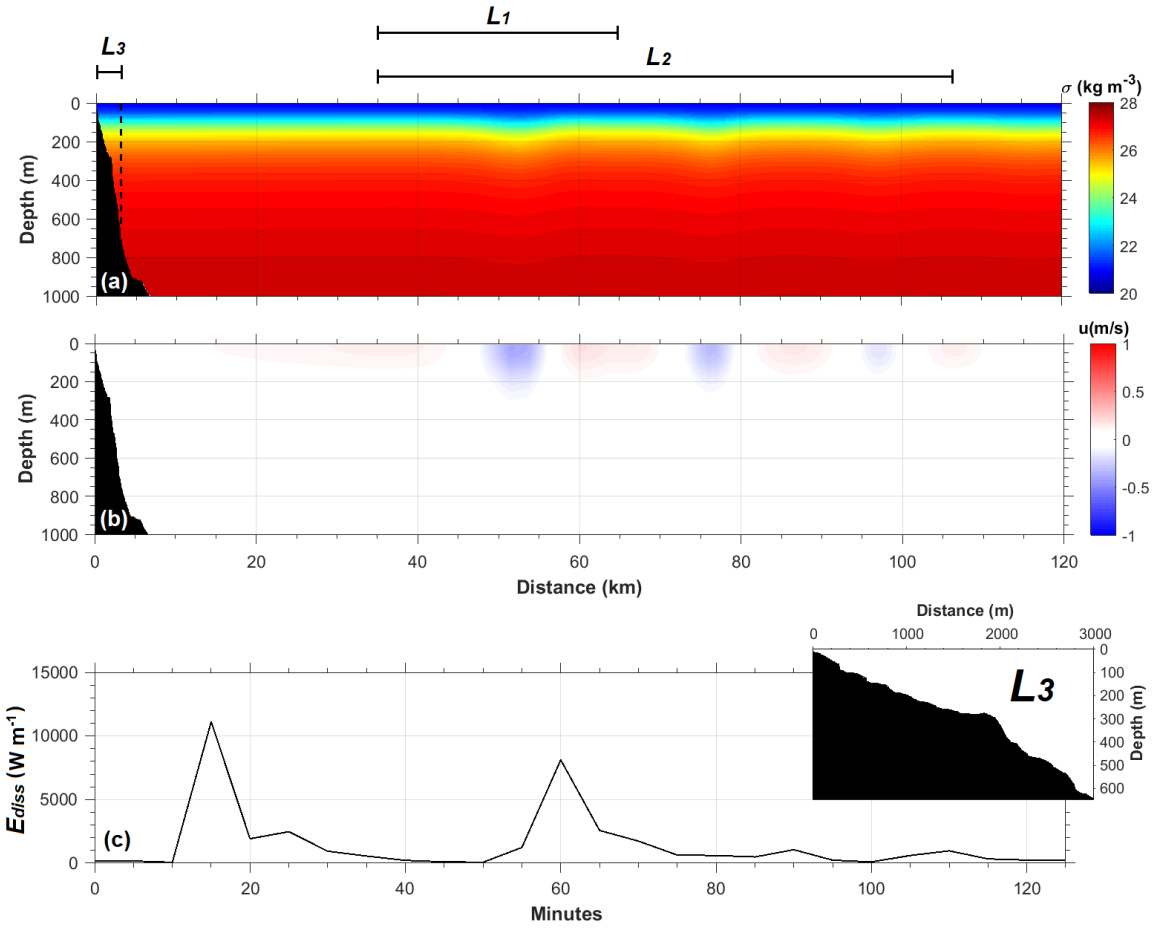

Figure 4.12 (a) Density field at time t = 9.33 minute of the shoaling simulation with L_1 [35:65] km, and L_2 [35:106] km refer to the domains of integration for the computation of the kinetic and available potential energy of the first leading wave and ISW train respectively. The domain L_3 [0:3] km refers to the integration domain over the Manado Bay shelf; (b) cross shore velocity and (c) time evolution of the energy dissipated over a 3 km length cross section of the Manado Bay shelf (area integrated of L_3).

4.4.3 Enhanced Mixing due to Shoaling ISW

Details on the spatio-temporal variability of the mixing patterns due to the shoaling ISWs, inferred from vertical density overturns using the Thorpe scale method to get the dissipation rate , are next illustrated with six snapshots of the first breaking of the leading wave in the shoaling experiment (**Figure 4.13**). This breaking leads to ~40 m density overturn (**Figure 4.13**.a, at t = 10 min), leading to enhanced dissipation rates and diffusivities up to 10^{-2} m^2s^{-3} (**Figure 4.13**.b, at t = 10 min) and 10^{-2} m^2s^{-1} (**Figure 4.13**.c, at t = 10 min), respectively. It also shows that as the breaking wave shoals over the shelf, the mixing event broadens over the shelf. Upslope running boluses can also be characterized by elevated L_T, dissipation rates

and diffusivities in the near bottom layer up to ~10 m; ~10^{-4} m^2s^{-3}; and ~10^{-3} m^2s^{-1}, respectively (**Figure 4.13**, at t=15 minute).

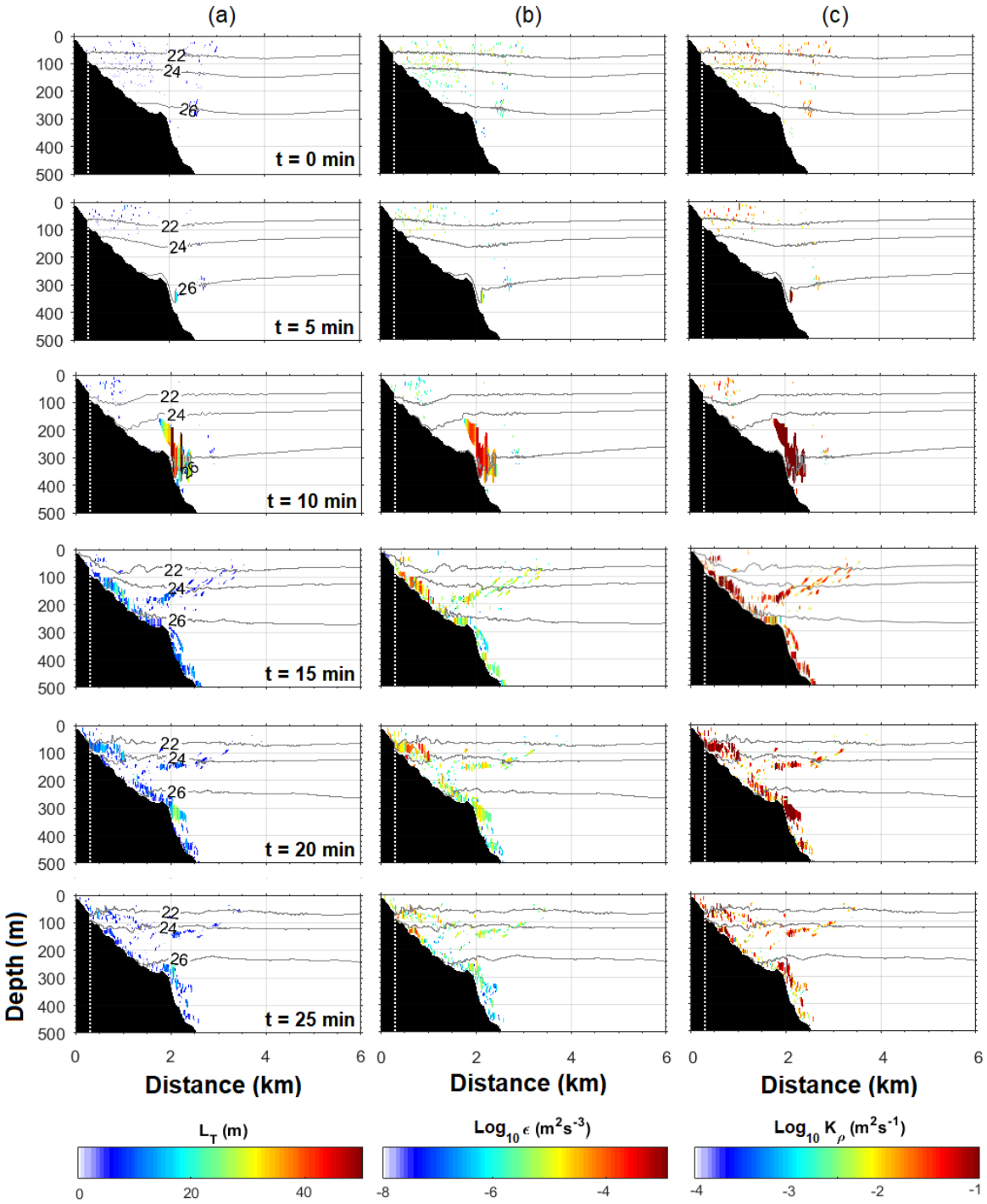

Figure 4.13 Time-depth sections during the first incoming solitary wave evolution over the Manado Bay Shelf: (a) Thorpe length (L_T), (b) dissipation rate in log_{10} scale (ε), and (c) vertical diffusivity in log_{10} scale (K_ρ). The white vertical dashed line refers to the observation site.

The time series of the depth-integrated turbulent kinetic energy dissipation rate and vertical diffusivity inferred from the simulation at the observation site shows the occurrence of peaks that are often correlated with upwelling fronts and, to a weaker extent, downwelling

fronts (see **Figure 4.14**.a). The mean dissipation rate and vertical diffusivity gained from the model is 3.51×10^{-7} $m^2 s^{-3}$ and 3.96×10^{-2} $m^2 s^{-1}$, respectively; with the standard deviation of 74.63×10^{-7} $m^2 s^{-3}$ and 2.08×10^{-2} $m^2 s^{-1}$, respectively.

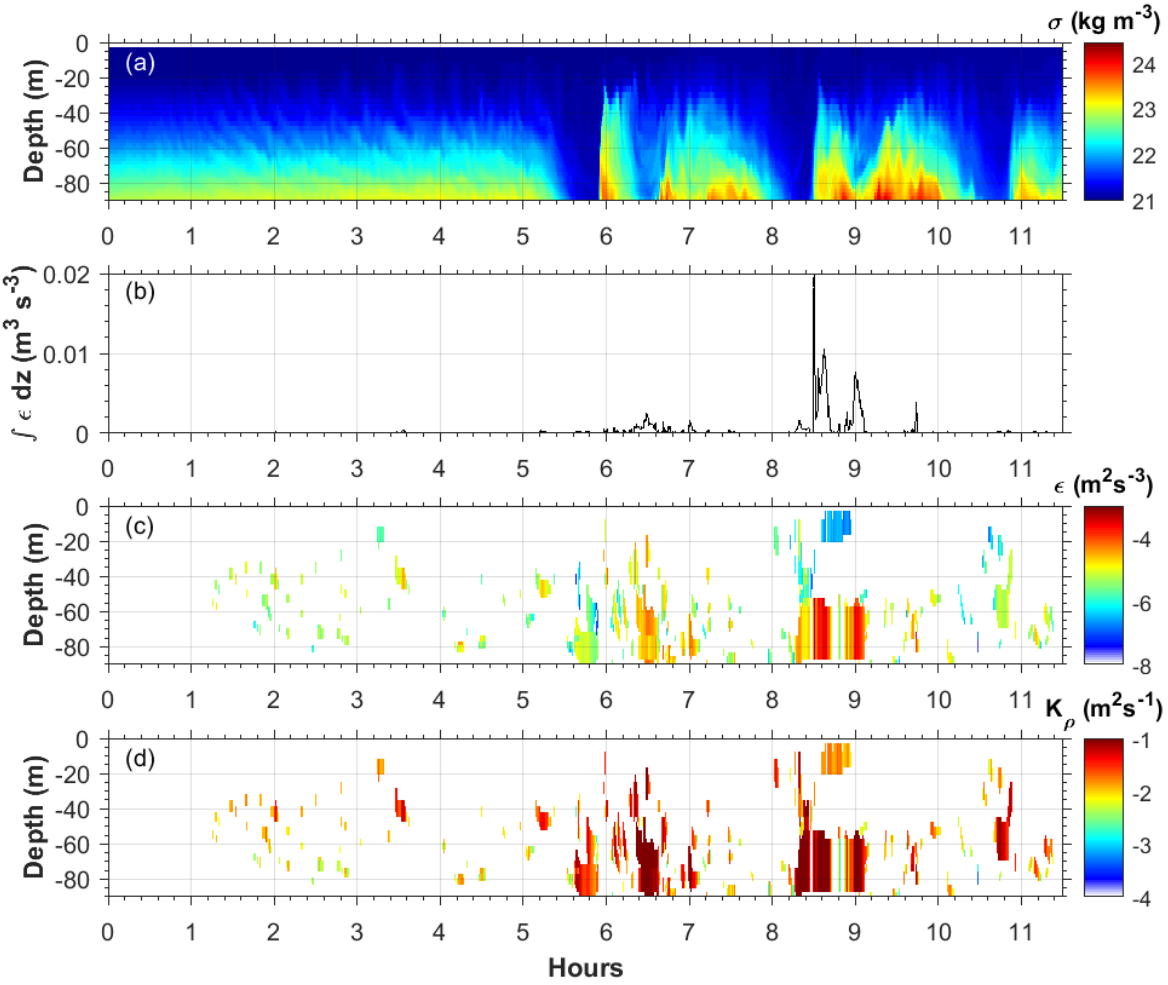

Figure 4.14 Shoaling simulation at the observation site: (a) temporal evolution of density anomaly; (b) temporal evolution of depth integrated dissipation rate; (c) temporal evolution of vertical profile of the dissipation rate in log_{10} scale; (d) temporal evolution of vertical profile of the eddy diffusivity in log_{10} scale.

From the observation, the highest turbulent kinetic energy dissipation rates and eddy diffusivities occurred in the lower layer on May 12th 2009, before a huge wave of depression was observed (**Figure 4.15**.a, b). Unfortunately, density measurements were lacking afterwards so that the dissipation induced by this wave of depression could not be estimated. Large vertical displacements were also observed on May 13th 2009, during a sequence of boluses appearance at 02.41-03.41 GMT+7. Internal wave oscillations were observed in the upper layer on May 13th 2009 leading to high turbulent kinetic energy dissipation rates. The mean dissipation rates yield a value of 3.30×10^{-6} $m^2 s^{-3}$ and a standard deviation of 13.78×10^{-6} $m^2 s^{-3}$.

This mean value is one order of magnitude higher compared to the simulation; and the vertical eddy diffusivity calculated with regime-based mixing efficiency yield a value of 4.22×10^{-3} $m^2 s^{-1}$ and a standard deviation of 15×10^{-3} $m^2 s^{-1}$. This mean value is one order lower than the simulation.

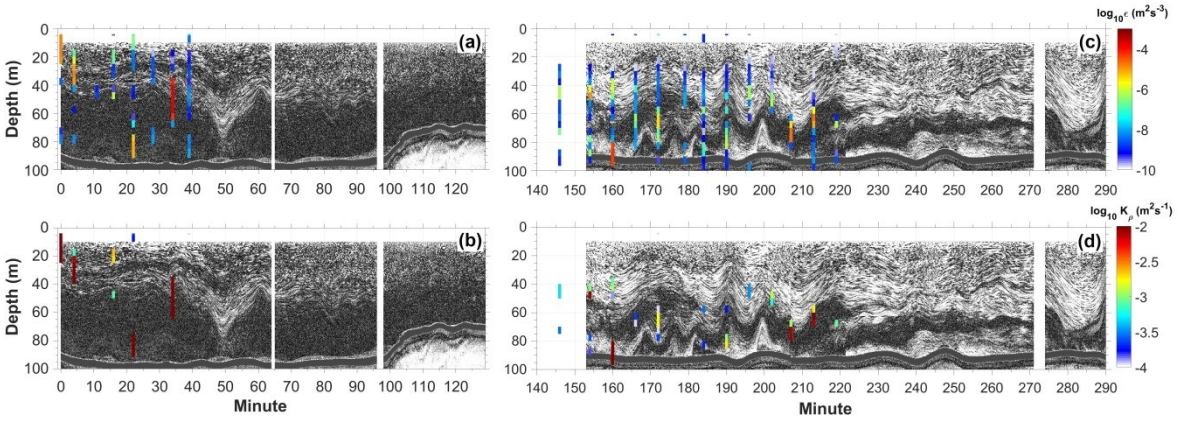

Figure 4.15 Dissipation rate, ε, and diapycnal diffusivity, K_ρ, observed on May 12th 2009 (a and b, respectively); and those observed on May 13th 2009 (c and d, respectively). The color bars refer to ε and K_ρ $\log_{10}$ values, with the lowest value, [$\varepsilon \leq 10^{-10}$ $m^2 s^{-3}$; $K_\rho \leq 10^{-4}$ $m^2 s^{-1}$] is set to transparent. The background image is inferred from the echogram signal (arbitrary scale) and reveals the appearance of IW events. The time scale is in minute starting on May 12th 2009 at 17.54 GMT+7 for (a) and (b) and on May 13th 2009 at 02.41 GMT+7 for (c) and (d).

The comparison of the mean vertical profile of ε from the simulation and observations shows that the model under-estimates epsilon in the upper layer (down to ~50 m depth) and over-estimates it in the lower layer, except for a few instances within 20-30 m depth and 50-55 m depth, where there is a good agreement (**Figure 4.16**). Sea surface cooling, that is not taken into account in the simulation may explain this surface elevated dissipation, while elevated dissipation deeper, around 40-50 m depth, may be related to the intensified stirring due to Kelvin-Helmholtz instabilities accompanying the internal waves activity which cannot be resolved by the simulation. In contrast, the mean vertical profile of K_ρ from the simulation is higher than the observations. We suggest that this condition deals with the degree of stratification field, which is not well representing the real situation, where the stratification in the simulation is less strong than the observation.

We also estimate the vertical diffusivity using Bouffard and Boegman (2013) formula to the observation and simulation. We found a mean value of 1.49×10^{-4} $m^2 s^{-1}$ and a standard deviation of 2.57×10^{-4} $m^2 s^{-1}$ from observation, which is comparable to the simulation result mean value 3.88×10^{-4} $m^2 s^{-1}$ and standard deviation 4.05×10^{-4} $m^2 s^{-1}$. Indeed, we suggest that these values are relatively low and less realistic if we consider a quite energetic pattern as can be indicated by the stirring process view from the observation and the model. **Figure 4.16**.b, c

shows the vertical mean profile of the vertical diffusivity inferred using Osborn (1980) and Bouffard and Boegman (2013) formula, respectively.

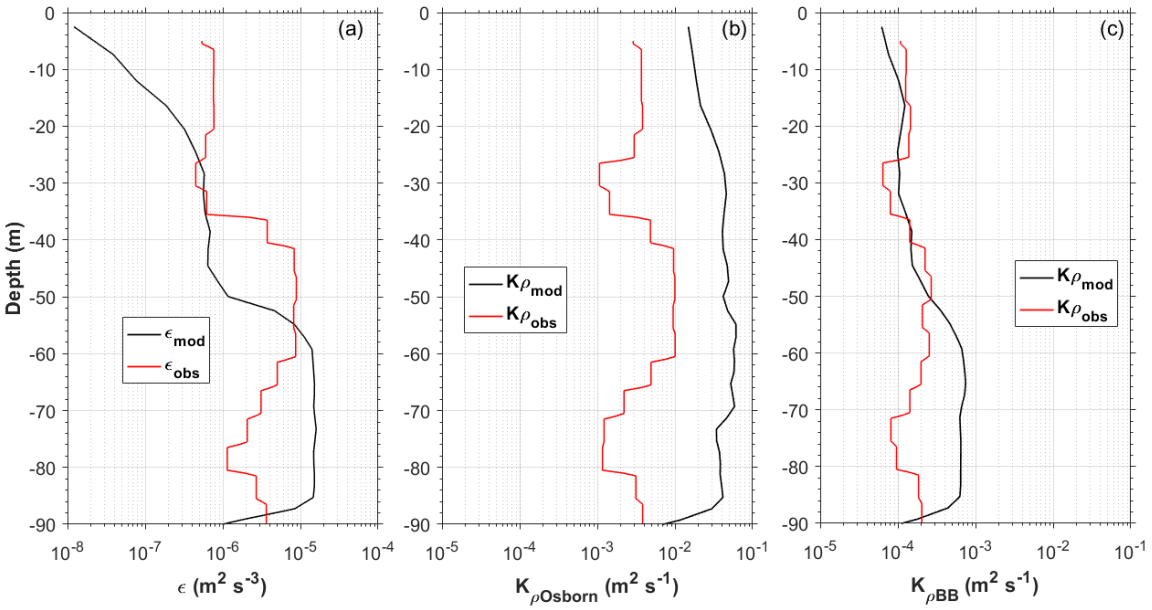

Figure 4.16 Vertical profiles of time-mean dissipation rate (a) and vertical diffusivity (b, c) inferred using Osborn (1980) and Bouffard and Boegman (2013) formula, respectively. The model values are displayed in black while the observation are displayed in red.

4.5 Summary

Indonesian seas are a region where ISWs are frequently observed on MODIS images (e.g. Jackson, 2007) but rarely studied (Aiki et al., 2011). Owing to their large amplitudes and their long-range propagation across interior seas, this raises the question of how much mixing they generate when they shoal in shallow areas. We investigated this question with a process-oriented study motivated by in-situ measurements of ISWs shoaling and boluses in Manado Bay on the Sulawesi Island. The origin of these ISWs, radiating from the Sibutu Passage, was inferred from remote sensing analysis (Jackson, 2007). Indeed the Sibutu Passage is a location of strong internal tide generation triggered by semi-diurnal tidal flow. These internal tides propagate toward both the Sulu and the Sulawesi Seas, which suggests that ISWs packets radiating in both Sulu and Sulawesi Sea out of the Sibutu Passage have a dominant semidiurnal component. The ISW packets observed in the Sulawesi Sea is suggested to be more frequent than those observed in the Sulu Sea (Kartadikaria et al., 2011). Idealized non-hydrostatic numerical simulations were performed along a section starting from the Sibutu Passage and ending at the Sulawesi Island. The simulations forced by the barotropic tidal flow gave evidence of the generation mechanism of ISWs, which are generated through a steepening mechanism of the internal tide during its propagating in the Sulawesi Sea. These semidiurnal ISW packets then reach the northern tip of Sulawesi Island, Manado Bay, where they eventually break.

Energy fluxes were inferred from the idealized non-hydrostatic simulations encompassing the generation area and the far-field domain with a 700 km length vertical section. In the generation area, the time-averaged tidal energy flux is of about 15 kW m^{-1}. This value compares well with the largest values mentioned in the literature, for instance that those observed in the mouth of Gaoping Canyon off Taiwan, 14 kW m^{-1} (Lee et al., 2009) and in the Hawaiian Ridge, ~16 kW m^{-1} across the 3000 m isobaths (Lee et al., 2006) thus confirming that the Sibutu Passage is a hotspot for internal tide generation. The simulations showed the progressive decrease of the internal tide energy flux mostly resulting from the growth of ISWs: the ISW energy flux increases from 0.8% at 200 km up to 32% of the total energy flux at 700 km, while the internal tide energy flux that represents 95% of the total energy flux at 200 km, does only contribute to 64% of the total energy flux. The idealized simulations provided a quantitative estimate of the efficiency of ISWs in pumping internal tide energy along its far-field propagation. They also provided estimates of the local dissipation in the generation area, of about 7×10^{-6} W kg^{-1}, much enhanced compared to the background maximum dissipation rate in the far-field domain of the order of 1×10^{-8} W kg^{-1}. The simulations also point out the

considerable enhanced dissipation induced by ISWs breaking, reaching dissipation rate of the order of $9x10^{-5}$ W kg^{-1}. Of course, these events are very localized and occur at most with a semi-diurnal periodicity.

Higher resolution numerical simulations were performed to focus on the details of the ISWs shoaling and turbulent mixing was inferred from both the simulations and the observations in Manado Bay. We showed that the ISWs in the Sulawesi Sea enhance the watermass mixing when shoaling over the shelf break of the northern coast of the Sulawesi Island, such as in the Manado Bay with dissipation rates up to ~10^{-6} m^2s^{-3}. Depth-averaged dissipation rates inferred from the simulations and the observations compared relatively well though an under-estimate of dissipation was found in the upper layer and an over-estimate in the lower layer. These differences may account for the absence of surface forcing in the simulations and a likely overestimation in the amplitude of the breaking ISW, a lack of resolution to mimic all small-scales instability processes. We also found that only a small fraction of the ISW energy, 3.5%, is dissipated in the simulations. This surprisingly small fraction may be explained by the bias of the method used, based on density overturns. It is likely that the model resolution induces a strong limitation for the reliability of this estimate. Compared to other regions, our in-situ turbulent kinetic energy dissipation rate estimates (observation) ~10^{-6} m^2s^{-3}, are comparable to those observed in the Irish Sea, ~10^{-6} m^2s^{-3}(Simpson et al., 1996); about one order of magnitude higher than those observed in the Scotian shelf, 5.3 x 10^{-7} m^2s^{-3} (Sandstrom and Oakey, 1995); and several order of magnitude higher compared to those observed in the Monterey Bay shelf, ε =7.4-55.8 x 10^{-9} m^2s^{-3} (Carter et al., 2005). On the opposite, they are much lower than the extreme dissipation rates observed in the South China Sea around Dongsha plateau ε = $1.5x10^{-4}$ m^2s^{-3} (Alford et al., 2015). Our estimated diffusivity value (observation) of the order of 10^{-3} m^2s^{-1}, is not among the largest: it is comparable to that observed at the Oregon shelf, K_ρ = 3.7-17 $x10^{-3}$ m^2s^{-1} (Nash and Moum, 2001) where the ISWs shoaling is enhanced by the presence of a 20 m high topographic bump. It is also two orders of magnitude lower than those observed in the South China Sea, >10^{-1} m^2s^{-1} (Alford et al., 2015). On the other hand, it is about two order of magnitude higher than those observed in Monterey Bay shelf, K_ρ = 6.1-37.8 $x10^{-5}$ m^2s^{-1} (Carter et al., 2005).

The total energy in each trough of the Sulawesi ISWs is around 0.32 GJ m^{-1} before it breaks over the Manado Bay shelf. This value is large but lower than the one observed in the South China Sea, ~1.8 GJ m^{-1} (Klymak et al., 2006).

An overall picture of the internal tide evolution and ISWs shoaling was inferred from two idealized numerical simulations, one of coarser spatial resolution that allows to draw estimates for internal tide and ISWs energy budgets and the second of finer spatial resolution that resolve ISWs shoaling at the shelf-break and slope providing mixing estimates. We have shown that with the help of these idealized simulations, we can draw an overall picture of the internal tide evolution and ISWs shoaling that is consistent with the observations. Such approach is a first step toward taking into account the ISW in state of the art regional models. This study is also the first stage toward a local energy budget of ISWs in the Sulawesi Sea and their impact on shallow water mixing, a comprehensive process that has not been taken into account yet by the regional models in the region.

4.6 Acknowledgments

The datasets were acquired during the EWIN (*Widya Nusantara Expedition*) 2009 Project, funded by Indonesian Institute of Sciences (LIPI). This study is also sponsored by Indonesian Endowment Fund Scholarship Program (LPDP)-Indonesian Ministry of Finance. We are grateful to Pak Priyadi Dwi Santoso, the technician from Research Center for Oceanography LIPI and to the crew of RV Baruna Jaya VIII for accompanying the data acquisition.

4.7 Appendix: criteria for Thorpe scale computation

Different procedures described in the literature were applied in order to eliminate spurious overturns in the computation of Thorpe scales.

1) The instrument density noise level was inferred from the standard deviation of density in well-mixed regions following a procedure widely applied in previous studies (e.g. Frants et al., 2013; Park et al., 2014). Density profiles were first de-trended over 10 m segment in the surface mixed layer and the standard deviation computed. The density noise level threshold was set to the 0.018 kg m^{-3}.

2) Once the threshold value determined, the intermediate profile method, first proposed by Ferron et al. (1998) and modified by Gargett and Garner (2008), was next applied. The purpose of the method is to prevent an underestimate of Thorpe displacements in regions of weak density gradient. Two intermediate profiles were first computed : the first one was created by setting to zero Thorpe displacement smaller than the threshold value starting from top to bottom while the second one was created by starting from bottom to top. The final intermediate profile was eventually obtained by averaging these two profiles.

3) The criterion proposed by Galbraith and Kelley (1996) (henceforth GK96) to eliminate any density overturn induced by spikes in the temperature and/or salinity profile due to a mismatch between the temperature and conductivity sensor response was applied. Only the turbulence patches having a tight relationship between density, temperature, and salinity will be considered as real the overturns. More generally the method states that either mixed or unmixed water masses, tend to lay on a local *T-S* relationship. Any imperfect measurement due to sensor response mismatch will lead to deviation in the form of loops pattern off the linear *T-S* relationship. The variation of density with respect to temperature and salinity using a simple linear model of *T-S* covariation was thus examined. The tightness of the T-S relationship was quantified with the standard deviation between the observations and the linear model. The resulted values are then divided by the rms of Thorpe length, L_T to get non-dimensional values of two ratios representing the linear correlation of density-salinity, ξ_S and density-temperature, ξ_T. We then consider the quantity $\xi = \max(\xi_S, \xi_T)$. The value near zero indicates a tight *T–S* relationship and large values signify a loose relationship. A threshold value equal to 0.66 was prescribed after visual inspection following previous authors recommendation (GK96 ; Stansfield et al., 2001). Note that our 0.66 value is slightly higher than the 0.5 value prescribed by GK96, was found more relevant for the large overturns observed in Manado Bay.

4) The last criterion applied aimed to eliminate spurious overturns based on their asymmetric shape. This method, proposed by Gargett and Garner (2008), relies on the observation that a perfect overturn contains equal lengths of positive and negative displacements. The overturn ratio, R_o, is defined for each overturn of vertical extension L, as follows : $R_o=\min(L^+/L, L^-/L)$ where L^+ and L^- are, respectively, the vertical extension of positive and negative Thorpe displacements. A single perfect overturn should have a R_o value of 0.5 while a more complex and/or imperfectly sampled overturn would have a lower R_o. We took the 0.2 as the threshold value so that the overturns with $R_o<0.2$ were discarded. Some

examples of Thorpe displacements selection tests are shown in **Figure 4.17** and **Figure 4.18**.

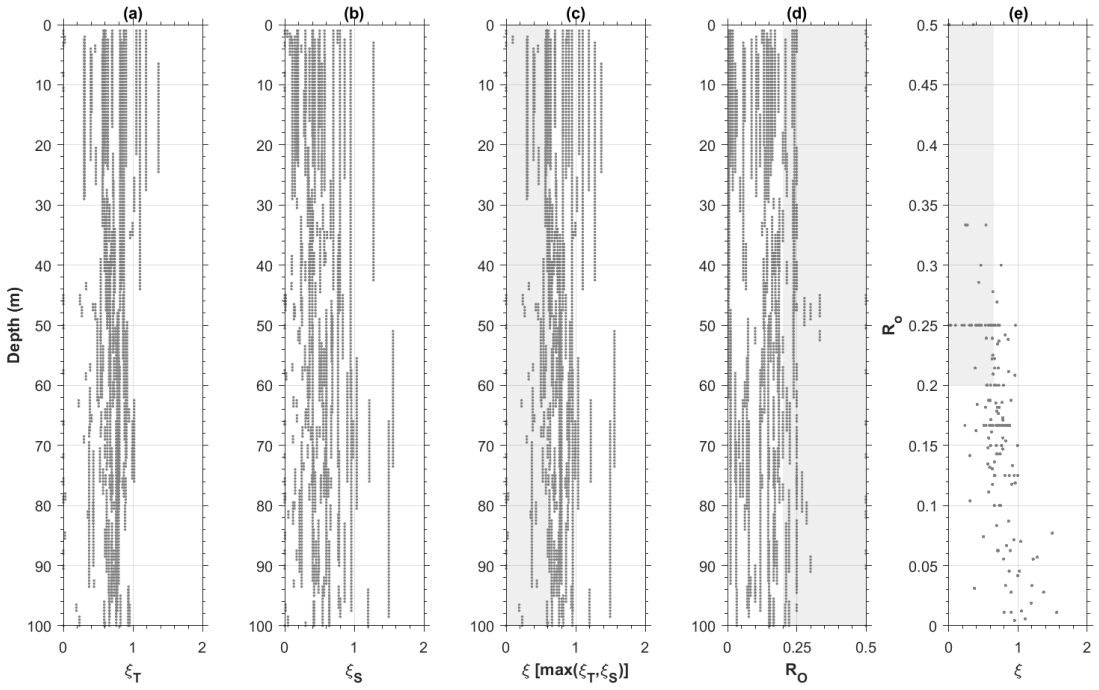

Figure 4.17 Overturn selection criteria used in this study: (a)-(c) are the distribution of all detected patches over depth vs the resultant ratio of temperature-density, ξ_T; temperature-density, ξ_S; and its maximum resultant ratio, ξ; respectively; (d) overturn ratio Ro; and (e) Ro vs ξ of all observed patches. The gray shading region in (c), (d) and (e) is acceptable overturns threshold zones ($\xi_T \leq 0.66$; $Ro \geq 0.2$).

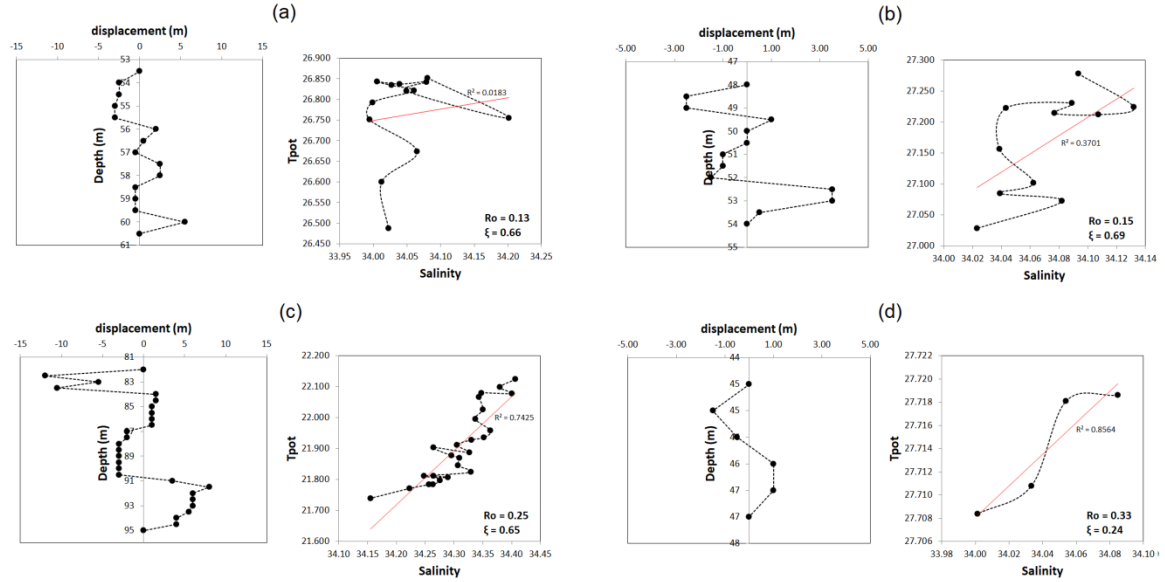

Figure 4.18 Some overturns that fail to pass the overturn selection criteria (Ro < 0.2 and ξ >0.66) (a, b); and overturns that pass the criterion (c, d).

5
Observation of Internal Tides, Nonlinear Internal Waves and Mixing Estimates in the Lombok Strait, Indonesia

Chapter 5
Observation of Internal Tides, Nonlinear Internal Waves and Mixing Estimates in the Lombok Strait, Indonesia (Paper to be submitted)

5.1 Introduction

The Indonesian throughflow (ITF) connects the Pacific and Indian oceans and represents a key passage of the thermohaline circulation (Gordon, 2005; Gordon and Fine, 1996). The strong mixing of Pacific waters observed there generates cold surface anomalies and fresh anomalies in the pycnocline which impacts the Indian and Pacific heat and freshwater budgets (Lee et al., 2002) as well as local deep atmospheric convection and wind regimes (Koch-Larrouy et al., 2010).

This mixing is mainly driven by internal tide induced turbulence as shown by previous in situ observations (Bouruet-Aubertot et al., 2018; Koch-Larrouy et al., 2015; Purwandana et al., 2019; Robertson and Ffield, 2005), satellite images of sea surface temperature (Ray and Susanto, 2016) and modeling studies (Hatayama, 2004; Koch-Larrouy et al., 2007; Nagai et al., 2017; Nagai and Hibiya, 2015; Nugroho et al., 2017; Schiller, 2004). This tidal mixing is particularly intense over rough topography, such as in the Lifamatola, Manipa, Ombai, and Lombok Straits, and the Sulu and Sibutu Island chains. One of the most important exit passages of the ITF is the Lombok Strait, located in the Lesser Sunda Islands waters, separating the islands of Bali and Lombok, between 115.3°-116.1° E and 8.2°-8.7° S and connecting the Kangean waters (western Flores Sea) in the north, and the Indian Ocean in the south. The Lombok Strait is part of the western route of the ITF, a bypass that connects directly the ITF flowing from Makassar after passing the Dewakang waters and represents 20% of the ITF (Hautala et al., 1996). In situ measurement in this strait from January 1985 to January 1996 (Murray and Arief, 1988) shows an average transport of 1.7 Sv (1 Sv = $1x10^{-6}$ m^3s^{-1}) with a maximum of 3.8-4.0 Sv towards the Indian Ocean during July and August 1985; and the minimum between 0-1 Sv is observed from December 1985 to January 1986. The flow in the Lombok strait is controlled by the presence of the Nusa Penida sill (hereinafter NPS) which reaches 350 m depth (Murray and Arief, 1988).

The Lombok Strait basin is dominated by Pacific water masses, i.e. North Pacific subtropical waters (NPSW), fed by the Makassar Strait throughflow and characterized by a σ_θ = 24.5 kg m^{-3} surface at 100-200 m a depth (Hautala et al., 1996; Wyrtki, 1961). This strait has

distinctive characteristics compared to the other exit passages along the Lesser Sunda Island chain. It is located close to the fresh water source from the rivers runoff in the Java Sea (the maximum river discharge from the Java, Sumatra and Kalimantan Islands occurs in April (Wyrtki, 1961)). The salinity of the Lombok Strait is exposed to the fresher water from the Java Sea and local precipitation during northwest monsoon (December-May). The freshening that can exceed 2 psu occurs from March to May (Sprintall et al., 2003). In the Lombok Strait, the watermass below this depth is actually restricted to flow into the Indian Ocean due to the existence of the NPS.

The spatial variation of the hydrodynamics of the Lombok Strait is also unique. A previous study indicated that the flow in the Lombok Strait is separated, a permanent southward flow in the upper layer and a reversing southward-northward flow in the lower layer (Hautala et al., 2001). The southward flow is controlled by the low-frequency component of the large-scale wind forcing from the Pacific Ocean; while the northward flow is controlled by the higher frequency component of the Indian Ocean forcing as described above (Potemra et al., 2002). The upper southward flow is observed in March-April and the reversing northward flow in May. The northward flow is correlated with semi-annual Kelvin wave events forced by westerly winds during the northwest to southeast monsoon transition period (November/December and April/May) in the equatorial Indian Ocean (Sprintall et al., 2003). Since the strait opens directly onto the Indian Ocean, intrusion of the Indian water may occur through the strait forced by the Kelvin waves as has been suggested by previous studies (Sprintall et al., 1999; Susanto et al., 2001; Wijffels et al., 2002). Longitudinally, the throughflow in the Lombok Strait is also varying. The stronger southward flow is observed in the western side of the strait, a phenomenon related to the higher sea level slope on the Lombok Island side than that on the Bali Island side (Hautala et al., 2001; Murray and Arief, 1988).

The tide in the Lombok Strait is produced by tidal waves propagating from the Indian Ocean with a dominant M2 semidiurnal period of 12.4 hours. The tidal flow can reach ± 3.5 m s^{-1} in the sill area (Murray and Arief, 1988). Numerical simulations have shown a strong conversion of barotropic to baroclinic internal tides at the NSP (Nagai and Hibiya, 2015; Nugroho et al., 2017) and evidenced the Lombok strait as a strong mixing hot spot. Analysis of satellite sea surface temperature also revealed a spring neap cycle in the Lombok strait evidencing strong mixing associated with the tides there (Ffield and Gordon, 1996; Ray and Susanto, 2016).

The strong Lombok strait internal tides can evolve into a train of large vertical displacement (~100m) small horizontal scale (~km) waves known as Internal Solitary Waves (ISW hereafter) (Aiki et al., 2011; Matthews et al., 2011). Their appearance is often observed from satellite images as sea surface alternating bands of slicks and rough patches propagating from NPS (Jackson, 2007) to the Kangean islands slope (**Figure 5.1**) and became a classical illustration of ISW observation from space. Yet, the only in situ observation of internal solitary waves in the Lombok Strait is a short snapshot of an Echosounder by (Susanto et al., 2005) evidencing an impressive solitary wave of ~150 m vertical displacement.

Internal tides are generated as barotropic tidal currents flow over the seafloor features, such as sills, leading to isopycnal displacements (e.g. Alford et al., 2015; Baines, 1982); wherein some occasion internal tides can evolve into ISWs through non-linearity mechanism. They can propagate over distances of several hundreds of km and break at continental slopes causing water masses mixing and cross-shelf exchanges. ISWs have been the subject of intense investigation in various regions such as the South China Sea, the Oregon shelf or the Bay of Biscay (Nash and Moum, 2001; Xie et al., 2013; Zhao and Alford, 2006). Satellite and numerical based studies in the Lombok Strait internal waves revealed that internal solitary waves propagate in the form of coherent arc based waves predominantly northward of the strait (Aiki et al., 2011; Matthews et al., 2011). These studies also suggest that the ITF, which is maximum during the southeast monsoon, tends to limit the long-range propagation of internal solitary waves.

Here, we present high frequency observations of the non-linear internal tides and associated high frequency waves during a spring tide period at the transition between southeast monsoon and north west monsoon. We also characterize the impact on turbulence in the pycnocline using both the Thorpe scale method applied to CTD profiles and Ellison scale method applied to high frequency time series of temperature sensors.

This paper is organized as follows. Section 5.2 describes the methodology, highlighting available dataset from the observations and mixing estimates from both observations and model. Section 5.3 presents results and discussion gained from observations, including the analysis of the characteristics of the observed ISW. The results are summarized in section 5.4.

5.2 Methodology

5.2.1 In situ observations

A field experiment was conducted on 3-5 November 2017 in the Lombok Strait waters at a fixed position, 8.56 S, 116.02 E offshore of the west coast of Lombok Island (~8 km) at a depth of 300 m during the transition from neap to spring tide (**Figure 5.1**). The detail of the measurements is shown in **Table 5.1**. High frequency imaging of the internal wave structure was obtained using a 200 kHz narrow-beam echosounder Simrad EK80 that covered up to 150 m depth. A 75 KHz downward-looking *Sontek* acoustic Doppler current profiler (ADCP) was moored on a floater connected to the anchored boat. The instrument was lowered at depth around 50 m and measured the currents between ~100 m depth with 5 m bin resolution and 1 minute time averaging. An *Anderaa Seaguard* RCM was also deployed at the depth ~150 m to get the current variability in the deeper layer, sampling with 1 minute temporal resolution. Temperature field variability was measured at high frequency (1 Hz) using 4 RBR duet sensors (temperature and pressure) and 2 RBR solo sensors (temperature only) that were attached at several depths between 80 m and 270 m. Note that the internal tide motion induced large heaving of the mooring instruments, and part of the water column sampled was not constant. Moreover, the mooring was anchored to the boat but could oscillate horizontally with an amplitude of ~100 m. The instantaneous absolute velocities can be biased by this motion, and for this reason we consider only in the analysis the horizontal shear and the time mean absolute velocity where high frequency oscillation of the ADCP position around the boat are smoothed. Temperature and salinity profiles were collected using a Sea Bird Electronics CTD 19 Plus from surface to depths of ~200 m around every two hours and 2-3 yoyo casts were repeated when a sequence of internal waves was observed in the echosounder. The profiles were de-spiked and averaged into 0.5 m using the SBE data processing modules. Data above 5 m were removed due to contamination of CTD probe soaking effect and ship's wake. Predicted tidal height, zonal and meridional current components gained from Oregon State University tidal inversion software (OTIS, Egbert and Erofeeva, 2002), including the observation time in the Lombok Strait and field observation design is showed in (**Figure 5.1**).

Table 5.1 Available in situ measurements in the Lombok Strait, 3-5 November 2017.

Date	Hour of CTD casts (GMT+8)	Other operated instruments
November, 3rd 2017	15.23; 18.18; 19.28; 21.24; 23.38	*ADCP, RCM, EK80, RBRs*
November, 4th 2017	02.12; 03.39; 04.30; 07.20; 09.27; 11.10; 13.25; 15.28; 15.46; 16.08; 18.40; 21.19	
November, 5th 2017	00.14; 02.07; 04.06; 04.26; 04.45; 07.18; 07.46; 08.00; 10.30; 12.22	

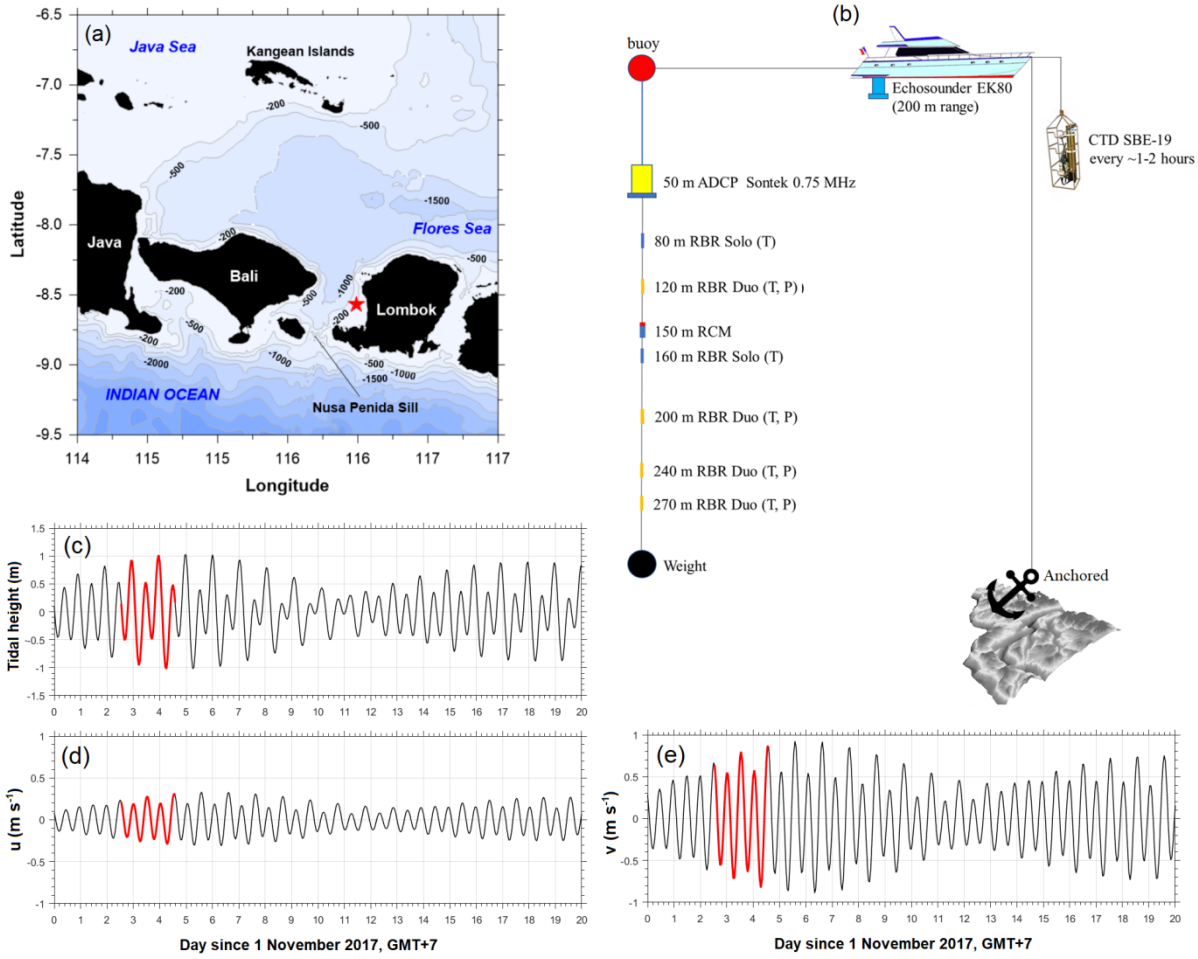

Figure 5.1 (a) Observation site in the Lombok Strait (red star), (b) the measurements scheme, which involved ADCP, CTD, echosounder and RBR sensors, (c, d, e) is the predicted tidal height, zonal current (*u*), and meridional current (*v*), respectively on 1-20 November 2017 above the Nusa Penida sills. Red plots indicate the timing of field observation on 3-5 November 2017.

5.2.2 *Mixing estimates*

Turbulence dissipation rate using both a classical Thorpe scale method and Ellison scale method from the CTD casts and high temporal resolution temperature sensors at a fixed depth measured by moored instruments, respectively. Note that the Ellison scale method employed in this study slightly has different definition compared to previous work, such as by Moum (1996) where it is estimated based on vertical fluctuation rather than temporal fluctuation. In our case, the screening for the temperature is crucial to omit any spurious fluctuations related to the high-frequency surface waves and internal waves. Our dissipation rate estimates by employing the time series data sets using Ellison scale method is similar to study by (Cimatoribus et al., 2014), which was applied for near bottom data sets. Here we applied for the middle layer, below the thermocline down to 50 m above the bottom. This study is also the first obsessive observation to characterize the internal tides generation and the ISWs formation, with a focus on their periodicity and early fate related to the local dissipation and mixing.

Thorpe scale analysis

Our first estimate of the dissipation rate is based on the classical Thorpe method, which is based on the identification of overturns in the density profiles. The Thorpe scale is defined as the RMS value of the displacements that one need to apply to re-order an unstable density profile in a stable way (Thorpe 1977, Ferron et al., 1998; Kunze et al., 2006; Park et al., 2014; Yang et al., 2014). Due to a large noise level observed from the unpumped CTD in the salinity profiles, we prefer to use the temperature-based estimates in this study (as for instance in Mater et al. (2015)). To this end, we need to assume that the potential temperature is a good proxy for the potential density. Here, it is a reasonable assumption since: 1) considering the temperature and salinity range variation observed, the temperature induced potential density variation is one order of magnitude larger (4 kg m^{-3}) than the salinity induced variation (0.4 kg m^{-3}), 2) the salinity and temperature variation both concur to a potential density increase with depth down to about 150 m depth, and 3) although the salinity slightly decrease below 150 m depth, its range of variation below this depth is very weak (~0.03 PSU) compared to the temperature variation (~3°C) resulting in a factor of ~30 between the temperature and salinity induced potential density variation. For the temperature, we set the noise level as 10 times the temperature sensor resolution of the SBE 19 *Seacat Profiler*, δ_T = 0.0001x10 °C, spurious noise induced inversions were then eliminated using the intermediate profile method, firstly proposed by Ferron et al. (1998) and later modified by Gargett and Garner (2008). A method

proposed by Gargett and Garner (2008) is also applied to reject a suspected false overturn, using the overturn ratio, R_o=min(L^+/L, L^-/L); where L^+ and L^- are, respectively the vertical distances occupied by positive and negative Thorpe displacement within an overturn of vertical extent L. A single perfect overturn should contain equal lengths of positive and negative displacements, hence R_o = 0.5 and imperfect overturn would have R_o less than 0.5. Mostly, false overturns are associated with values of R_o<0.2 (Gargett and Garner, 2008). Following (Dillon, 1982; Ferron et al., 1998; Moum, 1996a) we assume that L_T is having a linear relationship with the Ozmidov scale L_O = 0.8 L_T, where $Lo = (\varepsilon N^{-3})^{1/2}$, so that we get finally:

$$\varepsilon_{Th} = 0.64 {L_T}^2 N^3 \tag{5.1}$$

where N is the mean buoyancy frequency of the 2.5 m sliding mean in the overturn patch region, defined as

$$N^2 = \frac{g}{\rho_0}\frac{d\rho}{dz} \tag{5.2}$$

Ellison scale analysis

The high-resolution temporal resolution of the temperature time series allows us to use an alternative proxy of the dissipation rate in this study using Ellison scale. First as was done for the Thorpe scale we assume that the potential temperature is a good proxy for the potential density and we define the Ellison scale (L_E) as (Ellison, 1957)

$$L_E = \overline{(\theta'^2)}^{1/2} \Big/ \left(d\bar{\theta}/dz \right) \tag{5.3}$$

with θ' the potential temperature fluctuation around the (time) mean value $\bar{\theta}$. Note that the temperature time series is filtered to consider only the fluctuation expected to turbulent events as describes in detail as follow.

As in Cimatoribus et al. (2014), we define θ' as the potential temperature turbulent fluctuation around the (time) mean value $\bar{\theta}$. In a well-controlled experiment, Cimatoribus et al. (2014) have compared Thorpe scale and Ellison scale and demonstrated that they fall within a factor of 2. If we want L_E to be representative of turbulent overturns length scale, θ' must be representative of turbulent fluctuations, hence we need to define the mean value $\bar{\theta}$ carefully in order to avoid internal waves contamination in the temperature fluctuations (Itsweire et al.,

1986, Cimatoribus et al 2014). This was done through a high pass wavelet filtering in Cimatoribus et al. (2014) with a cut off frequency $f_c \cong 1/600$ Hz, here we chose to simply apply a high pass 8th order Butterworth filter with a much higher cut-off frequency $f_c = 1/60$ Hz. We chose this value in order to smooth as much as possible temperature fronts associated with the non-linear high frequency internal waves packet while preserving high frequency turbulent fluctuations. The large ratio of 10 between the cut-off frequency of Cimatoribus et al. (2014) and our study roughly matches the ratio of the buoyancy frequency N in the two experiments, i.e. $N \cong 1\text{x}10^{-4}$ rad s^{-1} in the low stratified environment of Cimatoribus et al. (2014) and $N \cong 2\text{x}10^{-3}$ rad s^{-1} in our strongly stratified environment. Our cut-off value is also close to the lower bound defining the turbulent inertial-convective sub-range chosen by Zhang and Moum (2010) on an equatorial mooring where the stratification is comparable the Lombok strait stratification. Zhang and Moum (2010) outlined the contamination of the temperature fluctuations by strong surface waves pumping of their mooring. They eliminated this contamination using its signature on the cross correlation between the accelerometers and the temperature signal. During our experiment, the conditions were almost flat, yet close examination of the temperature signal and spectra revealed occasional signature of contamination by surface wave in the form of oscillation at a period of ~0.1 Hz and an associated spectral peak. Lacking accelerometers, we derived an empirical criterion to eliminate these portions of the signal. We compute the spectral density $S(f)$ of the de-trended θ over 2000 s windows. The valuable frequency range related to the turbulent fluctuations is set $>1/60$ Hz and we define the frequency range possibly related to the contamination by the surface wave within a frequency of $[1/15 - 1/8]$ Hz. A reference fitted spectrum $S_R(f)$ is then built by a power law fitting of the temperature spectrum $S(f)$ omitting points in the possibly contaminated range $[1/15 - 1/8]$ Hz. Finally, the ratio $r = \int_{1/12}^{1/6} S(f)df / \int_{1/12}^{1/6} S_R(f)df$ of the variance of the signal in the surface waves frequency band is computed. By visual inspection of the spectra $S(f)$ and corresponding time series, we determined that surface wave contamination was not detectable for $r > 0.6$, with this criteria 20% of the data were rejected. **Figure 5.2** shows an example of rejected spectrum and accepted spectrum.

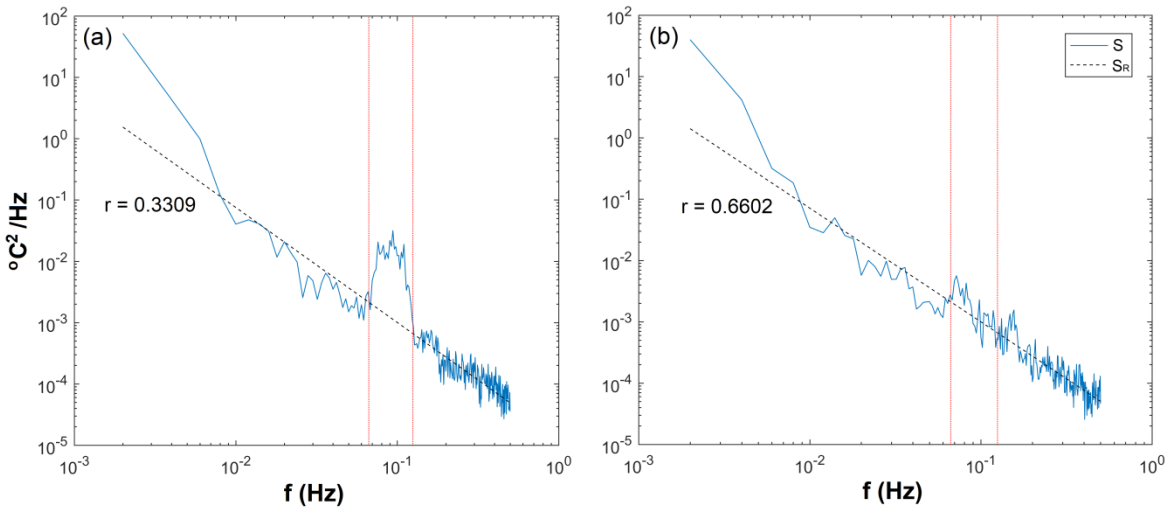

Figure 5.2 Spectrum of temperature fluctuations showing (a) contaminated by surface waves (r = 0.3309) and (b) not contaminated by surface waves (r = 0.6602). The black dashed line represents the power law fit $S_R(f)$ (see text for details). The red dashed lines mark the [1/15, 1/8] Hz which is the frequency band of possible surface waves.

An important source of error is the estimation of $d\overline{\theta}/dz$. Indeed, we estimate the mean temperature gradient from the temperature difference between successive temperature sensors, since these sensors are separated by a large distance of 40 m in average, this estimate may not represent the local gradient. Following the method of (Moum et al., 2011), an estimation of this local gradient can be obtained when surface waves dominate the signal over their frequency band Bw = [1/15 , 1/8] Hz. Indeed, in this case most of the temperature fluctuations generated in the range Bw results from vertical oscillations of the temperature sensors induced by the surface wave pumping of the mooring, as this is the case spectrum shown in **Figure 5.2**.a. The local temperature gradient can then be obtained by filtering the temperature and pressure/depth fluctuations in the range Bw and fitting θ against z to get the local slope $d\overline{\theta}/dz$. This was done for successive sequences of 120 s, an example of such a fit is shown in **Figure 5.3**.

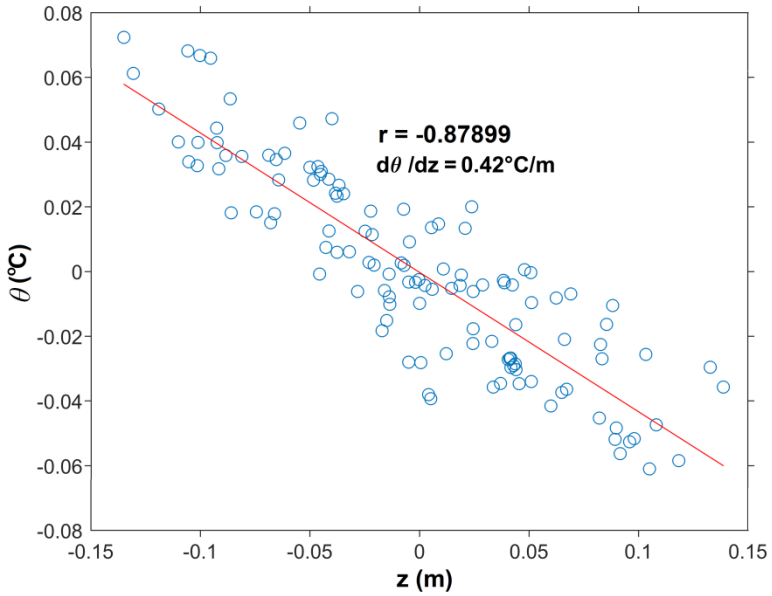

Figure 5.3 Fluctuations of temperature as a function of the sensor depth for a time sequence dominated by surface waves.

This estimate local estimate $\bar{\theta}_{z,local}$ can only be computed when surface waves dominate the frequency band *Bw*, that is ~20% of the time, but it can be used to estimate the dispersion between the local temperature gradient and the one based on temperature difference between two sensors $\bar{\theta}_{z,diff}$. The comparison is shown (in log scale) on **Figure 5.4**, we can see that although there is an important dispersion and there is no systematic bias between the two estimates. We find that 90% of $\bar{\theta}_{z,local}$ values are within [0.28, 4.6] $\bar{\theta}_{z,diff}$ (marked by white dashed lines). The dispersion for the $\log_{10}$ of the ratio $x = log_{10}(\bar{\theta}_{z,diff}/\bar{\theta}_{z,local})$ is close to Gaussian with a close to zero mean value of x = -0.017 and a standard deviation σ_x = 0.55 (**Figure 5.8**). In the following, we use this Gaussian fit to compute the confidence interval on $\bar{\theta}_{z,diff}$ and the resulting error on the computation of the Ellison scale and derived dissipation rate. Then, the Ellison scale, L_E is calculated using Eq. (5.3) and eventually, we determine the turbulent dissipation rate as:

$$\varepsilon_E = {L_E}^2 N^3 \tag{5.6}$$

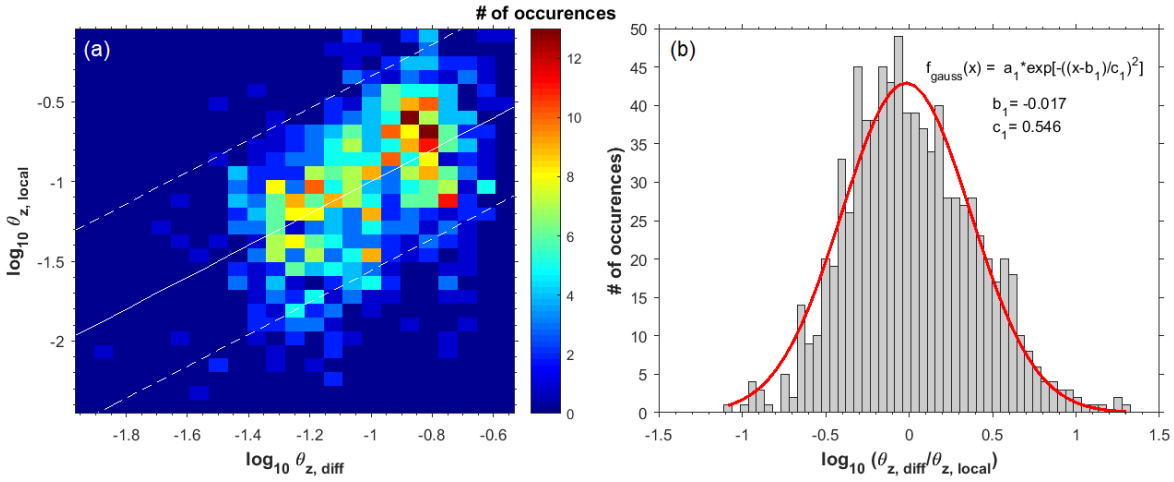

Figure 5.4 (a) Number of occurrences plot in bins of $\bar{\theta}_{z,diff}$ and $\bar{\theta}_{z,local}$, (b) distribution of $x = log_{10}(\bar{\theta}_{z,diff}/\bar{\theta}_{z,local})$ and its Gaussian fit. The white dashed lines in (a) represent 90% of $\bar{\theta}_{z,local}$ values are within [0.28, 4.6] $\bar{\theta}_{z,diff}$.

The Thorpe scale method provides ε estimates when density overturns or turbulent fluctuations overcomes the noise level or spurious process contamination (surface waves, mooring line motion). As a result, the statistics of ε is biased toward high values when no assumption is made for the main part of the water column where no density overturns or turbulent fluctuations are detected. For this part of the water, we assume a lower bound background dissipation rate ε from a fine-scale parameterization for internal waves. We set the background dissipation rate as $\varepsilon_{background} = \max(\varepsilon_{Overturn\text{-}background}, \varepsilon_{GM\text{-}background})$ where $\varepsilon_{Overturn\text{-}background}$ is the minimum resolvable dissipation rate by the CTD sensors, and $\varepsilon_{GM\text{-}background}$ is the Garrett and Munk (hereinafter, GM) dissipation rate. We set $\varepsilon_{Overturn\text{-}background}$ of 1 x 10^{-10} m^2s^{-3} as it has been used generally by previous authors (Alberty et al., 2017; Cuypers et al., 2017b; Frants et al., 2013; Koch-Larrouy et al., 2015). For the $\varepsilon_{GM\text{-}background}$, we assume that it follows the typical dissipation rate associated with GM wave field (Garrett and Munk, 1975). The $\varepsilon_{GM-background}$ is given by the fine-scale parameterization for internal waves (Gregg, 1989):

$$\varepsilon_{GM-background} = \varepsilon_0 \left(\frac{N^2}{{N_0}^2}\right)\left(\frac{S_{10}^2}{S_{GM}^2}\right) \tag{5.7}$$

where ε_0 = 7x10^{-10} m^2s^{-3} and N_0 = 3 cph is the canonical Garret and Munk (hereinafter GM) dissipation rate and respected buoyancy frequency reference, respectively. Such equation is based on the assumption of a constant shear to strain ratio equal to GM, (Polzin et al., 1995). Lacking shear measurements over the whole water column, we also assume that the local shear variance S_{10}^2 is equal to the canonical shear variance S_{GM}^2, thus verifies:

$$\varepsilon_{GM-background} = \varepsilon_0 \left(\frac{N^2}{{N_0}^2} \right) \tag{5.8}$$

This improved dissipation rate estimate that takes into account the background dissipation rate is later termed as $\varepsilon_{Th\text{-}GM}$, thus provides continuous profiles of dissipation rates as opposed to the standard Thorpe method, ε_{Th}.

5.3 Results and discussion

5.3.1 Hydrography

Our observations were conducted during a transition period from the southeast monsoon to the northwest monsoon so that we found less salty surface mixed layer than that of during the peak season of northwest monsoon, when the fresh water budget from the Java Sea entering the Lombok Strait. The stratification derived from the CTD profiles shows a thick pycnocline extending between 50 and 150 m depth with a maximum stratification near 85 m depth (**Figure 5.5**.d). The time mean currents (over the four M2 tidal periods recorded) show a strongly sheared structure with strong background westward zonal current of ~0.3 m s^{-1} and meridional current of ~0.5 m s^{-1} (see Appendix **Figure 5.10**) with northward and southward currents intruding and overlapping each other. We suggest that the persistent southward currents is related to the ITF current, while the northward currents is presumably influenced by semi-annual Kelvin wave events, which clearly appear during southeast monsoon transition period (November/December and April/May) as has been suggested by some previous studies (Sprintall et al., 2003, 1999; Susanto et al., 2001; Wijffels et al., 2002). The time mean squared shear measured by the ADCP between 55 and 100 m shows strong values exceeding the N^2 values and leading to near critical *Ri* values.

The time series of temperature recorded from the mooring sensors show a clear non-linear semidiurnal signal characterized by periodic large troughs (**Figure 5.6**.a). The peak to peak amplitude reaches ~90 m for the 20°C isotherm located in the pycnocline, which is larger than internal tides observed in the Makassar Strait and Buru strait (Purwandana et al., 2019); Seram Sea and Flores sea (Ffield and Robertson, 2008); and comparable to the largest observed internal tides in the North Halmahera Sea and Ombai Strait, which were associated to very large turbulent dissipation rates (Bouruet-Aubertot et al., 2018). The low pass filter (period >3 hours) of 18, 20, 22° C isotherms time series show that each M2 period is composed of one large trough (T_0) of ~70 m and two smaller troughs (T_1, T_2) of ~20 m, evidencing higher harmonics (M4, M6) in the signal.

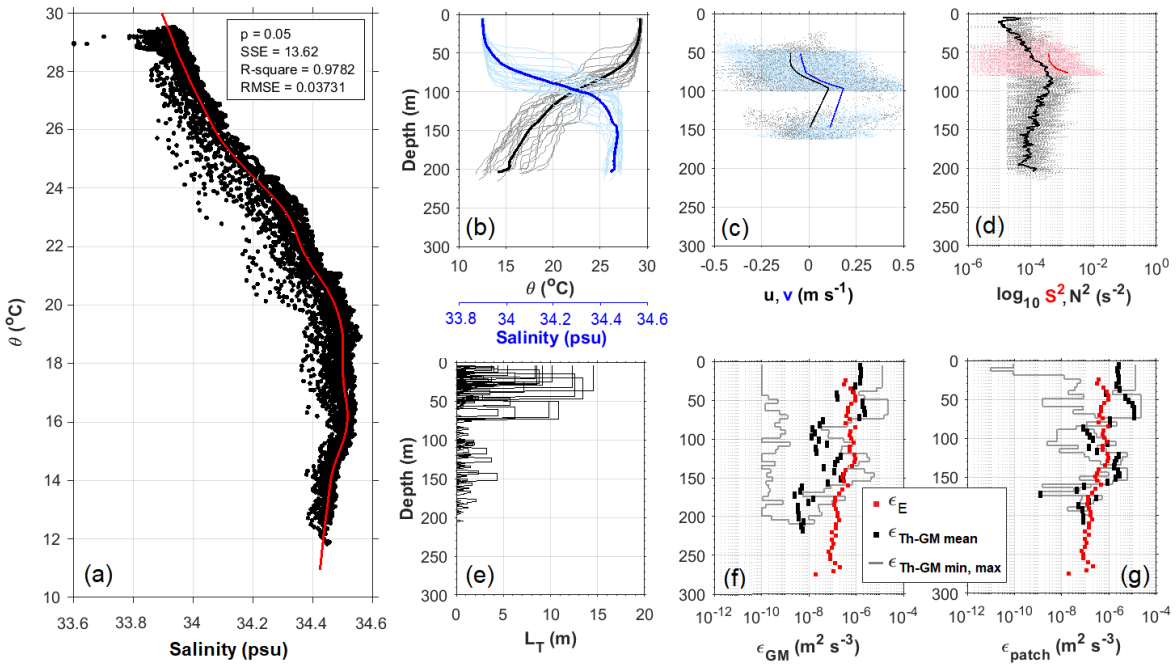

Figure 5.5 (a) Temperature-salinity relationship inferred using spline fit with the goodness values are indicated, (b) potential temperature and salinity profiles (grey and light blue plots, respectively) with its mean values (black and blue plots, respectively); (c) zonal, *u* and meridional, *v* (grey and light blue plots, respectively) with its mean values (black and blue plots, respectively); (d) the squared buoyancy and squared shear profiles (black and red dots, respectively) with its mean values (lines); (e) Thorpe length; (f) the 5 meters mean dissipation rate with background Garrett-Munk (GM) dissipation rate applied; and (g) that of considering the dissipation values in the turbulent patches only.

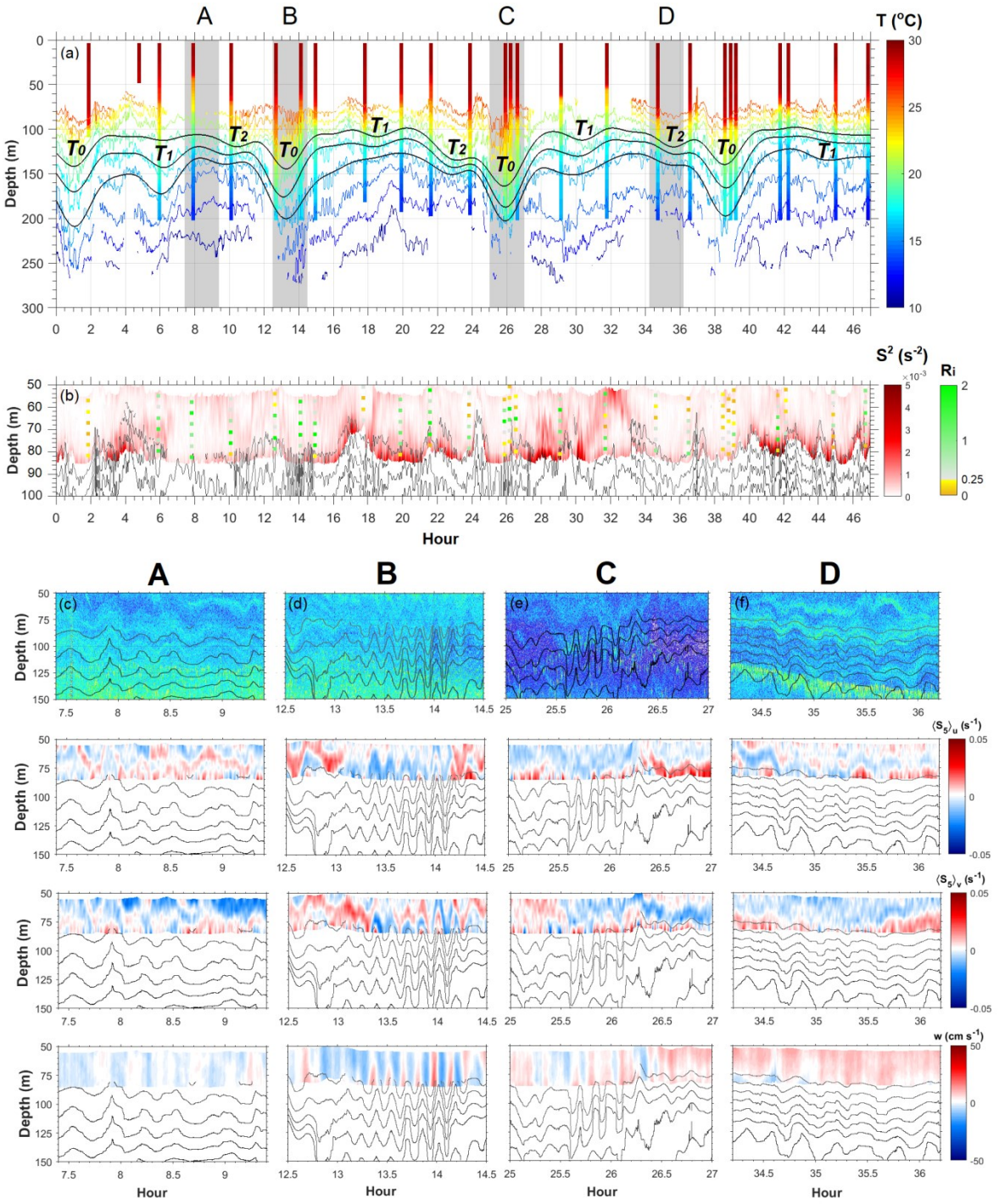

Figure 5.6 (a) Isotherm contours inferred from RBR sensors and temperature profiles from CTD casts. The black line is M2 low pass filtered for isotherm 18, 20, and 22° C. (b) is squared shear superimposed isotherms and Richardson number, *Ri*. (c, d, e, f) is the enlarged view of shaded area A, B, C and D in (a) for echosounder image in the first upper panel, zonal shear, $(S_5)_u$, meridional shear $(S_5)_v$ and vertical current *w*. Note that the vertical range of the valid current measurements is only between ~50-85 m. Enlarged images for annotated area A, B, C, D denote the appearance of fast period internal waves (B, C) and low period internal waves (A, D). T_0 and (T_1, T_2) is the large and the small trough, an indication of M2 and higher harmonic signals (M4, M6).

5.3.2 ISWs characteristics

The barotropic velocities over the NPS, U_{bar} reach ~0.9 m s^{-1} during the period we sampled, since the mode-1 phase speed, c_1 is typically of 1 m s^{-1}, the Froude number, $Fr = U_{bar}/c_1$ gets closer to supercritical and it is expected that ISW are generated by the Lee waves mechanism (Maxworthy, 1979). Numerical experiments study (Aiki et al., 2011) and satellite observations images (Astawa Karang et al., 2012) show that an ISW packet can already be formed at about 10-20 km from NPS which is consistent with a rapid formation by a Lee wave mechanism. In our observations, high frequency waves are observed nearly continuously but the largest amplitude wave-packet is observed in the large trough of the second tidal period (**Figure 5.6** events B). A significant wave packet is also observed during the third period (**Figure 5.6** event C) but no clear wave packet is observed within the large trough of the first and fourth period. The waves generated during these events have a strong vertical coherency, a maximum amplitude of ~40 m, a short period of 9-12 minutes, and are associated with strong vertical velocities reaching 20 cm s^{-1}. The wave packet A has also a clear signature in the echosounder consistent with the isotherms displacements, the echo-sounder signal for packet B was unfortunately too noisy to be exploited. The high frequency waves induce a clear heaving of a background strongly layered shear. Since the high frequency waves are highly coherent vertically, they do not likely contribute to this small-scale (~20 m vertical scale) shear structure. This background shear structure may result from the interaction of internal tide, ITF, Kelvin waves and possibly near inertial waves, but our measurements period is too short to characterize them.

Distinct high frequency wave packets are also generated on the front face of *T*2 (as shown by the close up A and D) and are likely generated by the higher tidal harmonics composing the internal tide. They are characterized by a longer wave period of ~20 minutes and smaller maximum amplitude of ~20 m. They are associated with weaker vertical velocities of ~5 cm s^{-1}. They also induce clear heaving of the small-scale shear structure.

The phasing of the largest high frequency waves (events B, C) with the large troughs is consistent with a lee wave mechanism, yet none of the high frequency waves observed are rank ordered and they do not show a typical $sech^2$ solitary waves profiles as is generally expected from the Lee waves mechanism (Apel et al., 1985; Maxworthy, 1979). This may be the result of an interaction with the sloping topography at our observation site. Indeed the depth variation and friction effects can alter the nonlinear terms driving the solitary wave packet evolution as was shown from classical extended KdV framework, in the Northwest

shelf of Australia by Holloway et al. (1999). Numerical and observational study in the strait of Gibraltar Vlasenko et al. (2009) has also evidenced frequent non ranked ordered packet that were attributed to multiple reflections from lateral boundaries along with friction and wave breaking. They also observe that if the non-rank ordered wave packet pursues its propagation over a flat bottom, the high frequency waves shall re-order. It is interesting to notice that satellite observation from the new HIMAWARI-8 satellite made on Nov 4 between 15.30 and 16.00 LT (local time) shows the propagation of a train of ISW with a clear pattern at the northern exit of the strait (**Figure 5.7**). These images were captured about 12 hours after we observed the main high frequency wave packets B. The leading ISW is about 80 km from our in-situ observation location, which suggests a phase speed of ~ 1.9 m s^{-1}, consistent with previous estimates (Susanto et al., 2005). The decreasing satellite signal intensity from the leading wave to the trailing waves suggest that wave packet is rank ordered when it exits Lombok Strait and that the non-rank order signal we observe is a local process.

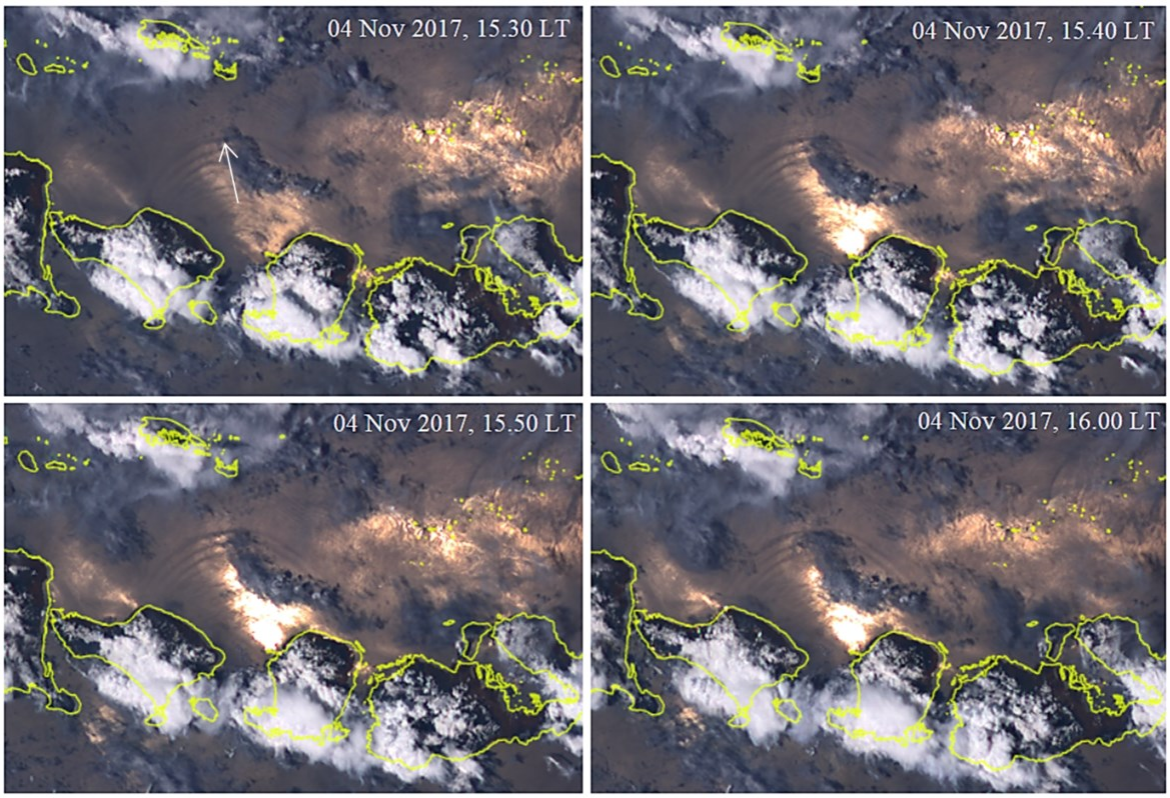

Figure 5.7 The observed ISWs signature (white arrow) by satellite images, HIMAWARI-8 on November 4th 2017: (a) at 15.30 LT, (b) 15.40 LT, (c) 15.50 LT and (d) 16.00 LT.

The fact that the ISW train is weaker on the third large trough and absent on the fourth large trough is surprising considering that the barotropic forcing is increasing. This

issue is somewhat related to the weaker northward meridional current (~stronger southward current/ITF current) hence potentially decreasing the ability of the waves to maintain their shape. Since the depth covered by our ADCP measurements was limited to the depth of ~50-100 m, the core of maximum vertical velocity may be deeper than the range of the measurements.

5.3.3 Dissipation estimates

Our ADCP measurements within the thermocline layer as shown in **Figure 5.5**.d shows a wide range of variation of the shear, its mean values is higher than the mean of squared buoyancy profile while the instantaneous profile shows frequent supercritical condition ($Ri=N^2/S^2$ <0.25), which is remarkable considering that we are located in the strongly stratified thermocline. Elevated dissipation rate are observed in the temporal evolution of $\varepsilon_{\text{E-patch}}$ in **Figure 5.5**.g, where the most persistent elevated dissipation rate occurred in the upper layer, >120 m depth.

The time and depth mean values of the dissipation rate result in an upper bound patch estimates of $\varepsilon_{\text{Th-patch}}=2.28\text{x}10^{-6}$ m^2s^{-3} and its standard deviation $3.15\text{x}10^{-6}$ m^2s^{-3}; the lower bound GM background estimate of $\varepsilon_{\text{Th-GM}}=4.95\text{x}10^{-7}$ m^2s^{-3} and its standard deviation $7.28\text{x}10^{-7}$ m^2s^{-3}; $\varepsilon_{\text{E}}=3.44\text{x}10^{-7}$ m^2s^{-3} and its standard deviation $5.70\text{x}10^{-7}$ m^2s^{-3}. These values characterize strong dissipation rates in the pycnocline which can be compared to the higher thermocline dissipation rate found in the Halmahera Sea during the INDOMIX expedition (Bouruet-Aubertot et al., 2018). The time-mean depth profiles of the dissipation rate varies in the range $[10^{-8}\text{-}10^{-6}]$ m^2s^{-3} with smaller values for the Thorpe method at the pycnocline peak, which may result from a bias in detection overturns for the strongest stratification. The discrepancy between the Thorpe and Ellison method is larger when we consider the lower bound GM background estimate that results from the much less frequent detection of overturns L_{T} than that of L_{E} (**Figure 5.5**.f).

Figure 5.8.a shows spatio-temporal evolution of the dissipation rate measured at six thermistors depths, which shows enhanced dissipation rate at M2 period. The time evolution of the depth integrated dissipation rate shows a comparable temporal evolution pattern between the vertical mean of ε_{Th} and ε_{E} as shown in **Figure 5.8**.b. A clear semidiurnal pattern emerge with peak dissipation exceeding $1\text{x}10^{-6}$ m^2s^{-3} and reaching up to $1\text{x}10^{-5}$ m^2s^{-3} observed within the large internal tide troughs (marked by vertical dashed lines in **Figure 5.8**.b). The time series of the dissipation rate from the Ellison estimate also show a decreasing trend of the dissipation rate with depth, with the higher values observed for the two shallower

temperature sensors (80 and 120 m average depth) surrounding the pycnocline peak where frequent supercritical conditions are observed from shear measurements.

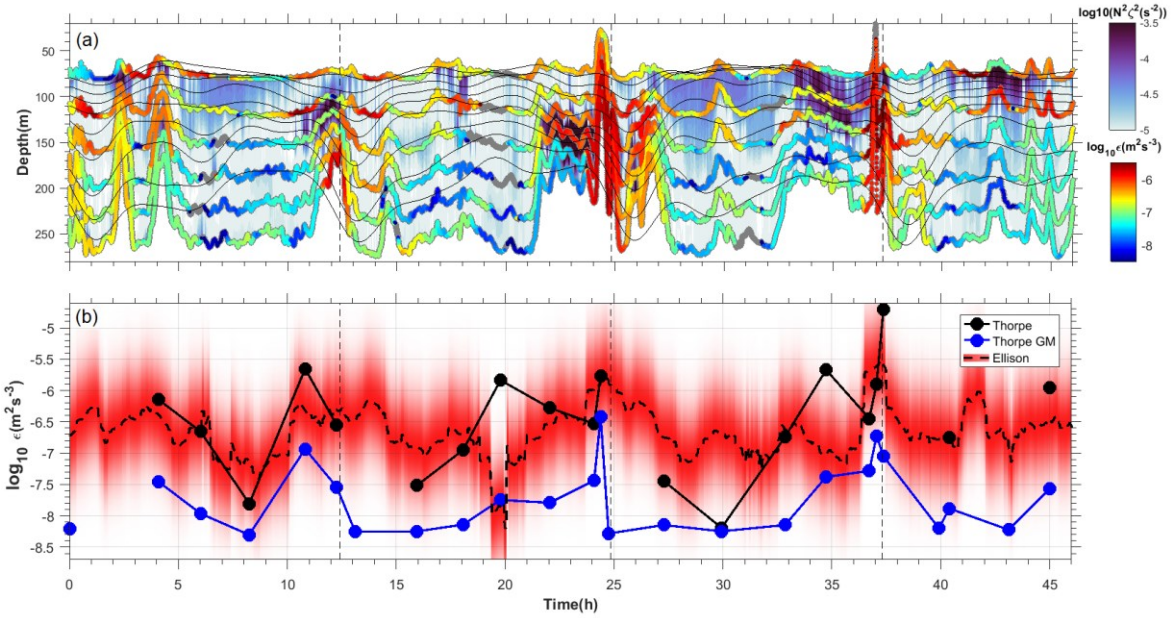

Figure 5.8 (a) Spatio-temporal evolution of the stratification scaled strain (scaled in $\log_{10}$, background blue contours), the dissipation rate estimated using Ellison scale (ε_E) at several mooring depth (scaled in $\log_{10}$, in rainbow contours; note that the profile fluctuations was following the sensors displacements); and the low pass filtered (<8h) of the isotherm profiles (black contours). (b) Mean over the depth covered by the mooring of the dissipation rates inferred using Thorpe scale patch and that considering the GM dissipation background (black dotted line and blue dotted line plots, respectively), and Ellison scale (dashed line for the mean and shaded red area for its fluctuations assuming the Gaussian distribution shown by Figure 5.4.b for the error made using $\bar{\theta}_{z,diff}$ to estimate the local gradient, note that the shading intensity decreases with the probability.

Since our shear measurements are limited to the 55-100 m depth, we also computed the background scaled strain from the temperature sensors as $\bar{N}^2\,{\zeta_z}^2$ with $\zeta_z = (N^2 - \bar{N}^2)/\bar{N}^2$ and N^2 is the time varying stratification computed from the temperature derived potential density and $\bar{N}^2$ its time average. Note that the mean values of $\bar{N}^2\,{\zeta_z}^2$ and S2 are related by the strain/shear ratio $R_\omega = \bar{N}^2\,\overline{{\zeta_z}^2}/\overline{S^2}$ which is expected to evolve between one for high frequency dominated internal waves field ($\omega \to N$) to infinity for low frequency internal waves field ($\omega \to f$) (Kunze et al., 1990). Here, the internal waves field is dominated by the M2 frequency and its harmonics, which represent relatively high frequency field compared to the local low value of $f = 0.17\ \omega$M2. Therefore, we can expect the scaled strain to be a reasonable proxy for S2. The scaled strain is shown in the background of **Figure 5.8**.a,

where a good correlation is observed between the high values of the dissipation rate ε_E and high scaled strain values.

We further inspect the correlation of the dissipation rate to available potential energy per unit time, scaled by the mean stratification, $(1/2)\bar{N}^3\zeta^2$ where $\zeta = (g/\rho_0)(d\rho/dz)/\bar{N}^2$. **Figure 5.9**.a shows the bin averaged occurrence of turbulent events in $[log_{10}(0.5\,\bar{N}^3\zeta^2), log_{10}(\varepsilon_E)]$ space. The $\log_{10}$ of the mean and the median value of ε_E for a given $log_{10}(\bar{N}^2\,\zeta_z{}^2)$ bin are superimposed as circles and crosses with a respective best fit $log_{10}\left(\overline{\varepsilon_E}_{0.5\bar{N}^3\,\zeta^2}\right) = 0.45\,log_{10}(0.5\,\bar{N}^3\zeta^2) - 5.36$ and $log_{10}\left(med(\varepsilon_E)_{0.5\bar{N}^3\,\zeta^2}\right) = 0.62\,log_{10}(0.5\,\bar{N}^3\zeta^2) - 6.26$. We also inspect the dependency of the dissipation rate to background scaled strain from the temperature sensors $\bar{N}^2\,\zeta_z{}^4$ to be compared to the canonical GM spectrum, the classical strain based wave-wave parameterization, $\varepsilon_E \sim \bar{N}^2\,\zeta_z{}^4$ (Whalen et al., 2012; Wijesekera et al., 1993). **Figure 5.9**.b shows the bin averaged occurrence of turbulent events in $[log_{10}(\bar{N}^2\,\zeta_z^4), log_{10}(\varepsilon_E)]$ space. We found a respective best fit $log_{10}\left(\overline{\varepsilon_E}_{\bar{N}^2\,\zeta_z^4}\right) = 0.06\,log_{10}(\bar{N}^2\zeta_z^4) - 6.11$ and $log_{10}\left(med(\varepsilon_E)_{\bar{N}^2\,\zeta_z{}^4}\right) = 0.10\,log_{10}(\bar{N}^2\zeta_z^4) - 7.20$. These suggest a power law dependence for the dissipation rate in the form $\varepsilon_E \sim (\bar{N}^2\,\zeta_z{}^2)^{\alpha}$ with a weak power law exponent $\alpha<0.5$. This findings suggest that specific parameterization is required to better characterize these highly nonlinear situations.

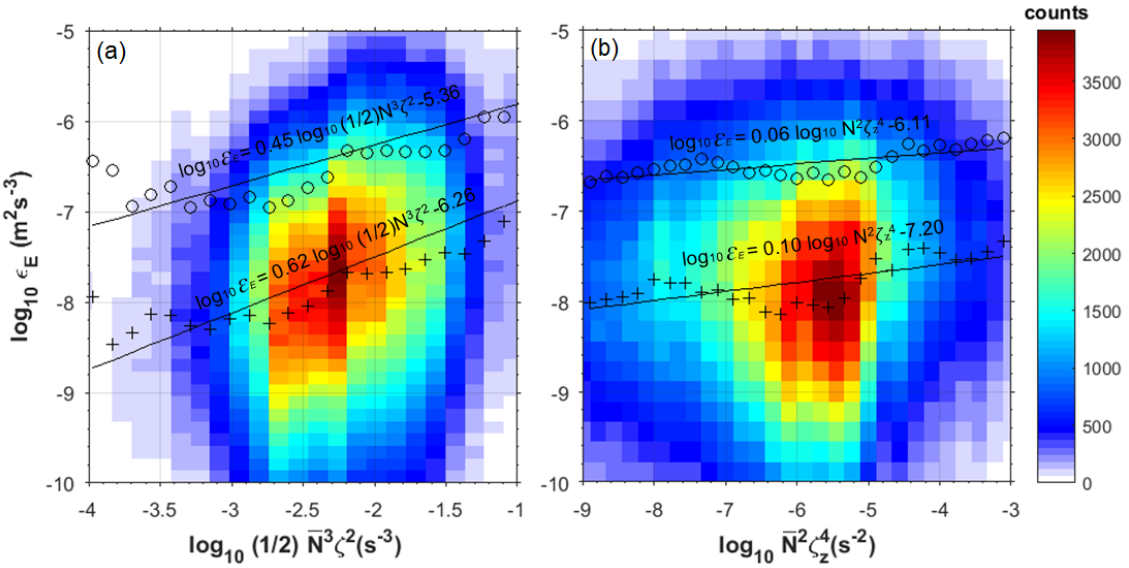

Figure 5.9 (a) Number of events matching a bin value of $(1/2)\bar{N}^3\zeta^2$ which represents the available potential energy s^{-1} and ε_E, (b) and those for $\bar{N}^2\zeta_z^4$ and ε_E. Black line plots indicate the mean (circle plots) and median value (cross plots) of the dissipation rate as a function of binned value of $(1/2)\bar{N}^3\zeta^2$ or $\bar{N}^2\zeta_z^4$ respectively.

5.4 Concluding remarks

We provide the first high frequency in-situ observations of strong semidiurnal internal tides (~90 m amplitude) in the Lombok Strait at a short distance of about 30 km from the generation source at the Nusa Penida sill. Frequent signatures of high frequency (10-20 minutes period), high vertical velocity internal wave trains are observed. The largest high frequency wave packets (with waves reaching up to 40 m) are observed within the M2 periodic large internal tide trough, but weaker high frequency waves packet seem to be associated with higher tidal harmonics. Although satellite observations during the same time period suggest the presence of a well-organized rank-ordered ISW packet north of the Lombok strait, the high frequency waves packet we observed are not rank ordered. We attribute this effect to possible interaction of the high frequency waves with the sloping topography. Another striking feature is the disappearance of ISW within the fourth observed internal tidal trough while the barotropic forcing is increasing. We have no clear explanation for this observation yet, it is possible that the strong mixing generated at the sill alter the stratification structure and the generation of ISW.

Two turbulence length scales the Thorpe and Ellison scales were used to estimate the turbulent dissipation rate from spotted time series of CTD measurements and high temporal resolution temperature sensors. The dissipation rate in the Lombok strait thermocline is high in the order of ~[10^{-6}-10^{-7}] m^2s^{-3}, comparable to that observed in other turbulent hot spots location such as the north and south Halmahera Straits and the Ombai Strait (Bouruet-Aubertot et al., 2018). The shear measurements made over a limited layer in the upper thermocline shows that frequent super critical conditions are reached. The shear vertical structure is characterized by small scale of ~20 m which is weakly influenced by the low mode high frequency waves but experience strong high frequency variation associate to the high frequency waves heaving. We also found a clear phasing between the M_2 internal tidal trough and the elevated dissipation rate estimated using both turbulent scales. We also investigated the dependence of the dissipation rate on the scaled strain and found a weak dependence compared to what is expected for canonical wave-wave parameterization of the dissipation rate in GM wave field.

5.5 Acknowledgments

This observation has been funded by Indonesian Endowment Fund Scholarship Program (LPDP), Indonesian Ministry of Finance; Nusantara Project, a joint program between Campus France and Indonesian Ministry of Research and Technology (KEMENRISTEK); and Research Center for Oceanography-Indonesian Institute of Sciences (LIPI). We are also grateful to all staffs of Marine Bio-industry Research Station of LIPI, Lombok, for preparing the accommodations during the field research.

5.6 Appendix

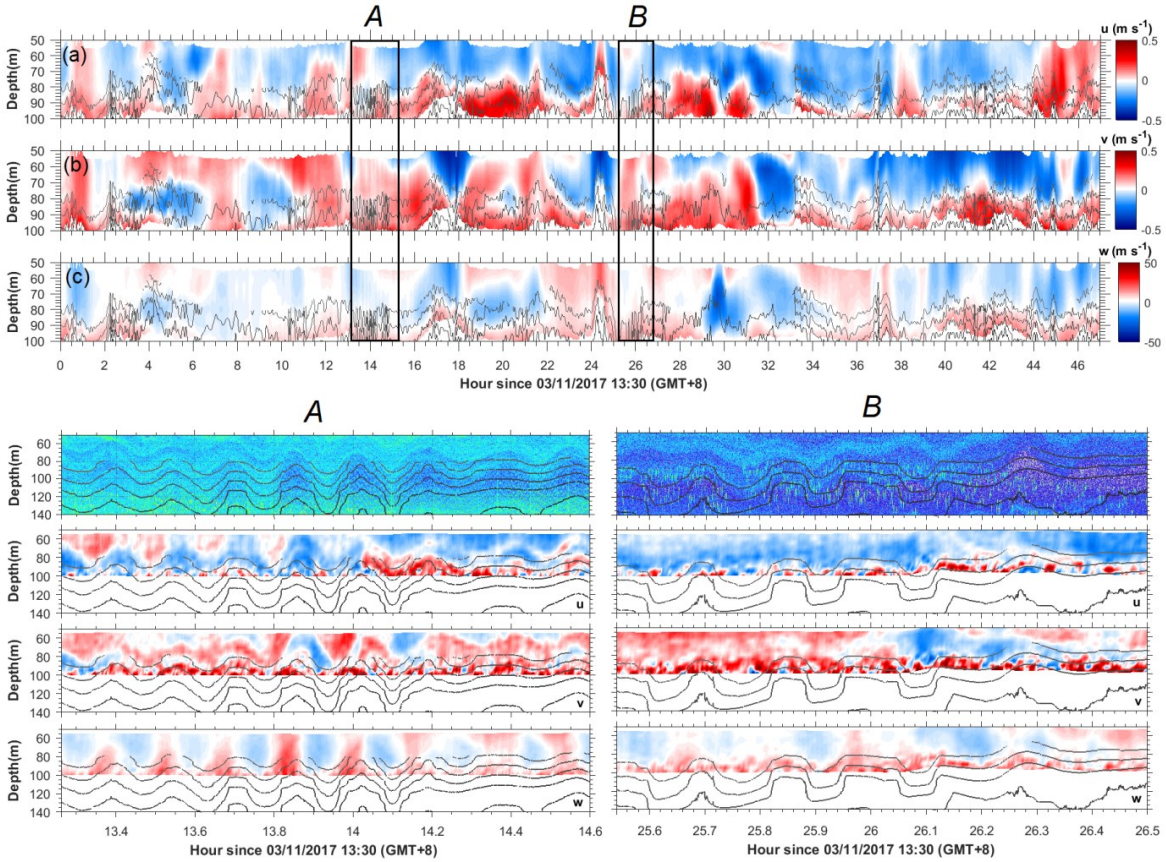

Figure 5.10 (a) zonal current component, *u*; (b) meridional current component, *v*; (c) vertical velocity, *w*. Enlarged view of event *A* and *B* is shown in the lower panel.

6
Conclusions and Perspectives

Chapter 6
Conclusions and Perspectives

6.1 Summary of the main results

Vertical turbulent mixing was known to be the main mechanism responsible for the transformation of the Pacific water masses flowing through the Indonesian seas toward the Indian Ocean. This thesis focused on this process with two main objectives: the first one was to get further insights on the spatial variability of turbulent mixing based on the analysis of a 21 years historical dataset of hydrological measurements while the second one aimed at better characterizing internal solitary waves all along their lifecycle.

The Indonesian seas are characterized by a complex bathymetry, featured by many straits and shallowing passages connecting interior semi enclosed basins. These geographical features, combined with an energetic barotropic tide, make it a favorable zone for internal tide generation and a region of intense mixing since most of the internal tide energy dissipates locally. The internal tide propagation is also strongly influenced by the presence of a permanent strong current, the Indonesian throughflow mainly involving the thermocline layer. The throughflow has two branches, the western one and the eastern one. The western route path with water masses originating from the North Pacific, goes through the Sulawesi Sea, the Makassar Strait and the Flores Sea. Part of the western route flow exits directly into the Indian Ocean through the Lombok Strait while the remaining western route flow enters eastward in the Banda Sea. The eastern route, involving water masses from the South Pacific, flows through the Halmahera Sea prior to flow into the Maluku Sea and the Seram Sea via the Lifamatola passage before entering the Banda Sea. The eastern route and the exit passages are characterized by the presence of shallow and narrow passages (e.g. Halmahera portals, Lifamatola passage, Buru Strait, Manipa Strait, and Lesser Sunda straits), that are regions of strong internal tide generation and where the turbulence is also enhanced by the accelerated mean flow current. Instead, there are almost no restricting passages along the western route except in the Sangihe sills at the gate of the ITF in the Mindanao Strait and Dewakang sills in the southern Makassar Strait.

Turbulent kinetic energy dissipation rates and vertical diffusivities were inferred from historical CTD measurements gathering an historical 26 years data from Indonesian and international cruises. Dissipation rates were inferred from the CTD using an improved Thorpe scale method, which was validated against microstructure measurements. Elevated dissipation

rates ~ [10^{-6}-10^{-7}] m^2s^{-3}, were observed in the near field stations, such as in the straits, narrowing passages and shallowing topography where internal tides are generated and ITF is intense, while lower dissipation rates ~ [10^{-8}-10^{-10}] m^2s^{-3} were observed in the far field stations and below the pycnocline. Along the western route of ITF, the main mixing hot spots are located in the Labani Channel and shallowing topography of the Dewakang waters; along the eastern route are located in the straits of Halmahera, Lifamatola, Buru; and in the exit passages are located in the Lombok, Sape and Ombai Straits. The eastern route is more dissipative than the western route, which is consistent with the existence of numerous narrowing channels of enhanced turbulence leading to a stronger erosion of the salinity peak of the Pacific waters along this eastern route. The spatial pattern of dissipation rates inferred from the high-resolution 3D hydrodynamics model output of Nagai and Hibiya (2015) showed a general agreement with the observations in the location of the mixing hot spots and suggests that the M_2 internal tide is the dominant factor driving the turbulent kinetic dissipation rates in the Indonesian seas. Yet the model also showed a bias toward lower dissipation rate in the pycnocline, that we attribute to the lack of representation of the ITF and mesoscale circulation and a bias toward higher dissipation rate in the weak mixing region, suggesting an overestimation of the background dissipation rate in calm waters.

The strong turbulence mostly originates from the degeneration of internal tides through various processes involving interaction with the strong currents, reflexion and scattering and nonlinear interactions. One peculiar process is the generation of internal solitary waves. The second part of this thesis addressed this question with a case study in the Sulawesi Sea where high frequency measurements, collected in 2009 by RCO-LIPI, revealed the presence of solitary waves in the Manado Bay. The starting point of the study was to estimate the dissipation rates of turbulent kinetic energy induced by the breaking of these waves in this coastal area. The question of the formation of these ISWs was then addressed based on satellite images and 2D numerical simulations. The origin of the ISWs was first inferred from SAR images giving evidence of their propagation from the Sibutu passage where large amplitude internal tides are generated. These observations were then used to set 2D non-hydrostatic numerical simulations along a relevant section starting from the generation area of the internal tides and ending in Manado Bay that reproduce the internal tide generation and fate. Our 2D non-hydrostatic simulations indicated that the ISWs in the Sulawesi Sea are formed through a non-linear steepening mechanism, predominantly triggered by semidiurnal tide over the Sibutu Passages. This mechanism is efficient in extracting energy from the internal tide leading to a decrease of its energy flux of a few tenth percent and quantifies the

potential impact of ISWs on turbulence generation in shallow areas. The internal tide energy flux emanated from the passage is comparable to that of existing tidal energy flux estimates, in the Gaoping Canyon off Taiwan (Lee et al., 2009) and in the Hawaiian Ridge (Lee et al., 2006); but higher compared to that of in the Monterey Submarine Canyon off California (Kunze et al., 2002) and Great Meteor Seamount (Gerkema and Van Haren, 2007). A simplified model, which does not involve the background mean current of the Sibutu throughflow, is a limiting factor in this study, which should be addressed in the future. Higher resolution simulations were next conducted in order to capture the shoaling internal waves observed in the Manado Bay. We found that the steep and sharp shelf break over the bay greatly enhanced the turbulent mixing consistently with the observations. A simplified simulation, which neglected sea surface cooling due to atmospheric forcing and less spatial resolution to resolve the KH instabilities are limiting factors in the simulation. Our in-situ dissipation rate estimates is comparable to that of observed in the Irish Sea, $\sim 10^{-6}$ m^2s^{-3} (Simpson et al., 1996), one order higher than those observed in the Scotian Shelf (Sandstrom and Oakey, 1995) and two order higher than in the Monterey Bay shelf (Carter et al., 2005), but lower than in the South China Sea around Dongsha plateau (Alford et al., 2015). The estimated diffusivity value is $\sim 10^{-4}$ m^2s^{-1} which is one order lower than in the Oregon shelf (Nash and Moum, 2001), one order higher than in the Monterey Bay shelf, (Carter et al., 2005), and three order lower than in the South China Sea (Alford et al., 2015).

Motivated by the curiosity to explore the nature of the high frequency spatio-temporal variability of the turbulent mixing, a short field observation was conducted in one of the remarkable internal tide generation sites in the Indonesian seas, the Lombok Strait. We reported the first in situ observation of the large amplitude non-linear internal tides generated by the semidiurnal tidal flow over Nusa Penida sills as well as an early stage signature of high frequency internal wave trains. The most prominent high frequency wave packet we observed were phased with the large internal tide trough but were not rank ordered as could be expected from the usual KdV theory, a feature that we attribute to the possible interaction with the sloping bottom of the Lombok Island shelf. On the opposite, satellite images acquired during the observation period showed that wave packet exiting the strait recovered a well-organized rank ordered structure. Two methods based on turbulence length scales were employed to estimate the dissipation rate, the Thorpe and the Ellison scales. The mean turbulent kinetic energy dissipation rate we observed in the Lombok Strait thermocline is $\sim[10^{-6}\text{-}10^{-7}]$ m^2s^{-3}, which is comparable to that observed in the thermocline north and south

Halmahera Straits, the Ombai Strait, ~10^{-7} m^2s^{-3} (Bouruet-Aubertot et al., 2018). We observed a good correlation between semidiurnal internal tide troughs and peak in the dissipation rate confirming that this one is mainly driven by the internal tide dynamics.

6.2 Perspectives

6.2.1 Mixing estimates from historical datasets in the Indonesian seas

Inferring the dissipation rates from the Thorpe method applied to CTD data sets present three limitations: (1) the dissipation rate can only be estimated where overturns are detected and a background dissipation is set somewhat arbitrarily in this case, (2) data must be processed to eliminate spurious overturns induced by noise from the profiles, (3) from a more fundamental point of view, the linear relationship between the Ozmidov scale and the Thorpe scale may not be universal and could depend on the dynamical context of the measurements, hence, ideally the Thorpe method needs to be validated by direct microstructure measurements. A proposed data processing, which tried to solve the first two issues, was presented in this thesis. Regarding the third issue, it was evidenced that our Thorpe estimates are comparable to the direct measurements with no systematic bias as a function of the energetic regime albeit of a large dispersion and performs relatively better than existing model studies. Yet the background dissipation rate we proposed is based on a simplified version of the Gregg-Henyey parameterization and has several caveats. It assumes that the background quieter energy level is correctly modeled by a GM field. Note that this assumption does not apply to the most energetic wave breaking events driving the detected overturns; there the turbulence is simply diagnosed without the necessity to call for a specific mechanism/parameterization. In other words, we somewhat assume that energetic internal tides driving the most prominent overturns propagate in a quieter GM background. We have no clear evidence for that. Moreover, in the improved Thorpe scale method we still imposes a minimum background dissipation rate of 10^{-10} m^2s^{-3} when the GM based dissipation rate gets lower than such value. This threshold was based on the minimum detected dissipation rate in the region but has no fundamental basis. The pdf of the dissipation rate that can be computed from detected overturns can be viewed as truncated pdf where a large part of the low dissipation rates associated to undetected overturns is missing. An alternative approach to the parameterized background dissipation rate used here, would be to fit a theoretical shape to these truncated pdfs, then the missing dissipation could be inferred form the fitted form. This approach was not pursued here because pdf would need to be built from restricted sub-sets of observations with comparable energy levels/stratification. With this restriction, the number of overturns detected within each sub-set seemed insufficient to provide a converged distribution. A keep growing number of CTD casts collected may allow in the future to pursue

such an approach, it will also improve our characterization and understanding the turbulent mixing characteristics in the Indonesian seas. Another important issue that could not be explored due to insufficient data sets is the temporal variation of the mixing induced by the seasonal variation of the ITF.

The absence of microstructure instruments owned by Indonesian marine research institutions up to now is a technical limitation to characterize and to validate model study and indirect observation based dissipation rate estimates. By 2022, this obstacle is expected to be raised as the Indonesian Institute of Sciences (LIPI) will launch its new research vessel, Baruna Jaya IX (**Figure 6.1**) with a standardized microstructure profiler instruments, VMP 500 by Rockland Scientific, Ltd.

Figure 6.1 Accepted design of Baruna Jaya IX-LIPI, which is scheduled to be built in 2020 and will be finished and launched in 2022.

6.2.2 Internal tide generation and enhanced mixing due to ISW breaking events

The Indonesian seas are the region of the world where the largest number of ISW are detected form space (Jackson, 2007). These processes are not resolved by current state of the art realistc regional models (Nugroho et al., 2017). The fraction of energy propagated by this wave and dissipating on the near shelves is therefore presently unknown in the Indonesian seas, studies from other prominet region of ISW regions have shown that they can have a dramatic impact on turbulent mixing in the near shore and resulting biogeochemical fluxes. This could be of crucial importance in the indonesian seas, which is a region of the world hosting one of the largest marine biodivesity albeit subjected to strong anthropic pressure. As we have shown two-dimensional non-hydrostatic simulation is a promising tool to estimate

the fraction of the internal tide energy flux, which eventually dissipates its energy over the shelves, away from its generation site. High spatio-temporal resolution simulation can also be used as a kind of proxy to the dissipation rate estimate as it was proved comparable to the observations. In the future, we expect to improve such simulation by adding involving a background mean flow, ideally by nesting the simulation in regional model. From the observational point of view, future fine structure characterization of the wave field and microstructure estimates of the dissipation rate shall also help us to better constraint these simulations. As was previously suggested by Cimatoribus et al. (2014) high frequency temperature time series is a promising tool to build times series of the dissipation rate using the Ellison scale. We have shown this feasability from our short experiment in the Lombok strait, despite of a sparse spatial resolution of the temperature sensors, anchored moored high frequency temperature sensors installation in expected ISW shoaling regions, as was done in several other areas (van Haren and Gostiaux, 2010, 2009), could probably help us to infer the importance of these processes in the Indonesian seas.

Bibliography

Adhyatma, D., Atmadipoera, A.S., Naulita, Y., Nugroho, D., Herlisman, 2019. Analysis of turbulent mixing in the Eastern Path of Indonesian Throughflow. IOP Conf. Ser. Earth Environ. Sci. 278, 012003. doi:10.1088/1755-1315/278/1/012003

Aiki, H., Matthews, J.P., Lamb, K.G., 2011. Modeling and energetics of tidally generated wave trains in the Lombok Strait: Impact of the Indonesian Throughflow. J. Geophys. Res. Ocean. 116. doi:10.1029/2010JC006589

Alberty, M.S., Sprintall, J., MacKinnon, J., Ganachaud, A., Cravatte, S., Eldin, G., Germineaud, C., Melet, A., 2017. Spatial patterns of mixing in the Solomon Sea. J. Geophys. Res. Ocean. 122, 4021–4039. doi:10.1002/2016JC012666

Alford, M.H., Gregg, M.C., 2001. Near-inertial mixing : Modulation of shear , strain and wave in the Banda Sea at low latitude. J. Geophys. Res. 106, 16947–16968.

Alford, M.H., Gregg, M.C., Ilyas, M., 1999. Diapycnal mixing in the Banda Sea: Results of the first microstructure measurements in the Indonesian Throughflow. Geophys. Res. Lett. 26, 2741. doi:10.1029/1999GL002337

Alford, M.H., Peacock, T., MacKinnon, J.A., Nash, J.D., Buijsman, M.C., Centuroni, L.R., Chao, S.-Y., Chang, M.-H., Farmer, D.M., Fringer, O.B., Fu, K.-H., Gallacher, P.C., Graber, H.C., Helfrich, K.R., Jachec, S.M., Jackson, C.R., Klymak, J.M., Ko, D.S., Jan, S., Johnston, T.M.S., Legg, S., Lee, I.-H., Lien, R.-C., Mercier, M.J., Moum, J.N., Musgrave, R., Park, J.-H., Pickering, A.I., Pinkel, R., Rainville, L., Ramp, S.R., Rudnick, D.L., Sarkar, S., Scotti, A., Simmons, H.L., St Laurent, L.C., Venayagamoorthy, S.K., Wang, Y.-H., Wang, J., Yang, Y.J., Paluszkiewicz, T., (David) Tang, T.-Y., 2015. The formation and fate of internal waves in the South China Sea. Nature 521, 65–69. doi:10.1038/nature14399

Alford, M.H., Zhao, Z., 2007. Global Patterns of Low-Mode Internal-Wave Propagation. Part I: Energy and Energy Flux. J. Phys. Oceanogr. 37, 1829–1848. doi:10.1175/JPO3085.1

Alonso, J., Vidal, J., Bruno, M., Ruiz-ca, A., Echevarr, F., Ruiz, J., 2002. The boiling-water phenomena at Camarinal Sill , the strait of Gibraltar 49, 4097–4113.

Anonym, 1900. The Dutch "Siboga" Expedition to the Malay Archipelago. Geogr. J. 16, 549–552. doi:10.2307/1774869

Apel, J.R., Holbrook, J.R., Liu, A.K., Tsai, J.J., 1985. The Sulu Sea Internal Soliton Experiment. J. Phys. Oceanogr. doi:10.1175/1520-0485(1985)015<1625:TSSISE>2.0.CO;2

Arneborg, L., 2002. Mixing Efficiencies in Patchy Turbulence. J. Phys. Oceanogr. 32, 1496–1506. doi:10.1175/1520-0485(2002)032<1496:MEIPT>2.0.CO;2

Astawa Karang, I.W.G., Nishio, F., Mitnik, L., Osawa, T., 2012. Spatial-Temporal Distribution and Characteristics of Internal Waves in the Lombok Strait Area Studied by Alos-Palsar Images. Earth Sci. Res. 1, 11–22. doi:10.5539/esr.v1n2p11

Atmadipoera, A., Molcard, R., Madec, G., Wijffels, S., Sprintall, J., Koch-Larrouy, A., Jaya, I., Supangat, A., 2009. Characteristics and variability of the Indonesian throughflow water at the outflow straits. Deep. Res. Part I Oceanogr. Res. Pap. 56, 1942–1954. doi:10.1016/j.dsr.2009.06.004

Awaji, T., 1982. Water Mixing in a Tidal Current and the Effect of Turbulence on Tidal Exchange through a Strait. J. Phys. Oceanogr. 12, 501–514. doi:10.1175/1520-0485(1982)012<0501:WMIATC>2.0.CO;2

Baines, P.G., 1982. On internal tide generation models. Deep Sea Res. Part A. Oceanogr. Res. Pap. 29, 307–338. doi:https://doi.org/10.1016/0198-0149(82)90098-X

Bingham, F.M., Lukas, R., 1994. The Southward Intrusion of North Pacific Intermediate Water along the Mindanao Coast. J. Phys. Oceanogr. doi:10.1175/1520-0485(1994)024<0141:tsionp>2.0.co;2

Bouffard, D., Boegman, L., 2013. A diapycnal diffusivity model for stratified environmental flows. Dyn. Atmos. Ocean. 61–62, 14–34. doi:10.1016/j.dynatmoce.2013.02.002

Bourgault, D., Blokhina, M.D., Mirshak, R., Kelley, D.E., 2007. Evolution of a shoaling internal solitary wavetrain. Geophys. Res. Lett. 34, 1–5. doi:10.1029/2006GL028462

Bourgault, D., Kelley, D.E., 2007. On the Reflectance of Uniform Slopes for Normally Incident Interfacial Solitary Waves. J. Phys. Oceanogr. 37, 1156–1162. doi:10.1175/JPO3059.1

Bourgault, D., Kelley, D.E., 2004. A laterally averaged nonhydrostatic ocean model. J. Atmos. Ocean. Technol. 21, 1910–1924. doi:10.1175/JTECH-1674.1

Bourgault, D., Kelley, D.E., Galbraith, P.S., 2008. Turbulence and boluses on an internal beach. J. Mar. Res. 66. doi:10.1357/002224008787536835

Bourgault, D., Morsilli, M., Richards, C., Neumeier, U., Kelley, D.E., 2014. Sediment resuspension and nepheloid layers induced by long internal solitary waves shoaling orthogonally on uniform slopes. Cont. Shelf Res. 72, 21–33. doi:10.1016/j.csr.2013.10.019

Bouruet-Aubertot, P., Cuypers, Y., Ferron, B., Dausse, D., Ménage, O., Atmadipoera, A., Jaya, I., Olivier, M., Atmadipoera, A., Jaya, I., 2018. Contrasted turbulence intensities in the Indonesian Throughflow: a challenge for parameterizing energy dissipation rate. Ocean Dyn. 68, 1–75. doi:10.1007/s10236-018-1159-3

Carrère, L., Lyard, F., 2003. Modeling the barotropic response of the global ocean to atmospheric wind and pressure forcing - comparisons with observations. Geophys. Res. Lett. 30, 1997–2000. doi:10.1029/2002GL016473

Carrere, L., Lyard, F., Cancet, M., Guillot, A., Roblou, L., 2012. FES 2012: a new global tidal model taking advantage of nearly 20 years of altimetry. 20 Years Prog. Radar Altimetry 6.

Carter, G.S., Gregg, M.C., Lien, R.C., 2005. Internal waves, solitary-like waves, and mixing on the Monterey Bay shelf. Cont. Shelf Res. 25, 1499–1520. doi:10.1016/j.csr.2005.04.011

Chong, J.C., Sprintall, J., Hautala, S., Morawitz, W.L., Bray, N.A., Pandoe, W., 2000. Shallow throughflow variability in the outflow straits of Indonesia. Geophys. Res. Lett. 27, 125–128.

Cimatoribus, A.A., Van Haren, H., Gostiaux, L., 2014. Comparison of ellison and thorpe scales from Eulerian ocean temperature observations. J. Geophys. Res. Ocean. 119, 7047–7065. doi:10.1002/2014JC010132

Cuypers, Y., Bouruet-Aubertot, P., Vialard, J., McPhaden, M.J., 2017a. Focusing of internal tides by near-inertial waves. Geophys. Res. Lett. 44, 2398–2406. doi:10.1002/2017GL072625

Cuypers, Y., Pous, S., Sprintall, J., Atmadipoera, A., Madec, G., Molcard, R., 2017b. Deep

circulation driven by strong vertical mixing in the Timor Basin. Ocean Dyn. 67, 191–209. doi:10.1007/s10236-016-1019-y

de Lavergne, C., Madec, G., Le Sommer, J., Nurser, A.J.G., Naveira Garabato, A.C., 2016. The Impact of a Variable Mixing Efficiency on the Abyssal Overturning. J. Phys. Oceanogr. 46. doi:10.1175/JPO-D-14-0259.1

Dillon, T.M., 1982. Vertical overturns: A comparison of Thorpe and Ozmidov length scales. J. Geophys. Res. 87, 9601. doi:10.1029/JC087iC12p09601

Dwi Susanto, R., Ffield, A., Gordon, A.L., Adi, T.R., 2012. Variability of Indonesian throughflow within Makassar Strait, 2004-2009. J. Geophys. Res. Ocean. 117, 2004–2009. doi:10.1029/2012JC008096

Egbert, G.D., Erofeeva, S.Y., 2002. Efficient Inverse Modeling of Barotropic Ocean Tides. J. Atmos. Ocean. Technol. 19, 183–204.

Ellison, T.H., 1957. Turbulent transport of heat and momentum from an infinite rough plane. J. Fluid Mech. 2, 456–466. doi:DOI: 10.1017/S0022112057000269

Farmer, D.M., Smith, D., 1980. Tidal interaction of stratified flow with a sill in Knight Inlet. Deep. Res. 27A, 239–254.

Ferron, B., Mercier, H., Speer, K., Gargett, A., Polzin, K., 1998. Mixing in the Romanche Fracture Zone. J. Phys. Oceanogr. 28, 1929–1945. doi:10.1175/1520-0485(1998)028<1929:MITRFZ>2.0.CO;2

Ffield, A., Gordon, A.L., 1996. Tidal Mixing Signatures in the Indonesian Seas. J. Phys. Oceanogr. doi:10.1175/1520-0485(1996)026<1924:TMSITI>2.0.CO;2

Ffield, A., Gordon, A.L., 1992. Vertical Mixing in the Indonesian Thermocline. J. Phys. Oceanogr. doi:10.1175/1520-0485(1992)022<0184:VMITIT>2.0.CO;2

Ffield, A., Robertson, R., 2008. Temperature finestructure in the Indonesian seas. J. Geophys. Res. Ocean. 113, 1–19. doi:10.1029/2006JC003864

Fieux, M., Andrié, C., Delecluse, P., Ilahude, A.G., Kartavtseff, A., Mantisi, F., Molcard, R., Swallow, J.C., 1994. Measurements within the Pacific-Indian oceans throughflow region. Deep. Res. Part I 41, 1091–1130. doi:10.1016/0967-0637(94)90020-5

Fieux, M., Molcard, R., 1996. Geostrophic transport of the Pacific-Indian Oceans throughflow. J. Geophys. Res. C Ocean. 101, 12421–12432.

Fine, R.A., Lukas, R., Bingham, F.M., Warner, M.J., Gammon, R.H., 1994. The western equatorial Pacific: A water mass crossroads. J. Geophys. Res. 99, 25063–25080. doi:10.1029/94jc02277

Finnigan, T.D., Luther, D.S., Lukas, R., 2002. Observations of Enhanced Diapycnal Mixing near the Hawaiian Ridge. J. Phys. Oceanogr. 32, 2988–3002. doi:10.1175/1520-0485(2002)032<2988:OOEDMN>2.0.CO;2

Frants, M., Damerell, G.M., Gille, S.T., Heywood, K.J., MacKinnon, J., Sprintall, J., 2013. An assessment of density-based finescale methods for estimating diapycnal diffusivity in the southern Ocean. J. Atmos. Ocean. Technol. 30, 2647–2661. doi:10.1175/JTECH-D-12-00241.1

Galbraith, P.S., Kelley, D.E., 1996. Identifying Overturns in CTD Profiles. J. Atmos. Ocean. Technol. 13, 688–702. doi:10.1146/annurev.fluid.39.050905.110314

Garcia Lafuente, J., Sarhan, T., Vargas, M., Vargas, J.M., Plaza, F., 1999. Tidal motions and tidally induced fluxes through La Linea submarine canyon, western Alboran Sea. J. Geophys. Res. 104, 3109–3119.

Gargett, A., Garner, T., 2008. Determining Thorpe scales from ship-lowered CTD density profiles. J. Atmos. Ocean. Technol. 25, 1657–1670. doi:10.1175/2008JTECHO541.1

Gargett, A.E., 1988. The scaling of turbulence in the presence of stable stratification. J. Geophys. Res. Ocean. 93, 5021–5036. doi:10.1029/JC093iC05p05021

Garrett, C., Munk, W., 1975. Space-time scales of internal waves: A progress report. J. Geophys. Res. 80, 291–297. doi:10.1029/JC080i003p00291

Garrett, C., Munk, W., 1972. Oceanic mixing by breaking internal waves. Deep Sea Res. Oceanogr. Abstr. 19, 823–832. doi:https://doi.org/10.1016/0011-7471(72)90001-0

Gerkema, T., 1996. A unified model for the generation and fission of internal tides in a rotating ocean. J. Mar. Res. 54, 421–450. doi:10.1357/0022240963213574

Gerkema, T., Van Haren, H., 2007. Internal tides and energy fluxes over Great Meteor Seamount. Ocean Sci. 3, 441–449. doi:10.5194/os-3-441-2007

Gordon, A.L., 2005. Oceanography of the Indonesian Seas and their throughflow. Oceanography 18, 14–27. doi:10.5670/oceanog.2005.18

Gordon, A.L., 2001. Interocean Exchange, in: Siedler, G., Church, J., Gould, J. (Eds.), Ocean Circulation and Climate. Academic Press, pp. 303–316.

Gordon, A.L., Fine, R.A., 1996. Pathways of water between the Pacific and Indian oceans in the Indonesian seas. Nature 379, 146–149. doi:10.1038/379146a0

Gordon, A.L., Giulivi, C.F., Ilahude, A.G., 2003. Deep topographic barriers within the Indonesian seas. Deep. Res. Part II Top. Stud. Oceanogr. 50, 2205–2228. doi:10.1016/S0967-0645(03)00053-5

Gordon, A.L., Huber, B.A., Metzger, E.J., Susanto, R.D., Hurlburt, H.E., Adi, T.R., 2012. South China Sea throughflow impact on the Indonesian throughflow. Geophys. Res. Lett. 39, 1–8. doi:10.1029/2012GL052021

Gordon, A.L., McClean, J.L., 1999. Thermohaline Stratification of the Indonesian Seas: Model and Observations*. J. Phys. Oceanogr. 29, 198–216. doi:10.1175/1520-0485(1999)029<0198:TSOTIS>2.0.CO;2

Gordon, A.L., Susanto, R.D., Ffield, A., Huber, B.A., Pranowo, W., Wirasantosa, S., 2008. Makassar Strait throughflow, 2004 to 2006. Geophys. Res. Lett. 35, 3–7. doi:10.1029/2008GL036372

Gregg, M.C., 1989. Scaling turbulent dissipation in the thermocline. J. Geophys. Res. Ocean. 94, 9686–9698. doi:10.1029/JC094iC07p09686

Gregg, M.C., 1988. Mixing in the Thermohaline Staircase East of Barbados, in: Nihoul, J.C.J., Jamart, B.M.B.T.-E.O.S. (Eds.), Small-Scale Turbulence and Mixing in the Ocean. Elsevier, pp. 453–470. doi:https://doi.org/10.1016/S0422-9894(08)70564-6

Gregg, M.C., 1987. Diapycnal mixing in the thermocline: A review. J. Geophys. Res. 92, 5249. doi:10.1029/JC092iC05p05249

Gregg, M.C., D'Asaro, E.A., Riley, J.J., Kunze, E., 2018. Mixing Efficiency in the Ocean. Ann. Rev. Mar. Sci. 10, 443–473. doi:10.1146/annurev-marine-121916-063643

Halpern, D., 1971. Semidiurnal internal tides in Massachusetts Bay. J. Geophys. Res. 76, 6573–

6584. doi:10.1029/JC076i027p06573

Hatayama, T., 2004. Transformation of the Indonesian throughflow water by vertical mixing and its relation to tidally generated internal waves. J. Oceanogr. 60, 569–585. doi:10.1023/B:JOCE.0000038350.32155.cb

Hatayama, T., Awaji, T., Akitomo, K., 1996. Tidal currents in the Indonesian Seas and their effect on transport and mixing. J. Geophys. Res. 101, 12,353-12,373.

Hautala, S.L., Reid, J.L., Bray, N., 1996. The distribution and mixing of Pacific water masses in the Indonesian Seas. J. Geophys. Res. 101, 12,375-12,389.

Hautala, S.L., Sprintall, J., Potemra, J.T., Chong, J.C., Pandoe, W., Bray, N., Ilahude, a. G., 2001. Velocity structure and transport of the Indonesian Throughflow in the major straits restricting flow into the Indian Ocean. J. Geophys. Res. 106, 19527. doi:10.1029/2000JC000577

Helfrich, K.R., 1992. Internal solitary wave breaking and run-up on a uniform slope. J. Fluid Mech 243, 133–154.

Henyey, F.S., Wright, J., Flatté, S.M., 1986. Energy and action flow through the internal wave field: An eikonal approach. J. Geophys. Res. Ocean. 91, 8487–8495. doi:10.1029/JC091iC07p08487

Hibiya, T., Nagasawa, M., Niwa, Y., 1998. Model Predicted Distribution of Internal Wave Energy for Diapycnal Mixing Processes in the Deep Waters of the North Pacific, in: Muller, P., Henderson, D. (Eds.), Dynamics of Oceanic Internal Gravity Waves: Proc.'Aha Huliko'a Hawaiian Winter Workshop. Hawaii Institute of Geophysics, pp. 205–215.

Holloway, P.E., 2001. A regional model of the semidiurnal internal tide on the Australian North West Shelf. J. Geophys. Res. 106, 19625. doi:10.1029/2000JC000675

Holloway, P.E., Pelinovsky, E., Talipova, T., 1999. Modeling internal tide generation and evolution into internal solitary waves on the Australian North West Shelf. Dyn. Ocean. Intern. Gravity Waves II Proc.'Aha Huliko 'a Hawaiian Winter Work.

Hosegood, P., Van Haren, H., 2004. Near-bed solibores over the continental slope in the Faeroe-Shetland Channel. Deep. Res. Part II Top. Stud. Oceanogr. 51, 2943–2971. doi:10.1016/j.dsr2.2004.09.016

Ilahude, a. G., Gordon, A.L., 1996. Thermocline stratification within the Indonesian Seas. J. Geophys. Res. doi:10.1029/95JC03798

Inoue, R., Yamazaki, H., Wolk, F., Kono, T., Yoshida, J., 2007. An Estimation of Buoyancy Flux for a Mixture of Turbulence and Double Diffusion. J. Phys. Oceanogr. 37, 611–624. doi:10.1175/JPO2996.1

Itsweire, E.C., Helland, K.N., Van Atta, C.W., 1986. The evolution of grid-generated turbulence in a stably stratified fluid. J. Fluid Mech. 162, 299–338. doi:10.1017/S0022112086002069

Ivey, G.N., Winters, K.B., Koseff, J.R., 2008. Density Stratification, Turbulence, but How Much Mixing? Annu. Rev. Fluid Mech. 40, 169–184. doi:10.1146/annurev.fluid.39.050905.110314

Jackson, C., 2007. Internal wave detection using the Moderate Resolution Imaging Spectroradiometer (MODIS). J. Geophys. Res. 112, C11012. doi:10.1029/2007JC004220

Jackson, C.R., Da Silva, J.C.B., Jeans, G., 2012. The Generation of Nonlinear Internal Waves. Oceanography 25, 108–123. doi:10.5670/oceanog.2012.46

Jeans, D.R.G., Sherwin, T.J., 2001. The variability of strongly non-linear solitary internal waves observed during an upwelling season on the Portuguese shelf 21, 1855–1878.

Kartadikaria, A.R., Miyazawa, Y., Varlamov, S.M., Nadaoka, K., 2011. Ocean circulation for the Indonesian seas driven by tides and atmospheric forcings: Comparison to observational data. J. Geophys. Res. Ocean. 116, 1–21. doi:10.1029/2011JC007196

Kashino, Y., Aoyama, M., Kawano, T., Hendiarti, N., Muneyama, K., Watanabe, H., Sea, P., 1996. The water masses between Mindanao and New Guinea. J. Geophys. Res. 101, 2,391-12,400.

Kashino, Y., Firing, E., Hacker, P., Sulaiman, A., Lukiyanto, 2001. Currents in the Celebes and Maluku Seas, February 1999. Geophys. Res. Lett. 28, 1263–1266. doi:10.1029/2000GL011630

Kashino, Y., Watanabe, H., Herunadi, B., Aoyama, M., Hartoyo, D., 1999. Current variability at the Pacific entrance of the Indonesian Throughflow. J. Geophys. Res. Ocean. 104, 11021–11035. doi:10.1029/1999JC900033

Klymak, J., Legg, S., Alford, M., Buijsman, M., Pinkel, R., Nash, J., 2012. The Direct Breaking of Internal Waves at Steep Topography. Oceanography 25, 150–159. doi:10.5670/oceanog.2012.50

Klymak, J.M., Legg, S.M., 2010. A simple mixing scheme for models that resolve breaking internal waves. Ocean Model. 33, 224–234. doi:10.1016/j.ocemod.2010.02.005

Klymak, J.M., Moum, J.N., 2003. Internal solitary waves of elevation advancing on a shoaling shelf. Geophys. Res. Lett. 30, 2045–2049. doi:10.1029/2003GL017706

Klymak, J.M., Pinkel, R., Liu, C.T., Liu, A.K., David, L., 2006. Prototypical solitons in the South China Sea. Geophys. Res. Lett. 33, 5–8. doi:10.1029/2006GL025932

Klymak, J.M., Pinkel, R., Rainville, L., 2008. Direct Breaking of the Internal Tide near Topography: Kaena Ridge, Hawaii. J. Phys. Oceanogr. 38, 380–399. doi:10.1175/2007JPO3728.1

Koch-Larrouy, A., Atmadipoera, A., van Beek, P., Madec, G., Aucan, J., Lyard, F., Grelet, J., Souhaut, M., 2015. Estimates of tidal mixing in the Indonesian archipelago from multidisciplinary INDOMIX in-situ data. Deep. Res. Part I Oceanogr. Res. Pap. 106, 136–153. doi:10.1016/j.dsr.2015.09.007

Koch-Larrouy, A., Lengaigne, M., Terray, P., Madec, G., Masson, S., 2010. Tidal mixing in the Indonesian seas and its effect on the tropical climate system. Clim. Dyn. 34, 891–904. doi:10.1007/s00382-009-0642-4

Koch-Larrouy, A., Madec, G., Bouruet-Aubertot, P., Gerkema, T., Bessières, L., Molcard, R., 2007. On the transformation of Pacific Water into Indonesian Throughflow Water by internal tidal mixing. Geophys. Res. Lett. 34. doi:10.1029/2006GL028405

Koseff, J.R., Holen, J.K., Monismith, S.G., Cloern, J.E., 1993. Coupled effects of vertical mixing and benthic grazing on phytoplankton populations in shallow, turbid estuaries. J. Mar. Res. 51, 843–868. doi:10.1357/0022240933223954

Kunze, E., Firing, E., Hummon, J.M., Chereskin, T.K., Thurnherr, A.M., 2006. Global Abyssal Mixing Inferred from Lowered ADCP Shear and CTD Strain Profiles. J. Phys. Oceanogr. 36, 1553–1576. doi:10.1175/JPO2926.1

Kunze, E., Rosenfeld, L.K., Carter, G.S., Gregg, M.C., 2002. Internal Waves in Monterey Submarine Canyon. J. Phys. Oceanogr. 32, 1890–1913. doi:10.1175/1520-0485(2002)032<1890:IWIMSC>2.0.CO;2

Kunze, E., Williams, A.J., Briscoe, M.G., 1990. Observations of shear and vertical stability from a neutrally buoyant float. J. Geophys. Res. 95, 18127. doi:10.1029/jc095ic10p18127

Lamb, K.G., Nguyen, V.T., 2009. Calculating Energy Flux in Internal Solitary Waves with an Application to Reflectance. J. Phys. Oceanogr. 39, 559–580. doi:10.1175/2008JPO3882.1

Ledwell, J.R., St. Laurent, L.C., Girton, J.B., Toole, J.M., 2011. Diapycnal Mixing in the Antarctic Circumpolar Current. J. Phys. Oceanogr. 41, 241–246. doi:10.1175/2010JPO4557.1

Lee, C.M., Sanford, T.B., Kunze, E., Nash, J.D., Merrifield, M.A., Holloway, P.E., 2006. Internal Tides and Turbulence along the 3000-m Isobath of the Hawaiian Ridge. J. Phys. Oceanogr. 36, 1165–1183. doi:10.1175/JPO2886.1

Lee, I.H., Lien, R.C., Liu, J.T., Chuang, W. ssn, 2009. Turbulent mixing and internal tides in Gaoping (Kaoping) Submarine Canyon, Taiwan. J. Mar. Syst. 76, 383–396. doi:10.1016/j.jmarsys.2007.08.005

Lee, T., Fukumori, I., Menemenlis, D., Xing, Z.F., Fu, L.-L., 2002. Effects of the Indonesian Throughflow on the Pacific and Indian oceans. J. Phys. Oceanogr. 32, 1404–1429. doi:Doi 10.1175/1520-0485(2002)032<1404:Eotito>2.0.Co;2

Li, L., Wang, C., Grimshaw, R., 2015. Observation of internal wave polarity conversion generated by a rising tide. Geophys. Res. Lett. 42, 4007–4013. doi:10.1002/2015GL063870

Liu, A.K., Holbrook, J.R., Apel, J.R., 1985. Nonlinear Internal Wave Evolution in the Sulu Sea. J. Phys. Oceanogr. doi:10.1175/1520-0485(1985)015<1613:NIWEIT>2.0.CO;2

Lozovatsky, I.D., Fernando, H.J.S., 2013. Mixing efficiency in natural Flows. Philos. Trans. R. Soc. A Math. Phys. Eng. Sci. 371. doi:10.1098/rsta.2012.0213

Lozovatsky, I.D., Roget, E., Fernando, H.J.S., Figueroa, M., Shapovalov, S., 2006. Sheared turbulence in a weakly stratified upper ocean. Deep. Res. Part I Oceanogr. Res. Pap. 53, 387–407. doi:10.1016/j.dsr.2005.10.002

MacKinnon, J.A., Zhao, Z., Whalen, C.B., Waterhouse, A.F., Trossman, D.S., Sun, O.M., St. Laurent, L.C., Simmons, H.L., Polzin, K., Pinkel, R., Pickering, A., Norton, N.J., Nash, J.D., Musgrave, R., Merchant, L.M., Melet, A. V., Mater, B., Legg, S., Large, W.G., Kunze, E., Klymak, J.M., Jochum, M., Jayne, S.R., Hallberg, R.W., Griffies, S.M., Diggs, S., Danabasoglu, G., Chassignet, E.P., Buijsman, M.C., Bryan, F.O., Briegleb, B.P., Barna, A., Arbic, B.K., Ansong, J.K., Alford, M.H., Sun, O.M., Barna, A., St. Laurent, L.C., Buijsman, M.C., Melet, A. V., Arbic, B.K., Large, W.G., MacKinnon, J.A., Jochum, M., Nash, J.D., Klymak, J.M., Pinkel, R., Musgrave, R., Ansong, J.K., Polzin, K., Chassignet, E.P., Pickering, A., Merchant, L.M., Simmons, H.L., Diggs, S., Mater, B., Jayne, S.R., Hallberg, R.W., Danabasoglu, G., Waterhouse, A.F., Trossman, D.S., Whalen, C.B., Zhao, Z., Briegleb, B.P., Alford, M.H., Bryan, F.O., Kunze, E., Legg, S., Norton, N.J., 2017. Climate Process Team on Internal Wave–Driven Ocean Mixing. Bull. Am. Meteorol. Soc. 98, 2429–2454. doi:10.1175/BAMS-D-16-0030.1

Masumoto, Y., Yamagata, T., 1996. Seasonal variations of the Indonesian throughflow in a general ocean circulation model. J. Geophys. Res. 101, 12,287-12,293.

Mater, B.D., Venayagamoorthy, S.K., St. Laurent, L., Moum, J.N., 2015. Biases in Thorpe-Scale Estimates of Turbulence Dissipation. Part I: Assessments from Large-Scale Overturns in Oceanographic Data. J. Phys. Oceanogr. 45, 2497–2521. doi:10.1175/JPO-D-14-0128.1

Matthews, J.P., Aiki, H., Masuda, S., Awaji, T., Ishikawa, Y., 2011. Monsoon regulation of Lombok Strait internal waves. J. Geophys. Res. Ocean. 116, 1–14. doi:10.1029/2010JC006403

Maxworthy, T., 1979. A note on the internal solitary waves produced by tidal flow over a three-dimensional ridge. J. Geophys. Res. 84.

Mayer, B., Damm, P.E., 2012. The Makassar Strait throughflow and its jet. J. Geophys. Res. Ocean. 117, 1–14. doi:10.1029/2011JC007809

Middleton, J.H., Foster, T.D., 1980. Fine structure measurements in a temperature-compensated halocline. J. Geophys. Res. Ocean. 85, 1107–1122. doi:10.1029/JC085iC02p01107

Molcard, R., Fieux, M., Syamsudin, F., 2001. The throughflow within Ombai Strait. Deep. Res. Part I Oceanogr. Res. Pap. 48, 1237–1253. doi:10.1016/S0967-0637(00)00084-4

Monismith, S.G., Koseff, J.R., White, B.L., 2018. Mixing Efficiency in the Presence of Stratification: When Is It Constant? Geophys. Res. Lett. 45, 5627–5634. doi:10.1029/2018GL077229

Moum, J.N., 1996a. Energy-containing scales of turbulence in the ocean thermocline. J. Geophys. Res. 101, 14095. doi:10.1029/96JC00507

Moum, J.N., 1996b. Efficiency of mixing in the main thermocline. J. Geophys. Res. Ocean. 101, 12177–12191. doi:10.1029/96JC00463

Moum, J.N., 1990. The Quest for Kϱ—Preliminary Results from Direct Measurements of Turbulent Fluxes in the Ocean. J. Phys. Oceanogr. 20, 1980–1984. doi:10.1175/1520-0485(1990)020<1980:TQFRFD>2.0.CO;2

Moum, J.N., Farmer, D.M., Smyth, W.D., Armi, L., Vagle, S., 2003. Structure and Generation of Turbulence at Interfaces Strained by Internal Solitary Waves Propagating Shoreward over the Continental Shelf. J. Phys. Oceanogr. 33, 2093–2112. doi:10.1175/1520-0485(2003)033<2093:SAGOTA>2.0.CO;2

Moum, J.N., Nash, J.D., Smyth, W.D., 2011. Narrowband oscillations in the upper equatorial Ocean. Part I: Interpretation as shear instabilities. J. Phys. Oceanogr. 41, 397–411. doi:10.1175/2010JPO4450.1

Munk, W., 2001. Spirals on the sea. Sci. Mar. 65, 193–198. doi:10.3989/scimar.2001.65s2193

Munk, W., Wunsch, C., 1998. Abyssal recipes II: energetics of tidal and wind mixing. Deep Sea Res. Part I Oceanogr. Res. Pap. 45, 1977–2010.

Murray, S.P., Arief, D., 1988. Throughflow into the Indian Ocean through the Lombok Strait, January 1985–January 1986. Nature 333, 444–447. doi:10.1038/333444a0

Nagai, T., Hibiya, T., 2015. Internal tides and associated vertical mixing in the Indonesian Archipelago. J. Geophys. Res. C Ocean. 3373–3390. doi:10.1002/2014JC010592

Nagai, T., Hibiya, T., Bouruet-Aubertot, P., 2017. Nonhydrostatic Simulations of Tide-Induced Mixing in the Halmahera Sea: A Possible Role in the Transformation of the Indonesian Throughflow Waters. J. Geophys. Res. Ocean. 122, 8933–8943. doi:10.1002/2017JC013381

Nam, S., Send, U., 2011. Direct evidence of deep water intrusions onto the continental shelf via surging internal tides. J. Geophys. Res. Ocean. 116, 1–15. doi:10.1029/2010JC006692

Nash, J.D., Alford, M.H., Kunze, E., 2005. Estimating internal wave energy fluxes in the ocean. J. Atmos. Ocean. Technol. 22, 1551–1570. doi:10.1175/JTECH1784.1

Nash, J.D., Moum, J.N., 2001. Internal hydraulic flows on the continental shelf: High drag states over a small bank. J. Geophys. Res. 106, 4593–4611. doi:10.1029/1999jc000183

Nugroho, D., Koch-larrouy, A., Gaspar, P., Lyard, F., Re, G., Tranchant, B., 2017. Modelling explicit tides in the Indonesian seas : An important process for surface sea water properties. Mar. Pollut. Bull. doi:10.1016/j.marpolbul.2017.06.033

Nycander, J., 2005. Generation of internal waves in the deep ocean by tides. J. Geophys. Res. C Ocean. 110, 1–9. doi:10.1029/2004JC002487

Oakey, N.S., 1982. Determination of the Rate of Dissipation of Turbulent Energy from Simultaneous Temperature and Velocity Shear Microstructure Measurements. J. Phys. Oceanogr. 12, 256–271. doi:10.1175/1520-0485(1982)012<0256:DOTROD>2.0.CO;2

Osborn, T.R., 1980. Estimates of the Local Rate of Vertical Diffusion from Dissipation Measurements. J. Phys. Oceanogr. doi:10.1175/1520-0485(1980)010<0083:EOTLRO>2.0.CO;2

Ozmidov, V.R., 1965. On the turbulent exchange in a stably stratified ocean. Izv. Acad. Sci. USSR. Atmos. Ocean. Phys. 1, 861–871.

Padman, L., Dillon, T.M., 1987. Vertical heat fluxes through the Beaufort Sea thermohaline staircase. J. Geophys. Res. Ocean. 92, 10799–10806. doi:10.1029/JC092iC10p10799

Park, Y.G., Whitehead, J.A., Gnanadeskian, A., 1994. Turbulent Mixing in Stratified Fluids: Layer Formation and Energetics. J. Fluid Mech. 279, 279–311. doi:10.1017/S0022112094003915

Park, Y.H., Lee, J.H., Durand, I., Hong, C.S., 2014. Validation of Thorpe-scale-derived vertical diffusivities against microstructure measurements in the Kerguelen region. Biogeosciences 11, 6927–6937. doi:10.5194/bg-11-6927-2014

Peters, H., Gregg, M.C., Toole, J.M., 1988. On the parameterization of equatorial turbulence. J. Geophys. Res. Ocean. 93, 1199–1218. doi:10.1029/JC093iC02p01199

Pineda, J., López, M., 2002. Temperature, stratification and barnacle larval settlement in two Californian sites. Cont. Shelf Res. 22, 1183–1198. doi:10.1016/S0278-4343(01)00098-X

Polzin, K.L., Toole, J.M., Schmitt, R.W., 1995. Finescale parameterizations of turbulent dissipation. J. Phys. Oceanogr. 25, 306–328. doi:10.1002/2013JC008979

Potemra, J.T., Hautala, S., Sprintall, J., Pandoe, W., 2002. Interaction between the Indonesian Seas and the Indian Ocean in Observations and Numerical Models *. J. Phys. Oceanogr. 32, 1838–1854.

Purwandana, A., 2014. Distribution of Turbulent Mixing in Alor Strait. Ilmu Kelaut. 19, 43–55.

Purwandana, A., 2008. Velocity structure and transport of the throughflow in Dampier Strait, West Papua. Segara 4, 133–141.

Purwandana, A., Cuypers, Y., Bouruet-aubertot, P., Nagai, T., Hibiya, T., Atmadipoera, A.S., 2019. Spatial structure of the turbulent mixing inferred from historical CTD data sets in

the Indonesian seas. Prog. Oceanogr. (under Rev.

Purwandana, A., Purba, M., Atmadipoera, A.S., Oseanografi-lipi, P., Perikanan, F., Bogor, I.P., Darmaga, K.I.P.B., 2014. Distribusi Percampuran Turbulen di Perairan Selat Alor. ILMU Kelaut. Indones. J. Mar. Sci. 19, 43–54. doi:10.14710/ik.ijms.19.1.43-54

Qu, T., Song, Y.T., 2009. Mindoro Strait and Sibutu Passage transports estimated from satellite data. Geophys. Res. Lett. 36, 1–5. doi:10.1029/2009GL037314

Ramp, S.R., Tang, T.Y., Duda, T.F., Lynch, J.F., Liu, A.K., Chiu, C.S., Bahr, F.L., Kim, H.R., Yang, Y.J., 2004. Internal solitons in the northeastern South China Sea Part I: Sources and deep water propagation. IEEE J. Ocean. Eng. 29, 1157–1181. doi:10.1109/JOE.2004.840839

Ray, R., Egbert, G., 2005. Tides in the Indonesian Seas. Oceanography 18, 74–79.

Ray, R.D., Susanto, R.D., 2016. Tidal mixing signatures in the Indonesian seas from high-resolution sea surface temperature data. Geophys. Res. Lett. 43, 8115–8123. doi:10.1002/2016GL069485

Reynolds, O., 1883. An experimental investigation of the circumstances which determine whether the motion of water in parallel channels shall be direct or sinuous and of the lSociety, The Royal Transactions, Philosophical Society, Royalaw of resistance in parallel channels. Soc. R. Trans. Philos. Soc. R. 174, 935–982.

Robertson, R., 2010. Tidal currents and mixing at the INSTANT mooring locations. Dyn. Atmos. Ocean. 50, 331–373. doi:10.1016/j.dynatmoce.2010.02.004

Robertson, R., Ffield, A., 2005. M2 Baroclinic Tides in the Indonesian Seas. Oceanography 18, 62–73. doi:10.5670/oceanog.2005.06

Ruddick, B., 1983. A practical indicator of the stability of the water column to double-diffusive activity. Deep Sea Res. Part A. Oceanogr. Res. Pap. 30, 1105–1107. doi:https://doi.org/10.1016/0198-0149(83)90063-8

Sandstrom, H., Oakey, N.S., 1995. Dissipation in Internal Tides and Solitary Waves. J. Phys. Oceanogr. doi:10.1175/1520-0485(1995)025<0604:DIITAS>2.0.CO;2

Schiller, A., 2004. Effects of explicit tidal forcing in an OGCM on the water-mass structure and circulation in the Indonesian throughflow region. Ocean Model. 6, 31–49. doi:10.1016/S1463-5003(02)00057-4

Scotti, A., 2015. Biases in Thorpe-Scale Estimates of Turbulence Dissipation. Part II: Energetics Arguments and Turbulence Simulations. J. Phys. Oceanogr. 45, 2522–2543. doi:10.1175/JPO-D-14-0092.1

Shih, L.H., Koseff, J.R., Ivey, G.N., Ferziger, J.H., 2005. Parameterization of turbulent fluxes and scales using homogeneous sheared stably stratified turbulence simulations. J. Fluid Mech. 525, 193–214. doi:DOI: 10.1017/S0022112004002587

Simmons, H.L., Hallberg, R.W., Arbic, B.K., 2004. Internal wave generation in a global baroclinic tide model. Deep. Res. Part II Top. Stud. Oceanogr. 51, 3043–3068. doi:10.1016/j.dsr2.2004.09.015

Simpson, J.H., Crawford, W.R., Rippeth, T.P., Campbell, A.R., Cheok, J.V.S., 1996. The Vertical Structure of Turbulent Dissipation in Shelf Seas. J. Phys. Oceanogr. doi:10.1175/1520-0485(1996)026<1579:TVSOTD>2.0.CO;2

Smagorinsky, J., 1963. General Circulation Experiments With the Primitive Equations. Mon. Weather Rev. 91, 99–164. doi:10.1175/1520-0493(1963)091<0099:GCEWTP>2.3.CO;2

Smyth, W.D., Moum, J.N., Caldwell, D.R., 2001. The Efficiency of Mixing in Turbulent Patches: Inferences from Direct Simulations and Microstructure Observations. J. Phys. Oceanogr. 31, 1969–1992. doi:10.1175/1520-0485(2001)031<1969:TEOMIT>2.0.CO;2

Sprintall, J., Chong, J., Syamsudin, F., Morawitz, W., Hautala, S., Bray, N., Wijffels, S., 1999. Dynamics of the South Java Current in the Indo-Australian Basin. Geophys. Res. Lett. 26, 2493–2496.

Sprintall, J., Potemra, J.T., Hautala, S.L., Bray, N.A., Pandoe, W.W., 2003. Temperature and salinity variability in the exit passages of the Indonesian Throughflow. Deep. Res. Part II Top. Stud. Oceanogr. 50, 2183–2204. doi:10.1016/S0967-0645(03)00052-3

Sprintall, J., Wijffels, S., Gordon, A.L., Ffield, A., Molcard, R., Susanto, R.D., Soesilo, I., Sopaheluwakan, J., Surachman, Y., van Aken, H.M., 2004. INSTANT: A New International Array to Measure the Indonesian Throughflow. Eos (Washington. DC). 85, 369–376. doi:10.1029/2004EO390001

Sprintall, J., Wijffels, S.E., Molcard, R., Jaya, I., 2009. Direct estimates of the indonesian throughflow entering the indian ocean: 2004-2006. J. Geophys. Res. Ocean. 114, 2004–2006. doi:10.1029/2008JC005257

Sprintall, Janet, Wuffels, S., Gordon, A.L., Field, A.F., Molcard, R., Susaoto, R.D., Soesilo, I., Sopaheluwakan, J., Surachman, Y., Van Aken, H.M., 2004. Instant: A new international array to measure the indonesian throughflow. Eos (Washington. DC). 85, 9–11. doi:10.1029/2004EO390002

St. Laurent, L., Alford, M.H., Paluszkiewicz, T., 2012. An introduction to the special issue on internal waves. Oceanography 25, 15–19. doi:10.5670/oceanog.2011.65

St. Laurent, L., Garrett, C., 2002. The Role of Internal Tides in Mixing the Deep Ocean. J. Phys. Oceanogr. 32, 2882–2899. doi:10.1175/1520-0485(2002)032<2882:TROITI>2.0.CO;2

St. Laurent, L.C., Simmons, H.L., Jayne, S.R., 2002. Estimating tidally driven mixing in the deep ocean. Geophys. Res. Lett. 29, 21-1-21–4. doi:10.1029/2002gl015633

Stansfield, K., Garrett, C., Dewey, R., 2001. The Probability Distribution of the Thorpe Displacement within Overturns in Juan de Fuca Strait. J. Phys. Oceanogr. 31, 3421–3434. doi:10.1175/1520-0485(2001)031<3421:TPDOTT>2.0.CO;2

Stern, M.E., 1960. The "Salt-Fountain" and Thermohaline Convection. Tellus 12, 172–175. doi:10.3402/tellusa.v12i2.9378

Susanto, R.D., Gordon, A.L., Zheng, Q., 2001. Upwelling along the coasts of Java and Sumatra and its relation to ENSO. Geophys. Res. Lett. doi:10.1029/2000GL011844

Susanto, R.D., Mitnik, L., Zheng, Q., 2005. Ocean Internal Waves Observed in the Lombok Strait. Oceanography 18, 80–87. doi:10.5670/oceanog.2005.08

Susanto, R.D., Wei, Z., Adi, R.T., Fan, B., Li, S., Fang, G., 2013. Observations of the Karimata Strait througflow from December 2007 to November 2008. Acta Oceanol. Sin. 32, 1–6. doi:10.1007/s13131-013-0307-3

Suteja, Y., Purba, M., Atmadipoera, A.S., 2015. Percampuran Turbulen di Selat Ombai. J. Ilmu dan Teknol. Kelaut. Trop. 7, 71–82.

Thorpe, S.A., 2005. The Turbulent Ocean. Cambridge University Press, Cambridge. doi:DOI: 10.1017/CBO9780511819933

Thorpe, S.A., 2004. Recent Developments in the Study of Ocean Turbulence. Annu. Rev. Earth Planet. Sci. 32, 91–109. doi:10.1146/annurev.earth.32.071603.152635

Thorpe, S.A., 1977. Turbulence and Mixing in a Scottish Loch. Philos. Trans. R. Soc. A Math. Phys. Eng. Sci. 286, 125–181. doi:10.1098/rsta.1977.0112

Tsuchiya, M., Lukas, R., Fine, R.A., Firing, E., Lindstrom, E., 1989. Source waters of the Pacific Equatorial Undercurrent. Prog. Oceanogr. 23, 101–147. doi:https://doi.org/10.1016/0079-6611(89)90012-8

van Aken, H.M., Brodjonegoro, I.S., Jaya, I., 2009. The deep-water motion through the Lifamatola Passage and its contribution to the Indonesian throughflow. Deep. Res. Part I Oceanogr. Res. Pap. 56, 1203–1216. doi:10.1016/j.dsr.2009.02.001

van Aken, H.M., Punjanan, J., Saimima, S., 1988. Physical aspects of the flushing of the east Indonesian basins. Netherlands J. Sea Res. 22, 315–339. doi:10.1016/0077-7579(88)90003-8

van Bennekom, A.J., 1988. Deep-water transit times in the eastern Indonesian basins, calculated from dissolved silica in deep and interstitial waters. Netherlands J. Sea Res. 22, 341–354. doi:10.1016/0077-7579(88)90004-X

van Haren, H., Gostiaux, L., 2010. A deep-ocean Kelvin-Helmholtz billow train. Geophys. Res. Lett. 37, 1–5. doi:10.1029/2009GL041890

van Haren, H., Gostiaux, L., 2009. High-resolution open-ocean temperature spectra. J. Geophys. Res. Ocean. 114, 1–14. doi:10.1029/2008JC004967

van Riel, P.M., 1932. The snellius expedition. ICES J. Mar. Sci. 7, 212–217. doi:10.1093/icesjms/7.2.212

van Riel, P.M., 1930. The Snellius Expedition. Nature 125, 761–762.

Venayagamoorthy, S.K., Fringer, O.B., 2007. On the formation and propagation of nonlinear internal boluses across a shelf break. J. Fluid Mech. 577, 137–159. doi:10.1017/S0022112007004624

Venayagamoorthy, S.K., Fringer, O.B., 2006. Numerical simulations of the interaction of internal waves with a shelf break. Phys. Fluids 18. doi:10.1063/1.2221863

Visser, W.. P., 2004. On the generation of internal waves in Lombok Strait through Kelvin-Helmholtz instability.

Vitousek, S., Fringer, O.B., 2011. Physical vs. numerical dispersion in nonhydrostatic ocean modeling. Ocean Model. 40, 72–86. doi:10.1016/j.ocemod.2011.07.002

Vladoiu, A., Bouruet-Aubertot, P., Cuypers, Y., Ferron, B., Schroeder, K., Borghini, M., Leizour, S., Ismail, S. Ben, 2019. Mixing efficiency from microstructure measurements in the Sicily Channel. Ocean Dyn. doi:10.1007/s10236-019-01274-2

Vlasenko, V., Sanchez Garrido, J.C., Stashchuk, N., Garcia Lafuente, J., Losada, M., 2009. Three-Dimensional Evolution of Large-Amplitude Internal Waves in the Strait of Gibraltar. J. Phys. Oceanogr. 39, 2230–2246. doi:10.1175/2009jpo4007.1

Walter, R.K., 2014. Nonlinear internal waves, internal bores, and turbulent mixing in the nearshore coastal environment 1–264.

Wattimena, M.C., Atmadipoera, A.S., Purba, M., Koch-larrouy, A., 2014. Variabilitas intra-musiman arus dekat-dasar di Laut Halmahera 6, 267–281.

Wattimena, M.C., Atmadipoera, A.S., Purba, M., Nurjaya, I.W., Syamsudin, F., 2018.

Indonesian Throughflow (ITF) variability in Halmahera Sea and its coherency with New Guinea Coastal Current. IOP Conf. Ser. Earth Environ. Sci. doi:10.1088/1755-1315/176/1/012011

Whalen, C.B., Talley, L.D., MacKinnon, J.A., 2012. Spatial and temporal variability of global ocean mixing inferred from Argo profiles. Geophys. Res. Lett. 39, 1–6. doi:10.1029/2012GL053196

Wijesekera, H., Padman, L., Dillon, T., Levine, M., Paulson, C., Pinkel, R., 1993. The Application of Internal-Wave Dissipation Models to a Region of Strong Mixing. J. Phys. Oceanogr. 23, 269–286. doi:10.1175/1520-0485(1993)023<0269:taoiwd>2.0.co;2

Wijffels, S., Sprintall, J., Fieux, M., Bray, N., 2002. The JADE and WOCE I10 / IR6 Throughflow sections in the southeast Indian Ocean . Part 1 : water mass distribution and variability. Deep Sea Res. Part II Top. Stud. Oceanogr. 49, 1341–1362.

Wunsch, C., Ferrari, R., 2004. Vertical mixing, energy, and the general circulation of the oceans. Annu. Rev. Fluid Mech. 36, 281–314. doi:10.1146/annurev.fluid.36.050802.122121

Wyrtki, K., 1987. Indonesian through flow and the associated pressure gradient. J. Geophys. Res. 92, 12941. doi:10.1029/JC092iC12p12941

Wyrtki, K., 1961. Physical oceanography of the Southeast Asian waters. Scietific Resultas Mar. Investig. South China Sea Gulf Thail. 2, 195. doi:10.1017/S0025315400054370

Xie, X.H., Cuypers, Y., Bouruet-Aubertot, P., Ferron, B., Pichon, A., Lourenço, A., Cortes, N., 2013. Large-amplitude internal tides, solitary waves, and turbulence in the central Bay of Biscay. Geophys. Res. Lett. 40, 2748–2754. doi:10.1002/grl.50533

Yamazaki, H., 1990. Stratified turbulence near a critical dissipation rate. J Phys Ocean. doi:10.1175/1520-0485(1990)020<1583:STNACD>2.0.CO;2

Yang, Q., Zhao, W., Li, M., Tian, J., 2014. Spatial Structure of Turbulent Mixing in the Northwestern Pacific Ocean. J. Phys. Oceanogr. 44, 2235–2247. doi:10.1175/JPO-D-13-0148.1

Yuan, D., Li, X., Wang, Z., Li, Y., Wang, J., Yang, Y., Hu, X., Tan, S., Zhou, H., Wardana, A.K., Surinati, D., Purwandana, A., Azis Ismail, M.F., Avianto, P., Dirhamsyah, D., Arifin, Z., Storch, J.-S. von, 2018. Observed Transport Variations in the Maluku Channel of the Indonesian Seas Associated with Western Boundary Current Changes. J. Phys. Oceanogr. 48, 1803–1813. doi:10.1175/JPO-D-17-0120.1

Zhang, Y., Moum, J.N., 2010. Inertial-Convective subrange estimates of thermal variance dissipation rate from moored temperature measurements. J. Atmos. Ocean. Technol. 27, 1950–1959. doi:10.1175/2010JTECHO746.1

Zhao, Z., Alford, M.H., 2006. Source and propagation of internal solitary waves in the northeastern South China Sea. J. Geophys. Res. Ocean. 111, 1–14. doi:10.1029/2006JC003644

Zhao, Z., Klemas, V., Zheng, Q., Yan, X.-H., 2004. Remote sensing evidence for baroclinic tide origin of internal solitary waves in the northeastern South China Sea. Geophys. Res. Lett. 31, n/a-n/a. doi:10.1029/2003gl019077